VNIVERSITAT DE VALÈNCIA

Precision measurements with the LHC and low-energy experiments: a model-independent analysis

Tesi Doctoral
Programa de Doctorat en Física - 3126

Víctor Bresó Pla

Directors: Dr. Martín González Alonso y Dr. Antonio Pich Zardoya

IFIC - CSIC/Universitat de València
Departament de Física Teòrica

València, octubre de 2023

Martín González Alonso, Investigador Distingit de la Universitat de València, i **Antonio Pich Zardoya**, catedràtic de la Universitat de València,

certifiquen:

que la present memòria, Precision measurements with the LHC and low-energy experiments: a model-independent analysis, ha sigut realitzada sota la seua direcció a l'Institut de Física Corpuscular, centre mixte de la Universitat de València y del CSIC, per **Víctor Ernesto Bresó Pla**, i constitueix la seua Tesi per a optar al grau de Doctor en Física.

I perquè així conste, en complimient de la legislació vigent, presenta en el Departament de Física Teórica de la Universitat de València la referida Tesi Doctoral, i firmen el present certificat.

València, a 28 de juliol de 2023,

Martín González Alonso

Antonio Pich Zardoya

A mi familia y amigos,
por creer en mí siempre.

List of scientific publications

This thesis is based on the following publications:

1. A_{FB} ***in the SMEFT: precision Z physics at the LHC***
   V. Bresó-Pla, A. Falkowski, M. González-Alonso
   Journal: JHEP 08 (2021) 021
   Preprint: 2103.12074

2. A_{FB} ***in the SMEFT: the LHC as a Z physics laboratory***
   V. Bresó-Pla
   Proceedings for the 32nd Rencontres de Blois conference

3. ***EFT analysis of CEνNS data***
   V. Bresó-Pla
   Journal: PoS ICHEP2022 (2022) 579
   Proceedings for the International Conference in Particle Physics (ICHEP) 2022

4. ***EFT analysis of New Physics at COHERENT***
   V. Bresó-Pla, A. Falkowski, M. González-Alonso, K. Monsálvez-Pozo
   Journal: JHEP 05 (2023) 074
   Preprint: 2301.07036

Contents

List of Acronyms

BR	Branching Ratio
BRN	Beam-Related Neutron
CC	Charged Current
CEnNS	Coherent Elastic Neutrino Scattering off Nuclei
ChPT	Chiral Perturbation Theory
CKM	Cabibbo-Kobayashi-Maskawa
CP	Charge Conjugation times Parity
CsI	Cesium and Iodine
CV	Central Value
DM	Dark Matter
EFT	Effective Field Theory
EW	Electroweak
EWPO	Electroweak Precision Observables
GIM	Glashow–Iliopoulos–Maiani
HQET	Heavy Quark Effective Field Theory
i.i.d	Independent and Identically Distributed
IR	Infrared
LAr	Liquid Argon
LEFT	Low-energy Effective Field Theory
LEP	Large Electron–Positron Collider
LHC	Large Hadron Collider
LLLL	4 Leptons
LLQQ	2 Leptons and 2 Quarks
LSZ	Lehmann–Symanzik–Zimmerman
NDA	Naive Dimensional Analysis
NC	Neutral Current
NIN	Neutrino-Induced Neutron
NSI	Non-Standard Interaction
NP	New Physics
PE	Photoelectron
PMNS	Pontecorvo-Maki-Nakagawa-Sakata
PDF	Parton Distribution Function
QCD	Quantum Chromodynamics
QED	Quantum Electrodynamics
QFT	Quantum Field Theory
QF	Quenching Factor

RGEs	Renormalization Group Equations
SCET	Soft Collinear Effective Field Theory
SILH	Strongly-Interacting Light Higgs
SM	Standard Model
SMEFT	Standard Model Effective Field Theory
SNS	Spallation Neutron Source
SS	Steady State
SSB	Spontaneous Symmetry Breaking
UV	Ultraviolet
WC	Wilson Coefficient
WCxf	Wilson Coefficient exchange format
WEFT	Weak Effective Field Theory

Preface

Particle physics is currently immersed in a trend of deep uncertainty. Looking at the history of the field, it is hard to see why this is the case. Over fifty years ago, a theory achieved the extraordinary accomplishment of fully describing the fundamental interactions that take place between elementary particles: the Standard Model. This theory has proven itself to be one of the most successful theories not only in the history of physics, but in the history of science altogether. From the theoretical side, it is a solid framework that is able to describe in a unified way three of the fundamental interactions of nature: the electromagnetic force, the weak nuclear force and the strong nuclear force. On the experimental side, it has been subject of countless tests that have pushed both theory and experiments to unprecedented levels of precision. Despite this, the Standard Model has been able to withstand all trials, and today it stands as a solid and self-consistent theoretical framework.

However, despite the numerous achievements that the Standard Model has attained, it is well known that it must be an incomplete description of nature. There are several theoretical considerations and experimental observations that, although not challenging the Standard Model directly, cannot be explained by it. This scenery has kick started a race to find a theory that can surpass and extend the Standard Model or, failing that, any experimental result that cannot be covered by its descriptions. This thesis is one more component in this quest for physics beyond the Standard Model. Our approach does not rely in any concrete model of new physics, and we also do not examine any specific experimental result that may stand in tension with the Standard Model prescriptions. Instead, we choose take a model independent perspective and use precision techniques to examine how well the Standard Model agrees with experimental data. The main idea is to understand if new physics effects can be inferred from precision measurements.

We will perform this task using effective field theories as our primary research tool, and we will focus on hunting for new physics effects in observables located in a low energy environment around and below the electroweak scale. Our results will come in the form of parameter fits, which will quantify the possible values that a new physics contribution can take according to the information contained in the data. One of our main priorities will be to target as many beyond the Standard Model signatures as possible. This will force us to consider many experimental sources and to understand in detail their interplay when it comes to new physics sensitivity. The main contribution of this thesis is the inclusion of two new experiments into this collection of inputs used in the new physics fit at low energies: the LHC (in particular, its $pp \to e^+e^-, \mu^+\mu^-$ observables) and the COHERENT experiment. As we will discuss in the main body of this work, each of them adds valuable information for unraveling potential new physics effects hidden in previously studied precision observables. All in all, the ultimate value that our results put forward is in the part they play in casting more light on what may lie beyond the Standard Model.

The content of this thesis is organized as follows. In Chapter 1 we will give a brief overview on the foundations of the Standard Model and on how it produces concrete predictions for observables in particle physics. In Chapter 2, we will describe in detail effective field theories, with special focus on the specific theory that we will be working with: the Standard Model Effective Field Theory. In this chapter we will also discuss the statistical tools that are used to build new physics parameter fits. Chapter 3 sets up the starting point of our work: a global fit focused on observables at the electroweak sector. The discussion presented there will provide the necessary context for our main contributions, which we will lay out in the following chapters. In Chapter 4 we will add measurements of the LHC Drell-Yan forward backward asymmetry taken at the Z boson peak to the global fit. As we will see, their input will provide crucial information for fitting new physics parameters linked to the Z couplings. We will continue expanding the global fit inputs in Chapter 5, where we will incorporate recent measurements from the COHERENT experiment, demonstrating how neutrino detection experiments have an important and rightful place in precision fits. In Chapter 6 we will follow up on the results from Chapter 4, including more information coming from LHC measurements. That specific analysis will target four-fermion interactions, clearing some notable blind spots in the global fit from Chapter 3. Finally, in Chapter 7 we will recapitulate our results and offer some final remarks. We close the thesis with a summary of its contents written in Valencian and an appendix to some of the topics discussed in Chapter 5.

Chapter 1

The Standard Model

The Standard Model (SM) [1–4] is a theory built to describe strong, weak and electromagnetic interactions. It is a quantum field theory formulated with gauge symmetry as its fundamental building block. It represents elementary particles as quantum fields characterized through representations of the Lorentz group and the local symmetry group $SU(3)_C \bigotimes SU(2)_L \bigotimes U(1)_Y$. The particle content consists of spin-one-half quarks and leptons, spin-one gauge bosons and the spin-zero Higgs boson. The interactions between the fermionic fields are described through the exchange of bosonic fields, and they are invariant under the action of the symmetry group. Through these guiding principles, the SM constitutes an elegant and simple framework able to describe the experimental data in particle physics with high precision, and it stands as one of the biggest achievements in modern physics. In this chapter we will briefly present this theory and discuss its most important features. We will focus specially on how the SM is able to produce predictions about physical phenomena, as we are mainly interested in its phenomenology. We will also dedicate special attention to its renormalizability, as the concepts involved in it will be essential to understand the tools that we will be using for new physics searches. We will close by describing the current problems and limitations that the SM is facing, setting the ground for the main work compiled in this thesis. For a more in depth review of the SM, we refer to [5].

1.1. Gauge invariance and the SM lagrangian

Gauge invariance is a fundamental principle in the SM. It manifests at the lagrangian level as a symmetry under phase transformations dependent on space-time coordinates. Imposing invariance under such transformations on fermionic fields requires the introduction of bosonic new fields whose properties are completely fixed by the symmetry requirements.

The fermionic content of the SM theory consists of all the known quarks and leptons, described by fields with definite chirality

$$q_L = \begin{pmatrix} u_L \\ d_L \end{pmatrix}, \quad l_L = \begin{pmatrix} \nu_L \\ e_L \end{pmatrix}, \quad u_R, \quad d_R, \quad e_R, \tag{1.1}$$

plus their respective antiparticles. Note that right-handed neutrinos do not appear on this list, as they have not been observed in nature. The left-handed fields transform as doublets under the $SU(2)_L$ group, while the right-handed fields are $SU(2)_L$ singlets. The more specific representations of the symmetry group under which these fields transform are shown in Table 1.1.

Table 1.1: Gauge symmetry group representations for the fermionic degrees of freedom in the SM. The representations in $SU(3)_C$ and $SU(2)_L$ are labeled by their dimensionality, while the $U(1)_Y$ representations are identified through the hypercharge Y.

Type	Particle	$SU(3)_C$	$SU(2)_L$	$U(1)_Y$
Quarks	q_L	3	2	1/6
	u_R	3	2	2/3
	d_R	3	2	-1/3
Leptons	l_L	1	2	-1/2
	e_R	1	1	-1

This particle set comes in three families or flavors, denoted as

$$u = \begin{pmatrix} u \\ c \\ t \end{pmatrix}, \quad d = \begin{pmatrix} d \\ s \\ b \end{pmatrix}, \quad e = \begin{pmatrix} e \\ \mu \\ \tau \end{pmatrix}, \quad \nu = \begin{pmatrix} \nu_e \\ \nu_\mu \\ \nu_\tau \end{pmatrix}. \tag{1.2}$$

These three particle families display identical physical properties, differing only in the flavor quantum number and the mass.

Given this collection of particles, the $SU(3)_C \otimes SU(2)_L \otimes U(1)_Y$ symmetry introduces as gauge fields eight massless gluons associated to the $SU(3)_C$ group and four bosons linked to the $SU(2)_L \otimes U(1)_Y$ group. Out of these, the $W_\mu^\pm$ and Z_μ fields are massive bosons mediating the weak interaction and the massless photon field A_μ mediates the electromagnetic interaction. We will examine in more detail the interactions involving these gauge fields by groups. First, we will discuss the interactions involving gluons, which are described by quantum chromodynamics (QCD), and then we will examine weak and electromagnetic interactions. These two types of forces are commonly studied together and interpreted as unified, as both their mediators are generated by the $SU(2)_L \otimes U(1)_Y$ group.

1.1.1. Quantum chromodynamics

Quantum chromodynamics is a gauge theory built to describe the strong interaction between quarks. Its main historical motivation is the same one that led to the discovery of quarks: given the big collection of hadronic states, it was observed that a natural classification could be achieved for them if they were composed of smaller elementary particles. In particular, this could be possible if mesons were $M \equiv q_1\bar{q}_2$ states and baryons were $B \equiv q_1q_2q_3$ states. Identifying these more fundamental particles as quarks, it was clear that their presence inside the hadrons required the introduction of a new quantum number in order to satisfy Fermi-Dirac statistics. This quantum number was called color, and it was necessary that each quark could adopt $N_C = 3$ different colors. Since no colored states are observed in nature, the introduction of this quantum number caused the postulation of the confinement hypothesis, by which all asymptotic states must be singlets in color space. The main consequence of confinement is that quarks cannot be observed as free states except at high energies.

The force holding together the colored quarks in hadronic states is the strong interaction, and its dynamics can be deduced by building a quantum field theory with a $SU(3)_C$ gauge symmetry in color space. If we want the theory to respect it, we need to introduce $N_C^2 - 1 = 8$ new massless boson fields $G_a^\mu(x)$ called gluons. Incorporating them to the Lagrangian, we end up with the

following expressions:

$$\begin{aligned}\mathcal{L}_{QCD} &= -\frac{1}{4}\left(\partial^\mu G_a^\nu - \partial^\nu G_a^\mu\right)\left(\partial_\mu G_\nu^a - \partial_\nu G_\mu^a\right) + \sum_f \bar{q}_f \left(i\gamma^\mu \partial_\mu - m_f\right) q_f \\ &\quad -g_s G_a^\mu \sum_f \bar{q}_f \gamma_\mu \left(\frac{\lambda^a}{2}\right) q_f + \frac{g_s}{2} f^{abc}\left(\partial^\mu G_a^\nu - \partial^\nu G_a^\mu\right) G_\mu^b G_\nu^c \\ &\quad -\frac{g_s^2}{4} f^{abc} f_{ade} G_b^\mu G_c^\nu G_\mu^d G_\nu^e, \end{aligned} \tag{1.3}$$

where g_s is the strong coupling constant. No mass term is possible for gluons, since that would be in conflict with the gauge symmetry. In this expression we can identify the quadratic terms for both the gluon and the quarks, the interaction pieces between the the two types of particles and cubic and quartic gluon self interactions emerging from the gluon kinetic piece due to the non-abelian nature of $SU(3)_C$. These new interactions, which were not present in QED, are all modulated by the same g_s involved in the fermionic interactions. The self interactions are key in explaining an important feature in QCD, which is asymptotic freedom, which is the weakening of the strong interaction at high energies. This phenomenon represents a sort of exception to confinement, as it serves to explain why quarks and gluons can be observed individually at high energy observables.

1.1.2. Electroweak theory

Weak interactions present some very unique features that distinguish them clearly from the other fundamental forces. The most important one is that there are two types of weak interaction processes, one involving charged currents and the other one dealing with neutral currents. Weak charged currents are characterized by being flavor-violating, and their vertices always feature a pair of fermions (leptons or quarks) with a unit of difference in their electric charges. The doublet partners are organized as $\{e^-\bar{\nu}_e,\ \mu^-\bar{\nu}_\mu,\ \tau^-\bar{\nu}_\tau,\ d'\bar{u},\ s'\bar{c},\ b'\bar{t}\}$.

On the other hand, weak neutral currents are very similar to electromagnetic interactions in the sense that both are flavor-conserving processes. The main differences between them are that 1) neutrinos can only be involved in neutral current processes through a weak interaction and 2) there is a different coupling strength between chirality states for weak vertices. This violation of parity is also present in weak charged currents, where it is maximal, since only left-handed (right-handed) (anti)fermion states participate in these weak transitions.

With all this information in mind, it seems like the simplest symmetry group that can be used to describe charged currents is $SU(2)$. As for the neutral currents, it is worth it to try describing it together with electromagnetic interaction due to their similarities. Thus, we can try out a gauge theory based on the following symmetry group:

$$G \equiv SU(2)_L \otimes U(1)_Y, \tag{1.4}$$

where L refers to left-handed fields and Y refers to the hypercharge, a parameter different from the electric charge whose meaning will be clear once we formulate the Lagrangian. Such a theory must feature four bosons. Two of them, W_μ^1 and W_μ^2 coming from $SU(2)_L$, will describe the weak charged current interactions, and they can be identified with the $W^\pm$ bosons. The remaining two, W_μ^3 and B_μ, will describe the neutral currents, and they can be connected with the Z boson and the photon.

The Lagrangian of this gauge theory will be

$$\mathcal{L}_{\rm EW} = -\frac{1}{4}B_{\mu\nu}B^{\mu\nu} - \frac{1}{4}W^i_{\mu\nu}W^{\mu\nu}_i + \mathcal{L}_{\rm CC} + \mathcal{L}_{\rm NC}. \tag{1.5}$$

In this expression, the first two terms correspond to the kinetic terms for the new gauge fields:

$$B_{\mu\nu} \equiv \partial_\mu B_\nu - \partial_\nu B_\mu, \qquad W^i_{\mu\nu} = \partial_\mu W^i_\nu - \partial_\nu W^i_\mu - g\epsilon^{ijk}W^j_\mu W^k_\nu. \tag{1.6}$$

As we can see, the W^i_μ field strength introduces self-interactions among the gauge fields, whose strength will be universally fixed by the g coupling. Again, none of the new fields can be massive since the gauge symmetry forbids the inclusion of mass terms.

Regarding the other two terms, $\mathcal{L}_{\rm CC}$ and $\mathcal{L}_{\rm NC}$ are the charged and neutral current Lagrangians, parametrized as

$$\begin{aligned} \mathcal{L}_{\rm CC} &= -\frac{g}{\sqrt{2}}\left[W^\dagger_\mu\left(\bar{u}_L\gamma^\mu V d_L + \bar{\nu}_L\gamma^\mu e_L\right) + \text{h.c.}\right]. \\ \mathcal{L}_{\rm NC} &= \mathcal{L}_{\rm QED} + \mathcal{L}^Z_{\rm NC} = -eA_\mu\sum_f \bar{f}\gamma^\mu Q_f f - \frac{e}{2\sin\theta_W\cos\theta_W}Z_\mu\sum_f \bar{f}\gamma^\mu\left(v_f - a_f\gamma^5\right)f. \end{aligned} \tag{1.7}$$

where, in the charged current Lagrangian, f_L the left-handed fermions, W_μ accounts for the two $W^\pm$ bosons, and g is the $SU(2)_L$ gauge coupling. Some comments are in order for the neutral current Lagrangian. First of all, we have clearly separated the electromagnetic interactions in $\mathcal{L}_{\rm QED}$ from the weak interactions in $\mathcal{L}^Z_{\rm NC}$. These interactions involve the Z_μ and photon A_μ fields respectively, which are different from the W^3_μ and B_μ gauge fields. A direct identification of the two sets of fields is not possible, as the B_μ boson does not reproduce the properties of the electromagnetic force. The actual Z and photon fields are orthogonal combinations of the gauge fields, given by:

$$\begin{pmatrix} W^3_\mu \\ B_\mu \end{pmatrix} = \begin{pmatrix} \cos\theta_W & \sin\theta_W \\ -\sin\theta_W & \cos\theta_W \end{pmatrix}\begin{pmatrix} Z_\mu \\ A_\mu \end{pmatrix}, \tag{1.8}$$

where θ_W is called the weak mixing angle. The identification of the A_μ field with the photon gives meaning to this parameter, as the following relation needs to be fulfilled:

$$g\sin\theta_W = g'\cos\theta_W = e, \tag{1.9}$$

g' is the $U(1)_Y$ coupling and e is the electromagnetic charge. Additionally, Eq. (1.8) also serves to identify the hypercharge Y as a meaningful quantum number, since it implies that:

$$Y = Q - T_3, \tag{1.10}$$

where T_3 is the weak isospin and Q is the electric charge operator. The values of the hypercharges and weak isospins for all SM fermions are given in Table 1.1. Finally, Eq. (1.8) also sets $v_f = T^f_3\left(1 - 4Q_f\sin^2\theta_W\right)$ and $a_f = T^f_3$.

Thus, it is clear that a $SU(2)_L \otimes U(1)_Y$ gauge symmetry is able to describe weak and electromagnetic interactions in a unified way. Combining this theory with QCD, we are able to construct the SM Lagrangian:

$$\mathcal{L}_{\rm SM} = -\frac{1}{4}G^i_{\mu\nu}G^{\mu\nu}_i - \frac{1}{4}B_{\mu\nu}B^{\mu\nu} - \frac{1}{4}W^i_{\mu\nu}W^{\mu\nu}_i - \sum_f i\bar{f}\not{D}f + \mathcal{L}_{\rm GF} + \mathcal{L}_{\rm ghost}, \tag{1.11}$$

with

$$\not{D} f = \gamma^\mu \left(\partial_\mu + i g_s G_\mu P_q + i g \tilde{W}_\mu P_L - i g' B_\mu y_f \right) f, \tag{1.12}$$

where $P_L = (1 - \gamma^5)/2$ is the left-handed chiral projector, the P_q operator is a projector to the quark states and we have used the W^i_μ and B_μ gauge fields for compactness. We have introduced two new terms in Eq. (1.11), $\mathcal{L}_{\text{GF}}$ and $\mathcal{L}_{\text{ghost}}$. The first one contains the gauge fixing terms, and is necessary to remove non-physical degrees of freedom introduced by the vector fields and preserve Lorentz covariance. The second one is the ghost Lagrangian, and it is added to remove some inconsistencies introduced by the gauge fixing terms [6].

With this, we have built a theory that is able to describe strong, weak and electromagnetic forces by exploiting the principles of gauge theory. However, the same symmetry laws that have allowed us to describe the three fundamental interactions also forbid the presence of mass terms both for the fermionic and bosonic fields. Therefore, we need to find a mechanism that allows us to give mass to the particles in our theory.

1.2. Masses in the SM

1.2.1. Spontaneous symmetry breaking

The mechanism by which gauge bosons and fermions get masses in the Standard Model is the Brout-Englert-Higgs mechanism [7, 8]. The idea is to introduce a new particle into the theory which fully respects the symmetries, but whose vacuum state is not invariant under them. This situation happens generally when we have a set of degenerate states at the minimum energy level. Physically, only one of those states can be the actual vacuum state, and when it is chosen the symmetry group in the theory gets broken. This process is called spontaneous symmetry breaking (SSB), and it will induce the appearance of new massless degrees of freedom in the theory called Goldstone bosons. These new particles can be understood as excitations of the new field over the vacuum which do not increase the energy of the state. Generally, this phenomenon is fully described by the Goldstone theorem [9].

At first sight, it would appear that SSB cannot bring us closer to introducing masses in the SM. In fact, it seems to make matters worse, since it introduces extra massless particles in the theory. However, it turns out that the interplay between the local gauge symmetry and the Goldstone bosons will yield mass terms for the gauge bosons.

To see this, we introduce a SSB mechanism that will allow us to define mass for the fermionic fields and the $W^\pm, Z$ bosons while leaving the photon and gluon fields massless. We start by defining the following $SU(2)_L$ doublet of complex scalar fields

$$\phi(x) \equiv \begin{pmatrix} \phi^{(+)}(x) \\ \phi^{(0)}(x) \end{pmatrix}. \tag{1.13}$$

The most general renormalizable Lagrangian involving these fields is

$$\mathcal{L}_S = (D_\mu \phi)^\dagger D^\mu \phi - \mu^2 \phi^\dagger \phi - \frac{\lambda}{2} \left(\phi^\dagger \phi \right)^2. \tag{1.14}$$

where we choose that $\lambda > 0$, $\mu^2 < 0$. If we want the ϕ doublet to respect the same symmetries as the SM fields then the covariant derivative must be given by

$$D^\mu \phi = \left[\partial_\mu + i g \tilde{W}_\mu(x) + i g' y_\phi B_\mu(x) \right] \phi, \tag{1.15}$$

where $y_\phi = 1/2$.

Now, to find the vacuum state associated to these fields, we identify all terms save for the kinetic piece as the scalar potential $V(\phi)$ and minimize it, we find that there are infinite degenerate states with minimal energy. The choice of one of these states as the true vacuum of the theory will induce SSB. In particular, by construction the $SU(2)_L \otimes U(1)_Y$ will get reduced to just $U(1)_{QED}$.

Once a vacuum state is chosen, three out of four fields in the scalar doublet can be recast as Goldstone bosons and absorbed into the $W^\pm$ and Z fields as their longitudinal degrees of freedom. This change is actually necessary if we want the weak mediators to become massive, since vector bosons must gain an additional degree of freedom if they become massive. The remaining scalar can then be expressed as an excitation H over the vacuum state v, which is identified as the electroweak vacuum expectation value (vev). This leaves us with an extra degree of freedom which cannot be accommodated in the already established SM particle content. Therefore, we are effectively introducing a new scalar particle in the SM, which is called the Higgs boson.

Applying all these changes to Eq. (1.14), we get the following expression:

$$\mathcal{L}_S = \frac{1}{2}\partial_\mu H\, \partial^\mu H + \left[\frac{g^2}{4} W_\mu^\dagger W^\mu + \frac{g^2}{8\cos^2\theta_W} Z_\mu Z^\mu\right](v+H)^2 - \frac{1}{2}M_H^2 H^2 + \frac{M_H^2}{2v}H^3 - \frac{M_H^2}{8v^2}H^4, \tag{1.16}$$

where $M_H = \sqrt{\lambda}v$. Thus, the SSB mechanism and the introduction of the new scalar doublet in the SM allows the $W^\pm$ and Z fields to obtain quadratic terms and hence become massive. The coefficients appearing along with these terms represent the boson masses, which verify the relations:

$$M_Z \cos\theta_W = M_W = \frac{1}{2}vg. \tag{1.17}$$

As for the Higgs boson, its dynamics are completely specified in Eq. (1.16). A very particular feature of the Higgs interaction terms is that their coupling constants are always proportional to the square of the masses of the involved boson. This means that the SM is able to provide a definite prediction for all Higgs interaction rates.

The introduction of the Higgs boson provides other important predictions for several SM parameters. Namely, Eq. (1.17) represents both a concrete relation between the $W^\pm$ and Z masses and a direct probe on the weak mixing angle θ_W. We can complement this last prediction with independent estimates coming from weak decay observables and establish a cross check on the SM. So far, this and all measured properties of the Higgs sector have faithfully reproduced the SM predictions when measured at the experiment [10–13].

1.2.2. Yukawa sector and flavor mixing

The previous development has allowed us to include massive mediating particles in the SM, but we still need to give mass to the fermionic fields if we want the SM to describe fully what is observed in nature. Thankfully, here we can also exploit the SSB mechanism to generate fermion masses, and we can even reutilize the same scalar doublet that helped us with the boson masses. More specifically, the inclusion of the Higgs doublet opens the door for new interaction terms to be present in the SM Lagrangian while still preserving the gauge symmetry. These interactions are the Yukawa couplings, and they introduce mass terms for the fermions.

After applying SSB, the Yukawa Lagrangian can be written as:

$$\mathcal{L}_Y = -\left(1+\frac{H}{v}\right)\left[\bar{d}_L^0 M_d^0 d_R^0 + \bar{u}_L^0 M_u^0 u_R^0 + \bar{l}_L^0 M_l^0 l_R^0 + \text{h.c.}\right], \tag{1.18}$$

where d^0, u^0, l^0 are field vectors in flavor space and the M^0 matrices are 3×3 in flavor space. These matrices contain the information about the mass of the fermions. However, they are not diagonal in general, so we will need to diagonalize them if we want to extract the mass values for each individual particle. This has important consequences for the fermionic content of the SM, since it establishes a distinction between the mass eigenstates and the states that participate in the weak interactions, the so-called weak eigenstates. This disconnect is manifest for weak charged current interactions, as can be seen if we express L_{CC} in Eq. (1.7) in terms of fermion mass eigenstates:

$$\mathcal{L}_{\text{CC}} = -\frac{g}{\sqrt{2}}\left[W_\mu^\dagger\left(\bar{u}_L\gamma^\mu V d_L + \bar{\nu}_L\gamma^\mu e_L\right) + \text{h.c.}\right], \tag{1.19}$$

where $\bar{u}_L^0\gamma^\mu d_L^0 \to \bar{u}_L\gamma^\mu V d_L$, $\bar{\nu}_L^0\gamma^\mu e_L^0 \to \bar{\nu}_L\gamma^\mu e_L$ and we drop the 0 superindex to identify the mass states. The V matrix is called the Cabibbo-Kobayashi-Maskawa (CKM) matrix [14, 15], and it predicts interactions between any quark with positive weak isospin with any other with negative weak isospin. On the other hand, no flavor-changing neutral currents are predicted in the SM at tree level (GIM mechanism [4]).

An equivalent flavor mixing structure is not present in the lepton sector within the SM. This is due to the assumption that the neutrinos are massless particles. If that is the case, a redefinition of the neutrino flavor can compensate the transition from weak to mass eigenstates for the charged leptons. However, there exists clear evidence that neutrinos actually have mass, due to the observation of neutrino oscillation at multiple experiments [16–24]. Given this fact, another flavor mixing matrix must be formulated to explain lepton masses. The matrix in this case is called the Pontecorvo-Maki-Nakagawa-Sakata (PMNS) matrix [25, 26], and its main distinction with the CKM matrix is that there appears to be no suppression of the flavor-violating elements with respect to the flavor-diagonal ones at the phenomenological level.

1.3. Observables in quantum field theory

Perhaps the most important aspect of any physical theory is its capability of making predictions about nature. A theory is as good as its experimental implications, so it is important to understand how the SM produces estimations of what can be observed in a measurement. However, this is not a straightforward task. The reason for that is that the SM is an interacting quantum field theory, and in this class of frameworks it is unknown how to deduce exact observable properties except in very select cases. In general, the best thing that we can do to extract predictions from these theories is to approximate their solutions through a perturbative approach. Under this scope, interactive terms in the Lagrangian are treated as perturbations on a free field theory, and it is possible to estimate measurable properties as accurately as we are willing to go in the perturbative series.

Many observables in quantum field theories are based on the phenomenon of scattering. When particles interact with each other, we can only observe the initial state in which they are before the scattering, and the final state that appears after the interaction. From a quantum perspective, we can only use the interaction laws dictated by the theory to estimate the probability that a given initial set of particles $|k_1, ..., k_m\rangle_{\text{in}}$ goes on to become a final set $|p_1, ..., p_n\rangle_{\text{out}}$. These are

called in- and out-states, and they are defined as asymptotic states in which the 4-momentum of every particle is defined. The overlap between these states is quantified by the scattering matrix, or the S matrix. This matrix basically describes how the state of a particle changes as it interacts with other particles.

To calculate its elements, we can first relate them to correlation functions through the Lehmann-Symanzik-Zimmerman (LSZ) reduction formula [27]:

$$\begin{aligned} {}_{\text{out}}\langle p_1,...,p_n|S|k_1,...,k_m\rangle_{\text{in}} &= \lim_{\substack{p_i\to m_i\\ k_j\to m_j}} \int \prod_{i=1}^{n}\left[d^4x_i\, e^{i(p_i x_i)}\frac{(p_i^2-m_i^2)}{i}\right]\prod_{j=1}^{m}\left[d^4x_j\, e^{-i(k_j y_j)}\frac{\left(k_j^2-m_j^2\right)}{i}\right] \\ &\times \langle\Omega|T\{\varphi(x_1)\cdots\varphi(x_n)\varphi(y_1)\cdots\varphi(y_m)\}|\Omega\rangle, \end{aligned} \tag{1.20}$$

where $\langle\Omega|T\{\varphi(x_1)\cdots\varphi(x_n)\varphi(y_1)\cdots\varphi(y_m)\}|\Omega\rangle$ is the $n+m$-point correlation function, defined as the expectation value of the time-ordered product of $n+m$ field operators on the vacuum state of the interactive theory $|\Omega\rangle$. In this expression, $\varphi(x)$ represents a generic field in the theory, and the $-i(p_i^2-m_i^2)$ serve as stand-ins for their corresponding inverse propagators, evaluated at their physical poles $p_i\to m_i$, $k_j\to m_j$. Physically, these quantities can be interpreted as the probability amplitudes for the propagation of particles across the positions x_i and y_j.

The reason why we want to express the S-matrix elements in terms of these correlation functions is because their values can be computed in perturbation theory in a systematic way. This can be seen if we first express the correlators in terms of fields and states in the free theory where particles do not interact:

$$\langle\Omega|T\{\varphi(x_1)\cdots\varphi(x_n)\}|\Omega\rangle = \frac{\langle 0|T\{\varphi_0(x_1)\cdots\varphi_0(x_n)\, e^{i\int d^4x\,\mathcal{L}_{\text{int}}[\varphi(x)]}\}|0\rangle}{\langle 0|T\{e^{i\int d^4x\,\mathcal{L}_{\text{int}}[\varphi(x)]}\}|0\rangle}, \tag{1.21}$$

where $\varphi_0(x_i)$ are the field operators in the free theory, $|0\rangle$ is its vacuum state and $\mathcal{L}_{\text{int}}[\varphi(x)]$ is the interactive part of the Lagrangian of the theory. Here we can already see that a perturbative series can be built from the exponential functions, provided that the interaction coupling strengths are small. If we perform said expansion, each of the resulting terms can be rewritten as a sum of products of Feynman propagators. More specifically, Wick's theorem [28] prescribes:

$$T\{\varphi_0(x_1)\cdots\varphi_0(x_n)\} = N(\varphi_0(x_1)\cdots\varphi_0(x_n)) + (\text{all possible contractions}), \tag{1.22}$$

where N denotes the normal ordering operation, and the field contractions are equal to Feynman propagators (e.g. $\overbrace{\phi_0(x)\phi_0(y)} = D_F(x-y)$). If we introduce this result in Eq. (1.21), every term involving an uncontracted field will cancel out, leaving us with the anticipated sum of products of Feynman propagators.

These terms can be organized in a graphic way through Feynman diagrams, which have a direct correspondence to functions of the momenta and the Lagrangian parameters through the Feynman rules. In a Feynman diagram, interactions are represented by vertices, virtual particles are represented by internal lines and in- and out-states are represented by external lines. Through this small set of base elements, it is possible to reproduce every possible local interaction at every step in the perturbative expansion.

This representation is very useful for the extraction of the S-matrix, because it reduces its computation to the construction of all possible connected (with all external lines connected to each other) and amputated (without internal lines linked to just one external leg) Feynman diagrams. Some examples of Feynman diagrams are displayed in Fig. 1.1.

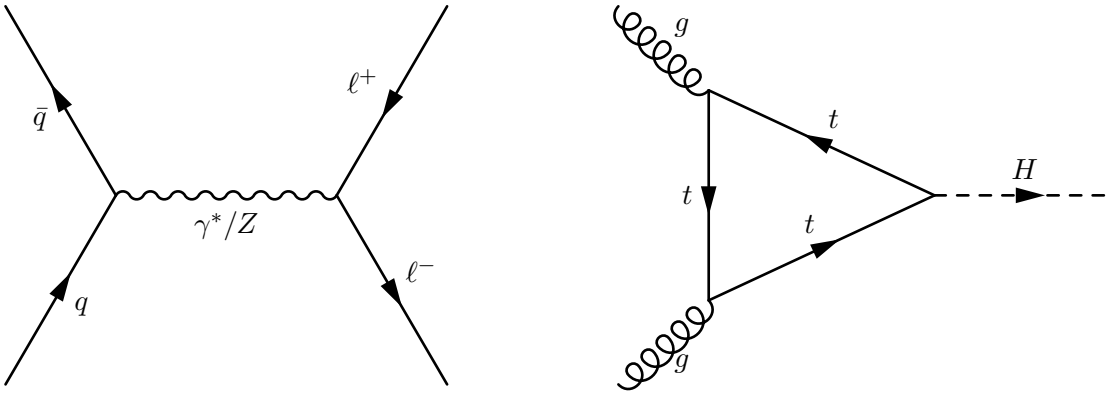

Fig. 1.1: Left: Feynman diagram of the Drell-Yan production of a pair of leptons at tree-level. Right: Feynman diagram of the Higgs boson production by gluon-gluon fusion through a top loop.

Beyond first order in perturbation theory, the so-called tree-level, the computation of higher order terms of the involves integrals in momentum space associated to the loops. These integrals very often generate divergences in the calculations, which require a dedicated treatment to ensure that the theory maintains its predictive features. We will explore this problem further in the next section.

Once the S-matrix element is obtained to whatever order in perturbation theory, proper observables such as decay length or cross sections can be easily deduced in terms of it. Thus, even though we cannot derive exact observable features from quantum field theories, perturbation theory allows us to compute them up to a given limited precision level. The accuracy of our predictions can be improved systematically by calculating successive higher order terms in the perturbative expansion.

1.3.1. Renormalization

In the current precision era of particle physics, the calculation of higher order terms of the S-matrix is necessary to meet the accuracy requirements set by experimental measurements. These contributions involve the computation of loop diagrams, which almost always contain ultraviolet (UV) divergences. These divergences need to be removed if we want quantum field theories to be predictive frameworks. The way to do this is through renormalization, which is a procedure that deals with infinites by performing a finite number of redefinitions on the parameters of the theory. This strategy establishes a clear distinction between the parameters that originally appear at the lagrangian level, called the "bare" parameters, from the actual measurable "physical" parameters that go into the observables. All these ideas are very relevant for the formulation and understanding of effective field theories, so we will briefly present here the main ideas involved in the field of renormalization. A more detailed discussion is provided in Ref. [29].

To understand how renormalization works, let us first study the nature and origin of the UV divergences. Considering a generic theory with a Lagrangian

$$\mathcal{L} = \sum_i C_i^{(0)} \mathcal{O}_i^{(0)}, \tag{1.23}$$

where $\mathcal{O}_i^{(0)}$ include all operators in the theory, built from all possible field combinations, and $C_i^{(0)}$ are their corresponding coupling constants or Wilson coefficients. The (0) index is present to signal that we initially formulate the theory with bare parameters.

If we try to derive observables from this Lagrangian beyond tree level, some of the Feynman diagrams that we have to consider will involve internal loops. The S-matrix computation requires integration over all internal momenta, so we will have to compute integrals of products of propagators over the whole momenta space. For instance, in QED, the loop integrals will generally take the form

$$\int \frac{d^4k_1...d^4k_L}{(k_i^\mu\gamma_\mu - m_i)...k_j^2...}, \tag{1.24}$$

where we have L loops and a given structure of fermion and photon propagators. This integral will naively be infinite if the difference between the powers of momenta in the numerator p_{num} and the powers of momenta in the denominator p_{den} fulfills that $p_{\text{num}} - p_{\text{den}} \geq -2$. This condition can be expressed in terms of the diagrammatic elements as:

$$D = 4L - P_e - 2P_\gamma, \tag{1.25}$$

where P_e and P_γ are the number of propagators for each particle type. Thus, if $D \geq 0$, the integral will be divergent, and if $D < 0$, the integral will be finite. The higher the value of D, the larger the order of the factors that generate the infinites. In some instances, the actual degree of divergence will be smaller than D thanks to some symmetries, so D is called the superficial degree of divergence.

Up to some sub-divergences, the divergent parts of this type of integrals are proportional to polynomials in external momenta. This fact hints at how the UV divergences can be removed, since S-matrix elements linked to local operators also take the form of polynomials in external momenta. More specifically, it is possible to get rid of the infinites of the theory by applying multiplicative redefinitions to the fields and couplings of the theory that cancel the divergent factors in the observables.

To see how this can be realized, we first need to parametrize the divergences arising from the loop integrals. This is done through the renormalization scheme. Ideally, the best way to characterize divergences would involve respecting the symmetries and essential features of the theory and it should not conflict with field redefinitions. This excludes the most naive approach, which would be to apply a hard cutoff Λ^2_{UV} on the UV region. Instead, the most convenient renormalization scheme is dimensional regularization [30, 31]. The main idea behind it is to perform an analytic continuation of the spacetime dimensions of the theory $d = 4 \to 4 - 2\epsilon$, with ϵ being an infinitesimal quantity. This small shift is enough to remove all UV divergences from the loop integrals relevant for the SM, as all of them will fulfill $D = 0$. Under this scheme, the integrals will yield $1/\epsilon$ poles, which will recover the divergent structures in the limit $\epsilon \to 0$.

Now that we have characterized the UV divergences through poles, we are ready to cancel them via field redefinitions. Returning to the general Lagrangian in Eq. (1.25), we rewrite the bare pieces as

$$C_i^{(0)} = \mu^{n_i\epsilon} Z_i C_i, \qquad \varphi^{(0)} = \sqrt{Z_\varphi}\varphi, \tag{1.26}$$

where φ are generic quantum fields, Z_i and Z_ϕ are the renormalization constants and μ is the renormalization scale, which is needed to keep the same dimensionality for the bare and the renormalized parameters. The parameter n_i will change depending on the dimensionality of $C_i^{(0)}$ (e.g., $n_i = 0$ if it is a mass coefficient and $n_i = 1$ if it is dimensionless). The scale μ will

cancel out eventually in the observable expressions, since it is an arbitrary quantity that we have introduced for convenience. The renormalization constants are chosen so that they cancel out the divergences that arise in the observables, leaving the renormalized fields and Wilson coefficients as the remaining finite physical elements that are actually observable. This reexpression implies that the bare Lagrangian is divergent in nature, but that is not a problem since Lagrangian terms are not observable, what matters is that in the end the observables are finite. This can be explicitly enforced by including renormalization constants in the formulation of the LSZ reduction formula in Eq. (1.20).

An additional redefinition is normally taken to make the cancellation of divergences more obvious. Namely, if we rewrite $Z_i = 1 + \delta_i$, then the bare Lagrangian can be expressed as

$$\mathcal{L} = \sum_i \mu^{n_i \epsilon} \left[C_i \mathcal{O}_i + \left(\delta_i + \delta_i^F \right) C_i \mathcal{O}_i \right], \tag{1.27}$$

where the δ_i^F factors are linked to the wave function renormalizations. Here we can identify two pieces: the renormalized Lagrangian and the counterterm Lagrangian, proportional to the δ factors, which are the counterterms themselves. These counterterms are fixed so that they cancel the loop integral divergences. When computing observables with this Lagrangian, the renormalized terms produce the usual Feynman rules with actual physical meaning. The counterterms will also give rise to additional Feynman diagrams, but they will be set up so that they cancel out with the UV divergences that may appear at every order in the perturbative expansion [32–34].

There is certain freedom in the choice of the counterterms. The only requirement for them is that they remove divergences, so the dividing line between the finite and infinite pieces can be drawn anywhere. In our case, we will employ the modified minimal subtraction ($\overline{\text{MS}}$) scheme [35], where the counterterms are disposed to remove the terms

$$\frac{1}{\hat{\epsilon}} = \frac{1}{\epsilon} - \gamma_E + \ln 4\pi, \tag{1.28}$$

where γ_E is the Euler constant. This scheme is the most commonly used for perturbative calculations in high-energy physics.

An important consequence of the renormalization procedure in dimensional regularization is that it introduces a dependence of the Wilson coefficients C_i in the renormalization scale μ. The nature of this relation is completely dependent on the renormalization strategy one chooses. For instance, if we had stuck to the hard cutoff approach, we would have also needed to introduce an additional scale Λ in the observable computations. However, the extra scale is much more manageable as it emerges in dimensional regularization, since under that scheme μ will only appear in logarithm arguments.

Regardless of the way that the renormalization scale manifests, we know that its dependence must somehow cancel out in the final observables, since we know that the experimental measurements do not depend on it. This fact allows us to formulate the renormalization group equations (RGE) [36–38], which can allow us to deduce the exact form of $C_i(\mu)$ up to finite pieces at any step in the loop expansion. This scaling law will be encoded in some elements of the RGEs which are called β-functions, which generally take the form

$$\mu \frac{\mathrm{d}C_i(\mu)}{\mathrm{d}\mu} = \beta \left(C_i(\mu) \right). \tag{1.29}$$

Note that the β can depend on any other renormalizable parameter in the theory. This feature implies that in some cases we can encounter a phenomena called operator mixing [39], by which

a bare operator gets renormalized as a linear combination of multiple operators. This situation arises whenever counterterms from more than one operator are needed to remove infinites from a given Feynman diagram.

In case we are normalizing a mass parameter $m_i(\mu)$, the form of the β-function shifts to

$$\mu \frac{\mathrm{d}C_i(\mu)}{\mathrm{d}\mu} = m_i(\mu)\gamma_m \left(C_i(\mu)\right). \tag{1.30}$$

where γ is normally called the anomalous dimension of m_i.

This kind of differential equations can be solved taking advantage of another independence of the theory on the renormalization scale, this time located at the Lagrangian level. More precisely, we know that the bare Lagrangian and thus its parameters $C_i^{(0)}$ do not change with the value of μ. This independence can be parametrized through a differential equation as

$$\mu \frac{\mathrm{d}}{\mathrm{d}\mu} \left(\mu^{n_i \epsilon} Z_i C_i\right) = 0. \tag{1.31}$$

Applying this kind of equations to solve the β-fucntions defines a path to obtain the dependence of the renormalized couplings in μ, or their "running", up to any order in the perturbation series. This method of calculating $C_i(\mu)$ is more convenient than estimating them through the calculation of the renormalization constants, because it is able to automatically resum all μ-dependent logarithms that are obtained in the process of computing loop integrals. That way, RGEs systematically account for all loop insertions at a given order and they also make it easy to compare the value of the coefficients at different scales through boundary conditions. Critically, they imply that, for any given coupling, there only exists one free parameter $C_i(\mu_0)$ evaluated at some chosen reference scale, and all other possible values are fully determined by the running.

Choosing a renormalization scheme that characterizes the theory parameters as functions of an arbitrary scale may seem inconvenient at face value, but it has certain advantages in practical cases. In many cases, loop amplitudes will end up depending on large logarithms depending on multiple scales. In those instances, having the possibility of manipulating the scales to make such terms smaller can be invaluable to preserve convergence in the perturbative expansion. Additionally, the running of parameters plays a central role in the formal development of effective field theories. More generally, concepts from renormalization theory are crucial to understand basic aspects of effective field theory such as the integration of high energy fields or operator mixing.

Renormalization group equations highlight a very important point, which is that the actual number of free parameters in a theory is equal to the number of parameters in its corresponding Lagrangian. These free parameters can only be determined by experimental inputs, and only when they are fixed can the theory offer full predictions about nature. Thus, if we have a theory whose Lagrangian has $N_{\mathcal{L}}$ parameters and we compute N observables with it, only $N - N_{\mathcal{L}}$ will constitute actual predictions, the rest will just be dedicated to fixing parameter values.

Finally, it is important to mention under which circumstances a quantum field theory cannot be renormalized. Generally, an operator of dimension d will contribute to a low energy observable as

$$\mathcal{M} \sim \left(\frac{p}{\Lambda}\right)^{d-4}, \tag{1.32}$$

where the amplitude has been normalized to be dimensionless and Λ is a fixed high scale of the theory, which is presumed to be larger than the kinematic scale p. Given this power law,

high-dimensional operators will be irrelevant at low energies, whereas low-dimensional operators will be important.[1]

These contributions of the operators at the amplitude level tells us something very important about their renormalizability. When trying to renormalize a theory that includes operators with dimension $n > 4$, at some point it will be necessary to compute integrals involving a quantity proportional to $(p/\Lambda)^{2(n-4)}$, which will diverge at infinity. To compensate these divergences, we would need to include a counterterm that requires the introduction of a $(2n-4)$-dimensional operator. This new operator would also need to be renormalized, requiring the inclusion of an even higher-dimensional operator. This process would continue indefinitely, implying that we would need an infinite amount of operators to renormalize such a theory. Conversely, theories with operators of just dimension 4 or lower do not produce high-dimensional divergencies in loop insertions, so only a finite number of operators are needed to cancel out all possible infinite structures.

This observation allows us to distinguish renormalizable theories (featuring operators with at most 4-dimensional operators) from non-renormalizable theories (contanining operators of dimension higher than 4). This is a very important observation, because renormalizability is an essential feature of the SM. It keeps its ultraviolet behavior under control and it limits the number of operators that can appear in the theory given a fixed particle content.

The consideration that non-renormalizable theories cannot be used to make predictions about nature was universally accepted by the particle physics community until the advent of effective field theories. Since their introduction and rise in popularity, this perspective has shifted, and nowadays contributions from high-dimensional operators are often considered when performing precision calculations of observables under beyond the SM (BSM) regimes. Further details about this matter will be given in the next chapter.

A final comment can be made about other type of divergences that can arise in QFT calculations. Throughout this section we have focused on ultraviolet divergences, but there are other type of divergences that emerge from the lower end of the energy spectrum when doing loop calculations. These are called infrared (IR) divergences, and they are treated through other techniques different from renormalization [40, 41].

1.4. Physics beyond the SM

The SM is an extremely successful theory. It allows us to understand the fundamental strong, weak and electromagnetic interactions and its predictions display an excellent agreement with all experimental tests. However, there exist several indications that it does not constitute a full description of all physical phenomena present at the subatomic level. From the theoretical side, we can list the following issues with the SM:

- **Strong CP problem:** The $SU(3)_C$ gauge symmetry theoretically allows for a term in the QCD Lagrangian that describes the interactions of quarks that would violate CP symmetry. This term involves a parameter called θ_{QCD}, which determines the strength of the CP-violating interactions. The problem is that observations suggest that θ_{QCD} is extremely

[1] A high-dimensional operator can also contribute to a low energy observable through a $(m/\Lambda)^{d-4}$ factor, where m is a light mass in the theory, or through a $(m/\Lambda)^{d-4}$ scaling , where v can be any scale emerging from SSB. The previous discussion still applies for this kind of dynamical dependence. In fact, it will always represent the limiting energy law for the amplitudes when $p \to 0$.

small, close to zero. The reason why this is a problem is that it is difficult to explain why θ_{QCD} should be so small without arbitrarily introducing fine tuning in the SM parameters.

- **Flavor puzzle:** There is no apparent reason why there exist three flavor families of particles. Additionally, the numerical values for the masses and flavor mixing parameters in the quark and lepton sectors display very different patterns. The lack of an explanation for both these features consitutes the flavor puzzle.

- **Hierarchy problem:** If we assume that there exist undiscovered particles at energies beyond the SM scale, then it is expected that their presence should be reflected in the value of the Higgs boson mass. This is because the Higgs boson is a scalar particle, so the value of its mass is very sensitive to radiative corrections proportional to the new particle scales. Since this is not observed, there must exist a mechanism that is responsible for keeping the observed Higgs boson mass close to the electroweak scale.

- **Quantum gravity:** The SM does not describe at all the gravitational interactions, so it needs to be extended somehow to include them.

On the other hand, there are some experimental observations that cannot be fully explained by the SM, so they point at some potential deficiencies in its theoretical structure:

- **Neutrino masses:** Even though no masses are predicted for neutrinos, the observation of neutrino oscillation undoubtedly indicates that neutrinos do have mass. It is relatively simple to extend the SM to accommodate massive neutrinos, but there are multiple mechanisms that can facilitate it without any clear indication as to which is the correct one. Additionally, it is unknown if neutrinos are Dirac or Majroana spinors.

- **Matter antimatter symmetry:** The SM predicts no explicit preference for matter over antimatter. However, we clearly observe that the universe is mostly made of matter.

- **Dark matter and dark energy:** Cosmological observations have determined that the 95% of the energy in the universe is due to poorly understood sources. First, there is dark matter, a type of matter that is not known to interact with any SM particle, and then we have dark energy, a type of energy that is thought to be the cause for the accelerated expansion of the universe. Only the remaining 5% is accounted for by the SM particle content. Thus, it is obvious that the SM must be extended to include the dynamics of these mysterious matter types.

- **Anomalies:** There are several measurements that stand in clear tension with their SM estimations. Their status is overall fuzzy enough that they cannot be declared as uncontested exceptions to the SM predictions, but they can potentially constitute hints for BSM physics. Some notable examples are the anomalies in the measurement of $(g-2)_\mu$ [42] and the B meson anomalies [43–45].

In spite of all of these issues being widely recognized, there is no definite solution for any of them. The reason for this is that there are no explicit hints of inconsistencies at the theoretical level in the SM, nor any obvious contradictions between SM predictions and experimental data. In the face of this situation, it can be argued that the best strategy when postulating corrections for the SM is to do so in a model independent way. This is the approach that we will follow in this thesis. To enforce this, we will use effective field theories as our main theoretical tool to

formulate new physics degrees of freedom and we will take advantage of current experimental data to probe these BSM contributions.

Chapter 2

Effective field theories

Effective field theories (EFTs) [46–49] are quantum field theories used to describe the behavior of physical systems at a specific energy scale. They are designed to be applicable when a system has a well defined hierarchy of scales, with some physical processes occurring at much higher energies than others [50].

The intuition that motivates the development of EFTs is the idea that it is possible to describe nature without understanding every aspect of it exactly. Different phenomena relevant at disparate energy levels naturally decouple. For instance, to describe conductivity we just need to understand the properties of materials at the atomic level, notions about strong interactions or the Higgs boson are completely unnecessary. Whatever is going on at a higher scale does not matter at the energy level of such a system. The implementation of this idea in a mathematically rigorous framework allows for the simplification of problems involving multiple energy scales, splitting them into several single scale calculations which are much simpler to grasp.

On a more technical level, apart from focusing physical analyses only on the relevant interactions and simplifying computations, EFTs can also be used to deal with large logarithms involving different energy scales. This kind of contributions can arise even in renormalizable theories, and only EFTs can allow us to make them tractable.

Additionally, there are some instances where we are forced to employ EFTs to characterize physical systems. This is the case in situations where the underlying theory is either not well understood or it is impossible to perform calculations in it. For example, when trying to characterize BSM physics, if we do not know the full theory that reproduces the SM at the observable energy range, EFTs are the only way to account for the unknown degrees of freedom in an indirect way. The specific particle content in the high energy regime is not needed for EFTs to be operational.

In an EFT, the physics at a given scale is described by an effective Lagrangian, which can be seen as a low energy approximation (of a more general theory) that is valid only up to a certain energy scale. In such an approximation, the contributions from the high energy environment are recast as operators of dimension 4 and higher that will only depend on the low energy degrees of freedom and some UV scale Λ. If we organize all terms attending to their dimensionality, we

can write the EFT Lagrangian generally as

$$\mathcal{L}_{\text{EFT}} = \mathcal{L}_{d\leq 4} + \sum_{d>4} \frac{c_i^{(d)}}{\Lambda^{d-4}} \mathcal{O}_i^{(d)}, \tag{2.1}$$

where we have separated the Λ scale from the Wilson coefficients so that the $c_i^{(d)}$ coefficients are dimensionless. We can always express the operators in this way because, in a 4-dimensional spacetime, the total Lagrangian must be 4-dimensional. This means that, when dealing with operators involving $d > 4$ field combinations, we need to include Wilson coefficients with a negative mass dimension to keep their dimensionality under control. These dimensionful coupling constants can only depend on physical scales of the theory, and we will later show that the only scale that can appear with a negative power in the Lagrangian is Λ. Under this framework, we can consider that the two general scales of the theory have been factorized: the short distance effects are characterized by the Wilson coefficients, and the long distance effects are captured by the field combinations $\mathcal{O}_i^{(d)}$ [51].

This Lagrangian will be able to provide accurate descriptions of physical phenomena as long as its use is restricted to a low range of energies, delimited by $p < \Lambda$. This observation reveals a major advantage to structuring the terms as in Eq. (2.1), because it allows us to classify them according to their relevance at the observable level. As we saw in Chapter 1.3.1, when computing an amplitude with one insertion of a d-dimensional operator, we will encounter the following scaling law

$$\mathcal{M} \sim \left(\frac{p}{\Lambda}\right)^{d-4}, \tag{2.2}$$

due to dimensional analysis. Given that the momentum scale p must always be lower than the UV scale Λ in the EFT context, this kind of contributions will become more and more irrelevant the higher d becomes.[1] This behavior can be generalized to a power counting law, by which the higher the dimensionality of an operator in the EFT Lagrangian, the more suppressed it will be in amplitude computations.

However, this same argument in Chapter 1.3.1 also lead us to the conclusion that theories with high-dimensional operators are non-renormalizable. This is a problem if we intend to use EFTs as regular quantum field theories, but it can be solved if we content ourselves with computing predictions up to a certain order in p/Λ. If we adhere to such a restriction, EFTs can be identified as series expansions on the Λ scale, and terms proportional to powers of p/Λ can be seen as corrections on the predictions from $d \leq 4$ operators. The high-dimensional operators would still need to be renormalized, but the new operators that will enter as counterterms are inconsequential, because they will eventually trespass the maximum order set by the EFT expansion and stop being relevant. Plus, we are confident that the EFT in the end can be renormalized if we consider all terms in the operator expansion, because it originates from a more general theory that can always be defined to be renormalizable. Thus, if we set a limit at a fixed order in the power counting, EFTs are just like regular quantum field theories.

Renormalizability is not the only property that is shared between a full theory and its EFT. Any symmetry that is present in the full theory, such as gauge invariance or parity conservation, is preserved when moving to the EFT environment, unless spontaneous symmetry breaking happens

[1] It should be noted that for EFTs describing unknown degrees of freedom above the SM scale, we will often encounter amplitudes that depend on $(v/\Lambda)^{d-4}$, where v is the electroweak vev. This kind of dynamical dependences will be important as some operators will not scale with the kinematic scale p and they will always set the limiting behavior when $p \to 0$.

at some intermediate scale. This is the case because an EFT in essence is just a reordering of the original theory where no real information is ever lost as long as all terms in the EFT expansion are considered. As such, the fundamental properties are always shared across both contexts.

Another important feature of EFTs is the invariance of their S-matrix elements under field redefinitions. When applying them, the field content of the theory gets fundamentally altered, but there is no effect at the observable level. Field redefinitions are also possible in ordinary quantum field theories, but they are limited to linear combinations of fields due to renormalizability restrictions. Such restrictions are not present in EFTs, where we can have arbitrary dimensions in the operators, the only requirement is that the field redefinitions must respect the EFT power counting. One of the most interesting options for field redefinitions is based on the use of equations of motion [52, 53]. This change of variables is very easy to implement at first order in the EFT expansion, it respects the power counting restriction and it is very useful to remove operators that contain derivatives. Beyond leading order, its utility gets diminished, and it is much practical to apply more targeted redefinitions [54–56].

This invariance allows for certain freedom in the choice of operators that appear at each order in the EFT expansion, and we can always exploit it to build the most convenient set of operators for each use case of the EFT. Later on we will explore how this and other techniques allow us to build nonredundant EFT operator sets, which we will identify as operator bases.

Now, to illustrate how EFTs work in practice, let us consider as an example what is perhaps the most classic EFT: the Fermi theory of low-energy weak interactions [57]. This EFT can be derived from the SM, and it is valid for small momenta compared to the W boson mass M_W. To deduce it, we start from the charged-current Lagrangian in Eq. (1.7):

$$\mathcal{L}_{\text{CC}} = -\frac{g}{\sqrt{2}}\left[W_\mu^\dagger \left(\bar{u}_L \gamma^\mu V d_L + \bar{\nu}_L \gamma^\mu e_L\right) + \text{h.c.}\right]. \tag{2.3}$$

From this expression, we can compute the semileptonic $d_\alpha \to u_\beta$ decay tree-level amplitude:

$$\mathcal{M} = \left(\frac{-ig}{\sqrt{2}}\right)^2 V_{\beta\alpha} \left((\bar{u}_\beta)_L \gamma^\mu (d_\alpha)_L\right) \left(\bar{l}_L \gamma^\nu \nu_L\right) \left(\frac{-ig_{\mu\nu}}{p^2 - M_W^2}\right), \tag{2.4}$$

At a low momentum range, the condition $p \ll M_W$ is satisfied, so we can expand the W propagator

$$\frac{1}{p^2 - M_W^2} = -\frac{1}{M_W^2}\left(1 + \frac{p^2}{M_W^2} + \frac{p^4}{M_W^4} + \cdots\right). \tag{2.5}$$

Now, if we retain only the leading order term and repeat the computation for every possible semileptonic decay, we can observe that the resulting amplitudes can also be produced by the Lagrangian

$$\mathcal{L} = -\frac{g^2}{2M_W^2}\left(\bar{u}_L \gamma^\mu V d_L\right)\left(\bar{l}_L \gamma_\mu \nu_L\right) + \mathcal{O}\left(\frac{1}{M_W^4}\right). \tag{2.6}$$

This expression at leading order is called the Fermi Lagrangian, and it constitutes an EFT for the SM. By construction, it is only valid at the low energy limit, and the successive operators in the EFT expansion can be deduced by identifying p/M_W in Eq. (2.5) as the expansion parameter. In this context, the W boson has disappeared, and the interactions mediated by its exchange are now described at the lowest level by a 6-dimensional 4-fermion operator. In the EFT language, it is said that the W boson has been "integrated out" [58–60]. This theory provides the same description as the full theory in the low energy environment, but it does not require any details

about weak interactions coming from the high-energy range. This can be clearly seen if we express the coupling constant in Eq. (2.6) in terms of the Fermi constant G_F:

$$\frac{G_F}{\sqrt{2}} \equiv \frac{g^2}{8M_W^2}. \tag{2.7}$$

G_F can be determined through measurement without any prior knowledge about the W boson or the full description of weak interactions, and still the EFT is able to predict with a very high accuracy the semileptonic decay dynamics. This scenario where the role of the W boson is ignored echos the historical development of the field of particle physics, in which the Fermi theory was formulated before the SM. Thus, we can clearly see how the low energy approximation provided by the EFT framework is able to decouple UV degrees of freedom from the IR dynamics and still provide accurate descriptions within its range of validity. This example is very simple, as it sits at the zero-th order in both the perturbative and EFT expansions, but it is still able to approximate the phenomenology of weak interactions in the low energy limit. The deduction of an EFT always follows this general philosophy: formulate process amplitudes in the full theory, expand them on the heavy scale and associate terms at each order in the series with high-dimensional effective operators.

EFTs nowadays are a prominent tool in the field of new physics searches, allowing for phenomenological analyses of high-energy scenarios in lower energy contexts. This is possible thanks to their ability to capture UV dynamics through high-dimensional operators. The new physics characterization that they offer is very convenient, because they are able to probe the new physics environments without requiring experimental access to their more explicit dynamics. Additionally, they are very flexible, because they provide concrete and accurate descriptions without considering the exact details of the physical phenomena across the complete energy spectrum. Further reviews on the topic and more formal aspects of EFTs can be found in Refs. [49, 61, 62].

There are two main types of BSM analyses in which EFTs can be applied: top-down and bottom-up. The top-down approach is concerned with the low energy behavior of specific new physics models. The objective is to capture the high energy dynamics through high-dimensional operators, connecting the Wilson coefficients in the EFT with parameters from the full theory. The results from this kind of studies serve as an indirect probe on the full theory parameters, and they also offer a way to classify new physics models. On the other hand, bottom-up analyses put the focus on the EFT itself, making it as generic as possible so that as many new physics signatures as possible can fit into it. In this kind of approach model independence is favored the most, while top-down analyses are more oriented towards model discrimination. Naturally, the EFTs that are used in the bottom-up approach feature very large parameter spaces, and the general objective is to simultaneously restrict as much of them as possible.

In the following, we will briefly discuss the matching procedure, which is a fundamental concept for top-down analyses and EFTs in general. This idea will help us better understand the relation of EFTs with their respective UV completions and their utility beyond new physics searches. Then, we will shift our focus to some key aspects of the bottom-up approach, which will allow us to introduce some very important ideas for the development of the main line of work in this thesis.

2.1. EFT matching

When working with EFTs, it is very important to understand the connection between a full theory and its EFT. As we saw previously in the Fermi theory example, the way an EFT is

built from a full theory is by computing all relevant process amplitudes, expanding them on the heavy scales and identifying the resulting terms as being generated with an effective Lagrangian involving only low energy fields. In other words, the main idea behind matching is to Taylor expand the operators in the heavy mass limit.

This procedure is straightforward when examining physics at tree-level, but it does not work when considering loops. This is because computing a loop amplitude I_F in the full theory and the corresponding $I_{\rm EFT}$ in the EFT produces different results once heavy scales are expanded everywhere, as the order of the mass expansion and the loop integral matters. Crucially, the difference is present only in divergent terms which are analytic in the light scales. This implies that the description of the two theories in the low energy environment is the same, but they differ in the UV regime. The root of the issue is that the full theory and the EFT are fundamentally independent, and this can be seen from the fact that they cannot be renormalized with the same counterterms. When two different renormalizations are applied to a theory, the fields that they contain will be essentially different, even if they share the same names. Again, this is not a problem as long as the S-matrix elements end up being the same in both frameworks.

The solution to this problem is to incorporate the difference between the renormalized amplitudes in the two theories as part of the matching. This difference is defined as:

$$I_M = [I_F + I_{F,\text{c.t.}}] - [I_{\rm EFT} + I_{\rm EFT,c.t.}]\,, \tag{2.8}$$

This procedure is possible because I_M is analytic in the light masses, so it can be absorbed into the EFT local operators by performing adequate shifts in the parameters of the Lagrangian.

This strategy for the matching not only allows EFTs to be usable beyond tree level, it also hints at a very important simplification of the whole matching procedure. As it stands at the moment, computing I_M is very cumbersome because it requires the computation of loop integrals and applying renormalization in two theories. However, I_M can also be calculated by just expanding the full theory amplitude I_F in the light scale. This makes sense intuitively: if $I_{\rm EFT}$ is obtained by expanding I_F in the heavy scales, the sum of $I_{\rm EFT}$ and the expansion on the light scales must amount to the total amplitude in the full theory. More specifically, in Eq. (2.8) the heavy scale expansion of I_F will cancel itself out with $I_{\rm EFT}$, so the matching condition for the EFT at one loop will be given by the remaining light scale expansion. This whole procedure is fully justified in the method of expansion by regions [63], and it works perfectly if the theory is regulated with dimensional regularization. Thus, the matching procedure gets reduced to formulating the EFT at tree level and then redefining its parameters using the information of the loop amplitude I_F expanded on the light scales. Even better, we only need to keep the finite parts of the integrals, as both infrared and UV divergences will cancel in I_M.

The requirement for dimensional regularization brings an additional perk to the procedure, which is that RGEs can be applied. As discussed in Chapter 1.3.1, RGEs allow for the resummation of large logarithm series, but it also makes it easier to describe operator mixing, which is a very common phenomenon when there are $d > 4$ operators. In general, RGEs prescribe

$$\mu\frac{d}{d\mu}c_i^{(5)} = \gamma_{ij}^5 c_j^{(5)}, \tag{2.9}$$

$$\mu\frac{d}{d\mu}c_i^{(6)} = \gamma_{ij}^6 c_j^{(6)} + \gamma_{ijk} c_j^{(5)} c_k^{(5)}, \tag{2.10}$$

and so on for Wilson coefficients in operators with higher dimensions. In these expressions, the γ^d functions are functions only of the $\mathcal{L}_{d\leq 4}$ parameters, and we can see that the power counting produces a clear structure for the mixing patterns.

On the other hand, there exists an important issue with dimensional regularization, which is that it is not able to describe how heavy particles decouple in low energy contexts. This is not an issue in mass-dependent renormalization schemes, because with them the β functions associated with heavy degrees of freedom go to zero as the renormalization scale μ decreases [64]. This does not happen in dimensional regularization, and in fact this feature threatens the perturbative character of the theory if left unchecked. The solution lies in integrating out the heavy particles as the different mass thresholds are crossed. Basically, if m is the mass of the heavy particle, for $\mu > m$ one uses a theory with the heavy particle field, and for $\mu < m$ the effects of the heavy particle are described indirectly with higher dimension operators. Thus, we are effectively introducing another EFT, we have the previous one for the high end of the energy spectrum and a new one for the low energy environment, matched accordingly to ensure that they produce the same S-matrix elements.

This procedure can be executed in a successive manner as we encounter more mass scales going down the energy spectrum. The end result will be a ladder of EFTs, each one specialized in a concrete region of the energy range and connected with each other through the matching conditions. Thus, if we want to work at a specific scale with an EFT, we would start with the full theory and evolve down its couplings with the RGEs until the mass of the heaviest particle is reached. At that point, that particle would be integrated out and the full theory would be matched with the resulting EFT. After that, the parameter running would resume until the new heaviest particle is reached, and the matching procedure would then be executed again. This process of matching and running would continue until the desired scale is reached, at which point the resulting EFT would offer us the best possible physical description at the corresponding energy region.

This ability of integrating out heavy particles is an EFT feature that has clear utility outside of the context of new physics searches. Another one is in renormalizable theories with multiple very different mass scales. When performing loop computations with them, we will encounter situations where multiple logarithms appear, and the use of a renormalization scale is not enough to make all of them small simultaneously. However, if we reparametrize the heavy degrees of freedom with an EFT, RGEs can be used to sum all large logarithms by running the renormalization scale from high to low values.

As a final note, it should be mentioned that this whole discussion is framed under the so-called diagrammatic matching procedure. This strategy is essentially based on the comparison of amplitudes or Feynman diagrams in the full theory with those in the EFT. Depending on the theories involved, it can be quite laborious to execute the matching, so in recent years there has been a substantial effort to automatize it [65–67]. Work being done in that direction is mostly rooted in functional or path integral matching [68–74]. In this approach, an EFT is calculated from a full theory by performing a path integral over the heavy degrees of freedom in the generating functional of the light sources:

$$\begin{aligned} Z\left[J_L\right] &= \int \mathcal{D}\phi_H \mathcal{D}\phi_L \exp\left[\int d^4x \left(\mathcal{L}_{\mathrm{F}}(\phi_L, \phi_H) + \phi_L J_L\right)\right] \\ &= \int \mathcal{D}\phi_L \exp\left[\int d^4x \left(\mathcal{L}_{\mathrm{EFT}}(\phi_L) + \phi_L J_L\right)\right], \end{aligned} \tag{2.11}$$

where ϕ_L and ϕ_H are the light and heavy fields in the theory, with scales m and M verifying $m < M$, $\mathcal{L}_{\mathrm{F}}(\phi_L, \phi_H)$ is the full theory Lagrangian and J_L is the source associated to the light fields. In this context, we can see how the operation of integrating out heavy fields is made manifest. The result of it is the exact same that is found in the diagrammatic approach: a set

of operators involving only the light fields which can be expressed as an infinite sum of high-dimensional local operators after applying operator product expansion. This procedure offers a very simple way to compute EFTs at tree level and one loop, and significant efforts are being made in extending it so it can also include higher order loop effects [70–74].

All in all, we have demonstrated how EFTs allow us to focus on a specific portion of the energy range covered by a quantum field theory. The guiding principle is to recast all UV degrees of freedom in an underlying general theory as high-dimensional operators through the matching procedure with no loss of information. We have seen that this framework can have the same features as ordinary QFTs, at the expense of a limited precision set by an expansion on Λ^{-d}. In spite of this limitation, EFTs are useful not only when dealing with a physical context where the UV properties are unknown, but also if the full theory that originates the EFT is available.

2.2. Bottom-up analyses

Bottom-up analyses with EFTs have a very simple aim: to build a predictive quantum field theory just with the knowledge of its low energy limit. Having this as a starting point for the development of an EFT heavily conditions the tools that we can use for the task. The UV behavior is still described indirectly with high dimensional operators, but here they cannot be built by matching, they can only be formulated according to global and local symmetries. The exact UV masses are also unknown, so they must be substituted by a nondescript scale Λ. This scale and the values of the EFT Wilson coefficients can only be known through additional information coming from the high energy environment. This ambiguity implies that the only restriction for the operator space comes from loose symmetry arguments. Thus, by construction, EFTs built from the bottom up feature a very large parameter space and generally can be matched to a big multiplicity of UV completions.

In this section we will illustrate how the bottom-up approach works on a practical level with an EFT built specifically to probe new physics environments: the Standard Model Effective Field Theory (SMEFT) [75, 76]. This EFT is built specifically to perform new physics searches and it is the main theoretical tool that is used in the main work of this thesis, so we will describe in detail its foundation and its utility for phenomenological analysis. In the following, we will describe its foundation and main features, and then we will discuss its utility for phenomenological analyses, with special focus on multiparameter new physics searches.

2.2.1. Foundations of the SMEFT

One of the most important EFTs that can be built within the bottom-up approach is the SMEFT [75, 76]. The layout of this theory is very simple: at the low end of the energy spectrum all physical processes are described by the SM degrees of freedom, and any other phenomena pertaining to a higher scale are described through high-dimensional effective operators. Imposing that the SM symmetry structure is carried over to the high energy environment, this framework is able to encode all possible physics BSM in a model-independent way. Naturally, for the higher-order operators to appear one needs to drop renormalizability in the SM lagrangian and allow for interaction terms with canonical dimensions $d > 4$.

The only requirements for this theory to be valid are that the new physics effects must all be ultraviolet with respect to the SM scale and that the electroweak symmetry is realized linearly. The first restriction obviously neglects any possible scenario with new particles whose masses

lie at or below the electroweak scale. Nevertheless, this is often not an issue even if these light degrees of freedom actually exist. Due to the lack of observations, it is safe to assume that any undiscovered light particle must be very weakly coupled to the SM fields, so we can often neglect their contributions in the SMEFT regime. As for the second requirement, the way the electroweak symmetry is realized is irrelevant in the SM, since all choices are connected by field redefinitions, but this is not the case when high dimensional operators come into play. Choosing a linear realization results in the SMEFT, while a nonlinear one leads to the so-called Higgs Effective Field Theory (HEFT), which features a more complex operator set that is reduced to the SMEFT under certain parameter configurations [77–79]. There are arguments both on the theoretical [80, 81] and the experimental side [12, 82, 83] that favor either the SMEFT or the HEFT. In our case, we choose to work with the SMEFT mainly due to its relative simplicity.

The interest behind the SMEFT comes mainly from its high degree of versatility. This theory is flexible enough to reproduce the low energy behavior of a multitude of new physics models that introduce new particles at a high energy scale. This is a very convenient setting, since any input on the values of the SMEFT Wilson coefficients can be used to probe many UV completions. The extrapolation is always realized in the same way. As explained in Chapter 2, first the low energy effective field theory for a given model is computed, and then the resulting high-dimensional operators are matched to the SMEFT operators. Thus, this framework sets up a very efficient information flow between the SMEFT and any BSM model of interest. Furthermore, the SMEFT offers both a consistency test and a steering aid for addressing potential new physics signals. In case a SM deviation is detected, the knowledge of the high dimensional operators involved in it can quickly point us to other regions in the observable space where additional BSM signatures should be found. In a similar fashion, phenomenological results coming from SMEFT analyses can allow us to either validate or dismiss a large variety of new physics models.

The SMEFT Lagrangian, just like any regular EFT, is expressed as an expansion in the UV scale Λ, where the low energy contributions will be described by the SM Lagrangian. Of all the operators in the EFT expansion, we will only keep those with $d = 5$ and $d = 6$, since they will constitute the leading contributions for NP in the observables. The Lagrangian takes the form

$$\mathcal{L}_{\text{SMEFT}} = \mathcal{L}_{\text{SM}} + \sum_i \frac{c_i}{\Lambda^2} O_i^{d=6}, \tag{2.12}$$

where $\mathcal{L}_{\text{SM}}$ is the SM Lagrangian, $O_i^{d=6}$ are the independent dimension-6 effective operators and c_i are their corresponding Wilson coefficients. The quantities c_i and Λ can never be separated, so we may be tempted to group them in a single paramater $c_i' = c_i/\Lambda^2$. The issue with this definition is that it produces dimensionful parameters, so it is customary to multiply the coefficients by the electroweak vacuum expectation value v to keep them dimensionless. In other words, we would be redefining them as

$$C_i \equiv c_i \frac{v^2}{\Lambda^2}. \tag{2.13}$$

Consequently, an additional v would appear in place of the NP scale Λ. This is the approach that we will be following in our studies. Another option would be to fix a specific value for Λ prior to the analysis, but that would represent an additional assumption about the full theory. Plus, it would compromise the validity of the EFT as $E \sim \Lambda$. In contrast, our approach will implicitly ensure that the new physics scale is always away enough from the kinematic range of the observables we analyze.

We have omitted the 5-dimensional operators because the SMEFT symmetries allow for just one of them: the Weinberg operator [84]. This is a very interesting Lagrangian term, because it

can singlehandedly provide an origin for neutrino masses and an explanation for their smallness, provided that Λ is set at a very large value or its WC is very small. However, it posits a violation of the lepton number by two units. This property is verified for all odd-dimensional operators, they always violate baryon and/or lepton number conservation [85]. We will not consider symmetry violations of this kind in our studies, so we neglect all of them in the following.[2]

As for higher dimensional operators, we generally ignore them on the count that they are subleading with respect to $d \leq 6$ contributions. This cutoff is easily imposed at the Lagrangian level, but it also needs to be present in the observables for consistency. This means that, for instance, amplitude terms depending on two or more insertions of a dimension-6 vertex cannot be considered if we work up to dimension 6, since they will be $\mathcal{O}(\Lambda^{-4})$. The only instances where these high dimensional terms are considered are in the event of exceptionally high experimental precision or in specific scenarios where linear dimension-6 terms are suppressed or become subdominant.

The remaining dimension six operators are disposed in a way that they span the whole operator space delimited by the theory symmetries. This procedure is arbitrary, but finding a valid collection of operators is not a trivial task. The main guideline is to enforce the symmetries of the theory, but applying them naively will lead to a significant number of redundant operators. Having redundant operators is inconvenient, because they lead to the same contributions to the S-matrix elements and unnecessarily bloat the operator set. There are multiple ways to remove them, but the most commonly used techniques are field redefinitions (see the beginning of Chapter 2), integration by parts, Fierz identities [86, 87] and Dirac structure reduction [88–90]. The first full operator basis that was built featuring no redundant operators is the Warsaw basis [76]. At dimension 6 and assuming baryon and lepton number conservation, it spans 59 operator structures, which result in 2499 interaction terms (1350 CP-even and 1149 CP-odd) once three flavor generations are considered. To organize them, we first express them in terms of the Higgs doublet H, the SM covariant derivative, field strength tensors $X_{\mu\nu} \in \{G_{\mu\nu}, W_{\mu\nu}, B_{\mu\nu}\}$ and three types of fermion currents: scalar $(\bar{\psi}_{L/R}\,\psi_{R/L})$, vector $(\bar{\psi}_{L/R}\,\gamma^{\mu}\psi_{L/R})$ and tensor $(\bar{\psi}_{L/R}\,\sigma^{\mu\nu}\psi_{R/L})$. Based on this language, 8 classes of operator structures can be defined, summarized in Table 2.1:

- X^3: 4 gauge operators with three field strength tensors.
- H^6: 1 operator consisting of six Higgs doublets.
- H^4D^2: Two operators with four Higgs doublets and two covariant derivatives.
- X^2H^2: 8 operators with two Higgs fields and two field strength tensors.
- ψ^2H^3: 3 non-hermitian operators with a scalar fermion current and three Higgs doublets.
- ψ^2XH: 8 non-hermitian operators with a tensor fermion current, a Higgs doublet and a field-strength tensor.
- ψ^2H^2D: 7 operators with a vector fermion current, two Higgs doublets and a covariant derivative.

[2] Alternatively, we can also dismiss the presence of odd-dimensional operators by assuming that there exist two NP scales, one that respects baryon/lepton number symmetries ($\Lambda_{\text{LNC/BNC}}$) and another that violates them ($\Lambda_{\text{LNV/BNV}}$). If $\Lambda_{\text{LNV/BNV}} \gg \Lambda_{\text{LNC/BNC}}$, then the terms coming from odd-dimensional will be so small compared to the even-dimensional ones that we can safely neglect them. This argument can also be used to explain accidental symmetries in the SMEFT (see footnote [3]).

- ψ^4: 25 4-fermion operators, which can be subdivided into five chiral structures $(\bar{L}L)(\bar{L}L)$, $(\bar{R}R)(\bar{R}R)$, $(\bar{L}L)(\bar{R}R)$, $(\bar{L}R)(\bar{R}L)$ and $(\bar{L}R)(\bar{L}R)$.

The Warsaw basis is the most commonly used operator set in the literature, but there exist multiple alternatives, which will be more or less convenient depending on the requirements of any given analysis. Other popular operator bases are the strongly-interacting light Higgs (SILH) basis [92, 93], developed for NP models with SSB triggered by a light composite Higgs, the HISZ basis [94], specialized in the characterization of NP effects in anomalous WWZ and $WW\gamma$ interactions, and the Green's basis [95], which is useful for functional matching or off-shell diagrammatic matching [95, 96] exercises.

One last option that is worth mentioning is the Higgs basis [97–101], which is the one that we will use in the phenomenological analyses to be presented in this thesis. This basis was built with the intent to circumvent some subtleties that are important when performing phenomenological analyses with the SMEFT. The first one has to do with the input parameters. In a SM analysis, the values for all couplings that are not predicted by the theory are fixed through measurements, but that correspondence is broken in a BSM regime. The values of the SM inputs will now be contaminated by NP, so we need to find a way to separate the SM information from the new contributions. The solution is to set up an input scheme, by which a set of SM couplings is rewritten as a combination of their measured values and the BSM contamination. This will in general introduce indirect EFT couplings in any given analysis, which need to be considered in order to properly characterize the observables in the NP regime.

The second issue that can be addressed with the Higgs basis is the disruption of the SM kinetic terms. In the SM, the kinetic terms for the mass eigenstates are set up to be diagonal and canonically normalized, but the presence of high dimensional operators can alter this disposition and modify the propagators.

Both of these effects can be accounted for in the Warsaw basis, but the Higgs basis takes care of them automatically and ensures that the NP contributions manifest mostly as interaction terms. Apart from that, it also sets up a much clearer correspondence between the NP couplings and the observables that are used to constrain them. It does so through the application of parameter redefinitions, the introduction of vanishing equations of motion pieces, and the application of integration by parts on several Lagrangian terms. More specifically, the Higgs basis is built from imposing the following conditions on the SMEFT Lagrangian after electroweak symmetry breaking:

- The kinetic terms are diagonal and canonically normalized.
- The parameters G_F, α, m_Z act as input parameters, redefined so that their relations with the couplings g_L, g_Y, v are the same as in the SM:

$$G_F = \frac{1}{\sqrt{2}v^2}, \quad \alpha(m_Z) = \frac{g_L^2 g_Y^2}{4\pi(g_L^2 + g_Y^2)}, \quad m_Z = \frac{\sqrt{g_L^2 + g_Y^2}}{2}v. \tag{2.14}$$

  There is some freedom in the parameters that act as input parameters, any specific choice will set up a different input scheme. Over the course of our studies, we will always work with the $\{G_F, \alpha, m_Z\}$ set.

- No derivatives are present in the Higgs self-interactions.

Table 2.1: Collection of SMEFT dimension-6 operators in the Warsaw basis organized according to the classification described in the main text. This table is adapted from the one presented in Ref. [91]. The flavor indices p, r, s, t are implicit in the operator names at the left-hand side of the tables.

$1:X^3$	
O_G	$f^{ABC}G_\mu^{A\nu}G_\nu^{B\rho}G_\rho^{C\mu}$
$O_{\widetilde{G}}$	$f^{ABC}\widetilde{G}_\mu^{A\nu}G_\nu^{B\rho}G_\rho^{C\mu}$
O_W	$\epsilon^{IJK}W_\mu^{I\nu}W_\nu^{B\rho}W_\rho^{K\mu}$
$O_{\widetilde{W}}$	$\epsilon^{IJK}\widetilde{W}_\mu^{I\nu}W_\nu^{B\rho}W_\rho^{K\mu}$

$2:H^6$	
O_H	$\left(H^\dagger H\right)^3$

$3:H^4D^2$	
$O_{H\Box}$	$\left(H^\dagger H\right)\Box\left(H^\dagger H\right)$
O_{HD}	$\left(H^\dagger D_\mu H\right)^*\left(H^\dagger D_\mu H\right)$

$4:X^2H^2$	
O_{HG}	$H^\dagger H G_{\mu\nu}^A G^{A\mu\nu}$
$O_{H\widetilde{G}}$	$H^\dagger H \widetilde{G}_{\mu\nu}^A G^{A\mu\nu}$
O_{HW}	$H^\dagger H W_{\mu\nu}^I W^{I\mu\nu}$
$O_{H\widetilde{W}}$	$H^\dagger H \widetilde{W}_{\mu\nu}^I W^{I\mu\nu}$
O_{HB}	$H^\dagger H B_{\mu\nu} B^{\mu\nu}$
$O_{H\widetilde{B}}$	$H^\dagger H \widetilde{B}_{\mu\nu} B^{\mu\nu}$
O_{HWB}	$H^\dagger \tau^I H W_{\mu\nu}^I B^{\mu\nu}$
$O_{H\widetilde{W}B}$	$H^\dagger \tau^I H \widetilde{W}_{\mu\nu}^I B^{\mu\nu}$

$5:\psi^2H^3+\text{h.c.}$	
O_{eH}	$\left(H^\dagger H\right)\left(\bar{l}_p e_r H\right)$
O_{uH}	$\left(H^\dagger H\right)\left(\bar{q}_p u_r \widetilde{H}\right)$
O_{dH}	$\left(H^\dagger H\right)\left(\bar{q}_p d_r \widetilde{H}\right)$

$6:\psi^2XH+\text{h.c.}$	
O_{eW}	$\left(\bar{l}_p\sigma^{\mu\nu}e_r\right)HW_{\mu\nu}^I$
O_{eB}	$\left(\bar{l}_p\sigma^{\mu\nu}e_r\right)HB_{\mu\nu}$
O_{uG}	$\left(\bar{q}_p\sigma^{\mu\nu}T^A u_r\right)\widetilde{H}G_{\mu\nu}^A$
O_{uW}	$\left(\bar{q}_p\sigma^{\mu\nu}u_r\right)\tau^I\widetilde{H}W_{\mu\nu}^I$
O_{uB}	$\left(\bar{q}_p\sigma^{\mu\nu}u_r\right)\widetilde{H}B_{\mu\nu}$
O_{dG}	$\left(\bar{q}_p\sigma^{\mu\nu}T^A d_r\right)HG_{\mu\nu}^A$
O_{dW}	$\left(\bar{q}_p\sigma^{\mu\nu}u_r\right)\tau^I HW_{\mu\nu}^I$
O_{dB}	$\left(\bar{q}_p\sigma^{\mu\nu}u_r\right)HB_{\mu\nu}$

$7:\psi^2H^2D$	
$O_{Hl}^{(1)}$	$\left(H^\dagger i\overleftrightarrow{D}_\mu H\right)\left(\bar{l}_p\gamma^\mu l_r\right)$
$O_{Hl}^{(3)}$	$\left(H^\dagger i\overleftrightarrow{D}_\mu H\right)\left(\bar{l}_p\tau^I\gamma^\mu l_r\right)$
O_{He}	$\left(H^\dagger i\overleftrightarrow{D}_\mu H\right)\left(\bar{e}_p\gamma^\mu e_r\right)$
$O_{Hq}^{(1)}$	$\left(H^\dagger i\overleftrightarrow{D}_\mu H\right)\left(\bar{q}_p\gamma^\mu q_r\right)$
$O_{Hq}^{(3)}$	$\left(H^\dagger i\overleftrightarrow{D}_\mu H\right)\left(\bar{q}_p\tau^I\gamma^\mu q_r\right)$
O_{Hu}	$\left(H^\dagger i\overleftrightarrow{D}_\mu H\right)\left(\bar{u}_p\gamma^\mu u_r\right)$
O_{Hd}	$\left(H^\dagger i\overleftrightarrow{D}_\mu H\right)\left(\bar{d}_p\gamma^\mu d_r\right)$
$O_{Hud}+\text{h.c.}$	$i\left(\widetilde{H}^\dagger D_\mu H\right)\left(\bar{u}_p\gamma^\mu d_r\right)$

$8:(\bar{L}L)(\bar{L}L)$	
O_{ll}	$\left(\bar{l}_p\gamma_\mu l_r\right)\left(\bar{l}_s\gamma^\mu l_t\right)$
$O_{qq}^{(1)}$	$\left(\bar{q}_p\gamma_\mu q_r\right)\left(\bar{q}_s\gamma^\mu q_t\right)$
$O_{qq}^{(3)}$	$\left(\bar{q}_p\gamma_\mu\tau^I q_r\right)\left(\bar{q}_s\gamma^\mu\tau^I q_t\right)$
$O_{lq}^{(1)}$	$\left(\bar{l}_p\gamma_\mu l_r\right)\left(\bar{q}_s\gamma^\mu q_t\right)$
$O_{lq}^{(3)}$	$\left(\bar{l}_p\gamma_\mu\tau^I l_r\right)\left(\bar{q}_s\gamma^\mu\tau^I q_t\right)$

$8:(\bar{L}R)(\bar{R}L)+\text{h.c.}$	
O_{ledq}	$(\bar{l}_p^j e_r)(\bar{d}_s q_{tj})$

$8:(\bar{R}R)(\bar{R}R)$	
O_{ee}	$\left(\bar{e}_p\gamma_\mu e_r\right)\left(\bar{e}_s\gamma^\mu e_t\right)$
O_{uu}	$\left(\bar{u}_p\gamma_\mu u_r\right)\left(\bar{u}_s\gamma^\mu u_t\right)$
O_{dd}	$\left(\bar{d}_p\gamma_\mu d_r\right)\left(\bar{d}_s\gamma^\mu d_t\right)$
O_{eu}	$\left(\bar{e}_p\gamma_\mu e_r\right)\left(\bar{u}_s\gamma^\mu u_t\right)$
O_{ed}	$\left(\bar{e}_p\gamma_\mu e_r\right)\left(\bar{d}_s\gamma^\mu d_t\right)$
$O_{ud}^{(1)}$	$\left(\bar{u}_p\gamma_\mu u_r\right)\left(\bar{d}_s\gamma^\mu d_t\right)$
$O_{ud}^{(3)}$	$\left(\bar{u}_p\gamma_\mu T^A u_r\right)\left(\bar{d}_s\gamma^\mu T^A d_t\right)$

$8:(\bar{L}L)(\bar{R}R)$	
O_{le}	$\left(\bar{l}_p\gamma_\mu l_r\right)\left(\bar{e}_s\gamma^\mu e_t\right)$
O_{lu}	$\left(\bar{u}_p\gamma_\mu u_r\right)\left(\bar{u}_s\gamma^\mu u_t\right)$
O_{ld}	$\left(\bar{l}_p\gamma_\mu l_r\right)\left(\bar{d}_s\gamma^\mu d_t\right)$
O_{qe}	$\left(\bar{q}_p\gamma_\mu q_r\right)\left(\bar{e}_s\gamma^\mu e_t\right)$
$O_{qu}^{(1)}$	$\left(\bar{q}_p\gamma_\mu q_r\right)\left(\bar{u}_s\gamma^\mu u_t\right)$
$O_{qu}^{(8)}$	$\left(\bar{q}_p\gamma_\mu T^A q_r\right)\left(\bar{u}_s\gamma^\mu T^A u_t\right)$
$O_{qd}^{(1)}$	$\left(\bar{q}_p\gamma_\mu q_r\right)\left(\bar{d}_s\gamma^\mu d_t\right)$
$O_{qd}^{(8)}$	$\left(\bar{q}_p\gamma_\mu T^A q_r\right)\left(\bar{d}_s\gamma^\mu T^A d_t\right)$

$8:(\bar{L}R)(\bar{L}R)+\text{h.c.}$	
$O_{quqd}^{(1)}$	$(\bar{q}_p^j u_r)\epsilon_{jk}(\bar{q}_s^k d_t)$
$O_{quqd}^{(8)}$	$(\bar{q}_p^j T^A u_r)\epsilon_{jk}(\bar{q}_s^k T^A d_t)$
$O_{lequ}^{(1)}$	$(\bar{l}_p^j e_r)\epsilon_{jk}(\bar{q}_s^k u_t)$
$O_{lequ}^{(3)}$	$(\bar{l}_p^j\sigma_{\mu\nu}e_r)\epsilon_{jk}(\bar{q}_s^k\sigma^{\mu\nu}u_t)$

- Non-derivative interactions between fermions and electroweak bosons take the form

$$\begin{aligned}\mathcal{L}_{\text{vertex}} \;=\; & -\frac{g_L}{\sqrt{2}}\left(W_\mu^+ \bar{u}_L \gamma_\mu (V + \delta g_L^{Wq}) d_L + W_\mu^+ \bar{u}_R \gamma_\mu \delta g_R^{Wq} d_R + \text{h.c.}\right) \\ & -\frac{g_L}{\sqrt{2}}\left(W_\mu^+ \bar{\nu}_L \gamma_\mu (\mathbf{I} + \delta g_L^{We}) e_L + \text{h.c.}\right) \\ & -\sqrt{g_L^2 + g_Y^2} Z_\mu \left[\sum_{f\in u,d,e,\nu} \bar{f}_L \gamma_\mu ((T_f^3 - s_\theta^2 Q_f)\,\mathbf{I} + \delta g_L^{Zf}) f_L\right] \\ & -\sqrt{g_L^2 + g_Y^2} Z_\mu \left[\sum_{f\in u,d,e} \bar{f}_R \gamma_\mu (-s_\theta^2 Q_f\,\mathbf{I} + \delta g_R^{Zf}) f_R\right]. \end{aligned} \tag{2.15}$$

  where f are the SM fermion fields, V is the unitary CKM matrix and all δg parameters are 3×3 matrices in flavor space.

- The interactions involving the Higgs boson, electroweak bosons and pairs of fermions are fixed by the vertex corrections δg in Eq. (2.15).

- Derivatives do not act on the Higgs field when coupled with electroweak bosons.

- In the $\{G_F, \alpha, m_Z\}$ input scheme, the W boson mass in the SM is fixed in terms of the inputs, but it will receive indirect BSM corrections as

$$\delta m_W = \frac{1}{2}\delta g_L^{We} + \frac{1}{2}\delta g_L^{W\mu} - \frac{v^2}{4}[C_{ll}]_{1221}, \tag{2.16}$$

  where the combination of Wilson coefficients is expressed in terms of the Higgs basis. These corrections are completely scheme dependent, we can always rearrange the inputs so that m_W is not contaminated at all by new physics.

If all these conditions are met, then the SMEFT Lagrangian will be written in terms of the Higgs basis. Every operator basis can be mapped to the Higgs basis without any loss in generality.

The only additional point that we need to keep in mind when working with the Higgs basis is that not all operators will be fully independent, some of them will be correlated due to SMEFT symmetries. Thus, in order to define a proper basis, a subset of independent couplings must be chosen as the concrete basis elements. Once that is done, the connection of the Higgs basis to any other operator basis can be unambiguously defined.

We restrain ourselves from discussing the full content of the SMEFT Lagrangian in terms of the Higgs basis and focus only on the parts that are relevant for the studies conducted in this thesis. In particular, we will be interested in terms involving one electroweak boson and a pair of fermions and in four-fermion interactions. The Lagrangian expression for the electroweak vertices has already been written down in Eq. (2.15), and the four-fermion operators do not change when going from the Warsaw basis to the Higgs basis. Wilson coefficients in Eq, (2.15)

can be expressed in terms of Warsaw basis parameters as follows:

$$\begin{aligned}
v^{-2}\delta g_L^{We} &= C_{Hl}^{(3)} + f(1/2,0) - f(-1/2,-1),\\
v^{-2}\delta g_L^{Ze} &= -\frac{1}{2}C_{Hl}^{(3)} - \frac{1}{2}C_{Hl}^{(1)} + f(-1/2,-1),\\
v^{-2}\delta g_R^{Ze} &= -\frac{1}{2}C_{He}^{(1)} + f(0,-1),\\
v^{-2}\delta g_L^{Zu} &= \frac{1}{2}VC_{Hq}^{(3)}V^\dagger - \frac{1}{2}VC_{Hq}^{(1)}V^\dagger + f(1/2,2/3),\\
v^{-2}\delta g_L^{Zd} &= -\frac{1}{2}C_{Hq}^{(3)} - \frac{1}{2}C_{Hq}^{(1)} + f(-1/2,-1/3),\\
v^{-2}\delta g_R^{Zu} &= -\frac{1}{2}C_{Hu} + f(0,2/3),\\
v^{-2}\delta g_R^{Zd} &= -\frac{1}{2}C_{Hd} + f(0,-1/3),
\end{aligned} \tag{2.17}$$

where

$$f(T^3,Q) \equiv \left\{ -Q\frac{g_L g_Y}{g_L^2 - g_Y^2}C_{HWB} - \left(\frac{1}{4}C_{HD} + \frac{1}{2}\Delta_{G_F}\right)\left(T^3 + Q\frac{g_Y^2}{g_L^2 - g_Y^2}\right)\right\}\mathbf{1}, \tag{2.18}$$

and $\Delta_{G_F} \equiv [C_{Hl}^{(3)}]_{11} + [C_{Hl}^{(3)}]_{22} - \frac{1}{2}[C_{ll}]_{1221}$. Here, we have adopted the conventions and notation of the *Wilson coefficient exchange format* (WCxf) [102]. For a similar mapping to the SILH basis [103] see Ref. [104].

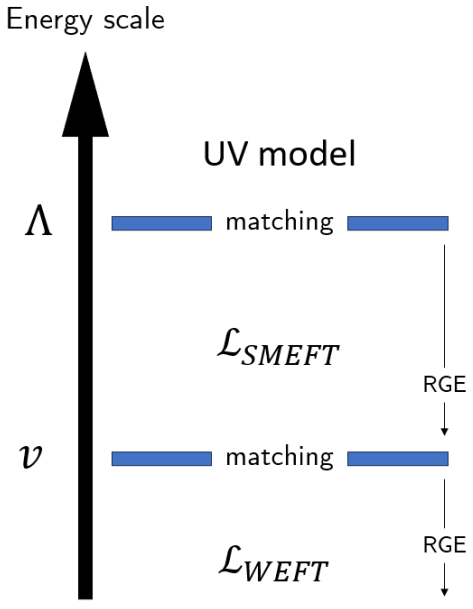

Fig. 2.1: Illustration of the EFT ladder connecting a UV model, the SMEFT and the WEFT built from the procedure of matching and running.

Concerning possible redundancies, the $SU(3)_C \times SU(2)_L \times U(1)_Y$ symmetry of the SMEFT Lagrangian, although here it has been reduced to a $SU(3)_C \times U(1)_{\rm em}$ due to SSB, implies some correlations between the W and Z couplings to fermions. More specifically, this means that not all the δg's are independent. Expressing δg in any basis of the Wilson coefficients one finds

$$\delta g_L^{Z\nu} = \delta g_L^{We} + \delta g_L^{Ze}, \qquad \delta g_L^{Wq} = \delta g_L^{Zu}V - V\delta g_L^{Zd}\,. \tag{2.19}$$

Given this dependence, we will not consider $\delta g_L^{Z\nu}$ nor δg_L^{Wq} as Higgs basis elements.

One last important point that should be considered when discussing the SMEFT is its connection to other EFTs defined for lower energy environments. If we are looking at processes that lie well below the electroweak scale, then it may be the case that the SMEFT is not the best tool for computing predictions, especially if we aim at a high precision level. As discussed in Chapter 2.1, we can integrate out the heavy degrees of freedom that lie beyond the scale of interest through the procedure of matching and running and work with an alternative EFT specialized in a lower energy environment.

For instance, if we integrate out the Higgs boson, the weak bosons and the top quark in the SMEFT, we will end up with the low-energy effective field theory (LEFT), also known as the weak effective field theory (WEFT) [56, 105]. We illustrate this process and the resulting EFT ladder composed by the unknown UV model, the SMEFT and the WEFT in Fig. 2.1. This theory can be regarded as an extension of the Fermi theory presented as an example in Chapter 2. More specifically, we will have a larger set of interactions due to the $SU(2)_L$ gauge invariance dropout, and the inclusion of BSM effects will expand the collection even further. Due to the closeness of all the high energy scales in this range, only one parameter is needed for capturing the high energy effects in the EFT expansion, which is typically chosen to be either v or M_W. In the NP regime, this expansion gets intermingled with the previous one in Λ, which increases the number of possible high-dimensional operators in the theory and also complicates the suppression patterns. In general, operators in the WEFT will be suppressed by

$$\frac{1}{v^\alpha}\frac{1}{\Lambda^\beta}, \tag{2.20}$$

where β will always be positive and α can take negative values as long as we express SM masses in terms of v. This scenario where multiple scales are present could also be present in the SMEFT itself, because as far as we know there could be multiple NP scales at the UV range. The most important scale for examining the validity of any EFT will be the smallest one, but the other ones can be important to explain accidental symmetries without requiring an extremely high NP scale.[3]

It is important to note that the WEFT is an EFT on its own, i.e., it does not need to have the SMEFT as its UV completion. Like any other low energy EFT, it can be built with the SM as the starting full theory, the only changes in its formulation will be in the matching conditions between the two frameworks and in the absence of the EFT expansion in $1/\Lambda$. In fact, most of its formal development was motivated by its utility for SM tests on heavy mesons.

The WEFT will be a very important tool for the work presented in this thesis, especially in the analysis discussed in Chapter 5. However, it is far from being the only lower energy EFT that is derivable from the SMEFT or the SM. Other important EFTs that can be built from integrating out heavy SM particles are the chiral perturbation theory (ChPT) [50, 106–108], the heavy quark effective theory (HQET) [109, 110] and the soft collinear effective field theory (SCET) [111–117].

In the following, we will describe how the SMEFT can be used for phenomenological searches. For more detailed discussions on the formal aspects of the SMEFT, see Refs. [49, 61, 104, 118].

2.2.2. SMEFT global fits

Using the SMEFT to characterize BSM physics focuses the bottom-up NP searches on the estimation of the SMEFT Wilson coefficients. The main objective is to establish the best possible limits on the SMEFT parameter space from experimental data and minimal theoretical assumptions. These studies are normally conducted by reexamining previously studied observables assuming a new physics regime. In such a context, predictions for the observables in the SM will get corrected by subleading terms involving the EFT operators, so a comparison with their

[3] In particular with the SMEFT, the very different bounds that are found on symmetry-violating and symmetry-preserving operators imply a very high energy for new particles if we assume there is just one UV scale. However, if we postulate an additional lower NP scale, we can accommodate the origin of the symmetry-preserving terms there and assign the symmetry-violating ones to the higher cutoff.

corresponding measurements will allow for the extraction of limits on the new physics couplings. This kind of procedure is often called an EFT or NP fit.

More often than not, a single observable will only be sensitive to a handful of Wilson coefficients, so its utility is quite limited when trying to probe the SMEFT parameter space. Furthermore, even in cases where an observable has access to a decent number of EFT operators, it is very likely that the available data is not enough to restrict all couplings simultaneously. For this reason, new physics searches benefit greatly from considering multiple observables that are sensitive to a diverse set of WC combinations. When an EFT fit considers all relevant NP parameters and it includes multiple experimental sources, we call it a global fit.

New physics effects in the SMEFT are expected to be small, since they are assumed to come from suppressed high energy contributions. To be able to observe them, it is then convenient to aim for the highest degree of precision in the fits. This requirement can make the limit estimation very challenging, but the good thing is that the task must be done just once. This is the big selling point of the SMEFT as a new physics probing tool in bottom-up analyses. The final constraints on its Wilson coefficients will account for all relevant input coming from the measurement, including experimental errors, cuts, parton distribution functions (PDFs), loop corrections, etc. All this information will be condensed in the limits, and from the SMEFT it is straightforward to transfer it to the parameters of any BSM model we may be interested in.

However, despite the benefits of the SMEFT as a tool for new physics searches, its generic nature also represents its biggest flaw. The huge amount of freedom in the configuration of BSM contributions translates to a very numerous collection of high-dimensional operators, even when taking a cutoff at $d = 6$. This means that a very extensive program involving a big variety of observables is necessary to map out significant portions of the parameter space. Besides that, this circumstance makes the pursuit of high precision in the SMEFT analyses even more important, since the limited amount of experimental inputs makes each of them very relevant for the extraction of acceptable bounds on the Wilson coefficients.

In practice, this type of analyses often rely on additional assumptions on the SMEFT to make the fits more tractable. The most common one is based on the assumption of extra symmetries for the effective operators. For instance, considering baryon and lepton number conservation leaves only six-dimensional operators as the SMEFT leading terms, and flavor universality or conservation can be applied to greatly reduce the number of independent parameters. On the measurement side, most global analyses focus on a specific class of observables, since it is expected that the NP contributions that are relevant in each experimental context will be uncorrelated from the rest of the parameter space.

Additionally, we can use also apply purely theoretical arguments to further constrain the structure of the theory. The most important ones are unitarity and positivity. Unitarity violation manifests itself in amplitudes that have an unbounded energy scaling behavior, which threaten the perturbative expansion of the theory. Constraints in the parameter space derived from preventing unitarity violation can be found in Refs. [119, 120]. As for positivity, this class of restrictions comes from a combined requirement of the unitarity and analyticity, which implies certain global sign fixes on combinations of Wilson coefficients. Deduction for this sort of bound on SMEFT parameters have been conducted in Refs. [121–126].

Analogue theoretical guidelines can also be used to estimate the sizes of Wilson coefficients even without any information about the underlying theory. Some of the most important ones are naive dimensional analysis (NDA) [127], and the ability to discriminate between high dimensional

operators that can be generated from tree-level processes in the full theory and those that can only come from loop diagrams [128–130]. However, in our studies we will focus on estimating the values of the SMEFT parameters through phenomenological inputs, so we will not further elaborate on these techniques.

Considering all these options, we now move on to describe how to build a SMEFT global fit. From a statistical perspective, our objective is to infer numerical values and uncertainties for a set of parameters using the information from an experimental data set. To accomplish this, we make use of the method of maximum likelihood. Our main motivation for choosing it is its capability to accommodate multiple experimental inputs in a simple manner. The following discussion closely follows the chapter on statistics presented by the PDG in its yearly review [131]. Given a list of N parameters $\boldsymbol{\theta} = (\theta_1, \cdots, \theta_N)$, their values under this method are estimated by maximizing the likelihood $L(\boldsymbol{\theta}) = P(\boldsymbol{y}|\boldsymbol{\theta})$, where $\boldsymbol{y}$ is a collection of measurements whose probability depends on $\boldsymbol{\theta}$. Alternatively, minimizing the logarithm of the likelihood yields the same results, and is often preferred due to some nice properties of the logarithm.

The computation of the minimum and of the associated uncertainties of the estimator can get simplified by imposing two conditions in the data we will analyze. First, we will mostly consider *i.i.d.* (independent and identically distributed) measurements. This type of data is very convenient, because all elements in the sample will be statistically independent and they will be generated by the same probability distribution $p(\boldsymbol{y}; \boldsymbol{\theta})$. The direct consequence of this in the likelihood is that it can be factorized as

$$L(\boldsymbol{\theta}) = \prod_{i=1}^{N} p(y_i; \boldsymbol{\theta}). \tag{2.21}$$

Thus, we will be able to easily add or subtract any number of data inputs in the likelihood. This property will be present in some but not all the data that we will analyze. In some instances we will encounter data sets that consist of samples which are not independent but are still generated by the same probability distribution. In those cases we will need to find a way to characterize the correlation between the different data points.

The second property that we will assume in the data is that it follows a Gaussian distribution. If each data point y_i^{exp} is produced from a distribution with mean y_i^{th} and variance σ_i^2, the log-likelihood can be related to the following sum of squares:

$$-2 \ln L(\boldsymbol{\theta}) + K = \sum_{i=1}^{N} \frac{\left(y_i - y_i^{\text{th}}(\boldsymbol{\theta})\right)^2}{\sigma_i^2} \equiv \chi^2(\boldsymbol{\theta}), \tag{2.22}$$

where K is a constant and the mean depends on the unknown parameters $\boldsymbol{\theta}$. Thus, maximizing the likelihood is equivalent to minimizing this square sum. If the data is correlated, this correspondence is maintained, but $\chi^2(\boldsymbol{\theta})$ changes to

$$\chi^2(\boldsymbol{\theta}) = \left(\boldsymbol{y}^{\text{exp}} - \boldsymbol{y}^{\text{th}}(\boldsymbol{\theta})\right)^T V^{-1} \left(\boldsymbol{y}^{\text{exp}} - \boldsymbol{y}^{\text{th}}(\boldsymbol{\theta})\right), \tag{2.23}$$

where $V_{ij} = \text{cov}(y_i, y_j)$ is the corresponding covariance matrix. Due to its simpler expression, we will always choose to work with $\chi^2(\boldsymbol{\theta})$ in our studies whenever we deal with Gaussian data.

These assumptions tremendously simplify the computation of uncertainties for the parameter estimations. Under a Gaussian regime, the covariance matrix for $\boldsymbol{\theta}$ can be calculated through the following set of derivatives:

$$(\hat{V}^{-1})_{ij} = -\left.\frac{\partial^2 \ln L}{\partial\theta_i \partial\theta_j}\right|_{\hat{\boldsymbol{\theta}}} \tag{2.24}$$

where $\hat{\boldsymbol{\theta}}$ are the expected values for the parameters of interest, defined so that they maximize the likelihood. This matrix contains the standard deviations $\hat{\sigma}_i$ in its diagonal elements and codifies the correlations between the estimates in its off-diagonal ones through the coefficients $\hat{\rho}_{ij} = \hat{V}_{ij} / (\hat{\sigma}_i \hat{\sigma}_j)$. This estimated covariance matrix is not to be confused with the one in (2.23), which is formulated as part of the description of the data.

Modeling the data with Gaussian distributions also allows us to easily estimate the probability that the true values of the parameters lie in a specific region in parameter space. This probability is quantified by the confidence level α, which marks the limit of the allowed region where the correct values of the parameters can be found. In a Gaussian fit where the mean is linear in $\boldsymbol{\theta}$, the probability distribution for the unknown parameters will also be described by a multivariate Gaussian function, whose mean will be $\hat{\boldsymbol{\theta}}$ and its variance $\hat{\boldsymbol{\sigma}}$. For the univariate case, the confidence level for an interval of θ will be given by

$$1 - \alpha = \frac{1}{\sqrt{2\pi}\hat{\sigma}} \int_{\hat{\theta}-\delta}^{\hat{\theta}+\delta} e^{-(\theta-\hat{\theta})^2/2\hat{\sigma}^2} d\theta, \tag{2.25}$$

where δ will represent the limits of the allowed interval. Normally, α is chosen so that δ corresponds to an integer number of standard deviations $\hat{\sigma}$. For instance, $\alpha = 0.32$ corresponds to the 1σ interval and $\alpha = 0.0455$ corresponds to the 2σ interval.

At this point we can draw a clear connection between the confidence interval formula evaluated at 1σ and the uncertainty estimator in (2.24), since at 1 dimension the single element of the covariance matrix is equal to the estimated standard deviation $\hat{\sigma}$. This connection is evident for fits with just one variable, but it also extends to multivariate analyses. More specifically, the covariance matrix $\hat{V}$ univocally defines the so-called 1σ allowed region (delimited by $\alpha = 0.32$) for any parameter space size. In a fit with n parameters, this region takes the form of an n-dimensional hyperellipse, whose parameters are completely specified by the covariance matrix in (2.24). More specifically, the center of the hyperellipse is located at $\hat{\boldsymbol{\theta}}$, its axes are given by the diagonal elements of the covariance matrix and the off-diagonal elements set its orientation. For instance, in the case of a 2-dimensional parameter space, the major axis of the ellipse can be calculated as

$$\tan 2\phi = \frac{2\rho_{12}\,\hat{\sigma}_1 \hat{\sigma}_2}{\hat{\sigma}_2^2 - \hat{\sigma}_1^2}. \tag{2.26}$$

The covariance matrix also allows us to calculate the confidence regions for any value of α. The reason for this is that Gaussian log-likelihoods are hyperparabolic functions of $\boldsymbol{\theta}$. This implies that the shape of any region will be the same as the one we may find at 1σ, the only difference between them will be in their global size.

When looking at non-linear likelihoods, the confidence regions cannot be fully extracted with the covariance matrix. Instead, they are generally expressed as a function of the displacement of the log-likelihood with respect to its minimum $\left(\Delta\chi^2(\boldsymbol{\theta}) \equiv \chi^2(\boldsymbol{\theta}) - \chi^2(\hat{\boldsymbol{\theta}})\right)$ through the cumulative distribution:

$$\alpha = 1 - F\left(\Delta\chi^2; \alpha\right). \tag{2.27}$$

An equivalent expression can also be formulated in terms of the displacement of the log-likelihood $\ln L(\boldsymbol{\theta})$. When applying this method on linear likelihoods, we will always reproduce the same hyperellipses we would obtain through the covariance matrices, but outside of that regime the allowed regions can take any shape without restriction.

Table 2.2: Values of $\Delta\chi^2$ corresponding to different confidence levels α for m-dimensional parameter estimations.

$(1-\alpha)(\%)$	m=1	m=2	m=3
68.27 (1σ)	1.00	2.30	3.53
90	2.71	4.61	6.25
95	3.84	5.99	7.82
95.45 (2σ)	4.00	6.18	8.03
99.73 (3σ)	9.00	11.83	14.16

Table 2.2 shows the correspondence between $\Delta\chi^2$ and α for some typically quoted confidence intervals in m-dimensional variable estimations. Note that the confidence region estimation can be done with the log-likelihood displacement even if the data does not follow a Gaussian law.

Another important point that should be considered when working with the maximum likelihood method is its treatment of systematic bias. The likelihood in Eq. (2.22) can account for both statistical and systematic uncertainties through the σ_i variables, but sometimes it is not the most adequate tool for modeling certain systematic sources. In such cases, it is possible to model this kind of errors by using nuisance parameters. These parameters enter the likelihood as extra unknown variables and are fitted together with $\boldsymbol{\theta}$. Through this operation, the impact coming from systematic uncertainties will be properly included in the fit results. This is the case thanks to the interplay of the nuisance parameters with $\boldsymbol{\theta}$ at the likelihood.

For Gaussian data, they can be generally added to the χ^2 function as

$$\chi^2(\boldsymbol{\theta},\boldsymbol{\alpha}) = (\boldsymbol{y}-\boldsymbol{\mu}(\boldsymbol{x},\boldsymbol{\theta},\boldsymbol{\alpha}))^T V^{-1} (\boldsymbol{y}-\boldsymbol{\mu}(\boldsymbol{x},\boldsymbol{\theta},\boldsymbol{\alpha})) + (\boldsymbol{\alpha}-\hat{\boldsymbol{\alpha}})^T V_{\boldsymbol{\alpha}}^{-1} (\boldsymbol{\alpha}-\hat{\boldsymbol{\alpha}}) , \tag{2.28}$$

where $\boldsymbol{\alpha}$ is the collection of nuisance parameters with expected value $\hat{\alpha}$, correlated through the covariance matrix V_α. Each nuisance parameter is linked to a different systematic source, and the magnitude of their associated errors is quantified in the diagonal elements of V_α.

One last important tool for any multiparameter fit is that of marginalization. The basic idea behind it is to evaluate the likelihood just at a subset of all the variables in $\boldsymbol{\theta}$ space while minimizing over the rest of parameters. Marginalization is the correct way to project the likelihood from the full parameter space to any subspace that we want. It is different from setting parameters to zero, since such an approach would imply that the absent parameters are completely neglected in the fit. Marginalization is the correct way to remove them from the confidence regions in a statistically appropriate manner.

This procedure is very useful when we want to represent allowed parameter regions in a graphical way. We will make use of it whenever we plot two-dimensional projections of the limits we find in the SMEFT parameter space. Special care should be taken when projecting the limits to one dimension in the graphical representation. For instance, if in a Gaussian fit we draw a 1σ ellipse in two-dimensional parameter space ($\Delta\chi^2 = 2.30$), the marginalized limits for just one of the couplings will not be obtained by just projecting the ellipse onto the axes. Instead, the correct procedure is to redraw the ellipse in the corresponding 1σ region for 1 parameter ($\Delta\chi^2$=1), and then we can project safely to obtain the individual bounds.

This circumstance explains very confusing occurrences such as an apparent enhancement of the allowed regions when combining two independent experimental probes. More specifically, if we have access to two complementary data inputs and we represent graphically their constraining

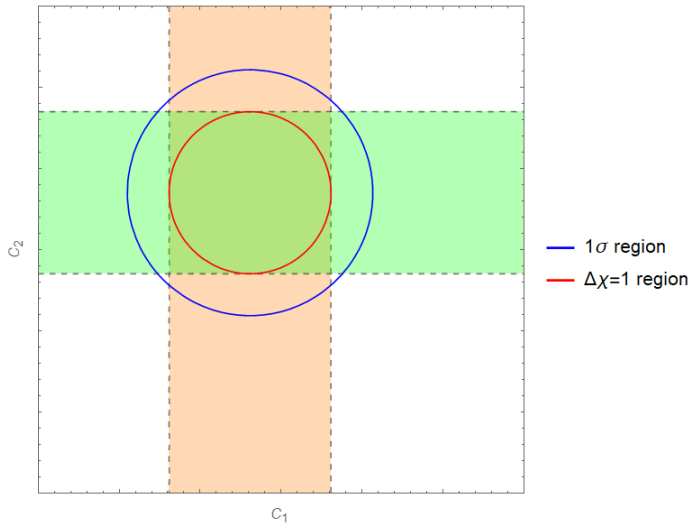

Fig. 2.2: Example result from the combination of two 1-dimensional 1σ parameter regions onto a 2-dimensional estimation. If we represent the 1σ region in the combined fit, the resulting area in parameter space is visually larger than what we would expect from the composition of the individual fits. If we instead plot the region corresponding to $\Delta\chi^2 = 1$, it limits itself to the intersection of the 1-dimensional regions and the visual intuition is preserved.

power, the combination of the separate $n\sigma$ bounds will not be the overlap of the two contours. The corresponding $n\sigma$ region in the combined fit will trespass over the expected limits. For this reason, whenever we perform combined fits in our studies, we will not change the $\Delta\chi^2$ boundary when moving from one fit to the other. That way, the improvement of the restriction will be perfectly clear in the graphical context. This kind of situation is graphically illustrated with an example plot in Fig. 2.2.

The marginalization procedure can be computationally challenging in non-Gaussian setups whenever we represent the bounds graphically, but it becomes trivial in Gaussian fits when we compute the results as a set of individual limits plus a covariance matrix. For instance, if we fit three parameters $\{x, y, z\}$ simultaneously and we want to marginalize over the z variable, then the procedure amounts to just:

$$\begin{pmatrix} \hat{x} \\ \hat{y} \\ \hat{z} \end{pmatrix} = \begin{pmatrix} x_0 \pm \delta x \\ y_0 \pm \delta y \\ z_0 \pm \delta z \end{pmatrix}, \ \rho = \begin{pmatrix} 1 & \rho_{12} & \rho_{13} \\ \rho_{12} & 1 & \rho_{23} \\ \rho_{13} & \rho_{23} & 1 \end{pmatrix} \rightarrow \begin{pmatrix} \hat{x} \\ \hat{y} \end{pmatrix} = \begin{pmatrix} x_0 \pm \delta x \\ y_0 \pm \delta y \end{pmatrix}, \ \rho = \begin{pmatrix} 1 & \rho_{12} \\ \rho_{12} & 1 \end{pmatrix}. \tag{2.29}$$

Marginalization is also very useful when dealing with nuisance parameters. Their presence usually obscures the allowed regions for the parameters with real physical meaning, but marginalizing over them we can project the likelihood from the full parameter space to a subspace containing only the interesting variables in the fit.

In our multiparameter phenomenological analyses, we will always aim at computing marginalized limits to properly account for all parameters in the fit. We will also consider scenarios where only one unknown parameter is present, but we keep in mind that the limits we obtain in those cases will give us just an estimation of the sensitivity of an observable to a given Wilson coefficient. The scenario where all possible parameters are considered will generally be the most useful when performing SMEFT fits. This is because the more simultaneous parameters in the fit the more flexibility we will have to adapt the limits to specific NP models.

All these statistical concepts can be applied to the particular problem of new physics searches in a straightforward way. In this context, $\boldsymbol{\mu}(\boldsymbol{x}, \boldsymbol{\theta})$ consists of the predicted values for every point in the data set $\boldsymbol{y}$, and the parameters $\boldsymbol{\theta}$ are identified with the new physics coefficients that we want to determine. Thus, by implementing the maximum likelihood method and assuming Gaussian data, we can estimate values for our parameters of interest up to whatever confidence level we may desire. However, in practice the involved computations can become challenging when the dependence between the observables and the new physics parameters is non-trivial.

Fortunately, this procedure gets greatly simplified if we consider that $\boldsymbol{y}^{\text{th}}(\boldsymbol{\theta})$ is a linear function on $\boldsymbol{\theta}$:

$$\boldsymbol{y}^{\text{th}}(\boldsymbol{\theta}) = \sum_{j=1}^{m} h_{ij}\theta_j, \tag{2.30}$$

where h_{ij} are the respective linear coefficients. If the number of unknown parameters m is lower than the size N of the data set, then the problem of minimizing χ^2 gets reduced to solving a system of m linear equations. Besides that, the task of drawing allowed regions gets very streamlined, since we know that they will always take the form of hyperellipses whose relative axis size and orientation are given by the estimated covariance matrix.

This scenario will be very common in our phenomenological analyses, since our restriction to only $d = 6$ operators will imply that our observable predictions will be linear in the Wilson coefficients. If we have N independent data points, it should be possible to constrain at most the same amount of parameters in a fit. However, in practice this is often not realized, since normally two or more measurements are sensitive to approximately the same combination of Wilson coefficients. If that is the case, either the data collection will not be enough to bound the entirety of parameter space, or it will only be able to do so in a feeble manner. Parts of parameter space that cannot be probed with the available data are characterized as blind or flat directions in the fit, defined as orthogonal linear combinations of parameters on which no restrictions can be established. Their treatment will be discussed in detail in the next chapter.

Working with linear fits gives an additional advantage, because we can obtain the directions in parameter space that are probed directly by our experimental inputs. The orthogonal and uncorrelated directions in parameter space constrained by the data will be obtained by diagonalizing the covariance matrix $\hat{V}$. This procedure is very useful, because it allows us to grasp the real constraining power that lies inside our data. Furthermore, it establishes a clear ranking of the directions in parameter space according to how well they can be restricted by the data. This represents a major aid in the interpretability of the fit results. More details about this procedure will be given when we apply it in Chapter 4.1.

In the following chapters, we will use these ideas in the computation of specific new physics global fits. The data sets that we will consider are assumed to be well modeled by Gaussian distributions except for the one analyzed in Chapter 5. The measurements considered there come in the form of binned event distributions, which are not appropriately described by a Gaussian likelihood. The general maximum likelihood method can still be applied, but the function that is minimized in this case is a Poissonian one:

$$-\ln \lambda(\boldsymbol{\theta}) = \sum_{i=1}^{N} \left[\mu_i(\boldsymbol{\theta}) - n_i + n_i \ln \left(\frac{n_i}{\mu_i(\boldsymbol{\theta})} \right) \right], \tag{2.31}$$

where n_i is the number of events in each bin. This expression implicitly accounts for statistical uncertainties, but systematic uncertainties still need to be characterized with nuisance parame-

ters. Previous guidelines concerning uncertainties, confidence regions, nuisance parameters and marginalization are still valid in this context.

All in all, the ideas presented in this chapter coming from the EFT framework and statistics will serve as the toolbox with which we will develop our own SMEFT global fit analyses. These studies represent the main work of this thesis, and we will discuss them in detail in the following chapters.

Chapter 3

EFTs for global analyses

We now understand the attractiveness of the SMEFT as a theoretical framework for new physics searches and how to apply it to perform global fits. In this chapter, we will put all these notions to use by examining potential new physics corrections in flavor-conserving experiments measuring at energy ranges at or below the electroweak scale ($E \leq v$). Our objective will be to provide constraints to all independent flavor-diagonal dimension-6 operators that may be linked to them. The relevant observables in this context will be sensitive to electroweak boson couplings to fermions and to 4-fermion operators between 2 leptons and 2 quarks (LLQQ) and 4 leptons (LLLL). This class of operators is interesting for multiple NP scenarios, specially in the flavor-generic setting where we are admitting different interaction strengths for the SM generations. For instance, all models attempting to explain the B-meson anomalies must introduce new particles with non-universal couplings to the light fermions. Thus, the results derived from this study will represent model-independent constraints that have to be satisfied by all such models.

As for the terms in the EFT expansion we will consider, we will restrict ourselves to leading order. All dimension-8 and higher operators will be neglected, as well as nonlinear contributions of the dimension-6 operators at the observable level. The main practical consequence of this decision is that the likelihood fit that we will execute will be Gaussian, which will make the limits we obtain much easier to compute and to interpret. Additionally, we will ignore loop terms for the effective operators, which scale as $\mathcal{O}\left(\frac{1}{16\pi^2\Lambda^2}\right)$ corrections. However, we will consider corrections induced by QCD and EW runnings, since the large diversity of experimental scales present in the fit will render them relevant.

We will parametrize the NP terms through the Higgs basis, set up with the $\{G_F, \alpha, m_Z\}$ input scheme. As was discussed in Chapter 2.2.1, the Higgs basis redefines these inputs so that their relations with the couplings the g_L, g_Y, v are the same as in the SM:

$$G_F = \frac{1}{\sqrt{2}v^2}, \quad \alpha(m_Z) = \frac{g_L^2 g_Y^2}{4\pi(g_L^2 + g_Y^2)}, \quad m_Z = \frac{\sqrt{g_L^2 + g_Y^2}}{2}v, \tag{3.1}$$

yielding $g_L = 0.6485$, $g_Y = 0.3580$ and $v = 246.22$ GeV, where we neglect their associated errors. Apart from that, the Higgs basis works with the Lagrangian after applying electroweak symmetry breaking and with the mass eigenstates for the fermion fields defined so that all kinetic and mass terms are diagonal and canonically normalized. This will allow us to express the NP terms as either corrections for the SM couplings or brand new exotic interaction terms.

In the following, we will describe the global fit presented in Ref. [132], which represents the foundation and main reference point for the main work that was developed for this thesis. In the next chapters, we will explain the updates for this analysis based on new information from the Z peak [133] and the neutrino sector [134].

3.1. Low-energy global fit

We now move on to discuss the details of the global SMEFT fit built from observables around and below the electroweak scale, which we will identify in the following as the low-energy electroweak sector. Again, in this chapter we will recap the work performed in Ref. [132], as it will be the baseline for the work to be presented in the rest of the thesis. We start by listing the effective operators that are relevant for the low-energy observables. Working in the Higgs basis, the operators involved in the fit are a subset of 4-lepton and 2-lepton-2-quark operators, as well as vertex corrections to electroweak gauge boson interactions with fermions:

$$\mathcal{L}_{\text{SMEFT}} \supset \mathcal{L}_{2l2q} + \mathcal{L}_{4l} + \mathcal{L}_{\text{vertex}}. \tag{3.2}$$

We first write the interactions involving electroweak bosons and a pair of SM fermions (*cf.* (2.15)):

$$\begin{aligned}
\mathcal{L}_{\text{vertex}} \;=\; & -\frac{g_L}{\sqrt{2}}\left(W_\mu^+ \bar{u}_L \gamma_\mu (V + \delta g_L^{Wq}) d_L + W_\mu^+ \bar{u}_R \gamma_\mu \delta g_R^{Wq} d_R + \text{h.c.}\right) \\
& -\frac{g_L}{\sqrt{2}}\left(W_\mu^+ \bar{\nu}_L \gamma_\mu (\mathbf{I} + \delta g_L^{We}) e_L + \text{h.c.}\right) \\
& -\sqrt{g_L^2 + g_Y^2} Z_\mu \left[\sum_{f\in u,d,e,\nu} \bar{f}_L \gamma_\mu ((T_f^3 - s_\theta^2 Q_f)\,\mathbf{I} + \delta g_L^{Zf}) f_L\right] \\
& -\sqrt{g_L^2 + g_Y^2} Z_\mu \left[\sum_{f\in u,d,e} \bar{f}_R \gamma_\mu (-s_\theta^2 Q_f\,\mathbf{I} + \delta g_R^{Zf}) f_R\right].
\end{aligned} \tag{3.3}$$

Here, the SM fermion fields f are 3-vectors in flavor space, written in the diagonal basis for their mass terms (for neutrinos, where their charged current interactions are diagonal in the limit $\delta g_L^{We} \to 0$) and V is the unitary CKM matrix, which we approximate by the unit matrix when it acts on $\mathcal{O}\left(\Lambda^{-2}\right)$ terms.[1] All the parameters are flavor-diagonal, since any flavor-violating terms would not interfere with the SM terms in the observable and would thus enter at $\mathcal{O}(\Lambda^{-4})$. Taking this into account, the notation is shortened as $\delta g_X^{Vf_J} \equiv [\delta g_X^{Vf}]_{JJ}$ to omit the generation indices $J = 1, 2, 3$.

Additionally, the input scheme forces the following corrections on the W boson mass:

$$\mathcal{L}_{\text{SMEFT}} \supset \frac{g_L^2 v^2}{4}\left(1 + \delta m_W\right)^2 W_\mu^+ W_\mu^- + \frac{(g_L^2 + g_Y^2) v^2}{8} Z_\mu Z_\mu, \tag{3.4}$$

where the W mass correction can be expressed as a linear combination of WCs from the Higgs basis: $\delta m_W = \frac{1}{2}\delta g_L^{We} + \frac{1}{2}\delta g_L^{W\mu} - \frac{v^2}{4}[C_{ll}]_{1221}$ (*cf.* (2.16)).

The use of these expressions implies that all indirect EFT corrections and loop contributions are absorbed into the definition of g_L, g_Y, v. Once their values are set, these parameters can be used to fix all the SM couplings for the nonderivative interactions thanks to the fermions'

[1] Going beyond this approximation requires introducing some input scheme for the CKM matrix elements [135].

quantum numbers: the weak isospin T_f^3 and the electric charge Q_f. In Eq. (3.3), the NP operators are expressed as deformations of the SM terms, parametrized through the vertex corrections δg, which are 3×3 matrices in flavor space that can be flavor-violating. The NP contributions are disposed in this way because it makes it easier to monitor their physical meaning. Their connection with the dimension-6 Wilson coefficients in the Warsaw basis can be found in Eq. (2.17).

It is important to keep in mind that some EFT operators in the Higgs basis are correlated with one another. This affects the $\delta g_L^{Z\nu}$ or δg_L^{Wq} in the fit, which can be expressed in terms of other Wilson coefficients as (*cf.* Eq. (2.19)):

$$\delta g_L^{Z\nu} = \delta g_L^{We} + \delta g_L^{Ze}, \qquad \delta g_L^{Wq} = \delta g_L^{Zu} V - V \delta g_L^{Zd} \ . \tag{3.5}$$

Given this dependence, these two couplings are not present explictly in the fit.

Thus, $\mathcal{L}_{\text{vertex}}$ contains the following 24 independent dimension-6 Wilson coefficients, expressed as flavor-diagonal vertex corrections to the SM couplings:

$$\delta g_L^{We_I},\ \delta g_L^{Ze_I},\ \delta g_R^{Ze_I},\ \delta g_L^{Zd_I},\ \delta g_R^{Zd_I},\ \delta g_L^{Zu_I},\ \delta g_R^{Zu_I},\ \delta g_R^{Wq_I}. \tag{3.6}$$

The $\delta g_R^{Wq_I}$ couplings are complex, but their imaginary parts are neglected in the fit. This is because only CP-conserving observables are examined, and in them the imaginary contribution only enters at second order. δm_W is not present in this list as it is fully dependent on other vertex corrections and 4-fermion couplings.

The flavor-diagonal 4-fermion operators contained in $\mathcal{L}_{2l2q}$ and $\mathcal{L}_{4l}$ are also considered in the analysis in Ref. [132]. There are 90 LLQQ operators, out of which 27 (the chirality-violating ones) are complex, and 27 LLLL operators, out of which 3 ($[O_{le}]_{IJJI}$) are complex. We list them in Tables 3.1 and 3.2, which represent an extract of the 4-fermion operators collected in Table 2.1, organized according to their flavor structure and chirality. The operators are defined in the flavor basis where the up-quark Yukawa matrices are diagonal. All flavor combinations not listed in those tables are not considered so as to satisfy the baryon and lepton number conservation and avoid redundant operators related by Fierz transformations. For the complex Wilson coefficients, hermitian conjugate terms are included for their respective operators in Eq. (2.12). For 4-lepton terms, the Wilson coefficients of equivalent operators are identified: $[C_{ll}]_{JKKJ} = [C_{ll}]_{KJJK}$, $[C_{ee}]_{JKKJ} = [C_{ee}]_{KJJK}$.[2] These pieces are manifestly invariant under the SM gauge group, and are actually the same as the analogous terms in the Warsaw basis.

To constrain all these EFT coefficients, the following χ^2 function was used in Ref. [132]

$$\chi^2 = \sum_{ij} \left[O_{i,\text{exp}} - O_{i,\text{th}}\right] (\sigma^{-2})_{ij} \left[O_{j,\text{exp}} - O_{j,\text{th}}\right], \tag{3.7}$$

where $O_{i,\text{exp}}$ are the measurements for the observables considered in the fit, $O_{i,\text{th}}$ are their corresponding theory predictions and σ^{-2} is the inverse of the covariance matrix, which includes in general the effects of uncertainties and correlations coming from both theory and experiment. The theory predictions depend on the EFT Wilson coefficients as

$$O_{i,\text{th}} = O_{i,\text{SM}} + \sum_k \alpha_{ik}\, C_k \ , \tag{3.8}$$

[2]In this convention, the normalization of the $[C_{ll}]_{JJJJ}$ and $[C_{ee}]_{JJJJ}$ Wilson coefficients differs by a factor of 1/2 from most of the SMEFT literature. The motivation for this normalization is that it makes it more straightforward to impose the $U(3)^5$ symmetry.

Table 3.1: Flavor-conserving 2-lepton and 2-quark operators in the SMEFT.

Chirality conserving ($I, J = 1, 2, 3$)	Chirality violating ($I, J = 1, 2, 3$)
$[O_{lq}]_{IIJJ} = \left(\bar{l}_I \gamma_\mu l_I\right)\left(\bar{q}_J \gamma^\mu q_J\right)$	$[O_{lequ}]_{IIJJ} = \left(\bar{l}_I^j e_I\right) \epsilon_{jk} \left(\bar{q}_J^k u_J\right)$
$\left[O_{lq}^{(3)}\right]_{IIJJ} = \left(\bar{l}_I \gamma_\mu \sigma_i l_I\right)\left(\bar{q}_J \gamma^\mu \sigma^i q_J\right)$	$\left[O_{lequ}^{(3)}\right]_{IIJJ} = \left(\bar{l}_I^j \sigma^{\mu\nu} e_I\right) \epsilon_{jk} \left(\bar{q}_J^k \sigma_{\mu\nu} u_J\right)$
$[O_{lu}]_{IIJJ} = \left(\bar{l}_I \gamma_\mu l_I\right)\left(\bar{u}_J \gamma^\mu u_J\right)$	$[O_{ledq}]_{IIJJ} = \left(\bar{l}_I e_I\right)\left(\bar{d}_J q_J\right)$
$[O_{ld}]_{IIJJ} = \left(\bar{l}_I \gamma_\mu l_I\right)\left(\bar{d}_J \gamma^\mu d_J\right)$	
$[O_{eq}]_{IIJJ} = \left(\bar{e}_I \gamma_\mu e_I\right)\left(\bar{q}_J \gamma^\mu q_J\right)$	
$[O_{eu}]_{IIJJ} = \left(\bar{e}_I \gamma_\mu e_I\right)\left(\bar{u}_J \gamma^\mu u_J\right)$	
$[O_{ed}]_{IIJJ} = \left(\bar{e}_R^I \gamma_\mu e_I\right)\left(\bar{d}_J \gamma^\mu d_J\right)$	

Table 3.2: Flavor-conserving 4-lepton operators in the SMEFT.

One flavor ($I = 1, 2, 3$)	Two flavors ($I < J = 1, 2, 3$)
$[O_{ll}]_{IIII} = \frac{1}{2}\left(\bar{l}_I \gamma_\mu l_I\right)\left(\bar{l}_I \gamma^\mu l_I\right)$	$[O_{ll}]_{IIJJ} = \left(\bar{l}_I \gamma_\mu l_I\right)\left(\bar{l}_J \gamma^\mu l_J\right)$
	$[O_{ll}]_{IJJI} = \left(\bar{l}_I \gamma_\mu l_J\right)\left(\bar{l}_J \gamma^\mu l_I\right)$
$[O_{le}]_{IIII} = \left(\bar{l}_I \gamma_\mu l_I\right)\left(\bar{e}_I \gamma^\mu e_I\right)$	$[O_{le}]_{IIJJ} = \left(\bar{l}_I \gamma_\mu l_I\right)\left(\bar{e}_J \gamma^\mu e_J\right)$
	$[O_{le}]_{JJII} = \left(\bar{l}_J \gamma_\mu l_J\right)\left(\bar{e}_I \gamma^\mu e_I\right)$
	$[O_{le}]_{IJJI} = \left(\bar{l}_I \gamma_\mu l_J\right)\left(\bar{e}_J \gamma^\mu e_I\right)$
$[O_{ee}]_{IIII} = \frac{1}{2}\left(\bar{e}_I \gamma_\mu e_I\right)\left(\bar{e}_I \gamma^\mu e_I\right)$	$[O_{ee}]_{IIJJ} = \left(\bar{e}_I \gamma_\mu e_I\right)\left(\bar{e}_J \gamma^\mu e_J\right)$

where $C_k \equiv c_k \frac{v^2}{\Lambda^2}$ runs over all the couplings listed in this section (*cf.* Eq. (2.13)). Again, only linear terms in the NP parameters are considered to ensure that only dimension-6 effects enter the analysis. The specific set of observables used on this fit will be given in the next section. The uncertainties of the SM predictions for all of them are subleading compared to the experimental uncertainties and thus neglected in σ^{-2}. The α_{ik} coefficients in Eq. (4.3) are calculated at tree-level. Finite loop corrections [136] are neglected in this work; see e.g. [137] for estimates of their effects in the context of a different fit.

Log-enhanced one-loop corrections generated through running to higher/lower scales can be included via the renormalization group equation [91]. The QCD effects are taken into account integrally. The immense majority of the Wilson coefficients have null anomalous dimensions, only the chirality-violating LLQQ coefficients display a QCD running, which is considered for this analysis up to 3 loops [138]. As for the EW corrections, they are expected to be numerically negligible due to the small coupling constants associated to them. Only the contributions affecting the same chirality-violating terms affected by QCD corrections turn out to be significant, thanks to the presence of operator mixing and the high sensitivity to the pseudoscalar coupling $\epsilon_P^{d\mu}(\mu)$ (see Eq. (3.10) for its definition in terms of Higgs basis WCs). Thus, the 1-loop anomalous dimensions tied to these operators are taken into account for the fit [138].

All in all, the analysis in Ref. [132] aimed at constraining 141 independent NP parameters simultaneously in a global fit. Given the available observables at the low-energy scale, it was not be possible to build a fully closed global fit, the analysis was only be sensitive to a subset of the Wilson coefficients and features multiple blind directions. Additionally, some of the measurements considered in Ref. [132] have subpar precision for the standards of a SMEFT analysis, specially those linked to the third generation interactions. These statements still apply partially for our subsequent contributions in Chapter 4 and Chapter 5. All these shortcomings should be addressed through new and better experimental inputs. This is the price to pay if we want results without imposing strong assumptions on NP. However, in exchange we gain a very high degree of robustness in any results we may obtain. The only two points where this approach can be called into question are in the potential proximity of the NP degrees of freedom to the weak scale, and in the neglect of the loop corrections for the dimension-6 operators. If those terms were to be included, the parameter space would inevitably be expanded even further with more $D = 6$ Wilson coefficients. Work in this direction has already been done in Refs. [136, 139], where 1-loop corrections have been computed for a large number of observables (but not yet for all observables we will consider in this thesis).

As a final note, in the $U(3)^5$ symmetric limit, which we will study in Chapter 5, the Wilson coefficients in this fit reduce to

$$\begin{pmatrix} \delta g_L^{We_J} \\ \delta g_L^{Ze_J} \\ \delta g_R^{Ze_J} \\ \delta g_L^{Zu_J} \\ \delta g_R^{Zu_J} \\ \delta g_L^{Zd_J} \\ \delta g_R^{Zd_J} \end{pmatrix} = \begin{pmatrix} \delta g_L^{We} \\ \delta g_L^{Ze} \\ \delta g_R^{Ze} \\ \delta g_L^{Zu} \\ \delta g_R^{Zu} \\ \delta g_L^{Zd} \\ \delta g_R^{Zd} \end{pmatrix}, \quad \begin{pmatrix} [C_{ll}]_{JJJJ} \\ [C_{ll}]_{IJJI}, I \neq J \\ [C_{ll}]_{IIJJ}, I \neq J \\ [C_{le}]_{IIJJ} \\ [C_{ee}]_{IIJJ} \end{pmatrix} = \begin{pmatrix} C_{ll}^{(1)} + C_{ll}^{(3)} \\ 2C_{ll}^{(3)} \\ C_{ll}^{(1)} - C_{ll}^{(3)} \\ C_{le} \\ C_{ee} \end{pmatrix}, \quad \begin{pmatrix} [C_{lq}^{(3)}]_{JJNN} \\ [C_{lq}^{(1)}]_{JJNN} \\ [C_{eq}]_{JJNN} \\ [C_{lu}]_{JJNN} \\ [C_{ld}]_{JJNN} \\ [C_{eu}]_{JJNN} \\ [C_{ed}]_{JJNN} \end{pmatrix} = \begin{pmatrix} C_{lq}^{(3)} \\ C_{lq}^{(1)} \\ C_{eq} \\ C_{lu} \\ C_{ld} \\ C_{eu} \\ C_{ed} \end{pmatrix}, \tag{3.9}$$

while the remaining Wilson coefficients in Section 3.1 and Tables 3.1 and 3.2 should be set to zero.

3.1.1. Experimental input

When selecting the adequate observables to fit the NP parameter space, it is convenient to organize them attending to which are most sensitive to vertex corrections and which are also sensitive to 4-fermion operators. For the vertex corrections, Ref. [132] restricts itself to the so-called *pole observables*, where a single Z or W boson is produced and decays on-shell. This class of observables do not receive relevant corrections from 4-fermion operators, as they are relatively suppressed by $\Gamma_V/m_V \sim 1/16\pi^2$ [140] or by a loop factor [136]. Similar suppressions apply to other types of corrections that may affect pole observables, leaving them particularly sensitive to just vertex corrections. This matter will be discussed in detail in Chapter 4.

The set of observables used in [132] to constrain vertex corrections were taken from Ref. [141]. Its specific contents will be discussed in Chapter 4, since we will use them again for own analysis. Along with the inputs reported in Ref. [141], we will also consider several updates and new additions to the experimental results.

For the 4-fermion operators, there is a huge variety of measurements coming from multiple experimental contexts that can be sensitive to them, so they cannot be assigned to a concrete group of observables as easily as vertex corrections. A summary of the ones used in Ref. [132] along with their SM predictions is given in Table 3.3.

3.1.2. Blind directions

As discussed at length in Ref. [132], not all Wilson coefficients in Section 3.1 and Tables 3.1 and 3.2 can be constrained by the observables considered in the analysis. Some of the Wilson coefficients are not constrained at all by these observables (at least in the tree-level approximation), while others display flat directions (only certain linear combinations of Wilson coefficients are constrained, but not all of them independently). A relative abundance of insensitivities is to be expected because the observables considered in Ref. [132] mainly involve first generation quarks and leptons. Despite them, the fit can still be performed by just focusing on the remaining parameters. As for the blind directions, there exist 9 in the fit, all of them involving LLQQ couplings. They can be rotated away from the fit by redefining 12 of the WCs in the parameter

Table 3.3: Collection of low-energy measurements sensitive to LLQQ and LLLL 4-fermion interactions in the global fit. The ρ parameters accounts for the degree of correlation between the different experimental inputs. The observables from the process $e^+e^- \to f\bar{f}$ are measured at different center of mass energies, indicated in the table by $f(\sqrt{s})$. This table is adapted from Ref. [132].

Class	Observable	Exp. value	Ref. & Comments	SM value
$\nu_e\nu_e qq$	$R_{\nu_e\bar{\nu}_e}$	0.41(14)	CHARM [142]	0.33
$\nu_\mu\nu_\mu qq$	$\left(g_L^{\nu_\mu}\right)^2$	0.3005(28)	PDG [143], $\rho \approx 1$	0.3034
	$\left(g_R^{\nu_\mu}\right)^2$	0.0329(30)		0.0302
	$\theta_L^{\nu_\mu}$	2.500(35)		2.4631
	$\theta_R^{\nu_\mu}$	$4.56^{+0.42}_{-0.27}$		5.1765
PV low-E $eeqq$	$g_{AV}^{eu} + 2g_{AV}^{ed}$	0.489(5)	PDG [143], $\rho \neq 1$	0.4951
	$2g_{AV}^{eu} - g_{AV}^{ed}$	-0.708(16)		-0.7192
	$2g_{VA}^{eu} - g_{VA}^{ed}$	-0.144(68)		-0.0949
	$g_{VA}^{eu} - g_{VA}^{ed}$	-0.042(57) -0.120(74)	SAMPLE [144]	-0.0627
PV low-E $\mu\mu qq$	$b_{\rm SPS}(\lambda = 0.81)$	-1.47(42) $\cdot 10^{-4}$	SPS [145]	-1.56 $\cdot 10^{-4}$
	$b_{\rm SPS}(\lambda = 0.66)$	-1.74(81) $\cdot 10^{-4}$		-1.57 $\cdot 10^{-4}$
$d(s) \to ul\nu$	$\Delta_{\rm CKM}$	-12(84) $\cdot 10^{-5}$	Ref. [146], $\rho \neq 1$	0
	ϵ_R^{de}	-13(17) $\cdot 10^{-3}$		
	ϵ_S^{de}	14(13) $\cdot 10^{-4}$		
	ϵ_P^{de}	40(78) $\cdot 10^{-7}$		
	ϵ_T^{de}	1(8) $\cdot 10^{-4}$		
	Δ_{LP}^{d}	19(38) $\cdot 10^{-3}$		
$e^+e^- \to q\bar{q}$	$\sigma(q\bar{q})$	$f(\sqrt{s})$	LEPEWWG [147], $\rho \neq 1$	$f(\sqrt{s})$
	σ_c, σ_b		LEPEWWG [148], VENUS [149], TOPAZ [150]	
	A_{FB}^{cc}, A_{FB}^{bb}			
$\nu_\mu\nu_\mu ee$	$g_{LV}^{\nu_\mu e}$	-0.040(15)	PDG [143], $\rho \neq 1$	-0.0396
	$g_{LA}^{\nu_\mu e}$	-0.507(14)		-0.5064
$e^-e^- \to e^-e^-$	g_{AV}^{ee}	0.0190(27)	PDG [143]	0.0225
$\nu_\mu\gamma^* \to \nu_\mu\mu^+\nu^-$	$\frac{\sigma}{\sigma_{\rm SM}}$	1.58(57) 0.82(28)	CHARM [151] CCFR [152]	1
$\tau \to l\nu\nu$	$G_{\tau e}^2/G_F^2$	1.0029(46)	PDG [153]	1
	$G_{\tau\mu}^2/G_F^2$	0.981(18)		0
$e^+e^- \to l^+l^-$	$\frac{d\sigma(ee)}{d\cos\theta}$	$f(\sqrt{s})$	LEPEWWG [147], $\rho \approx 1$	$f(\sqrt{s})$
	$\sigma_\mu, \sigma_\tau, \mathcal{P}_\tau$		LEPEWWG [148] VENUS [154]	
	$\mathrm{A}_{\rm FB}^{\mu}, \mathrm{A}_{\rm FB}^{\tau}$			

list through the following combinations:

$$
\begin{aligned}
[\hat{C}_{eq}]_{ee11} =& [C_{eq}]_{ee11} + [C_{lq}^{(1)}]_{ee11}, \\
[\hat{C}_{lu}]_{ee11} =& [C_{lu}]_{ee11} + [C_{lq}^{(1)}]_{ee11} - [\hat{C}_{eq}]_{ee11}, \\
[\hat{C}_{ld}]_{ee11} =& [C_{ld}]_{ee11} + [C_{lq}^{(1)}]_{ee11} - [\hat{C}_{eq}]_{ee11}, \\
[\hat{C}_{eu}]_{ee11} =& [C_{eu}]_{ee11} - [C_{lq}^{(1)}]_{ee11}, \\
[\hat{C}_{ed}]_{ee11} =& [C_{ed}]_{ee11} - [C_{lq}^{(1)}]_{ee11}, \\
[\hat{C}_{lq}^{(3)}]_{ee22} =& [C_{lq}^{(3)}]_{ee22} - [C_{lq}^{(1)}]_{ee22}, \\
[\hat{C}_{ld}]_{ee22} =& [C_{ld}]_{ee22} + \left(5 - \frac{3g_L^2}{g_Y^2}\right) [C_{lq}^{(1)}]_{ee22} - [\hat{C}_{eq}]_{ee11}, \\
[\hat{C}_{ed}]_{ee22} =& [C_{ed}]_{ee22} - \left(3 - \frac{3g_L^2}{g_Y^2}\right) [C_{lq}^{(1)}]_{ee22} - [\hat{C}_{eq}]_{ee11}, \\
[\hat{C}_{lq}^{(3)}]_{ee33} =& [C_{lq}^{(3)}]_{ee33} + [C_{lq}^{(1)}]_{ee33}, \\
[\hat{C}_{eq}]_{\mu\mu 11} =& [C_{eq}]_{\mu\mu 11} + [C_{ed}]_{\mu\mu 11} - 2[C_{eu}]_{\mu\mu 11}, \\
\epsilon_P^{d\mu}(2\text{ GeV}) =& 0.86[C_{ledq}]_{\mu\mu 11} - 0.86[C_{lequ}^{(1)}]_{\mu\mu 11} + 0.012[C_{lequ}^{(3)}]_{\mu\mu 11}, \\
[\hat{C}_{ll}]_{\mu\mu\mu\mu} =& [C_{ll}]_{\mu\mu\mu\mu} + \frac{2g_Y^2}{g_L^2 + 3g_Y^2}[C_{le}]_{\mu\mu\mu\mu}.
\end{aligned}
\tag{3.10}
$$

Through this change, the global likelihood depends on the Wilson coefficients on the right-hand sides of Eqs. (3.10) only via the $\hat{C}$ and $\epsilon_P^{d\mu}(2\text{ GeV})$ combinations. Let us stress that the Wilson coefficients in the right hand side of $\epsilon_P^{d\mu}(2\text{ GeV})$ in Eq. (3.10) are defined at $\mu = m_Z$.

3.1.3. Marginalized limits

From this point, using all the measurements we have discussed Ref. [132] was able to constrain 65 combinations of dimension-6 SMEFT Wilson coefficients at once (21 vertex corrections δg, 27 LLQQ and 17 LLLL 4-fermion operators), including all correlations. Minimizing the Gaussian

χ^2 likelihood in Eq. (3.7), the following 1σ intervals were found

$$\begin{pmatrix} \delta g_L^{We} \\ \delta g_L^{W\mu} \\ \delta g_L^{W\tau} \\ \delta g_L^{Ze} \\ \delta g_R^{Ze} \\ \delta g_L^{Z\mu} \\ \delta g_R^{Z\mu} \\ \delta g_L^{Z\tau} \\ \delta g_R^{Z\tau} \\ \delta g_R^{Wq_1} \\ \delta g_L^{Zu} \\ \delta g_R^{Zu} \\ \delta g_L^{Zd} \\ \delta g_R^{Zd} \\ \delta g_L^{Zc} \\ \delta g_R^{Zc} \\ \delta g_L^{Zs} \\ \delta g_R^{Zs} \\ \delta g_L^{Zt} \\ \delta g_L^{Zb} \\ \delta g_R^{Zb} \end{pmatrix} = \begin{pmatrix} -1.3(3.2) \\ -2.8(2.6) \\ 1.5(4.0) \\ -0.19(28) \\ 0.43(27) \\ 0.1(1.2) \\ 0.0(1.4) \\ -0.09(59) \\ 0.62(62) \\ -13(17) \\ -8(31) \\ 14(51) \\ -9(44) \\ 30(160) \\ -1.5(3.6) \\ -3.3(5.3) \\ 9(28) \\ 34(49) \\ -3(38) \\ 3.3(1.7) \\ 23(8.8) \end{pmatrix} \times 10^{-3}, \quad \begin{pmatrix} [C_{ll}]_{eeee} \\ [C_{le}]_{eeee} \\ [C_{ee}]_{eeee} \\ [C_{ll}]_{e\mu\mu e} \\ [C_{ll}]_{ee\mu\mu} \\ [C_{le}]_{ee\mu\mu} \\ [C_{le}]_{\mu\mu ee} \\ [C_{ee}]_{ee\mu\mu} \\ [C_{ll}]_{e\tau\tau e} \\ [C_{ll}]_{ee\tau\tau} \\ [C_{le}]_{ee\tau\tau} \\ [C_{le}]_{\tau\tau ee} \\ [C_{ee}]_{ee\tau\tau} \\ [\hat{C}_{ll}]_{\mu\mu\mu\mu} \\ [C_{ll}]_{\mu\tau\tau\mu} \end{pmatrix} = \begin{pmatrix} 1.01(38) \\ -0.22(22) \\ 0.20(38) \\ -4.8(1.6) \\ 1.5(2.1) \\ 1.5(2.2) \\ -1.4(2.2) \\ 3.4(2.6) \\ 1.5(1.3) \\ 0(11) \\ -2.3(7.2) \\ 1.7(7.2) \\ -1(12) \\ -2(21) \\ 3.0(2.3) \end{pmatrix} \times 10^{-2}, \tag{3.11}$$

$$\begin{pmatrix} [C_{lq}^{(3)}]_{ee11} \\ [\hat{C}_{eq}]_{ee11} \\ [\hat{C}_{lu}]_{ee11} \\ [\hat{C}_{ld}]_{ee11} \\ [\hat{C}_{eu}]_{ee11} \\ [\hat{C}_{ed}]_{ee11} \\ [C_{lequ}^{(1)}]_{ee11} \\ [C_{ledq}]_{ee11} \\ [C_{lequ}^{(3)}]_{ee11} \\ [\hat{C}_{lq}^{(3)}]_{ee22} \\ [C_{lu}]_{ee22} \\ [\hat{C}_{ld}]_{ee22} \\ [C_{eq}]_{ee22} \\ [C_{eu}]_{ee22} \\ [\hat{C}_{ed}]_{ee22} \\ [\hat{C}_{lq}^{(3)}]_{ee33} \\ [C_{ld}]_{ee33} \\ [C_{eq}]_{ee33} \\ [C_{ed}]_{ee33} \end{pmatrix} = \begin{pmatrix} -2.2(3.2) \\ 100(180) \\ -5(11) \\ -5(23) \\ -1(12) \\ -4(21) \\ -0.080(75) \\ -0.079(74) \\ -0.02(19) \\ -61(32) \\ 2.4(8.0) \\ -310(130) \\ -21(28) \\ -87(46) \\ 270(140) \\ -8.6(8.0) \\ -1(10) \\ -3.2(5.1) \\ 18(20) \end{pmatrix} \times 10^{-2}\ , \quad \begin{pmatrix} [C_{lq}^{(3)}]_{\mu\mu 11} \\ [C_{lq}^{(1)}]_{\mu\mu 11} \\ [C_{lu}]_{\mu\mu 11} \\ [C_{ld}]_{\mu\mu 11} \\ [\hat{C}_{eq}]_{\mu\mu 11} \\ \epsilon_P^{d\mu}(2\text{ GeV}) \end{pmatrix} = \begin{pmatrix} -1.2(3.9) \\ 1.3(7.6) \\ 15(12) \\ 25(34) \\ 4(41) \\ -0.02(15) \end{pmatrix} \times 10^{-2}.$$

We restrain ourselves from copying here the 65×65 correlation matrix. Besides the blind directions and omitted parameters in the fit, several combinations of parameters were observed to be poorly constrained. In particular, the fit is insensitive to the combination $[\hat{c}_{ed} + 0.6\hat{c}_{ld}]_{ee22}$,

which is probed by observables at the LEP-2 collider. This can be explained by considering the narrow range of $\sqrt{\hat{s}}$ that is covered by the data. Additionally, $[C_{eq}]_{ee11}$ is barely probed due to the lack of precision in the electron neutrino scattering on nucleons that are used to constrain it. For this coupling specifically, the inclusion of new observables from the COHERENT experiment notably improves its constrain in the fit, see Chapter 5.

Additionally, there is a combination of the light quark vertex corrections $\{\delta g_L^{Zd}, \delta g_L^{Zu}, \delta g_R^{Zd}, \delta g_R^{Zu}\}$ which was only feebly constrained with data coming from the D0 experiment [155]. These bounds can be improved by including Z-pole observables from the LHC in the low-energy fit. Further details about this topic will be discussed in Chapter 4.

All in all, this result represents a clear picture of the landscape of electroweak precision observables that have proven their relevance to the electroweak EFT global fit. In the next chapters, we will explore the role that new experimental inputs can play in improving and expanding these limits. We will focus on experimental contexts which only recently have reached competitive enough levels of precision to contribute significantly to the fit. In particular, we will examine new information coming from the Z-pole data in the LHC in Chapter 4 and recent measurements of the coherent elastic neutrino scattering off nuclei in Chapter 5.

Chapter 4

A_{FB} in the SMEFT: precision Z physics at the LHC

In the previous chapter we presented an ambitious global fit of SMEFT couplings at the low-energy environment ($E \leq v$). Despite relying on a very extensive collection of observables, it still left unexplored a large portion of parameter space. Thus, it is very susceptible to be improved upon the introduction of any new experimental inputs. As we anticipated in the last chapter, there is a clear way to improve the fit by focusing on the addition of new data sensitive to vertex corrections originating from the LHC. However, one may argue naively that vertex corrections limits should be the least likely to improve upon the inclusion of new data. Thus, before jumping into the discussion of how this can actually be realized, it is worth it to explain where this expectation comes from and how it is subverted for the specific case we are dealing with.

The main reason why we normally would not expect any improvement on the vertex correction bounds is that they come mainly from pole observables. There is very little room for NP effects linked to this class of observables, since they have been studied in experiments with a very high degree of precision. Some of the most important experiments contributing to this endeavour are those conducted at the LEP collider. Arguably, the most important legacy of LEP is a set of electroweak precision measurements of the masses and partial decay widths of the Z and W bosons [156, 157]. The precision program initiated by LEP has exerted enormous influence on the particle physics research. On the one hand, it offered historically important guidelines for subsequent discoveries of the remaining SM degrees of freedom: the top quark and the Higgs boson. On the other hand, it severely restricted the options for new physics near the electroweak scale. In this latter context, the benefits of model-independent characterization of electroweak precision observables were quickly recognized, first in the framework of the oblique parameters [158], and later in the general EFT framework [140].

The Tevatron and the LHC also hold a remarkable place in the study of pole observables. First, they allow us to expand the precision program onto the top and the Higgs sectors. But even in the field of the classic electroweak observables hadron colliders have a chance to compete, despite having a less clean environment than LEP. This has been spectacularly demonstrated by the various measurements of the W mass at hadron colliders [159–161]. Also the total width [162, 163] and certain ratios of leptonic decay widths [164–166] of the W boson are measured more precisely in hadron colliders than in LEP-2. A similar result is however lacking regarding the Z

boson mass and couplings. Naively, this is understandable, as in this case hadron colliders have to compete with a per mille or better accuracy of LEP-1. For instance, the determinations of the weak mixing angle at the LHC [167–169] are currently at least a factor of three less precise than the one in LEP.

This assessment about the lack of competitiveness of LHC Z data may be true when performing fits within the SM or a small number of NP parameters, but it is called into question when considering global fits. When looking at a single parameter, it is very difficult for hadron colliders to outclass the superior precision at LEP. However, if we are dealing with multiple parameters and we want to establish limits for all of them at the same time, it is likely that one or more blind directions emerge. This may be because we have less observables than couplings to constrain, or maybe because the combined input coming from the experiment is insensitive to specific directions in parameter space. In such a context, using additional experimental information, even if it has limited precision, may be necessary to close the global fit.

This is precisely the scenario that we found in the SMEFT electroweak global fit described in Chapter 3. As it turns out, there exists a combination of corrections to the Z boson coupling to the up and down quarks that LEP alone is unable to probe. The fit in Ref. [132] was only able to lift the blind direction by making use of D0 data taken at the Tevatron, a proton-antiproton hadron collider [170, 171]. This class of experiments is particularly sensitive to interactions involving a Z-boson and a pair of quarks, since the quarks contained in the hadronic initial states can annihilate into an on-shell Z-boson.

Still, as we pointed out at the end of Chapter 3, the information from D0 was only able to achieve a very weak limit for the flat direction in the global fit due to its limited precision. In this chapter we will propose an alternative to the D0 input that is rooted in data coming from a more modern hadron collider: the LHC. More generally, we will provide a proof-of-principle demonstration that the LHC precision measurements at the Z-pole can compete with and complement LEP in the context of the SMEFT.

In order to do so, we will first show exactly how LEP alone cannot simultaneously constrain all higher-dimensional SMEFT operators that modify the Z boson coupling to the up and down quarks. We will refer to these pieces of data as coming from "traditional" pole observables, to better distinguish them from the new inputs we will be discussing. Then, we will show how measurements from the Drell-Yan forward-backward asymmetry at the LHC will be able to lift the blind direction in the SMEFT electroweak global fit. Lastly, we will compare the results we get using LHC and Tevatron data and provide an extensive discussion on them. This study is fully based on the published work in Ref. [133].

4.1. Traditional pole observables

Since in this chapter we are focusing on the electroweak observables at the boson poles, we will only need to keep track of non-derivative interactions between the heavy vector bosons and fermions, which we already parametrized in Eqs. (3.3) and (3.4). The important feature of this class of observables is that, at leading order, new physics enters *only* via δg.

Other effects of dimension-6 operators enter the pole observables with various suppression factors. In particular, the contributions from 4-fermion operators are suppressed by $\Gamma_V/m_V \sim 1/16\pi^2$ [140] or by a loop factor [136] relatively to those of δg and are neglected here. As for the dipole interactions, $d_f \bar{f} \sigma_{\mu\nu} f V_{\mu\nu}$, their interference with the SM amplitudes is suppressed by the small fermion masses, while the quadratic effects in d_i are $\mathcal{O}(\Lambda^{-4})$ in the EFT expansion and

are consistently neglected. Finally, we also do not need to consider the $\delta g^{Zt}_{L/R}$. This last coupling was probed in the analysis presented in Chapter 3, but we will not include it in the present fit since Ref. [132] was able to restrict it only through a V_{tb} measurement in the single-top t-channel production at the LHC [172], which is not a pole observable.

Thus, restricting to pole observables largely simplifies the analysis, allowing one to avoid dealing with the huge parameter space of the SMEFT and instead to focus on a relatively small number of parameters δg. To be specific, we will discuss model-independent constraints on the following 20 independent real parameters:

$$\delta g^{We}_L,\, \delta g^{W\mu}_L,\, \delta g^{W\tau}_L,\, \delta g^{Ze}_{L/R},\, \delta g^{Z\mu}_{L/R},\, \delta g^{Z\tau}_{L/R},\, \delta g^{Zd}_{L/R},\, \delta g^{Zs}_{L/R},\, \delta g^{Zb}_{L/R},\, \delta g^{Zu}_{L/R},\, \delta g^{Zc}_{L/R},\, \delta m_W, \tag{4.1}$$

where we have again shortened the notation $\delta g^{Vf_J}_X \equiv [\delta g^{Vf}_X]_{JJ}$ because we will always be working with the diagonal elements of the vertex corrections. This parameter list can be identified with the one in Eq. (3.6), with the difference that here we do not consider $\delta g^{Zt}_{L/R}$ and we add δm_W. $\delta g^{Wq_1}_R$ is also absent because it affects the pole observables quadratically (because there are no SM right-handed currents to interfere with) and thus are neglected as $\mathcal{O}(\Lambda^{-4})$ effects.

This completes the description of the new physics effects that we will want to restrict in our electroweak fit. We will present our results in the form of a Gaussian likelihood function for the parameters in Eq. (3.6), which encodes simultaneous constraints on the 19 δg's and δm_W including all correlations. We will use the same expression as in Eq. (3.7), which we reinstate here:

$$\chi^2 = \sum_{ij} \left[O_{i,\text{exp}} - O_{i,\text{th}}\right] (\sigma^{-2})_{ij} \left[O_{j,\text{exp}} - O_{j,\text{th}}\right], \tag{4.2}$$

where

$$O_{i,\text{th}} = O_{i,\text{SM}} + \sum_k \alpha_{ik}\, \delta g_k \ , \tag{4.3}$$

The only difference is that the theory prediction here will only depend only on the δg_k parameters listed in Eq. (4.1). As for the observable collection, we will work with an updated list of the pole observables used in the fit of Ref. [132] and presented in Chapter 3. To organize them, we distinguish the observables associated to the Z-pole from the ones linked to the W-pole.

The Z-pole observables we will use are those carried out at LEP-1 and SLC, which we list in Table 4.1. The experimental values are taken from the classic report of Ref. [156], with minor modifications affecting the Z width, the hadronic cross section σ_{had} and the FB asymmetry of b quarks to take into account the recent results of Refs. [173, 174]. We also include the measurements of A_s and R_{uc} [131, 175] that, despite being less precise, are needed to remove flat directions in the EFT parameter space. For the SM predictions we use the values obtained in Ref. [176], which are calculated using the $\{g_L = 0.6485,\, g_Y = 0.3580,\, v\}$ couplings and the known state of the art expressions.

In the case of the W boson, the pole observables that we consider were measured at LEP-2, Tevatron and LHC, and they are summarized in Table 4.2. We stress that this dataset includes recent LHC results concerning the leptonic branching ratios of the W boson [164, 166, 177]. We include the not-so-precise measurements of R_{Wc} [131] to remove flat directions. We obtain the SM predictions from Ref. [178], except for the W mass where we use the semi-analytic expression from Ref. [179].

We are now ready to obtain limits for the Wilson coefficients in our fit. We will do so by minimizing the χ^2 function with all NP couplings present simultaneously. These will represent a

Table 4.1: Z **pole observables**. The experimental errors of the observables not separated by horizontal lines are correlated, which is taken into account in the fit. The first A_e and A_τ values come from the combination of leptonic polarization and left-right asymmetry measurements at SLD, while the second values come from the LEP-1 measurements of the polarization of the $\tau^\pm$ leptons.

Observable	Experimental value	SM prediction	Definition
Γ_Z [GeV]	2.4955 ± 0.0023 [156, 173]	2.4941	$\sum_f \Gamma(Z \to f\bar{f})$
σ_{had} [nb]	41.4802 ± 0.0325 [156, 173]	41.4842	$\frac{12\pi}{m_Z^2} \frac{\Gamma(Z\to e^+e^-)\Gamma(Z\to q\bar{q})}{\Gamma_Z^2}$
R_e	20.804 ± 0.050 [156]	20.734	$\frac{\sum_q \Gamma(Z\to q\bar{q})}{\Gamma(Z\to e^+e^-)}$
R_μ	20.785 ± 0.033 [156]	20.734	$\frac{\sum_q \Gamma(Z\to q\bar{q})}{\Gamma(Z\to \mu^+\mu^-)}$
R_τ	20.764 ± 0.045 [156]	20.781	$\frac{\sum_q \Gamma(Z\to q\bar{q})}{\Gamma(Z\to \tau^+\tau^-)}$
$A_{\text{FB}}^{0,e}$	0.0145 ± 0.0025 [156]	0.0162	$\frac{3}{4}A_e^2$
$A_{\text{FB}}^{0,\mu}$	0.0169 ± 0.0013 [156]	0.0162	$\frac{3}{4}A_eA_\mu$
$A_{\text{FB}}^{0,\tau}$	0.0188 ± 0.0017 [156]	0.0162	$\frac{3}{4}A_eA_\tau$
R_b	0.21629 ± 0.00066 [156]	0.21581	$\frac{\Gamma(Z\to b\bar{b})}{\sum_q \Gamma(Z\to q\bar{q})}$
R_c	0.1721 ± 0.0030 [156]	0.1722	$\frac{\Gamma(Z\to c\bar{c})}{\sum_q \Gamma(Z\to q\bar{q})}$
A_b^{FB}	0.0996 ± 0.0016 [156, 174]	0.1032	$\frac{3}{4}A_eA_b$
A_c^{FB}	0.0707 ± 0.0035 [156]	0.0736	$\frac{3}{4}A_eA_c$
A_e	0.1516 ± 0.0021 [156]	0.1470	$\frac{\Gamma(Z\to e_L^+e_L^-)-\Gamma(Z\to e_R^+e_R^-)}{\Gamma(Z\to e^+e^-)}$
A_μ	0.142 ± 0.015 [156]	0.1470	$\frac{\Gamma(Z\to \mu_L^+\mu_L^-)-\Gamma(Z\to \mu_R^+\mu_R^-)}{\Gamma(Z\to \mu^+\mu^-)}$
A_τ	0.136 ± 0.015 [156]	0.1470	$\frac{\Gamma(Z\to \tau_L^+\tau_L^-)-\Gamma(Z\to \tau_R^+\tau_R^-)}{\Gamma(Z\to \tau^+\tau^-)}$
A_e	0.1498 ± 0.0049 [156]	0.1470	$\frac{\Gamma(Z\to e_L^+e_L^-)-\Gamma(Z\to e_R^+e_R^-)}{\Gamma(Z\to e^+e^-)}$
A_τ	0.1439 ± 0.0043 [156]	0.1470	$\frac{\Gamma(Z\to \tau_L^+\tau_L^-)-\Gamma(Z\to \tau_R^+\tau_R^-)}{\Gamma(Z\to \tau^+\tau^-)}$
A_b	0.923 ± 0.020 [156]	0.935	$\frac{\Gamma(Z\to b_Lb_L)-\Gamma(Z\to b_Rb_R)}{\Gamma(Z\to b\bar{b})}$
A_c	0.670 ± 0.027 [156]	0.668	$\frac{\Gamma(Z\to c_L\bar{c}_L)-\Gamma(Z\to c_R\bar{c}_R)}{\Gamma(Z\to c\bar{c})}$
A_s	0.895 ± 0.091 [175]	0.936	$\frac{\Gamma(Z\to s_L\bar{s}_L)-\Gamma(Z\to s_R\bar{s}_R)}{\Gamma(Z\to s\bar{s})}$
R_{uc}	0.166 ± 0.009 [131]	0.172	$\frac{\Gamma(Z\to u\bar{u})+\Gamma(Z\to c\bar{c})}{2\sum_q \Gamma(Z\to q\bar{q})}$

Table 4.2: W **pole observables**. The experimental errors of the observables not separated by horizontal lines are correlated, which is taken into account in the fit.

Observable	Experimental value	SM prediction
m_W [GeV]	80.379 ± 0.012 [131]	80.356
Γ_W [GeV]	2.085 ± 0.042 [131]	2.088
$\mathrm{Br}(W \to e\nu)$	0.1071 ± 0.0016 [157]	0.1082
$\mathrm{Br}(W \to \mu\nu)$	0.1063 ± 0.0015 [157]	0.1082
$\mathrm{Br}(W \to \tau\nu)$	0.1138 ± 0.0021 [157]	0.1081
$\mathrm{Br}(W \to \mu\nu)/\mathrm{Br}(W \to e\nu)$	0.982 ± 0.024 [180]	1.000
$\mathrm{Br}(W \to \mu\nu)/\mathrm{Br}(W \to e\nu)$	1.020 ± 0.019 [164]	1.000
$\mathrm{Br}(W \to \mu\nu)/\mathrm{Br}(W \to e\nu)$	1.003 ± 0.010 [165]	1.000
$\mathrm{Br}(W \to \tau\nu)/\mathrm{Br}(W \to e\nu)$	0.961 ± 0.061 [131, 177]	0.999
$\mathrm{Br}(W \to \tau\nu)/\mathrm{Br}(W \to \mu\nu)$	0.992 ± 0.013 [166]	0.999
$\Gamma(W \to cX)/\Gamma(W \to \text{ hadrons})$	0.49 ± 0.04 [131]	0.50

minor update on the bounds we showed in (3.11) thanks to the new additions to the experimental inputs. Although we fit all 20 coefficients at once, it is instructive to discuss the results by groups. For the leptonic couplings, we find the following central values and 1σ errors:

$$[\delta g_L^{We}]_{ii} = \begin{pmatrix} -1.3 \pm 3.2 \\ -2.8 \pm 2.6 \\ 1.5 \pm 4.0 \end{pmatrix} \times 10^{-3}, \tag{4.4}$$

$$[\delta g_L^{Ze}]_{ii} = \begin{pmatrix} -0.19 \pm 0.28 \\ 0.1 \pm 1.2 \\ -0.09 \pm 0.59 \end{pmatrix} \times 10^{-3}, \quad [\delta g_R^{Ze}]_{ii} = \begin{pmatrix} -0.43 \pm 0.27 \\ 0.0 \pm 1.4 \\ 0.62 \pm 0.62 \end{pmatrix} \times 10^{-3}\ . \tag{4.5}$$

For the couplings involving strange, charm and bottom quarks, we obtain

$$\delta g_L^{Zs} = (1.3 \pm 4.1) \times 10^{-2}, \qquad \delta g_R^{Zs} = (2.2 \pm 5.6) \times 10^{-2}, \tag{4.6}$$

$$\delta g_L^{Zc} = (-1.3 \pm 3.7) \times 10^{-3}, \qquad \delta g_R^{Zc} = (-3.2 \pm 5.4) \times 10^{-3}, \tag{4.7}$$

$$\delta g_L^{Zb} = (3.1 \pm 1.7) \times 10^{-3}, \qquad \delta g_R^{Zb} = (21.8 \pm 8.8) \times 10^{-3}\ . \tag{4.8}$$

The data also constrain the SMEFT corrections to the W mass: $\delta m_W = (2.9 \pm 1.6) \times 10^{-4}$. We see that the Z and W pole observables in Tables 4.1 and 4.2 simultaneously constrain all leptonic and heavy quark vertex corrections with (typically) per mille level accuracy. On the other hand, they *cannot* simultaneously constrain all light quark vertex corrections; in fact, only 3 linear combinations of δg_L^{Zu}, δg_R^{Zu}, δg_L^{Zd} and δg_R^{Zd} are probed by these observables. It is possible to show that the linear combination

$$\delta g_L^{Zu} + \delta g_L^{Zd} + \frac{3g_L^2 - g_Y^2}{4g_Y^2}\delta g_R^{Zu} + \frac{3g_L^2 + g_Y^2}{2g_Y^2}\delta g_R^{Zd}, \tag{4.9}$$

is **not** probed at all by the observables in Tables 4.1 and 4.2. In other words, it is a flat direction in the $\mathcal{O}(\Lambda^{-2})$ EFT fit. In order to characterize the constraints on the light quark couplings, it is convenient to introduce new variables x, y, z, t related by a rotation to the light quark vertex

corrections:

$$\begin{pmatrix} x \\ y \\ z \\ t \end{pmatrix} = R \begin{pmatrix} \delta g_L^{Zu} \\ \delta g_R^{Zu} \\ \delta g_L^{Zd} \\ \delta g_R^{Zd} \end{pmatrix} = \begin{pmatrix} 0.93 & -0.29 & -0.23 & -0.01 \\ 0.18 & 0.87 & -0.33 & -0.33 \\ 0.27 & 0.18 & 0.90 & -0.29 \\ 0.17 & 0.37 & 0.17 & 0.90 \end{pmatrix} \begin{pmatrix} \delta g_L^{Zu} \\ \delta g_R^{Zu} \\ \delta g_L^{Zd} \\ \delta g_R^{Zd} \end{pmatrix}, \tag{4.10}$$

where R is an $SO(4)$ matrix such that: 1) t is proportional to the flat direction in Eq. (4.9); 2) x, y, z are mutually uncorrelated and orthogonal in the fit. To obtain these limits we need to perform the fit twice. The first estimation is done on the δg parameters, from which we are only interested in the resulting covariance matrix. We then diagonalize this matrix, since its eigenvectors represent the orthogonal and uncorrelated combinations that we are looking for. Identifying the eigenvectors as the x, y, z and t linear combinations, we execute the fit a second time, working with the likelihood expressed in terms of these new variables. From it, we can extract the limits displayed in (4.10) completely free of correlations.

The limits we obtain through this procedure are automatically distributed according to the particular sensitivities of the observables we are working with. For instance, if we had a single experimental input, upon applying this procedure we would find a concrete bound only on one specific direction in parameter space but no limit on any of its orthogonal partners. The particular combination that would get constrained would be precisely the one that our data is sensitive to. In the case of our fit, the observables we are working with can cover decently for the three variables x, y, z. However, we find no constrain to the t linear combination because the observables in Tables 4.1 and 4.2 have no sensitivity to it. This is what defines it as a flat direction in the fit.

The specific limits on the combinations x, y, z established by the above-discussed pole observables are:

$$\begin{pmatrix} x \\ y \\ z \end{pmatrix} = \begin{pmatrix} -0.9 \pm 1.8 \\ 0.3 \pm 3.3 \\ -2.4 \pm 4.8 \end{pmatrix} \times 10^{-2}. \tag{4.11}$$

Given the presence of the flat direction t, another experimental input is needed to simultaneously constrain all four light quark vertex corrections. In Ref. [141] the measurement of $Zq\bar{q}$ couplings in Tevatron's D0 [155] is employed to that purpose. However the resulting limit is very loose: $t = (0.1 \pm 17) \times 10^{-2}$, which is an order of magnitude weaker than the constraints in Eq. (4.11) on the remaining three combinations.

This result is coming from a hadron collider experiment, so it could be possible that a similar observable measured in the context of the LHC could also lift the blind direction and even improve upon the limits set by D0. This is a very likely prospect, since the LHC experiments are reporting notable improvements on their precision power from all fronts, including the electroweak sector (see, for instance, the most recent extractions of the weak angle [169] or the strong coupling constant [181]). In the following of this chapter we show that indeed leptonic Z asymmetries at the LHC provide a more promising and precise route to constrain t and lift the flat direction in the SMEFT fit of W and Z pole observables.

In the following we show that measurements of on-shell Z production in hadron colliders can be important from the global SMEFT perspective, even if the accuracy is somewhat inferior compared to the most precise LEP-1 measurements. More specifically, leptonic Z asymmetries at the LHC provide a more promising and more precise route to constrain t and lift the flat direction in the SMEFT fit of W and Z pole observables.

4.2. The Drell-Yan forward-backward asymmetry at the LHC

The natural LHC process to probe the Z interactions with light quarks is the Drell-Yan production of lepton pairs, $pp \to Z/\gamma^* \to l^+l^-$. Indeed, at the parton level the intermediate Z is produced via $q\bar{q} \to Z$, providing tree-level sensitivity to the Zqq couplings. We will focus on the FB asymmetry in the Drell-Yan production, which is a particularly clean observable thanks to cancellations of various QCD and PDF uncertainties, and for which high precision has been achieved both on the experimental and the theory side [182–185]. This observable has been used to extract with high accuracy the weak mixing angle [169], and it is currently being discussed as a possible tool to further constrain the parton distribution functions [186, 187].

At the partonic level, the asymmetry appears in the decay angle θ^* of the negatively charged lepton with respect to the incoming quark direction in the center of mass frame. It is non-zero already in the SM, due to parity-violating Z couplings to fermions. In the SM the differential cross section of the partonic process $q\bar{q} \to Z/\gamma^* \to \ell^+\ell^-$ is given at leading order by [188]:

$$\begin{aligned}\frac{d\hat{\sigma}_{q\bar{q}}\left(\hat{s}, cos\theta^*\right)}{d\cos\theta^*} &\propto \hat{\sigma}^{even}_{q\bar{q}}\left(\hat{s}, \cos\theta^*\right) + \hat{\sigma}^{odd}_{q\bar{q}}\left(\hat{s}, \cos\theta^*\right) \\ &\propto H^{even}_{q\bar{q}}\left(\hat{s}\right)\left(1+\cos^2\theta^*\right) + H^{odd}_{q\bar{q}}\left(\hat{s}\right)\cos\theta^*, \end{aligned} \tag{4.12}$$

where

$$\begin{aligned} H^{even}_{q\bar{q}}\left(\hat{s}\right) &= \frac{3}{2}\frac{\hat{s}}{\left(\hat{s}-m_Z^2\right)^2+m_Z^2\Gamma_Z^2}\left(\left(g_V^{Zq}\right)^2+\left(g_A^{Zq}\right)^2\right)\left(\left(g_V^{Zl}\right)^2+\left(g_A^{Zl}\right)^2\right)+ \\ &\quad +\frac{3\left(Q_q\right)^2\left(Q_l\right)^2}{2\hat{s}}+\frac{3\left(\hat{s}-m_Z^2\right)}{\left(\hat{s}-m_Z^2\right)^2+m_Z^2\Gamma_Z^2}Q_qQ_l\,g_V^{Zq}g_V^{Zl}, \end{aligned} \tag{4.13}$$

$$H^{odd}_{q\bar{q}}\left(\hat{s}\right) = \frac{12\hat{s}}{\left(\hat{s}-m_Z^2\right)^2+m_Z^2\Gamma_Z^2}g_V^{Zq}g_A^{Zq}g_V^{Zl}g_A^{Zl}+\frac{6\left(\hat{s}-m_Z^2\right)}{\left(\hat{s}-m_Z^2\right)^2+m_Z^2\Gamma_Z^2}Q_qQ_l\,g_A^{Zq}g_A^{Zl}. \tag{4.14}$$

Here, $\hat{s}$ is the invariant mass of the dilepton system, Q_f are the electric charges and $g_{V/A}^{Zf} \equiv g_R^{Zf} \pm g_L^{Zf}$ are the vector/axial couplings of the Z boson to fermions. It is trivial to include the effect of SMEFT corrections to the Zff couplings in the differential cross-sections given above. As long as we stay near the Z pole ($\hat{s} \approx M_Z$) the corrections due to 4-fermion SMEFT operators are suppressed by $\Gamma_Z/m_Z \sim 0.02$, and can be neglected in the leading order approximation.[1] Note that there are no vertex corrections to photon couplings.

The term proportional to $\cos\theta^*$ in Eq. (4.12) will induce a difference in the number of events with a negative lepton going in the forward ($\cos\theta^* > 0$) and backward ($\cos\theta^* < 0$) directions. This asymmetry cannot be directly observed at the LHC because there we are not dealing with quarks as incoming particles, but with protons. Thus, we must modify Eq. (4.12) by including PDF. Moreover, having two identical particles in the initial state introduces an important complication: the absence of a preferred direction that one can use to build an asymmetry. In other words, we do not know *in every individual event* which proton contains the quark and which one contains the antiquark that are annihilating. In order to circumvent this issue, the asymmetry is defined with respect to the longitudinal boost of the dilepton system on an event-by-event basis. Equivalently, one assumes that the momentum of the quark is larger than that of the

[1] Note that finite (i.e. not log-enhanced) 1-loop SMEFT corrections, also neglected in our approximation, are suppressed by a numerically similar factor.

antiquark [182, 183, 188], which is only true on average. This inevitably introduces a distorsion on the asymmetry at the parton level, which can be analytically parametrized through a dilution factor, as shown below.

An additional complication arises because (anti)quarks might have non-zero transverse momentum, which impedes us from equating the direction of the quark-antiquark pair in the partonic interaction to the beam direction. This effect can be minimized working in the so-called Collins-Soper frame [189], where θ^* is defined as the angle between ℓ^- and the axis that bisects the angle between the quark-momentum direction and the opposite directions to the antiquark momentum. This subtlety is not relevant for our work, which is restricted to studying the tree-level SMEFT corrections, in which case the transverse momentum of the incoming quarks is zero.

All these changes can be implemented analytically. To do so, we introduce the PDFs $f_a(x_i, \hat{s})$ into the partonic Drell-Yan process. These functions will describe the probability for partons of type a to have a fraction x_i of the proton momentum $p = \sqrt{s}/2$, where s is the proton-proton invariant mass. Through them, we can express the proton-proton differential cross section as:

$$\frac{d\sigma_{pp}\left(px_1, px_2, \cos\theta^*\right)}{dx_1\, dx_2\, d\cos\theta^*} \propto \sum_{q=u,d,s,c,b} \Big(\hat{\sigma}^{even}_{q\bar{q}}\left(\hat{s}, \mathrm{sgn}(x_1 - x_2)\cos\theta^*\right) f_q\left(x_1, \hat{s}\right) f_{\bar{q}}\left(x_2, \hat{s}\right) + \hat{\sigma}^{even}_{q\bar{q}}\left(\hat{s}, \mathrm{sgn}(x_2 - x_1)\cos\theta^*\right) f_q\left(x_2, \hat{s}\right) f_{\bar{q}}\left(x_1, \hat{s}\right)\Big) \quad (4.15)$$

where the first term describes the events where the (anti)quark will hold the $x_1(x_2)$ fraction of momentum and the second term captures the opposite scenario. This exact assignation is counteracted through the inclusion of the sgn functions, which explicitly impose that the quark direction must coincide with the dilepton system boost.

At this point, it is convenient to execute a change of variables from the momentum fractions (x_1, x_2) by the partonic center of mass energy $\hat{s}$ and the dilepton rapidity Y. The connection between the two sets is given by

$$Y = \frac{1}{2}\log\left(\frac{\hat{E} + \hat{p}_z}{\hat{E} - \hat{p}_z}\right) = \frac{1}{2}\log\left(\frac{x_1}{x_2}\right), \quad (4.16)$$

$$\hat{s} = \hat{E}^2 - \hat{p}^2 = x_1 x_2 s, \quad (4.17)$$

where $\hat{E}$ is the energy of the dilepton system and $\hat{p_z}$ is the longitudinal momentum in the laboratory frame. At leading order in momentum, this component comprises the totality of the momentum, $\hat{p} = |\hat{p}_z|$.

All in all, once these changes are implemented, Eq. (4.12) transforms into [188]:

$$\frac{d\sigma_{pp}\left(Y, \hat{s}, \cos\theta^*\right)}{dY\, d\hat{s}\, d\cos\theta^*} \propto \sum_{q=u,d,s,c,b} \left[\hat{\sigma}^{even}_{q\bar{q}}\left(\hat{s}, \cos\theta^*\right) + D_{q\bar{q}}\left(Y, \hat{s}\right)\hat{\sigma}^{odd}_{q\bar{q}}\left(\hat{s}, \cos\theta^*\right)\right] F_{q\bar{q}}\left(Y, \hat{s}\right), \quad (4.18)$$

where $F_{q\bar{q}}\left(Y, \hat{s}\right)$ is called the parton factor and $D_{q\bar{q}}\left(Y, \hat{s}\right)$ is the dilution factor to which we alluded previously. They depend on the PDFs as:

$$F_{q\bar{q}}(Y,\hat{s}) = f_q\left(e^{+Y}\sqrt{\frac{\hat{s}}{s}},\hat{s}\right) f_{\bar{q}}\left(e^{-Y}\sqrt{\frac{\hat{s}}{s}},\hat{s}\right) + f_q\left(e^{-Y}\sqrt{\frac{\hat{s}}{s}},\hat{s}\right) f_{\bar{q}}\left(e^{+Y}\sqrt{\frac{\hat{s}}{s}},\hat{s}\right), \quad (4.19)$$

$$D_{q\bar{q}}(Y,\hat{s}) = \frac{f_q\left(e^{+|Y|}\sqrt{\frac{\hat{s}}{s}},\hat{s}\right) f_{\bar{q}}\left(e^{-|Y|}\sqrt{\frac{\hat{s}}{s}},\hat{s}\right) - f_q\left(e^{-|Y|}\sqrt{\frac{\hat{s}}{s}},\hat{s}\right) f_{\bar{q}}\left(e^{+|Y|}\sqrt{\frac{\hat{s}}{s}},\hat{s}\right)}{F_{q\bar{q}}(\hat{s},Y)} \quad (4.20)$$

The parton factor $F_{q\bar{q}}(Y,\hat{s})$ will act as a global correction of the partonic cross section based on the PDFs. This quantity will decrease as the dilepton center of mass energy approaches the scale of the proton-proton interaction. As for the dilution factor $D_{q\bar{q}}(Y,\hat{s})$, as we expected, it reflects the distorsion induced by our ignorance about the quark direction. This factor will range between 0 and 1 fo $0 < |Y| < 4$, and its effect will be stronger for smaller values of rapidity. This makes sense because at low rapidities both sea and valence quarks have a high chance of appearing, while at higher values valence quarks will take precedence. This poses a problem for the LHC, as the majority of its measurements will take place at rapidity ranges where $D_{q\bar{q}}(Y,\hat{s})$ will be small. Using this hadronic differential cross-section, the FB asymmetry is defined as:

$$A_{FB}(Y,\hat{s}) = \frac{\sigma_F(Y,\hat{s}) - \sigma_B(Y,\hat{s})}{\sigma_F(Y,\hat{s}) + \sigma_B(Y,\hat{s})}, \quad (4.21)$$

where the forward and backward cross-sections, σ_F and σ_B, are obtained by integrating the differential cross section over the positive and negative values of $\cos\theta^*$, respectively. It should also be noted that, to calculate A_{FB} integrated over the Y and $\hat{s}$ bins, one should integrate independently σ_F and σ_B and then calculate the integrated A_{FB} from that input.

The dependence of the asymmetry on the invariant mass and rapidity of the dilepton system effectively increases the number of independent observables at our disposal. In this work we restrict ourselves to the dilepton masses close to the Z peak, so that contributions from 4-fermion operators can be neglected and only vertex corrections need to be considered.[2] Corrections to the leptonic Z couplings can also be neglected, due to the very stringent LEP-1 constraints shown in Eq. (4.5). The effects due to the vertex correction involving the s, b and c quarks are suppressed by the small PDFs of the heavy quarks in the proton, and again can be neglected given the LEP-1 constraints. Using measurements of the asymmetry at different rapidity bins, we will be able to probe different combinations of Zqq couplings. In principle, four distinct rapidity bins are enough to disentangle all four $\delta g_{L/R}^{Zd/Zu}$ corrections, although this may be hindered in practice by large correlations between the bins, as we will see in the following.

4.3. Numerical analysis

In this section we set bounds on the Z couplings to light quarks using the measurement of the ATLAS collaboration of the angular distributions of leptons from the Drell-Yan process. This data was taken at a center-of-mass energy of $\sqrt{s} = 8$ TeV data [191] and a luminosity of 20.1 fb^{-1}. In particular we will use the measurement of the so-called A_4 angular coefficient,

[2]We have checked that the width of the $\hat{s}$-bin (20 GeV) is small enough so that 4-fermion operators can be safely neglected in our analysis. More precisely, the contributions proportional to 4-fermion Wilson coefficients C_{4F} (measured in units of $1/v^2$) are suppressed by numerical factors of order 0.01. Given the constraints from high-p_T tails of the Drell-Yan distributions at the LHC, which typically require $|C_{4F}| < 10^{-3}$ [190], the 4-fermion contributions at the Z-pole are completely unobservable with the current accuracy.

which is defined upon expanding the Drell-Yan differential cross section in harmonic polynomials. According to this expansion, the full 5-dimensional differential cross section at leading order in the EW expansion can be parametrized as:

$$\frac{d\sigma}{dp_T\, dY\, d\hat{s}\, d\cos\theta^*\, d\phi} = \frac{3}{16\pi}\frac{d\sigma^{U+L}}{dp_T\, dY\, d\hat{s}} \quad \Big\{\big(1+\cos^2\theta\big) + \tfrac{1}{2}\mathrm{A}_0\left(1-3\cos^2\theta\right) + \mathrm{A}_1 \sin 2\theta\cos\phi + \tfrac{1}{2}\,\mathrm{A}_2 \sin^2\theta\cos 2\phi + \mathrm{A}_3 \sin\theta\cos\phi + \mathrm{A}_4\cos\theta + \mathrm{A}_5 \sin^2\theta\sin 2\phi + \mathrm{A}_6 \sin 2\theta\sin\phi + \mathrm{A}_7 \sin\theta\sin\phi\Big\}\,. \tag{4.22}$$

where σ^{U+L} is the unpolarised cross section and $A_{0-7}(p_T, Y, \hat{s})$ are eight dimensionless angular coefficients, which represent ratios of helicity cross-sections with respect to σ^{U+L}. This expression depends on the variables Y, $\hat{s}$, $\cos\theta^*$, which are the same kinematic variables as in Eq. (4.18), with the decay angle θ^* also defined in the Collins-Soper frame, the dilepton transverse momentum p_T and the polar angle ϕ. This decomposition is based on the spin correlation effects taking place between the initial-state spin-1/2 partons and the final-state spin-1/2 leptons mediated by a spin-1 intermediate state. As we can see, it allows us to fully describe the dependence of Drell-Yan production in the $\cos\theta^*$ and ϕ variables. This characterization is valid both at the parton and hadron levels.

Crucially, at leading order in QCD, all angular coefficients except A_4 go to zero, and the cross section after integrating over p_T and ϕ gets reduced to:

$$\frac{d\sigma}{dY\, d\hat{s}\, d\cos\theta^*} = \frac{3}{16\pi}\frac{d\sigma^{U+L}}{dY\, d\hat{s}} \quad \Big\{\big(1+\cos^2\theta\big) + \mathrm{A}_4\cos\theta\Big\}\,,$$

where the A_4 has been redefined accordingly. If we compare this formula with (4.18), it can be proven that their dependence on θ^* is identical. In fact, A_4 enjoys the same cancellations of hadronic, QCD and EW effects as $\mathrm{A_{FB}}$ by virtue of them both being a ratio of cross sections. We can then conclude that the angular coefficient A_4 is related to the FB asymmetry by $\mathrm{A_{FB}} = (3/8)\mathrm{A}_4$. This equation holds at all orders in QCD when considering the full phase space of the individual decay leptons. Thus, the results of the previous sections are immediately applicable to this measurement, up to the trivial 3/8 numerical factor.

We choose to only use this piece of data and not additional inputs coming from other relevant experiments such as CMS [169, 184] and LHCb [167] mainly because of the lack of explicit SM theory predictions for the observables each of them measure. We also limit ourselves to $\sqrt{s} = 8$ TeV data just because currently there are no measurements of $\mathrm{A_{FB}}$ at a higher collision energy.

Table 4.3 shows the results of the ATLAS measurements of A_4 for dileptons at the Z peak ($80\ \mathrm{GeV} < \sqrt{\hat{s}} < 100\ \mathrm{GeV}$). As we can see, the asymmetry was measured for four values of the dilepton rapidity, which will allow us to separate (at least formally) the four corrections of the Z boson to up and down quarks. Table 4.3 also shows the SM predictions, as given in the ATLAS paper [191], which were calculated at NNLO in QCD [192–194].[3] We can see that, contrary to the traditional pole observables, the theory errors are comparable to the experimental ones and cannot be neglected.

[3]Similar Drell-Yan studies by CMS [169, 184] and LHCb [167] do not provide explicitly the SM predictions for their observables and often do not probe the dependence on the dilepton rapidity. We also limit ourselves to $\sqrt{s} = 8$ TeV data because currently there are no $\mathrm{A_{FB}}$ measurements at higher energies.

Table 4.3: ATLAS A_4 measurements obtained in Ref. [191] using $\sqrt{s} = 8$ TeV data for a dilepton invariant mass in the range (80 GeV, 100 GeV). The SM predictions, obtained at NNLO in QCD, are also taken from Ref. [191].

|Y|	Experimental value	SM prediction
0.0 - 0.8	0.0195 ± 0.0015	0.0144 ± 0.0007
0.8 - 1.6	0.0448 ± 0.0016	0.0471 ± 0.0017
1.6 - 2.5	0.0923 ± 0.0026	0.0928 ± 0.0021
2.5 - 3.6	0.1445 ± 0.0046	0.1464 ± 0.0021

The theory predictions are modified in the presence of nonstandard corrections. Working at linear order in them we have:

$$A_{4,i}^{th} = A_{4,i}^{SM} \left(1 + \alpha_{ik}\, \delta g_k\right) \tag{4.23}$$

where the i index corresponds to the four rapidity bins (see Table 4.3) and $\delta g_k = \{g_L^{Zu}, g_R^{Zu}, g_L^{Zd}, g_R^{Zd}\}$. The numerical factors α_{ik} are calculated using Eqs. (4.18)-(4.21), after integration over the $\hat{s}$ and Y bins and using the MMHT2014lo68cl PDF set [195].

Concerning the α_{ik} uncertainties, we can prove numerically under which conditions they can be neglected in the new physics fit. Starting from Eq. (4.23), we can consider two sets of values for the theoretical quantities involved in the expression ($\{\mathrm{A}_{4,1}^{\mathrm{SM}},\ \alpha_{k,1}\}$ and $\{\mathrm{A}_{4,2}^{\mathrm{SM}},\ \alpha_{k,2}\}$) contained within their respective error intervals. We can equate the theoretical estimation given by these two sets of parameters to their corresponding experimental measurement $\mathrm{A}_4^{\mathrm{exp}}$, yielding two possible values for one of the EFT couplings δg_i:

$$\delta g_{j,1} = \frac{\mathrm{A}_4^{\mathrm{exp}} - \mathrm{A}_{4,1}^{\mathrm{SM}}\left(1 + \alpha_{k,1}\delta g_k\right)}{\mathrm{A}_{4,1}^{\mathrm{SM}}\alpha_{j,1}}, \quad \delta g_{j,2} = \frac{\mathrm{A}_4^{\mathrm{exp}} - \mathrm{A}_{4,2}^{\mathrm{SM}}\left(1 + \alpha_{k,2}\delta g_k\right)}{\mathrm{A}_{4,2}^{\mathrm{SM}}\alpha_{j,2}}, \tag{4.24}$$

where $j \neq k$ and we are omitting the rapidity index i. We can introduce errors for $\mathrm{A}_4^{\mathrm{SM}}$ and α_k through the redefinitions $\mathrm{A}_{4,2}^{\mathrm{SM}} = \mathrm{A}_{4,1}^{\mathrm{SM}}(1 + \delta\mathrm{A}_4^{\mathrm{SM}})$ and $\alpha_{k,2} = \alpha_{i,1}(1 + \delta\alpha_k)$. Additionally, we can also include the experimental error by setting $\mathrm{A}_4^{\mathrm{exp}} = \hat{\mathrm{A}}_4^{\mathrm{exp}}\left(1 + \delta\mathrm{A}_4^{\mathrm{exp}}\right)$. If we substitute these expressions in Eq. (4.24) and estimate the δg_j uncertainty as $\delta g_{j,1} - \delta g_{j,2}$:

$$\Delta\left(\delta g_j\right) = \delta g_{j,2} - \delta g_{j,1} \approx -\frac{\hat{\mathrm{A}}_4^{\mathrm{exp}}\left(\delta\mathrm{A}_4^{\mathrm{SM}} + \delta A_4^{exp}\right)}{\mathrm{A}_{4,1}^{\mathrm{SM}}\alpha_{j,1}}\left[1 + \frac{\mathrm{A}_4^{\mathrm{exp}} - \mathrm{A}_{4,1}^{\mathrm{SM}}}{\mathrm{A}_4^{\mathrm{exp}}\delta\mathrm{A}_4}\delta\alpha_j\right], \tag{4.25}$$

where we assume that all errors are small. Looking at this expression, it is clear that we can neglect $\delta\alpha_j$ if the tension between the SM and the experimental value, given by $\frac{\hat{\mathrm{A}}_4^{\mathrm{exp}} - \mathrm{A}_4^{\mathrm{SM}}}{\mathrm{A}_4^{\mathrm{exp}}}\left(\delta\mathrm{A}_4^{\mathrm{SM}} + \delta\hat{\mathrm{A}}_4^{\mathrm{exp}}\right)$, is much smaller than $1/\delta\alpha_j$. This condition is always satisfied when considering the uncertainties of the MMHT2014lo68cl PDF set and the PDF choice, so we can safely neglect $\delta\alpha_j$ hereafter. Let us note that this exercise is only valid if quadratic terms in the NP couplings can be neglected.

We use a semi-analytical approach, instead of a purely numerical one, because the cross section we are interested in is free of kinematic cuts, except for those on the dilepton invariant mass and rapidity. This follows from the definition of the A_4 angular coefficient, which includes an integration over the whole individual lepton phase space, which is carried out in the measurement through an unfolding procedure [191]. Our semi-analytical approach simplifies the analysis and

avoids uncertainties from the numerical simulation, which may be significant due to the small size of the FB asymmetry. Nonetheless, we have crosschecked our results using a numerical approach, in which the cross sections are calculated using MadGraph [196] and processed by MadAnalysis5 [197]. Neglected contributions from parton shower or detector effects are expected to be small for this process, which only involves light leptons in the final state.

With the results in Table 4.3 and Eq. (4.23) we build the following χ^2 function:

$$\chi^2\left(\delta g_k\right) = \sum_i \left(\frac{\mathrm{A}_{4,i}^{\mathrm{SM}}\left(1+\alpha_{ik}\delta g_k\right) - \mathrm{A}_{4,i}^{\mathrm{exp}}}{\delta \mathrm{A}_{4,i}} \right)^2 , \tag{4.26}$$

where the sum runs over the four bins of rapidity displayed in Table 4.3. Experimental and SM errors are combined in quadrature in $\delta \mathrm{A}_{4,i}$.

Before minimizing the full χ^2 function, it is instructive to see how each rapidity bin of the A_4 measurement performs in restricting the EFT couplings. We find:

$$\begin{aligned}
0.0 < |Y| < 0.8: &\qquad 0.63\,\delta g_L^{Zu} + 0.71\,\delta g_R^{Zu} - 0.20\,\delta g_L^{Zd} - 0.22\,\delta g_R^{Zd} = 0.088(29)\ , \\
0.8 < |Y| < 1.6: &\qquad 0.60\,\delta g_L^{Zu} + 0.74\,\delta g_R^{Zu} - 0.18\,\delta g_L^{Zd} - 0.22\,\delta g_R^{Zd} = -0.012(12)\ , \\
1.6 < |Y| < 2.5: &\qquad 0.53\,\delta g_L^{Zu} + 0.80\,\delta g_R^{Zu} - 0.16\,\delta g_L^{Zd} - 0.23\,\delta g_R^{Zd} = -0.0014(92)\ , \\
2.5 < |Y| < 3.6: &\qquad 0.43\,\delta g_L^{Zu} + 0.86\,\delta g_R^{Zu} - 0.18\,\delta g_L^{Zd} - 0.21\,\delta g_R^{Zd} = -0.0030(81)\ ,
\end{aligned} \tag{4.27}$$

where we have normalized each combination to ease the comparison. We can see that the limits reach a percent-level accuracy. The limits from the lowest rapidity bin are the weakest because it is affected the most by the smearing out of the asymmetry: in this bin the direction of the boost of the dilepton system is often opposite to the direction of the incoming quark.

Let us now minimize the full likelihood in Eq. (3.7), i.e., we combine the four constraints in Eq. (4.27). We can see by eye that each bin constrains a similar linear combination of the quark couplings. Therefore we can already anticipate that attempts to constrain simultaneously all four vertex corrections using just the ATLAS data will suffer from large correlations. Instead, it is more instructive to show the constraints on the four linear combinations that are orthonormal and uncorrelated, which we denote as $\{x', y', z', t'\}$, similarly to our approach in (4.10). We find:

$$\begin{pmatrix}
x' = 0.21\delta g_L^{Zu} + 0.19\delta g_R^{Zu} + 0.46\delta g_L^{Zd} + 0.84\delta g_R^{Zd} \\
y' = 0.03\delta g_L^{Zu} - 0.07\delta g_R^{Zu} - 0.87\delta g_L^{Zd} + 0.49\delta g_R^{Zd} \\
z' = 0.83\delta g_L^{Zu} - 0.54\delta g_R^{Zu} + 0.02\delta g_L^{Zd} - 0.10\delta g_R^{Zd} \\
t' = 0.51\delta g_L^{Zu} + 0.82\delta g_R^{Zu} - 0.17\delta g_L^{Zd} - 0.22\delta g_R^{Zd}
\end{pmatrix} = \begin{pmatrix}
-10 \pm 4 \\
0.5 \pm 0.4 \\
0.04 \pm 0.06 \\
-0.001 \pm 0.005
\end{pmatrix} . \tag{4.28}$$

As anticipated, only a single direction, which we denote as t', is constrained at 0.5% level. The constraints on the directions orthogonal to t' are much weaker, and those on x' are practically void within the EFT validity regime. This means that the ATLAS data alone cannot give us useful constraints on all Z boson couplings to quarks. Nevertheless, the input from ATLAS will be invaluable once combined with the other probes of the Zqq couplings, as we will quantify in the next subsection.

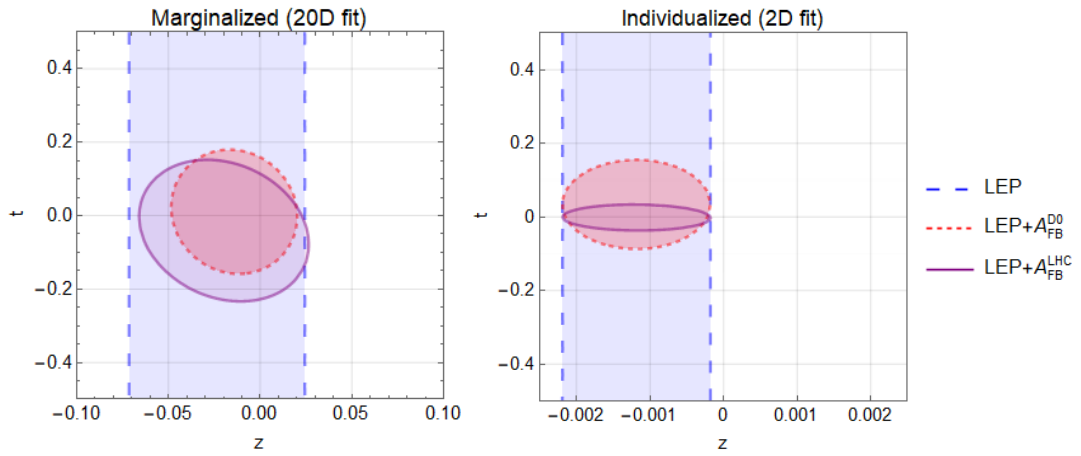

Fig. 4.1: Allowed regions (corresponding to $\Delta\chi^2 = 1$) for the z and t combinations of vertex corrections, see Eqs. (4.10) for their definition. The blue vertical band is obtained using LEP data and the rest of traditional pole observables, whereas the purple and orange ellipses add the FB asymmetry measurements at LHC and D0 respectively (see main text for details). The left panel is obtained marginalizing over the remaining EFT parameters, *cf.* Eq. (3.6), whereas the right panel is obtained setting all of them to zero. Note the horizontal scale is not the same in both plots.

4.4. Impact of A_{FB} on the global fit

Combining the A_{FB} limits obtained above with those extracted from the traditional pole observables in Eq. (4.11) we find:

$$\begin{pmatrix} x \\ y \\ z \\ t \end{pmatrix} = \begin{pmatrix} -0.004 \pm 0.017 \\ 0.010 \pm 0.032 \\ -0.021 \pm 0.046 \\ -0.03 \pm 0.19 \end{pmatrix}, \quad \rho = \begin{pmatrix} 1. & -0.09 & -0.08 & -0.04 \\ -0.09 & 1. & -0.09 & -0.93 \\ -0.08 & -0.09 & 1. & -0.19 \\ -0.04 & -0.93 & -0.19 & 1. \end{pmatrix}. \tag{4.29}$$

Comparing with Eq. (4.11), we see that the marginalized bounds on x, y and z are essentially the same, but the t combination is not anymore unconstrained. The per mille level A_{FB} constraint on t', *cf.* Eq. (4.28), generates a much weaker bound on t because these combinations of Z couplings happen to be quite orthogonal ($t \cdot t' = 0.16$). In spite of this, the A_{FB} bound on t is stringent enough to make a significant impact when added to the traditional pole data. In Eq. (4.29) this is reflected by the large correlation between y and t, which was zero before the inclusion of the A_{FB} data. This is illustrated in Fig. 4.1, which shows the impact of the inclusion of the FB asymmetry on the z and t combinations of vertex corrections.

Beyond the numerical impact on the extracted bounds, the inclusion of the FB asymmetry in the analysis strengthens the robustness of the EFT approach. In fact, the inclusion of $(\delta g)^2$ corrections in the analysis would have a major impact on both LEP and LHC results since $\mathcal{O}(1)$ corrections cannot be excluded by each dataset separately. However, such large corrections are not anymore possible once both datasets are used together. This is clearly illustrated in Fig. 4.2.

The importance of A_{FB} data is even clearer in simple New Physics scenarios where only some Zqq couplings are modified. Fig. 4.3 shows that the situation is similar for other pairs of vertex corrections. The fact that A_{FB}^{LHC} provides crucial information in such simple scenarios despite the extremely precise LEP measurements is highly nontrivial and represents one of our main

findings. Similar conclusions are obtained in a global SMEFT fit with specific flavor symmetries, such as $U(3)^5$ and $U(1)^5 \times U(2)^5$.

4.5. D0 measurement

As mentioned at the beginning of this chapter, Ref. [132] (also Ref. [141]) included in its dataset the determination of the light quark couplings to the Z boson at D0 [155]. This allowed them to lift the flat direction that appears when only traditional pole observables are used. Such determination of the light quark couplings was obtained by D0 from the FB asymmetry in $p\bar{p} \to e^+e^-$ with 5 fb^{-1} at $\sqrt{s} = 1.96$ TeV [155]. That extraction used dilepton masses up to 1 TeV, so technically speaking it assumes that 4-fermion operators are absent or much smaller than vertex corrections. However, one expects that the D0 determination is dominated by the bins near the Z-pole, which have the largest statistics. This is confirmed by our simulations. For this reason, the removal of off-peak bins is not expected to change the D0 extraction of the vertex corrections.

Such D0 results are sensitive to individual vertex corrections at the 2%-level or worse, which is ~ 4 times weaker than the sensitivity of the LHC A_{FB} data, *cf.* Eq. (4.28). Combining the traditional observables with the D0 input we obtain:

$$\begin{pmatrix} x \\ y \\ z \\ t \end{pmatrix} = \begin{pmatrix} -0.009 \pm 0.017 \\ 0.007 \pm 0.023 \\ -0.014 \pm 0.034 \\ 0.01 \pm 0.17 \end{pmatrix}, \quad \rho = \begin{pmatrix} 1 & -0.19 & 0.18 & 0.00 \\ -0.19 & 1 & 0.04 & -0.68 \\ 0.18 & 0.04 & 1 & -0.07 \\ 0.00 & -0.68 & -0.07 & 1 \end{pmatrix}. \tag{4.30}$$

The comparison of the D0 limits with the LHC+LEP results of Eq. (4.29) is complicated because one has to compare marginalized bounds *and* correlations. The former are more stringent in the D0+LEP case, but the latter are higher in the LHC+LEP case, which reflects the fact that the LHC constrains a specific combination much strongly than D0. This means that both LHC and D0 measurements of the A_{FB} asymmetries bring relevant information to the global fit, although for simple scenarios the LHC will typically have a more important effect, as shown in Fig. 4.1 (right panel) and Fig. 4.3.

However, several caveats should be made concerning the D0 extractions. First, the limits will slightly weaken if one only uses the A_{FB} measurement at the Z pole. Since D0 does not study

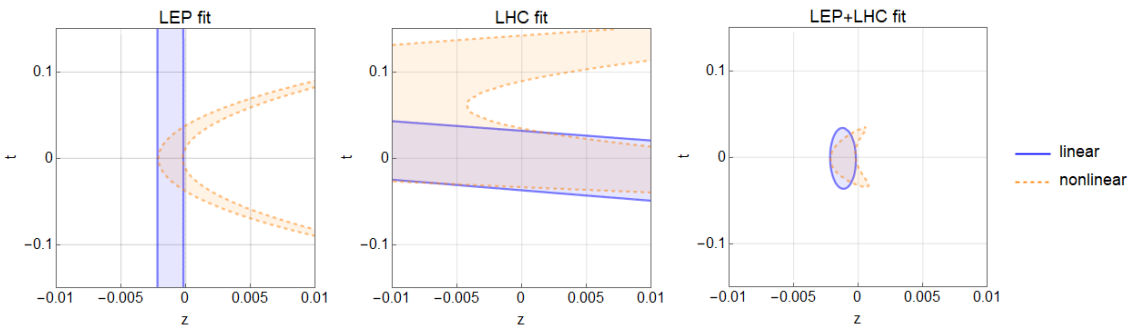

Fig. 4.2: Comparison between linear and nonlinear contours ($\Delta\chi^2 = 1$) in a 2D fit using the traditional pole observables (LEP fit, left panel), the ATLAS FB asymmetry data (LHC fit, central panel) and the combination of both (right panel).

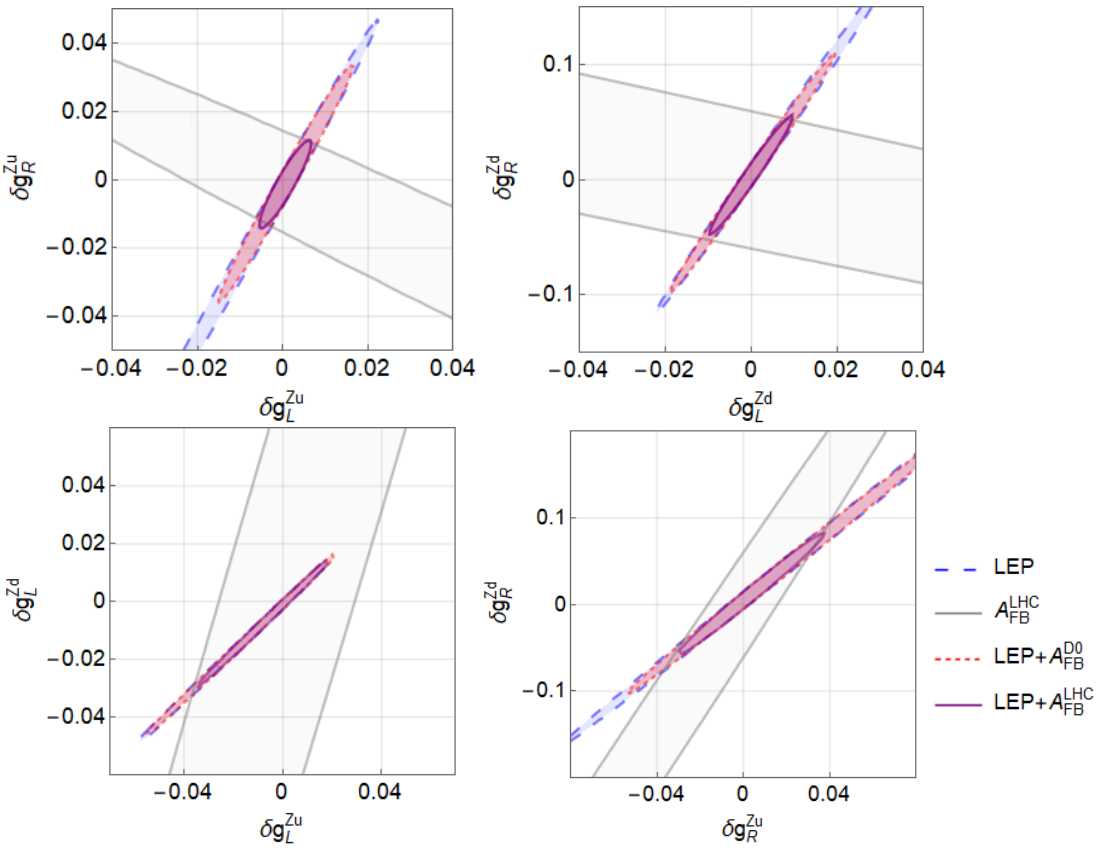

Fig. 4.3: Allowed regions (at 95% CL) for four pairs of corrections of the Z couplings to light quarks. In each case, only that pair of corrections is different from zero, the rest are given by their SM values. Note the scale is different in each panel.

the dependence of the FB asymmetry with the dilepton rapidity, there is only one measurement at the Z pole. Thus, one will be able to probe only one combination of couplings, contrary to the ATLAS case. Additionally, LHC collaborations are still active and taking data, so one can expect significant improvements on that front.

4.6. Combined fit results

We conclude the analysis with a combined fit that includes traditional pole observables (mainly LEP) as well as the above-discussed measurements of the FB asymmetries by ATLAS and D0. The values obtained for the (x, y, z, t) variables are the following:

$$\begin{pmatrix} x \\ y \\ z \\ t \end{pmatrix} = \begin{pmatrix} -0.005 \pm 0.016 \\ 0.009 \pm 0.022 \\ -0.014 \pm 0.032 \\ -0.03 \pm 0.13 \end{pmatrix}, \quad \rho = \begin{pmatrix} 1. & -0.25 & 0.1 & 0.01 \\ -0.25 & 1. & -0.03 & -0.91 \\ 0.1 & -0.03 & 1. & -0.26 \\ 0.01 & -0.91 & -0.26 & 1. \end{pmatrix}, \tag{4.31}$$

Using Eq. (4.10) we translate this into constraints on the corrections of the Z couplings to light quarks, which after all are the main subject of our study:

$$\begin{pmatrix} \delta g_L^{Zu} \\ \delta g_R^{Zu} \\ \delta g_L^{Zd} \\ \delta g_R^{Zd} \end{pmatrix} = \begin{pmatrix} -0.012 \pm 0.024 \\ -0.005 \pm 0.032 \\ -0.020 \pm 0.037 \\ -0.03 \pm 0.13 \end{pmatrix}, \quad \rho = \begin{pmatrix} 1 & 0.51 & 0.68 & 0.69 \\ 0.51 & 1 & 0.56 & 0.94 \\ 0.68 & 0.56 & 1 & 0.54 \\ 0.69 & 0.94 & 0.54 & 1 \end{pmatrix}. \tag{4.32}$$

These values are marginalized over the 16 remaining EFT parameters that also contribute to the fit observables, *cf.* Eq. (3.6). The full set of constraints and the $20x20$ correlation matrix is given by

$$\begin{pmatrix} \delta g_L^{We} \\ \delta g_L^{W\mu} \\ \delta g_L^{W\tau} \\ \delta g_L^{Ze} \\ \delta g_L^{Z\mu} \\ \delta g_L^{Z\tau} \\ \delta g_R^{Ze} \\ \delta g_R^{Z\mu} \\ \delta g_R^{Z\tau} \\ \delta g_L^{Zu} \\ \delta g_R^{Zu} \\ \delta g_L^{Zd} \\ \delta g_R^{Zd} \\ \delta g_L^{Zs} \\ \delta g_R^{Zs} \\ \delta g_L^{Zc} \\ \delta g_R^{Zc} \\ \delta g_L^{Zb} \\ \delta g_R^{Zb} \\ \delta m_W \end{pmatrix} = \begin{pmatrix} -1.2 \pm 3.2 \\ -2.7 \pm 2.6 \\ 1.5 \pm 4.0 \\ -0.20 \pm 0.28 \\ 0.1 \pm 1.2 \\ -0.09 \pm 0.59 \\ -0.43 \pm 0.27 \\ 0.0 \pm 1.4 \\ 0.62 \pm 0.62 \\ -12 \pm 24 \\ -5 \pm 32 \\ -20 \pm 37 \\ -30 \pm 130 \\ 11 \pm 28 \\ 32 \pm 48 \\ -1.5 \pm 3.6 \\ -3.3 \pm 5.3 \\ 3.1 \pm 1.7 \\ 21.9 \pm 8.8 \\ 0.29 \pm 0.16 \end{pmatrix} \times 10^{-3}. \tag{4.33}$$

The correlation matrix is given in Table 4.4. Despite appearances, the W mass corrections δm_W is not completely uncorrelated with the vertex correction, but the correlation coefficients are of order 0.001, and are approximated as zero above.

The results above are enough to reproduce the full Gaussian likelihood function for our parameters. Using the map in Eq. (2.17), it can be translated into a likelihood for the Wilson coefficients in the Warsaw basis at the scale $\mu = m_Z$. In this step, the map should be used for $V \to \mathbf{I}$, since our fit results are formally valid in this limit. That can be evolved to other RG scales using e.g. the public code `DsixTools` [198] or `Wilson` [199]. Our general likelihood can always be restricted to more constrained flavor scenarios [200, 201] or to the universal scenario with oblique parameters [202]. We also show the limits that we find when considering one operator at a time in Fig. 4.4 and Fig. 4.5.

Table 4.4: Correlation matrix for the limits obtained in Eq. (4.33) from the global fit built with information from traditional pole observables and the Drell-Yan forward-backward asymmetries measured by ATLAS and D0.

$$
\begin{pmatrix}
1 & 0.2 & -0.59 & -0.22 & -0.09 & 0.01 & 0.16 & -0.13 & -0.08 & -0.04 & -0.06 & -0.03 & -0.06 & -0.02 & -0.04 & -0.01 & 0.01 & 0.04 & 0.01 & 0. \\
0.2 & 1 & -0.39 & -0.27 & -0.11 & 0.01 & 0.2 & -0.16 & -0.1 & -0.04 & -0.06 & -0.03 & -0.07 & -0.03 & -0.04 & -0.01 & 0.01 & 0.05 & 0.01 & 0. \\
-0.59 & -0.39 & 1 & -0.18 & -0.07 & 0.01 & 0.13 & -0.11 & -0.07 & 0. & 0. & 0. & 0. & 0. & 0. & -0.01 & 0. & 0.04 & 0.01 & 0. \\
-0.22 & -0.27 & -0.18 & 1 & -0.09 & -0.07 & 0.16 & -0.04 & 0.04 & 0.04 & 0.06 & 0.03 & 0.06 & 0.03 & 0.04 & 0.07 & 0.08 & -0.36 & -0.35 & 0. \\
-0.09 & -0.11 & -0.07 & -0.09 & 1 & -0.04 & -0.04 & 0.91 & -0.04 & 0. & 0.01 & 0.01 & 0.01 & 0.01 & 0.01 & -0.02 & -0.01 & 0.06 & 0.04 & 0. \\
0.01 & 0.01 & 0.01 & -0.07 & 0.06 & 1 & 0.02 & -0.03 & 0.41 & -0.01 & -0.01 & -0.01 & -0.02 & -0.01 & -0.01 & -0.02 & 0.01 & 0.07 & 0.01 & 0. \\
0.16 & 0.2 & 0.13 & 0.16 & -0.04 & 0.02 & 1 & -0.07 & -0.04 & -0.02 & -0.03 & -0.02 & -0.03 & -0.01 & -0.02 & 0.06 & 0.11 & -0.34 & -0.38 & 0. \\
-0.13 & -0.16 & -0.11 & -0.04 & 0.91 & -0.03 & -0.07 & 1 & 0.04 & 0.02 & 0.03 & 0.02 & 0.03 & 0.01 & 0.02 & 0. & -0.01 & 0.01 & 0.03 & 0. \\
-0.08 & -0.1 & -0.07 & 0.04 & -0.04 & 0.41 & -0.04 & 0.04 & 1 & 0.02 & 0.03 & 0.01 & 0.03 & 0.01 & 0.02 & 0.01 & -0.01 & -0.04 & 0. & 0. \\
-0.04 & -0.04 & 0. & 0.04 & 0. & -0.01 & -0.02 & 0.02 & 0.02 & 1 & 0.5 & 0.68 & 0.69 & 0.07 & -0.29 & -0.05 & 0.09 & -0.02 & -0.01 & 0. \\
-0.06 & -0.06 & 0. & 0.06 & 0.01 & -0.01 & -0.03 & 0.03 & 0.03 & 0.5 & 1 & 0.55 & 0.94 & -0.11 & -0.39 & 0.07 & 0.07 & -0.03 & -0.02 & 0. \\
-0.03 & -0.03 & 0. & 0.03 & 0.01 & -0.01 & -0.02 & 0.02 & 0.01 & 0.68 & 0.55 & 1 & 0.54 & -0.64 & -0.08 & -0.02 & 0.05 & -0.01 & 0. & 0. \\
-0.06 & -0.07 & 0. & 0.06 & 0.01 & -0.02 & -0.03 & 0.03 & 0.01 & 0.69 & 0.94 & 0.54 & 1 & 0.07 & -0.46 & 0.05 & 0.09 & -0.03 & -0.02 & 0. \\
-0.02 & -0.03 & 0. & 0.03 & 0.01 & 0. & -0.01 & 0.01 & 0.01 & 0.07 & -0.11 & -0.64 & 0.07 & 1 & -0.01 & 0.1 & 0.03 & -0.02 & -0.01 & 0. \\
-0.04 & -0.04 & 0. & 0.04 & 0.01 & -0.01 & -0.02 & 0.02 & 0.02 & -0.29 & -0.39 & -0.08 & -0.46 & -0.01 & 1 & 0.04 & 0.05 & -0.02 & -0.01 & 0. \\
-0.01 & -0.01 & -0.01 & 0.07 & -0.02 & -0.02 & 0.06 & 0. & 0.01 & -0.05 & 0.07 & -0.02 & 0.05 & 0.1 & 0.04 & 1 & 0.32 & -0.11 & -0.15 & 0. \\
0.01 & 0.01 & 0. & 0.08 & -0.01 & 0.01 & 0.11 & -0.01 & 0.01 & 0.09 & 0.07 & 0.05 & 0.09 & 0.03 & 0.05 & 0.32 & 1 & -0.17 & -0.14 & 0. \\
0.04 & 0.05 & 0.04 & -0.36 & 0.06 & 0.07 & -0.34 & 0.01 & -0.04 & -0.02 & -0.03 & -0.01 & -0.03 & -0.02 & -0.02 & -0.11 & -0.17 & 1 & 0.9 & 0. \\
0.01 & 0.01 & 0.01 & -0.35 & 0.04 & 0.01 & -0.38 & 0.03 & 0. & -0.01 & -0.02 & 0. & -0.02 & -0.01 & -0.01 & -0.15 & -0.14 & 0.9 & 1 & 0. \\
0. & 0. & 0. & 0. & 0. & 0. & 0. & 0. & 0. & 0. & 0. & 0. & 0. & 0. & 0. & 0. & 0. & 0. & 0. & 1
\end{pmatrix}
$$

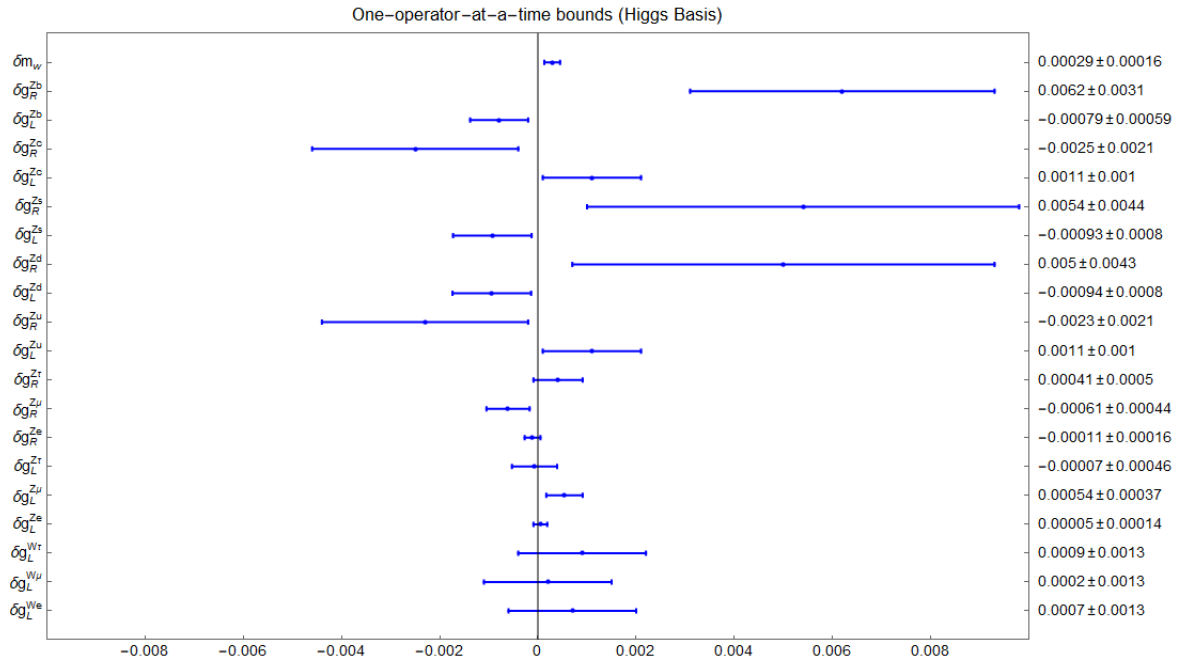

Fig. 4.4: Constraints obtained from our final electroweak fit, which uses traditional pole observables (Table 4.1 and Table 4.2), LHC A_{FB} data (Table 4.3) and D0 A_{FB} data [155], when considering one Higgs-basis operator at a time.

4.7. Discussion of the results

In this chapter we have discussed the impact of LHC Z-pole measurements on constraining the Wilson coefficients of dimension-6 operators in the SMEFT (mainly vertex corrections). Naively, in this domain the LHC should not be able to compete with LEP because the latter measured multiple Z-pole observables with per mille precision in a cleaner environment. However, LEP leaves one unconstrained direction among Z boson couplings to up and down quarks. Indeed, one of the linear combinations defined in Eq. (4.10) and denoted as t is not probed at all by LEP observables. Information from hadron colliders allows one to plug this hole. In particular, the Drell-Yan $pp \to \ell^+\ell^-$ and $p\bar{p} \to \ell^+\ell^-$ processes are sensitive to the Z boson coupling to light quarks making up the proton and anti-proton. Most importantly for our sake, they are sensitive to *different* linear combinations of these couplings than LEP. Therefore, Drell-Yan measurements in hadron colliders are complementary to the LEP observables and provide precious inputs to the electroweak fit. Here we have exemplified this general fact using the FB asymmetry in $pp \to Z/\gamma^* \to \ell^+\ell^-$ measured by the ATLAS experiment. One of our main results is that the flat direction along the t variable is indeed lifted with the inclusion of the ATLAS input, *cf.* Eq. (4.29). Interestingly enough, we find that the ATLAS A_{FB} information provides a significant improvement on LEP-only bounds on the Zqq vertex corrections even in simple scenarios with few free parameters, as shown in Fig. 4.3.

We would like to remark that the importance of hadron colliders for the electroweak fit is more general and goes beyond improving our knowledge of the Zuu and Zdd couplings. This is illustrated in Fig. 4.6, where we compare constraints on selected parameters with and without the use of hadron collider observables. First, as shown in this chapter, constraints on other combinations of $Zq\bar{q}$ couplings, namely x, y, z (*cf.* (4.10), also probed by LEP), are significantly

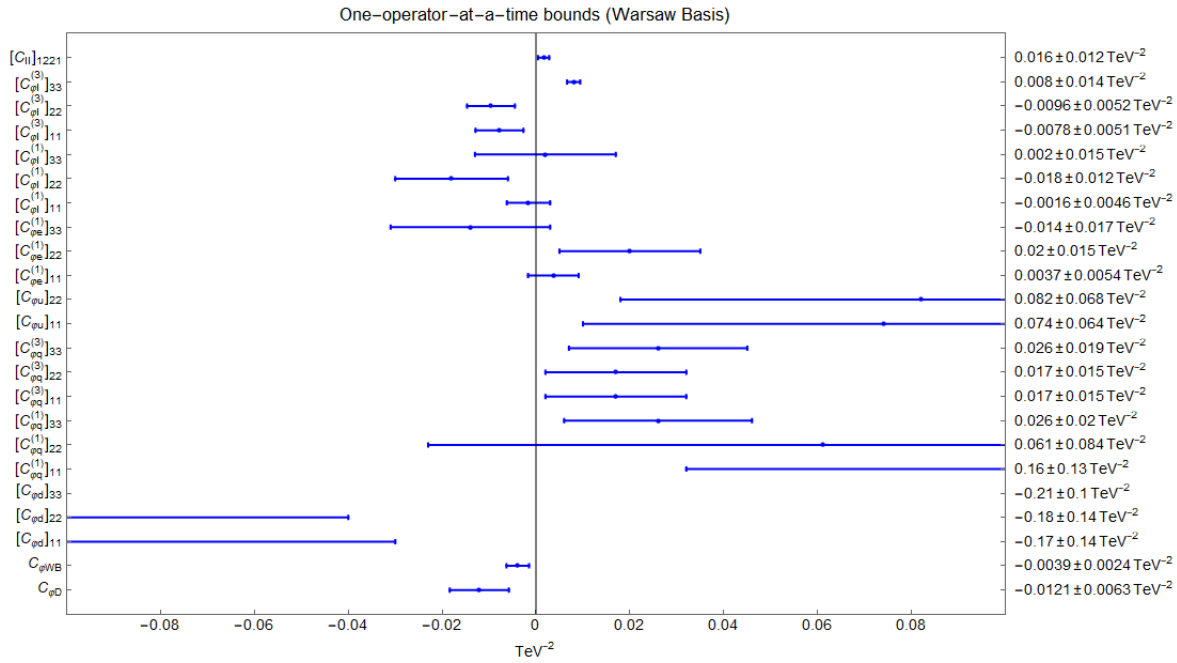

Fig. 4.5: Constraints obtained from our final electroweak fit, which uses traditional pole observables (Table 4.1 and Table 4.2), LHC A_{FB} data (Table 4.3) and D0 A_{FB} data [155], when considering one Warsaw-basis operator at a time.

improved by including information from the FB asymmetry in lepton Drell-Yan production. Even more spectacular improvements happen in the W boson sector. Indeed, LEP could produce $W^{\pm}$ only in the LEP-2 phase and in much lower numbers than Z, resulting in a lower accuracy of the W observables. It is well known that the precision with which the W mass was measured at LEP-2 has been surpassed by the Tevatron and the LHC. It may be less known that a similar improvement has been achieved for the W boson couplings to leptons. Thanks mainly to the recent measurements of leptonic branching fractions of W in ATLAS and LHCb [164–166] the error bars on the parameters $\delta g_L^{W\ell}$ are improved by approximately a factor of two for $\ell = e, \mu, \tau$. Moreover, tensions with the SM visible in the LEP measurements, which in the past were subject to some theoretical scrutiny [203–205], are now all gone away.

These results, reported in Ref. [133], have already found practical applications in probing the parameter spaces of concrete new physics models. In particular, the limits presented in this chapter have been used to test a leptoquark model [206], a Z' model [207], a 4321 gauge model [208], a neutrino mass model [209], a vector-like lepton model [210] and a quantum gravity model [211]. All of these models are formulated with the ultimate intent of solving some of the important problems that the SM is currently facing, such as the flavour puzzle, the neutrino mass mechanism, quantum gravity or the flavor and $(g-2)_\mu$ anomalies (see Chapter 1.4 for more details on all of them).

A brief comment can be made on the relevance that this analysis can have in addressing the tension in the measurement of the bottom quark forward-backward asymmetry at LEP [156]. At present, there exists a 2.5σ tension with the SM tied to that observable, and no additional probe has been able to neither verify nor dispel it. This discrepancy is fully contained in the electroweak sector, so there is a possibility that new information from the LHC could be able to cast some light on the controversy. Perhaps the procedure that we have used to address the light

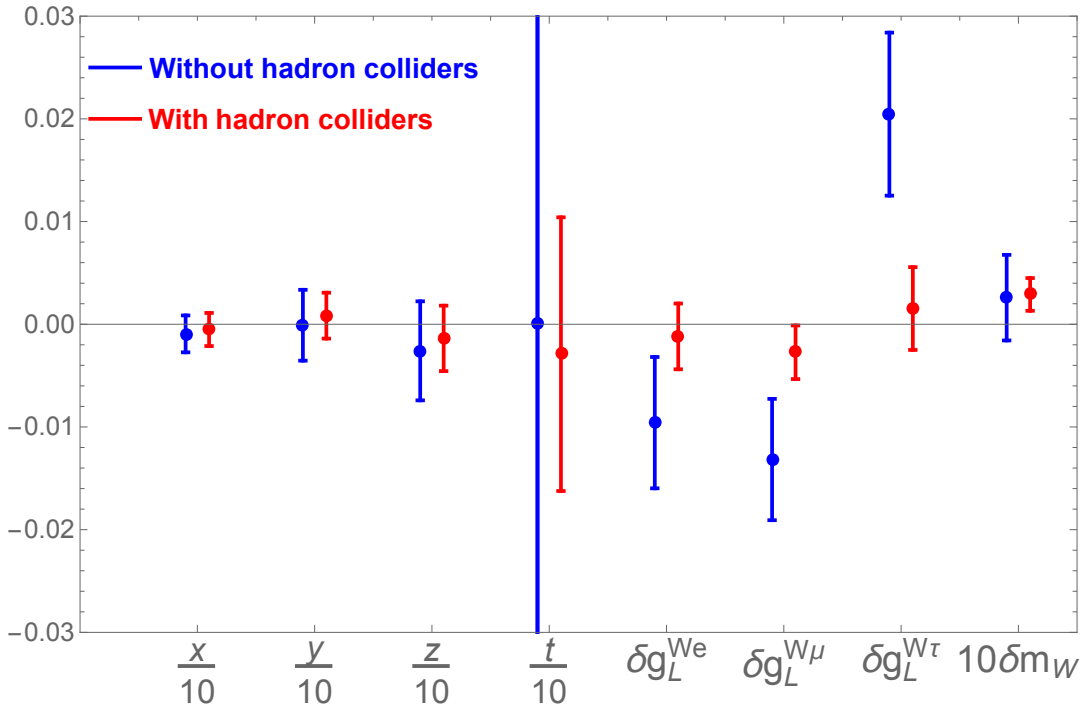

Fig. 4.6: Comparison of the marginalized constraints on selected parameters in the electroweak fit, with (red error bars) and without (blue error bars) using hadron collider observables. Here, x, y, z, t defined in Eq. (4.10) are linear combinations of the non-SM corrections to the coupling between the Z boson and light quarks, $\delta g_L^{W\ell}$ are corrections to the coupling between the W boson and left-handed leptons, and δm_W is a correction to the W boson mass.

quark vertex corrections can be extrapolated and be valuable in probing Zbb couplings. However, a quick survey of the potential measurements that could help in this task reveals that the LHC cannot compete with the LEP data in the b sector [212–214]. However, Ref. [215] suggests that the precision level expected at the High Luminosity-LHC [216] could be enough to meaningfully address the anomaly.

We close with some comments on the perspectives of improving the electroweak fit using future results. Currently, the error for the ATLAS A_4 measurement (used in our study) is dominated by statistics, therefore the bounds on Zqq couplings should be tightened once more data is analyzed. The current and future measurements of Drell-Yan dilepton production by CMS and LHCb could be analyzed following a similar procedure to ours. It is worth noting that Drell-Yan production at the Tevatron probes a different combination of the Zqq vertex correction due to it being a $p\bar{p}$ collider, therefore it would be advantageous to include the final 10 fb^{-1} Tevatron results in the fit as well. Ideally, all these analyses would be done by the experimental collaboration themselves, who are in the best position to assess the pertinent systematic errors and correlations.

The potential improvements on the measurement are not limited to the experimental side. As can be seen in Table 4.3, the theoretical errors for the A_4 predictions are on par with their corresponding experimental uncertainties, so we can also get a lot of benefit from upgrading the theoretical estimation of the observable. This is a novelty for electroweak precision observables, but it represents nonetheless an interesting direction to pursue if we want to optimize this kind of new physics fits.

Next, information from Drell-Yan cross sections (in addition to asymmetries) could be added, and the off-pole data could be analyzed at the same time in the context of a more general fit to both vertex corrections and 4-fermion operators [132, 217]. This is the line of research we are currently exploring as the main focus for the continuation of the work presented in this chapter. A discussion of our progress on it will be provided in Chapter 6. Our constraints do not include vertex corrections to the Ztt coupling, but these can be accommodated too in a more comprehensive fit [218–221].

Additionally, there always exists the possibility of upgrading our computation of the Drell-Yan cross section at NLO in the SMEFT. Substantial work has already been done in that direction [139, 222], which demonstrates that improvements at the percent level can be achieved and that new phenomenological signatures occur first at one loop. This represents a very attractive prospect for future work, since going beyond tree level significantly increases the number of parameters in our fit and thus grants sensitivity to more diverse new physics signatures.

Finally, it would be interesting to analyze the potential of the High-Luminosity LHC and other future colliders for improving the constraints on Zqq vertex corrections. We expect that these future studies will increase even further the impact of hadron colliders on the electroweak precision program.

Chapter 5

EFT analysis of New Physics at COHERENT

Another experimental context where precision measurements are starting to become commonplace is that of neutrino physics. Neutrino scattering on matter (electrons, nucleons, nuclei) probes the interaction strength and structure of the weak force. In the SM context, it represents a measure of the weak mixing angle, although currently it cannot compete with the much more precise determination based on the W mass and Z-pole physics. More generally, it is sensitive to new BSM particles interacting with neutrinos. These effects, much like with the collider observables, can be characterized within an EFT framework if we assume the new degrees of freedom are heavy. Applying that description to neutrino data can reveal some combinations of NP parameters that could be interesting in the context of an EFT global fit. More specifically, neutrino observables can provide a very valuable experimental input for the improvement of the global fit presented in Chapter 3.

To explore that possibility, we choose to examine recent precision measurements of coherent elastic neutrino scattering on nuclei (CEνNS). The process was theorized long ago [223, 224], but the experimental challenges were overcome only recently by the COHERENT experiment [225]. The peculiarity of CEνNS is that vector interactions between neutrino and nuclear constituents (nucleons or quarks) add up coherently. Consequently, possible small deviations between the actual neutrino interaction strength and that predicted by the SM are also amplified. This effect, roughly proportional to the number of neutrons in the nucleus, makes CEνNS a powerful probe of BSM physics.

If we want to apply EFTs to CEνNS observables, it is important to consider the energy scales at which this kind of interactions are relevant. In the previous chapter, we performed our analysis within the SMEFT, which is a relevant theory at scales above the Z mass. However, CEνNS interactions take place well below that energy regime, so we will need to reconsider if the SMEFT is the best tool to quantify NP effects linked to them. Thankfully, EFTs have the flexibility of being adaptable to a multitude of scales by integrating out all particles above the physical scale of interest (see Chapter 2.1 for more details). In the case of CEνNS , the ideal framework for new physics searches is the WEFT. In it, both neutral current (NC) and charged current (CC) probed by CEνNS experiments are described through effective 4-fermion interactions between neutrinos and quarks. The Wilson coefficients of operators involving neutrinos in this framework can be translated into the language of non-standard interactions (NSI) [226] prevalent in the neutrino

literature.[1] Nevertheless, this is still not the most natural description for CEνNS, since the interaction strictly involves nuclear components, not quarks. If we want to work with nucleons as relevant degrees of freedom, then we need to match the WEFT with a nucleon-level EFT. This transition will allow us to deal with the effective 4-fermion contact interactions between neutrinos and nucleons that are probed by COHERENT. Thus, we will have to use the WEFT operators to build neutron and proton weak charges [230]. In the SM, the CEνNS event rate is simply proportional to the square of these weak charges weighted by the number of protons and neutrons in the target nucleus [231]. Moreover, the observed CEνNS rate is obviously also sensitive to BSM effects in neutrino production.

In this chapter, we will apply these ideas to interpret the results of the COHERENT experiment in the language of the EFTs. We analyze the entirety of the available COHERENT data to extract the nuclear and nucleon weak charges (which we properly generalize so that production effects are taken into account). We translate these into constraints on the WEFT Wilson coefficients. Our results are provided in a completely general form that is straightforward to apply to any BSM model or EFT analysis. In fact, we analyze the impact of current CEνNS data in the global SMEFT fit to electroweak precision observables (EWPO) introduced in Chapter 3 and expanded in Chapter 4, which includes all the data inputs considered in the previous chapter. We will demonstrate that this impact is non-trivial, significantly reducing the allowed parameter space for the SMEFT Wilson coefficients. Moreover, from the point of view of EWPO and SMEFT, COHERENT is the most relevant neutrino-detection experiment to date!

There are several ways in which this study improves on the previous literature regarding the EFT approach to COHERENT data [231–248]:

- This is one of the first instances, together with the recent Refs. [247, 248], where the entire COHERENT dataset presently available (2D energy and time distributions with argon and cesium-iodine targets) [249, 250] is used to probe fundamental interactions, and thus represents the current state of the art.
- We perform for the first time a complete analysis in the framework of WEFT, including the nonlinear effects of the various Wilson coefficients in detection and production. The latter, as well as the non-trivial interplay between the two, have not been correctly discussed before. We remark that correlated effects in production and detection are generic in new physics models, since the $SU(2)_L$ gauge symmetry relates CC and NC interactions.
- We identify the linear combinations of EFT Wilson coefficients that are strongly constrained by COHERENT.
- The model-independent SMEFT analysis of COHERENT data and the combination with other EWPO is performed for the first time.

5.1. Theory framework: EFT ladder

5.1.1. EFT below the electroweak scale

Given the low energies involved in CEνNS, our starting point will be the most general effective Lagrangian below the electroweak scale with the SM particle content, the WEFT La-

[1] For NC non-standard interactions (NSI) [227] the NSI coefficients are in a simple correspondence with the Wilson coefficients of WEFT NC operators involving neutrinos [228]. For CC NSIs [226] the situation is much subtler, as discussed in Ref. [229].

grangian [251]. Let us stress that right-handed neutrinos are not part of the WEFT particle content.

Here we focus on the lepton-number-conserving parts of the WEFT Lagrangian that are relevant for COHERENT physics, namely the NC interactions mediating CEνNS and the CC interactions involved in pion and muon decay. Let us first present the NC interactions between neutrinos and quarks [228, 251]:

$$\mathcal{L}_{\text{WEFT}} \subset -\frac{1}{v^2}\sum_{q=u,d}\left\{[g_V^{qq}\,\mathbb{1}+\epsilon_V^{qq}]_{\alpha\beta}\,(\bar{q}\gamma^\mu q)\,(\bar{\nu}_\alpha\gamma_\mu P_L\nu_\beta)+[g_A^{qq}\,\mathbb{1}+\epsilon_A^{qq}]_{\alpha\beta}\left(\bar{q}\gamma^\mu\gamma^5 q\right)(\bar{\nu}_\alpha\gamma_\mu P_L\nu_\beta)\right\}, \tag{5.1}$$

where $P_{L,R}=\left(1\mp\gamma^5\right)/2$ are the chirality projection operators and $\mathbb{1}$ is the unit matrix. The dimensionful normalization factor is related to the measured value of the Fermi constant $G_F\approx 1.166\times10^{-5}$ GeV^{-2} [153] via $v\equiv(\sqrt{2}G_F)^{-1/2}\approx 246.22$ GeV (*cf.* Eq. (3.1)). In the coefficients of the operators we separated the SM values $g_{V,A}^{qq}$ from the new physics contributions $\epsilon_{V,A}^{qq}$. The former are given at tree-level by

$$g_V^{qq}=T_q^3-2Q_q\sin^2\theta_W,\qquad g_A^{qq}=-T_q^3\ , \tag{5.2}$$

where T_q^3 and Q_q are the weak isospin and charges of the quark q and θ_W is the weak mixing angle. See Ref. [230] for the discussion of radiative corrections and numerical values of these SM couplings. The parameters $\epsilon_{V,A}^{qq}$ are zero in the SM limit and more generally they are Hermitian matrices (in the neutrino indices). As is well known [223], the contribution of the vector Wilson coefficients to the coherent neutrino scattering rate is enhanced by $(A-Z)^2$, where $A-Z$ is the number of neutrons in the nucleus. On the other hand, the contribution of the axial Wilson coefficients does not benefit from such an enhancement, and moreover it vanishes completely for scattering on spin-zero nuclei. In view of the current experimental uncertainties, we can thus neglect the axial contributions in the following, leaving us only with the vector Wilson coefficients.[2] To lighten the notation the vector subindex will be omitted and we will work instead with the more compact notation $\epsilon_{\alpha\beta}^{qq}\equiv[\epsilon_V^{qq}]_{\alpha\beta}$.

Let us now introduce the parts of the WEFT Lagrangian that describe the interactions relevant for neutrino production at COHERENT. Pion decay is described by [251, 253]

$$\begin{aligned}\mathcal{L}_{\text{WEFT}} \subset -\frac{2\,V_{ud}}{v^2}\Big\{&[1+\epsilon_L^{ud}]_{\alpha\beta}\,(\bar{u}\gamma^\mu P_L d)\left(\bar{\ell}_\alpha\gamma_\mu P_L\nu_\beta\right)+[\epsilon_R^{ud}]_{\alpha\beta}\,(\bar{u}\gamma^\mu P_R d)\left(\bar{\ell}_\alpha\gamma_\mu P_L\nu_\beta\right)\\&+\frac{1}{2}\left[\epsilon_S^{ud}\right]_{\alpha\beta}(\bar{u}d)\left(\bar{\ell}_\alpha P_L\nu_\beta\right)-\frac{1}{2}\left[\epsilon_P^{ud}\right]_{\alpha\beta}\left(\bar{u}\gamma^5 d\right)\left(\bar{\ell}_\alpha P_L\nu_\beta\right)\\&+\frac{1}{4}\left[\epsilon_T^{ud}\right]_{\alpha\beta}(\bar{u}\sigma^{\mu\nu}P_L d)\left(\bar{\ell}_\alpha\sigma_{\mu\nu}P_L\nu_\beta\right)\Big\}\ ,\end{aligned} \tag{5.3}$$

where $\ell_\alpha=e,\mu,\tau$ are charged lepton fields, V_{ud} is the (1,1) element of the Cabibbo–Kobayashi–Maskawa (CKM) matrix. Here, new physics is parametrized by $\epsilon_{L,R,S,P,T}^{ud}$, which are general complex matrices in the lepton indices. Finally, the WEFT interactions describing muon decay are [251, 253]:

$$\begin{aligned}\mathcal{L}_{\text{WEFT}} \subset -\frac{2}{v_0^2}\Big\{&\left(\delta_{\alpha a}\delta_{\beta b}+[\rho_L]_{a\alpha\beta b}\right)\left(\bar{\ell}_a\gamma^\mu P_L\nu_\alpha\right)(\bar{\nu}_\beta\gamma_\mu P_L\ell_b)\\&-2\,[\rho_R]_{a\alpha\beta b}\left(\bar{\ell}_a P_L\nu_\alpha\right)(\bar{\nu}_\beta P_R\ell_b)\Big\}.\end{aligned} \tag{5.4}$$

[2] See Ref. [252] for a detailed discussion of the axial contributions to coherent neutrino scattering.

Here new physics is parametrized by the $[\rho_{L,R}]_{a\alpha\beta b}$ tensors. Hermiticity of the Lagrangian implies $[\rho_L]^*_{a\alpha\beta b} = [\rho_L]_{b\beta\alpha a}$, while $[\rho_R]_{a\alpha\beta b}$ is a general complex tensor. Contrary to Eqs. (5.1) and (5.3), in the case of Eq. (5.4) we cannot normalize the interactions using v. This is because that parameter is defined via G_F, which is extracted from the experimental measurement of the muon decay rate, to which the interactions in Eq. (5.4) contribute. Instead, we use the tree-level value of the Higgs vacuum expectation value, v_0. Using Eq. (5.4) it is trivial to calculate the muon decay width and relate v and v_0, finding $v_0^2 = v^2\big(1 + 2\,\mathrm{Re}\,[\rho_L]_{\mu\mu ee} + \sum_{\alpha\beta}\sum_{X=L,R}\big|[\rho_X]_{\mu\alpha\beta e}\big|^2\big)^{1/2}_{\mu\simeq m_\mu}$. In other words, we are working with an input scheme such that the $\mu \to e\bar{\nu}\nu$ decay rate is controlled, exactly as in the SM, by v (equivalently, by G_F), without any tree-level dependence on the $\rho_{L,R}$ Wilson coefficients.[3]

Likewise, one should also take into account that new physics effects in Eq. (5.3) affect the extraction of the CKM factor V_{ud}. See Refs. [254, 255] for the discussion of this issue in the context of extracting V_{ud} from beta decays. For the present purpose, however, V_{ud} appears in COHERENT observables in combination with the pion decay constant $f_{\pi^\pm}$, and the product of the two is usually extracted from the experimental measurements of $\pi \to \mu\nu$ decay width.

In the WEFT Lagrangian above, the quarks u, d and charged leptons ℓ_α are in the basis where their kinetic and mass terms are diagonal, whereas the neutrino fields ν_α are taken in the flavor basis. The latter are connected to neutrino mass eigenstates through the Pontecorvo-Maki-Nakagawa-Sakata (PMNS) mixing matrix: $\nu_\alpha = \sum_{n=1}^3 U_{\alpha n}\nu_n$. As usual, flavor indices are denoted with Greek letters, whereas mass eigenstate indices are denoted with Roman letters.

The Wilson coefficients $\epsilon_X^{ff'}$ and ρ_X parametrize the effect of new interactions mediated by non-standard heavy particles (heavy compared with the COHERENT physics scale), such as, e.g. leptoquarks or Z' and W' vector bosons. It is customary to define the Wilson coefficients in Eq. (5.3) at the renormalization scale $\mu = 2\,\mathrm{GeV}$ in the $\overline{\mathrm{MS}}$ scheme, since lattice QCD provides hadronic decay constants at that scale and scheme. We make the analogous scale choice for the Wilson coefficients $\epsilon^{qq}_{\alpha\beta}$ in Eq. (5.1). Below 2 GeV, the quark-level Lagrangians will be matched in the next subsection to the nucleon-level EFT. On the other hand, for the Wilson coefficients in the leptonic interactions in Eq. (5.4) it is convenient to choose a lower renormalization scale, $\mu \simeq m_\mu$. In any case, in this study we will take into account only the one-loop QCD running of the Wilson coefficients, which can lead to substantial effects, but only concerns the parameters $\epsilon_{S,P,T}$ in Eq. (5.3) [138]. Although the Wilson coefficients are complex in general we will treat them as real for the sake of simplicity.

5.1.2. Nucleon-level EFT

The EFT Lagrangian in the preceding subsection contains quarks fields. However, in the COHERENT experiment some of the neutrinos are produced in pion decay, and they subsequently scatter on heavy nuclei. Thus, we need to connect the quark-level formalism to hadronic- and nuclear-level observables. Regarding pions, it is customary to connect the WEFT Lagrangian in Eq. (5.3) directly to the decay amplitude, using the matrix element of the quark bilinears between a pion state and the vacuum, see Section 5.2.1. On the other hand, regarding scattering on nuclei, it is convenient to introduce an intermediate step in the form of an effective Lagrangian where

[3]The discussion is much simpler if one truncates the WEFT predictions at the linear level, as it is commonly done. In that case it is sufficient to replace $v_0 \to v$ in Eq. (5.4), with the restriction that $\mathrm{Re}\,[\rho_L]_{\mu\mu ee}$ vanishes at the scale $\mu \simeq m_\mu$ [132]. In this work, however, we will analyze the COHERENT constraints beyond the linear level, and for this reason we introduce the more general input scheme.

the degrees of freedom are nucleons rather than quarks. To match the nucleon- and quark-level Lagrangians we need the matrix elements of the quark operators between the nucleon states. Let us denote the incoming nucleon momentum k, and the outgoing nucleon momentum k'. In the near-zero recoil limit, $k - k' \approx 0$, we have

$$\langle N(k',s')|\,\bar{q}\gamma^\mu q\,|N(k,s)\rangle \;=\; F_1^{q,N}\bar{u}_N(k',s')\gamma^\mu u_N(k,s), \tag{5.5}$$

where $N = p, n$, and $u_N(k,s)$ is the usual Dirac spinor wave function of the nucleon N. Isospin symmetry implies $F_1^{u,p} = F_1^{d,n}$ and $F_1^{u,n} = F_1^{d,p}$. For the vector part, conservation of the electromagnetic current implies

$$\begin{aligned}\langle p(k',s')|\,(2/3)\bar{u}\gamma^\mu u - (1/3)\bar{d}\gamma^\mu d\,|p(k,s)\rangle &= (+1)\bar{u}_p(k',s')\gamma^\mu u_p(k,s),\\ \langle n(k',s')|\,(2/3)\bar{u}\gamma^\mu u - (1/3)\bar{d}\gamma^\mu d\,|n(k,s)\rangle &= 0.\end{aligned} \tag{5.6}$$

Thus, in the limit where the strange content of the nucleon is ignored[4] one finds that $(2/3)F_1^{u,p} - (1/3)F_1^{d,p} = 1$ and $2F_1^{u,n} = F_1^{d,n}$ (thus $2F_1^{d,p} = F_1^{u,p}$), so finally

$$F_1^{d,p} = F_1^{u,n} = 1, \qquad F_1^{u,p} = F_1^{d,n} = 2. \tag{5.7}$$

Using these matrix elements, we can write down the effective Lagrangian for vector NC interactions between neutrinos and nucleons:

$$\mathcal{L}_{\text{nucleon}} \supset -\frac{1}{2v^2}\sum_{N=p,n}\sum_{\alpha,\beta=e,\mu,\tau}(\bar{\nu}_\alpha\gamma_\mu P_L\nu_\beta)g_{\alpha\beta}^{\nu N}(\bar{N}\gamma^\mu N)\ , \tag{5.8}$$

where the leading order matching of the Wilson coefficients of the two EFTs reads

$$\begin{aligned} g_{\alpha\beta}^{\nu p} &= 2\left[(2\,g_V^{uu} + g_V^{dd})\,\mathbb{1} + (2\,\epsilon^{uu} + \epsilon^{dd})\right]_{\alpha\beta}\ .\\ g_{\alpha\beta}^{\nu n} &= 2\left[(g_V^{uu} + 2g_V^{dd})\,\mathbb{1} + (\epsilon^{uu} + 2\epsilon^{dd})\right]_{\alpha\beta}\ . \end{aligned} \tag{5.9}$$

In the SM limit at tree level we have

$$\begin{aligned}[g_{\alpha\beta}^{\nu p}]_{\text{SM}} &= \big(1 - 4\sin^2\theta_W\big)\delta_{\alpha\beta}\\ [g_{\alpha\beta}^{\nu n}]_{\text{SM}} &= -\,\delta_{\alpha\beta}.\end{aligned} \tag{5.10}$$

One can see that the NC interactions between neutrinos and vector nucleon currents are approximately protophobic, due to the accidental fact that $\sin^2\theta_W \approx 1/4$. For this reason, low-energy neutrinos scatter mostly on neutrons in nuclei.

At leading order, the nucleon weak charge Q_w^N can be defined simply as the value of the effective couplings in Eq. (5.8) at some fixed renormalization scale, $[Q_w^N]_{\alpha\beta} \equiv g_{\alpha\beta}^{\nu N}(\mu)$. One can generalize this definition so that it includes radiative corrections, which cancels the renormalization scale dependence, but it becomes process dependent [256]. In that approach, the SM values for the weak charges are the following

$$\begin{aligned}[Q_w^p]_{ee}^{\text{SM}} &= 0.0747(34), \qquad [Q_w^p]_{\mu\mu}^{\text{SM}} = 0.0582(34),\\ [Q_w^n]_{\alpha\alpha}^{\text{SM}} &= -\,1.02352(25).\end{aligned} \tag{5.11}$$

[4] See Ref. [252] for the corrections due to the strange content. Taking this into account in our analysis would introduce a weak dependence of the COHERENT observables on the WEFT Wilson coefficients ϵ_V^{ss}. However, currently COHERENT is sensitive only to $|\epsilon_{\alpha\beta}^{ss}| \gtrsim 1$, and for this reason we ignore the strange content of the nucleon.

Note that with this definition the proton weak charge depends slightly on the neutrino flavor. The difference between the proton weak charge experienced by electron- and muon-neutrinos is however numerically irrelevant at present, given the accuracy of the COHERENT experiment. Accordingly, we will just neglect such differences and work with the muonic weak charge also in relation with electron neutrinos (see Chapter 5.2.1).

In order to connect the nucleon-level EFT to the nuclear scattering observables, it is convenient to take the non-relativistic limit of the Lagrangian in Eq. (5.8), since that will allow us to calculate observables for nuclei of arbitrary spin. At the zero-recoil level it takes the form

$$\mathcal{L}_{\rm NR} \supset -\frac{1}{2v^2}\sum_{N=p,n}\sum_{\alpha,\beta=e,\mu,\tau} g^{\nu N}_{\alpha\beta}(\psi^\dagger_N\psi_N)(\bar\nu_\alpha\gamma^0 P_L\nu_\beta) + \mathcal{O}(\nabla/m_N). \tag{5.12}$$

Above, we traded the relativistic nucleon Dirac fields for the non-relativistic ones denoted as ψ_N, which satisfy the Schrödinger equations of motion. We also dropped all terms containing spatial derivatives ∇, which correspond to recoil effects.[5] Now, coherent neutrino scattering amplitudes will involve matrix elements of $\psi^\dagger_N\psi_N$ between nuclear states. For a nucleus $\mathcal{N}$ with momentum k, energy $E_\mathcal{N}$, charge Z, mass number A, spin J, and spin projection along the z-axis J_z, the rotational and isospin symmetry requires the matrix elements to take the form

$$\begin{aligned}\langle\mathcal{N}(k',J'_z)|\,\psi^\dagger_p\psi_p\,|\mathcal{N}(k,J_z)\rangle =& 2\sqrt{E_\mathcal{N}E'_\mathcal{N}}\,\mathcal{F}_p(q^2)Z\delta_{J'_zJ_z},\\ \langle\mathcal{N}(k',J'_z)|\,\psi^\dagger_n\psi_n\,|\mathcal{N}(k,J_z)\rangle =& 2\sqrt{E_\mathcal{N}E'_\mathcal{N}}\,\mathcal{F}_n(q^2)(A-Z)\delta_{J'_zJ_z},\end{aligned} \tag{5.13}$$

where the primed variables refer the final nuclear state ($E_\mathcal{N} = m_\mathcal{N} \approx E'_\mathcal{N}$ in the target rest frame). The nucleon form factors $\mathcal{F}_{p,n}(q^2)$ are equal to 1 at $q^2 \equiv (k-k')^2 = 0$ due to isospin symmetry, although we will not take that limit in our studies. The factor $A-Z$ in the neutron matrix element is at the origin of the coherent enhancement of the neutrino scattering on heavy nuclei.

5.2. COHERENT event rate

Let us consider neutrinos produced by a source S through the process $S \to X_\alpha\nu_k$, where X_α is a one- or more-body final state that contains a charged lepton $\ell_\alpha = e,\mu,\tau$, and ν_k is a neutrino-mass eigenstate ($k = 1,2,3$). These neutrinos propagate a distance L — conserving its mass index k — and are detected via the process $\nu_k\mathcal{N} \to \nu_j\mathcal{N}$, where $j = 1,2,3$ is again a mass index and $\mathcal{N}$ denotes the target nucleus. Let us consider the differential number of detected events per time t, incident neutrino energy E_ν, nuclear recoil energy T and target particle

$$R^S_\alpha(t,T,E_\nu) \equiv \frac{1}{N_T}\frac{dN^S_\alpha}{dt\,dE_\nu\,dT}\ , \tag{5.14}$$

where N_T stands for the number of target particles. Previous calculations of the CEνNS rate [223, 231, 232, 252] have been carried out within the SM or under the assumption that the neutrino production is unaffected by New Physics (NP) and that one can thus simply calculate the rate as a flux times cross-section, i.e., $R^S_\alpha = \sum_\beta d\Phi_{SM}(S\to X_\alpha\nu_\alpha)/dE_\nu \times d\sigma(\nu_\alpha\mathcal{N}\to\nu_\beta\mathcal{N})/dT$, where $\nu_{\alpha,\beta}$ are neutrino flavor eigenstates. In this work we present a derivation that is more general in

[5] This formalism can be generalized to include recoil effects, see Ref. [257] for a study along these lines in the context of beta decay.

the treatment of new physics contributions. We calculate the event rate in terms of the WEFT Wilson coefficients introduced in Chapter 5.1. The interactions of neutrinos relevant for their production and detection are assumed to be most general at the leading order in the WEFT expansion, i.e., we allow for the simultaneous presence of all interactions described in Eqs. (5.1), (5.3) and (5.4). We allow for arbitrary flavor mixing, both via the PMNS matrix, as well as via the various WEFT Wilson coefficients of 4-fermion interactions. Finally, we take into account that NP affecting neutrino production also affects the muon and pion decay widths, which are used in the COHERENT analysis and to determine some of the input observables (such as G_F).

For this derivation, we need to connect the observable event rate in Eq. (5.14) with the production and detection QFT amplitudes, denoted by $\mathcal{M}^{\mathrm{P}}_{\alpha k} \equiv \mathcal{M}\left(S \to X_\alpha \nu_k\right)$ and $\mathcal{M}^{\mathrm{D}}_{jk} \equiv \mathcal{M}\left(\nu_k \mathcal{N} \to \nu_j \mathcal{N}\right)$, which encode the fundamental physics taking place at production and detection. This connection was obtained in Ref. [229] using a QFT approach for the case of neutrino oscillation observables with charged-current interactions both at production and detection. The main idea behind such derivation was, instead of considering the neutrino production and detection separately, to treat both interactions as a single process [258]. That way, by characterizing the source and target as time-independent wave packets and assuming that their width is much smaller than the oscillation length, it is possible to formulate the oscillation observable fully within the QFT framework. Additionally, the derivation assumes that neutrinos are emitted isotropically from a source at rest. This condition is met in the case of COHERENT. In this context, neutrino oscillation arises as a consequence of the interference of different neutrino mass eigenstates in the propagator. In our CC-NC configuration, this combination of production and detection translates into the following process

$$S\mathcal{N} \to X_\alpha \mathcal{N} \nu_j \,, \tag{5.15}$$

where the ν_k neutrino is considered just as an intermediate particle in the amplitude. We can adapt the result found in Ref. [229] to describe the CEνNS rate observed at COHERENT taking into account the various differences. There, the process being described consisted of a production interaction $S \to X_\alpha \nu_k$, where X_α is a nondescript state containing one charged lepton with flavor α, and a detection interaction $\nu_k T \to Y_\beta$, where Y_β also contains another charged lepton with flavor β. Under this scenario, the differential rate of detected neutrinos per target particle for an interaction with the source and target separated by a distance L is found to be

$$R_{\alpha\beta} = \frac{N_S}{32\pi L^2 m_S m_{\mathcal{N}} E_\nu} \sum_{k,l} e^{-i\frac{L\Delta m^2_{kl}}{2E_\nu}} \int d\Pi_{P'} \mathcal{M}^P_{\alpha k} \bar{\mathcal{M}}^P_{\alpha l} \int d\Pi_D \mathcal{M}^D_{\beta k} \bar{\mathcal{M}}^D_{\beta l} \,, \tag{5.16}$$

where complex conjugation is denoted with a bar, $m_{S,\mathcal{N}}$ are the masses of the source and target particles respectively and $\Delta m^2_{kl} \equiv m^2_k - m^2_l$ is the mass squared difference between neutrino (mass) eigenstates, which appears in the formula through the usual $e^{-i\,L\Delta m^2_{kl}/(2E_\nu)}$ oscillatory factor. The phase space elements for the production and detection processes, $d\Pi_P$ and $d\Pi_D$, are defined as usual: $d\Pi \equiv \frac{d^3k_1}{(2\pi)^3 2E_1} \cdots \frac{d^3k_n}{(2\pi)^3 2E_n} (2\pi)^4 \delta^4(\sum p_n - \sum k_i)$, where k_i and E_i are the 4-momenta and energies of the final states and $\sum p_n$ is the total 4-momentum of the initial state. The production phase space is modified as $d\Pi_P \equiv d\Pi_{P'} dE_\nu$ to extract the outgoing neutrino energy from it, and the integration sign includes a sum and averaging over all unobserved degrees of freedom.

In adapting this expression for the COHERENT context, we first need to note that in NC neutrino scattering we have no information about the neutrino final flavor eigenstate (or mass) and hence, we should sum over the corresponding flavor index β. In the context of our deduction,

we change the flavor index β in $\mathcal{M}^D_{\beta k}$ to a mass index j for convenience applying the PMNS matrix, which effectively achieves the same.[6] Secondly, the time variation of the number of source particles N_S cannot be neglected in this case (in fact, it produces a time-dependent signal that is measured). Furthermore, at COHERENT one measures the differential number of events per recoil energy T, and thus we will not integrate over that detection kinematic variable. This implies that we will need to redefine the detection phase space so that $d\Pi_D \equiv d\Pi_{D'} dT$. Finally, the incident neutrino energy is not observed in COHERENT, which can be taken into account trivially integrating R^S_α over that variable.

All in all, the event rate for a source S is given by

$$R^S_\alpha = \frac{N_S(t)}{32\pi L^2 m_S m_{\mathcal{N}} E_\nu} \sum_{j,k,l} \int d\Pi_{P'} \mathcal{M}^P_{\alpha k} \bar{\mathcal{M}}^P_{\alpha l} \int d\Pi_{D'} \mathcal{M}^D_{jk} \bar{\mathcal{M}}^D_{jl} \ . \tag{5.17}$$

Here, $N_S(t) = n_{\rm POT}\, r_{S/p}\, \tau_S\, g_S(t)$ is the time-dependent number of source particles S, where $n_{\rm POT}$ is the total number of protons on target delivered at the Spallation Neutron Source (SNS), $r_{S/p}$ is the number of S particles produced per proton, τ_S is the S lifetime and $g_S(t)$ encodes the N_S time dependence (normalized to one over each bunch characteristic cycle of the proton beam at the SNS). The precise form of $g_S(t)$ depends on several factors such as the S lifetime, time-dependent efficiency and the time-structure of the S pulse. Finally, we have approximated the $e^{-i\, L \Delta m^2_{kl}/(2E_\nu)}$ oscillatory factor to one given the short baseline at COHERENT. This oscillatory factor will also get cancelled for all values of L if the NC interactions do not violate flavor. However, since we will be considering NP corrections with all kinds of flavor signatures, we can only neglect oscillations appealing to the experimental context.

For antineutrinos the event rate is defined equivalently.

5.2.1. Production and detection amplitudes

Let us first discuss the detection process. The amplitude for neutrino scattering on nuclei as a function of the nucleon-level EFT parameters in Eq. (5.8) reads

$$\begin{aligned} \mathcal{M}^D_{jk} &\equiv \mathcal{M}(\nu_k \mathcal{N} \to \nu_j \mathcal{N}) \\ &= -\frac{1}{v^2}\sqrt{E_{\mathcal{N}} E'_{\mathcal{N}}} \Big(Z [U^\dagger g^{\nu p} U]_{jk} \mathcal{F}_p(q^2) + (A-Z)[U^\dagger g^{\nu n} U]_{jk} \mathcal{F}_n(q^2) \Big) (\bar{u}_{\nu_j} P_L u_{\nu_k}), \end{aligned} \tag{5.18}$$

where $u_{\nu_{k,j}}$ are the Dirac wave functions of the incoming and outgoing neutrinos. Taking into account the current uncertainties affecting the COHERENT event rate, it is convenient to approximate neutron and proton form factors to be equal, $\mathcal{F}_p(q^2) = \mathcal{F}_n(q^2) \equiv \mathcal{F}(q^2)$, which allows us to write the detection amplitude in the more compact form:

$$\mathcal{M}^D_{jk} = -\frac{1}{v^2}\sqrt{E_{\mathcal{N}} E'_{\mathcal{N}}}\, [U^\dagger \mathcal{Q}\, U]_{jk}\, (\bar{u}_{\nu_j} P_L u_{\nu_k})\, \mathcal{F}(q^2) \ , \tag{5.19}$$

where the (dimensionless and Hermitian) nuclear weak charge is defined as

$$[\mathcal{Q}]_{\alpha\beta} = Z g^{\nu p}_{\alpha\beta} + (A-Z) g^{\nu n}_{\alpha\beta} \ . \tag{5.20}$$

[6] In performing this operation, we take that the PMNS matrix is unitary following the assumption coming from the SMEFT. Despite this, our approach does include the so-called non-unitarity PMNS matrix (widely studied in the neutrino literature), which takes the form of dimension-6 operators in our framework [229].

When examining antineutrinos, the detection amplitude is almost the same, the only differences are that the (j,k) indices should be exchanged in the right-hand side and it should be written in terms of antispinors v_{ν_i} instead of spinors u_{ν_i}.

To work instead with different neutron and proton form factors would entail working with q^2-dependent weak charges (or, equivalently, with the $g^{\nu N}$ coefficients instead of the weak charges), which would make our subsequent discussion and intermediate results more cumbersome. Additionally, the final results for the quark-level WEFT Wilson coefficients are not expected to be affected by this approximation given current uncertainties. On the other hand, the q^2 dependence in the form factor can not be neglected in the studied recoil energy range. To describe it, we will make use of the Helm parametrization [259] (see Appendix A for further details). Other recoil effects are numerically unimportant given the current experimental precision.

On the production side we have the 2-body leptonic pion decay $\pi^+ \to \ell_\alpha^+ \nu_k$ ($\alpha = e, \mu$) and the 3-body muon decay $\mu^+ \to \bar{\nu}_m e^+ \nu_k$. Their amplitudes are given by[7]

$$\begin{aligned}
\mathcal{M}^{P,\pi}_{\alpha k} &\equiv \mathcal{M}(\pi^+ \to \ell_\alpha^+ \nu_k) = -i\, m_\mu f_{\pi^\pm} \frac{V_{ud}}{v^2} [\mathcal{P}U]^*_{\alpha k} (\bar{u}_{\nu_k} P_L v_{\ell_\alpha}) \,, \\
\mathcal{M}^{P,\mu}_{mk} &\equiv \mathcal{M}(\mu^+ \to \bar{\nu}_m e^+ \nu_k) = -i \frac{2}{v^2} [U^\dagger \mathcal{P}_L^T U]_{km} (\bar{v}_\mu \gamma^\mu P_L v_{\bar{\nu}_m})(\bar{u}_{\nu_k} \gamma_\mu P_L v_e) \\
&\qquad -i \frac{4}{v^2} [U^\dagger \mathcal{P}_R^T U]_{km} (\bar{v}_\mu P_L v_{\bar{\nu}_m})(\bar{u}_{\nu_k} P_R v_e) \,,
\end{aligned} \tag{5.21}$$

where v_α, $\bar{u}_{\nu_k}$ are the Dirac spinor wave functions of the charged lepton and the neutrino, respectively, and the pion decay constant $f_{\pi^\pm}$ is defined by $\langle 0|\bar{d}\gamma_\mu\gamma_5 u(0)|\pi^+(p)\rangle = i p_\mu f_{\pi^\pm}$. Above we introduced the shorthand notation

$$\begin{aligned}
[\mathcal{P}]_{\alpha\beta} &\equiv \delta_{\alpha\beta} + [\epsilon_L]_{\alpha\beta} - [\epsilon_R]_{\alpha\beta} - [\epsilon_P]_{\alpha\beta} \frac{m^2_{\pi^\pm}}{m_{\ell_\alpha}(m_u + m_d)} \,, \\
[\mathcal{P}_L]_{\alpha\beta} &\equiv \delta_{\alpha\mu}\delta_{\beta e} + [\rho_L]_{\mu\alpha\beta e} \,, \\
[\mathcal{P}_R]_{\alpha\beta} &\equiv [\rho_R]_{\mu\alpha\beta e} \,.
\end{aligned} \tag{5.22}$$

The transposition in the $\mathcal{P}_{L,R}$ matrices in Eq. (5.21) is defined such that it only affects the two neutrino indices when applied to the $\rho_{L,R}$ Wilson coefficients.

5.2.2. Amplitudes product and phase space integrations

On the detection side, for neutrinos we find

$$\sum_j \int d\Pi_{D'} \mathcal{M}^D_{jk} \bar{\mathcal{M}}^D_{jl} = [U^\dagger \mathcal{Q}^2 U]_{lk} \frac{\mathcal{F}(q^2)^2\, m_\mathcal{N} E_\nu (T + m_\mathcal{N})}{2\pi v^4} \left(1 - \frac{(m_\mathcal{N} + 2E_\nu)\, T}{2E_\nu^2}\right) , \tag{5.23}$$

where $T = E'_\mathcal{N} - m_\mathcal{N}$ is the (kinematic) nuclear recoil energy, and thus $q^2 = 2M_\mathcal{N} T$. The same result holds for antineutrinos except for the ordering of the (l,k) indices on the right-hand side.

On the production side, for pion-decay neutrinos we obtain

$$\int d\Pi_{P'} \mathcal{M}^{P,\pi}_{\mu k} \bar{\mathcal{M}}^{P,\pi}_{\mu l} = [\mathcal{P}U]_{\mu l} [U^\dagger \mathcal{P}^\dagger]_{k\mu} \frac{V_{ud}^2 f^2_{\pi^\pm} m^2_\mu (m^2_{\pi^\pm} - m^2_\mu)^2}{8\pi m^2_{\pi^\pm} v^4} \delta\Big(E_\nu - E_{\nu,\pi}\Big) \,, \tag{5.24}$$

[7] In the muon decay amplitude $\mathcal{M}^{P,\mu}_{mk}$ we omit the charged lepton subindex ($\alpha = e$ in this case) and we include both the neutrino and antineutrino mass eigenstate indices. This allows us to use the same notation for the neutrino and antineutrino rates.

where $E_{\nu,\pi} = (m_{\pi^\pm}^2 - m_\mu^2)/(2m_{\pi^\pm})$ is the energy of the neutrino emitted in the 2-body pion decay. On the other hand, for muon-decay neutrinos and muon-decay antineutrinos we find, respectively, the following results[8]

$$\begin{aligned}
\sum_m \int d\Pi_{P'} \mathcal{M}^{P,\mu}_{mk} \bar{\mathcal{M}}^{P,\mu}_{ml} &= \frac{m_\mu^5}{\pi^3 v^4} \left(\frac{E_\nu}{m_\mu}\right)^2 \left(\frac{1}{2} - \frac{E_\nu}{m_\mu}\right) \left[U^\dagger P_L^T \mathcal{P}_L^* U + p_{RR}\, U^\dagger P_R^T \mathcal{P}_R^* U\right]_{kl} , \\
\sum_m \int d\Pi_{P'} \mathcal{M}^{P,\mu}_{km} \bar{\mathcal{M}}^{P,\mu}_{lm} &= \frac{m_\mu^5}{3\pi^3 v^4} \left(\frac{E_\nu}{m_\mu}\right)^2 \left(\frac{3}{4} - \frac{E_\nu}{m_\mu}\right) \left[U^\dagger P_L^* \mathcal{P}_L^T U + \bar{p}_{RR}\, U^\dagger P_R^* \mathcal{P}_R^T U\right]_{lk} ,
\end{aligned} \tag{5.25}$$

where $p_{RR} = 1/\bar{p}_{RR} = (3m_\mu - 4E_\nu)/(6m_\mu - 12E_\nu)$. We have neglected $\mathcal{O}(m_e/m_\mu)$ corrections, which include the crossed RL and LR terms.

We would like to write these results in terms of the observable pion and muon decay widths, since COHERENT uses those quantities in their flux predictions. They can be obtained from the expressions above integrating over the (anti)neutrino energy and working with equal neutrino indices in $\mathcal{M}^P$ and $\bar{\mathcal{M}}^P$, which are summed over. This gives

$$\begin{aligned}
\Gamma_{\pi\to\mu\nu} &= \frac{1}{2m_{\pi^\pm}} \sum_k \int dE_\nu \int d\Pi_{P'} \mathcal{M}^{P,\pi}_{\mu k} \bar{\mathcal{M}}^{P,\pi}_{\mu k} = \frac{V_{ud}^2 f_{\pi^\pm}^2 m_\mu^2 (m_{\pi^\pm}^2 - m_\mu^2)^2}{16\pi m_{\pi^\pm}^3 v^4} [\mathcal{P}\mathcal{P}^\dagger]_{\mu\mu} , \\
\Gamma_{\mu\to e\bar{\nu}\nu} &= \frac{1}{2m_\mu} \sum_{k,m} \int dE_\nu \int d\Pi_{P'} \mathcal{M}^{P,\mu}_{mk} \bar{\mathcal{M}}^{P,\mu}_{mk} = \frac{m_\mu^5}{384\pi^3 v_0^4} \mathrm{Tr}\left(\mathcal{P}_L \mathcal{P}_L^\dagger + \mathcal{P}_R \mathcal{P}_R^\dagger\right) ,
\end{aligned} \tag{5.26}$$

up to radiative and m_e/m_μ corrections. The muon decay width can be expressed as $\Gamma_{\mu\to e\bar{\nu}\nu} = m_\mu^5/(384\pi^3 v^4)$, which represents the definition of v (equivalently, of $G_F \equiv (\sqrt{2}v^2)^{-1}$), and remains valid in the presence of new physics.[9] In other words, in our input scheme the possible new physics contamination in the determination of the Fermi constant is absorbed into the parameter v, whose value is fixed by experiment. These NP effects are also absorbed in the Wilson coefficients $\epsilon_{V,A}^{qq}$ and ϵ_X^{ud}, since v is used in their definitions, *cf.* Eqs. (5.1) and (5.3). This can be seen explicitly matching to the Warsaw-basis SMEFT, *cf.* Sections 3.1 and 5.6.

Using these results we can rewrite Eq. (5.24) and Eq. (5.25) as

$$\begin{aligned}
\int d\Pi_{P'} \mathcal{M}^{P,\pi}_{\mu k} \bar{\mathcal{M}}^{P,\pi}_{\mu l} &= 2\, m_{\pi^\pm} \Gamma_{\pi\to\mu\nu} \frac{[\mathcal{P}U]_{\mu l} [U^\dagger \mathcal{P}^\dagger]_{k\mu}}{[\mathcal{P}\mathcal{P}^\dagger]_{\mu\mu}} \delta\Big(E_\nu - E_{\nu,\pi}\Big) , \\
\sum_m \int d\Pi_{P'} \mathcal{M}^{P,\mu}_{mk} \bar{\mathcal{M}}^{P,\mu}_{ml} &= 384\, \Gamma_{\mu\to e\bar{\nu}\nu} \left(\frac{E_\nu}{m_\mu}\right)^2 \left(\frac{1}{2} - \frac{E_\nu}{m_\mu}\right) \frac{\left[U^\dagger P_L^T \mathcal{P}_L^* U + p_{RR}\, U^\dagger P_R^T \mathcal{P}_R^* U\right]_{kl}}{\mathrm{Tr}\left(\mathcal{P}_L \mathcal{P}_L^\dagger + \mathcal{P}_R \mathcal{P}_R^\dagger\right)} , \\
\sum_m \int d\Pi_{P'} \mathcal{M}^{P,\mu}_{km} \bar{\mathcal{M}}^{P,\mu}_{lm} &= 128\, \Gamma_{\mu\to e\bar{\nu}\nu} \left(\frac{E_\nu}{m_\mu}\right)^2 \left(\frac{3}{4} - \frac{E_\nu}{m_\mu}\right) \frac{\left[U^\dagger P_L^* \mathcal{P}_L^T U + \bar{p}_{RR}\, U^\dagger P_R^* \mathcal{P}_R^T U\right]_{lk}}{\mathrm{Tr}\left(\mathcal{P}_L \mathcal{P}_L^\dagger + \mathcal{P}_R \mathcal{P}_R^\dagger\right)} .
\end{aligned} \tag{5.27}$$

The NP effects that appear in the numerators (involving the PMNS matrix) are those contributing directly to the production amplitudes in Eq. (5.24) and Eq. (5.25), whereas those in the denominators enter indirectly because they affect the pion and muon decay widths. We will

[8] For the sake of clarity we have written explicitly the sum over the (anti)neutrino of mass m_k instead of considering it implicit inside the integral sign.

[9] It is straightforward to see this implies $v_0^2 = v^2 \left(\mathrm{Tr}\left(\mathcal{P}_L \mathcal{P}_L^\dagger + \mathcal{P}_R \mathcal{P}_R^\dagger\right)\right)^{1/2}_{\mu\simeq m_\mu}$, which is consistent with the discussion after Eq. (5.4).

refer to these contributions as direct and indirect NP effects respectively.[10] We stress that both contributions appear at the same order and are generated by the same EFT operators, so it is not consistent to include only the direct piece.

5.2.3. Event rate

The total rate per recoil energy T and time t detected at COHERENT is given by:

$$\frac{dN}{dt\,dT} = N_T \int dE_\nu \left(R_\mu^\pi + R_e^\mu + \bar{R}_e^\mu\right) , \tag{5.28}$$

where R_μ^π and R_e^μ ($\bar{R}_e^\mu$) denote the event rates mediated by neutrinos produced in pion decay and by (anti)neutrinos produced in muon decays respectively. These three event rates are obtained plugging the results of Eq. (5.27) in Eq. (5.17). The integral over the neutrino energy is trivial in the pion-decay case since the neutrino energy is fixed, whereas for muon decay the lower integration limit is $E_\nu^{min}(T) = \frac{T}{2}\left(1+\sqrt{1+2\frac{m_\mathcal{N}}{T}}\right)$ (i.e. the minimum energy required to produce CEνNS with a recoil energy T) and the upper one is simply $m_\mu/2$. Working in the $L=0$ limit and separating the events in prompt (i.e. produced in pion decays) and delayed (i.e. produced in muon decays), we can rewrite Eq. (5.28) as

$$\frac{dN}{dt\,dT} = g_\pi(t)\,\frac{dN^{\text{prompt}}}{dT} + g_\mu(t)\,\frac{dN^{\text{delayed}}}{dT} , \tag{5.29}$$

where $g_{\pi,\mu}(t)$ encode the $N_{\pi,\mu}$ time dependences (normalized to one over each bunch cycle), as discussed at the beginning of Chapter 5.2. The prompt and delayed components are given by

$$\begin{aligned}
\frac{dN^{\text{prompt}}}{dT} &= n_{\text{POT}} f_{\nu/p}^\pi \frac{N_T\,\mathcal{F}(q^2)^2\,(m_\mathcal{N}+T)}{32\,\pi^2 v^4 L^2} f_\mu(T)\tilde{Q}_\mu^2 , \\
\frac{dN^{\text{delayed}}}{dT} &= n_{\text{POT}} f_{\nu/p}^\mu \frac{N_T\,\mathcal{F}(q^2)^2\,(m_\mathcal{N}+T)}{8\,\pi^2 v^4 L^2} \left(f_e(T)\,\tilde{Q}_e^2 + f_{\bar{\mu}}(T)\,\tilde{Q}_{\bar{\mu}}^2\right) .
\end{aligned} \tag{5.30}$$

The generalized squared charges $\tilde{Q}_f^2$ are defined as the following positive and target-dependent quantities[11]

$$\begin{aligned}
\tilde{Q}_\mu^2 &\equiv \frac{\left[\mathcal{P}\mathcal{Q}^2\mathcal{P}^\dagger\right]_{\mu\mu}}{\left(\mathcal{P}\mathcal{P}^\dagger\right)_{\mu\mu}} , \\
\tilde{Q}_e^2 &= \frac{\text{Tr}\left(\mathcal{P}_L^* \mathcal{Q}^2 P_L^T + \mathcal{P}_R^T \mathcal{Q}^2 P_R^*\right)}{\text{Tr}\left(\mathcal{P}_L\mathcal{P}_L^\dagger + \mathcal{P}_R\mathcal{P}_R^\dagger\right)} , \qquad \tilde{Q}_{\bar{\mu}}^2 \equiv \frac{\text{Tr}\left(\mathcal{P}_L^T \mathcal{Q}^2 P_L^* + \mathcal{P}_R^* \mathcal{Q}^2 P_R^T\right)}{\text{Tr}\left(\mathcal{P}_L\mathcal{P}_L^\dagger + \mathcal{P}_R\mathcal{P}_R^\dagger\right)} .
\end{aligned} \tag{5.31}$$

[10] Equivalently, indirect effects account for the NP contamination introduced through the extraction of v and $V_{ud} f_{\pi^\pm}$ from the experimental pion and muon decay widths.

[11] Let us note that the RR term in $\tilde{Q}_{\bar{\mu}}^2$ ($\tilde{Q}_e^2$) is generated by non-standard effects in ν-mediated ($\bar{\nu}$-mediated) events. Thus one should only identify the $f_{\bar{\mu}}\,\tilde{Q}_{\bar{\mu}}^2$ ($f_e\,\tilde{Q}_e^2$) terms in the delayed event rate with $\bar{\nu}$-mediated (ν-mediated) events if the RR contributions are zero. The same caveat holds for the flavor indices $\bar{\mu}$ and e used in those two terms, which only refer to the flavor of the mediating (anti)neutrino in the case of flavor-diagonal interactions in production (and no RR terms).

As for the $f_f(T)$ functions, their explicit expressions are:

$$\begin{aligned}
f_\mu(T) &= 1 - \frac{(m_\mathcal{N} + 2E_{\nu,\pi})\,T}{2E_{\nu,\pi}^2}\ , \\
f_{\bar{\mu}}(T) &= 16\left(\frac{E_\nu^3}{m_\mu^3} - \frac{E_\nu^4}{m_\mu^4} + \frac{4E_\nu^3 T}{3m_\mu^4} - \frac{3E_\nu^2 T}{2m_\mu^3} - \frac{3E_\nu m_\mathcal{N} T}{2m_\mu^3} + \frac{E_\nu^2 m_\mathcal{N} T}{m_\mu^4}\right)\Bigg|_{E_\nu^{min}(T)}^{m_\mu/2}\ , \\
f_e(T) &= 16\left(\frac{2E_\nu^3}{m_\mu^3} - \frac{3\,E_\nu^4}{m_\mu^4} + \frac{4E_\nu^3 T}{m_\mu^4} - \frac{3\,E_\nu^2 T}{m_\mu^3} - \frac{3\,E_\nu m_\mathcal{N} T}{m_\mu^3} + \frac{3\,E_\nu^2 m_\mathcal{N} T}{m_\mu^4}\right)\Bigg|_{E_\nu^{min}(T)}^{m_\mu/2}\ . \qquad (5.32)
\end{aligned}$$

Finally, the number of (anti)neutrinos produced per proton via pion (muon) decay, $f_{\nu/p}^{\pi(\mu)}$, are given by

$$\begin{aligned}
f_{\nu/p}^{\pi} &\equiv r_{\pi/p}\,\tau_\pi\,\Gamma_{\pi\to\mu\nu} = r_{\pi/p}\,BR(\pi\to\mu\nu)_{\rm exp} \approx r_{\pi/p}\ , \\
f_{\nu/p}^{\mu} &\equiv r_{\mu/p}\,\tau_\mu\,\Gamma_{\mu\to e\bar{\nu}\nu} = r_{\mu/p}\,BR(\mu\to e\bar{\nu}\nu)_{\rm exp}\ \approx r_{\mu/p}\ . \qquad (5.33)
\end{aligned}$$

Finally, the allowed values for the recoil energy are $T \in \{0, T_{max}^a\}$ where $T_{max}^{\rm prompt} = 2E_{\nu,\pi}^2/(m_N + 2E_{\nu,\pi})$ for prompt neutrinos and $T_{max}^{\rm delayed} = m_\mu^2/(2(m_\mu + M_N))$ for the delayed ones.

The prompt and delayed event rates in Eq. (5.30) represent one of the main results of this work, which is thus worth analyzing in some detail. First, let us note that the PMNS factors are not present anymore (they were removed using the unitarity condition $UU^\dagger = U^\dagger U = 1$), which means that COHERENT is not sensitive to the PMNS mixing angles and phases, as expected in an $L \approx 0$ experiment. Secondly, let us note that expressions for the rates in Eq. (5.30) are equal to the SM expressions except for the fact that the nuclear weak charge has been replaced by a generalized weak charge that (i) is different for muon neutrino, electron neutrino and muon antineutrino; and (ii) contains non-standard effects affecting detection *and* production. To put this in more explicit terms, we can re-write the prompt and delayed event rates as follows:

$$\begin{aligned}
\frac{dN^{\rm prompt}}{dT} &= N_T \int dE_\nu \frac{d\Phi_{\nu_\mu}}{dE_\nu}\frac{d\tilde{\sigma}_{\nu_\mu}}{dT}\ , \\
\frac{dN^{\rm delayed}}{dT} &= N_T \int dE_\nu \left(\frac{d\Phi_{\nu_e}}{dE_\nu}\frac{d\tilde{\sigma}_{\nu_e}}{dT} + \frac{d\Phi_{\bar{\nu}_\mu}}{dE_\nu}\frac{d\tilde{\sigma}_{\bar{\nu}_\mu}}{dT}\right)\ , \qquad (5.34)
\end{aligned}$$

where the fluxes are defined in the usual form:

$$\begin{aligned}
\frac{d\phi_{\nu_\mu}}{dE_\nu} &= \frac{N_{\nu_\mu}}{4\pi L^2}\delta(E_\nu - E_{\nu,\pi})\ , \\
\frac{d\phi_{\nu_e}}{dE_\nu} &= \frac{N_{\nu_e}}{4\pi L^2}\frac{192E_\nu^2}{m_\mu^3}\left(\frac{1}{2} - \frac{E_\nu}{m_\mu}\right)\ , \\
\frac{d\phi_{\bar{\nu}_\mu}}{dE_\nu} &= \frac{N_{\bar{\nu}_\mu}}{4\pi L^2}\frac{64E_\nu^2}{m_\mu^3}\left(\frac{3}{4} - \frac{E_\nu}{m_\mu}\right)\ , \qquad (5.35)
\end{aligned}$$

where

$$\begin{aligned}
N_{\nu_\mu} &= n_{\rm POT}\,r_{\pi/p}\,BR(\pi\to\mu\nu)_{\rm exp}\ , \\
N_{\bar{\nu}_\mu} &= N_{\nu_e} = n_{\rm POT}\,r_{\mu/p}\,BR(\mu\to e\bar{\nu}\nu)_{\rm exp}\ . \qquad (5.36)
\end{aligned}$$

As for the cross sections, they are also defined in the usual form but using the generalized charges $\tilde{Q}_f$, that is

$$\frac{d\tilde{\sigma}_f}{dT} = (m_{\mathcal{N}} + T)\frac{(\mathcal{F}(T))^2}{2v^4\,\pi}\left(1 - \frac{(m_{\mathcal{N}} + 2E_\nu)\,T}{2E_\nu^2}\right)\tilde{Q}_f^2\ . \tag{5.37}$$

Even though we started from very general premises, the final result is similar to the SM formulas and to the usual NSI expressions (with NP only in the detection side), except for the introduction of the generalized weak charges. This unexpected result makes the phenomenological analysis very simple, since it represents a simple modification with respect to the standard approach in the previous literature. The conceptual change is however much deeper and one should keep in mind that in our general analysis the generalized weak charges contain non-standard lepton flavor-violating effects affecting neutrino production. For instance, our general expression includes possible contributions through the process $\pi \to \mu\,\nu_\tau$, despite not having introduced a ν_τ flux in Eq. (5.34). Thus one should keep in mind that the event rate in Eq. (5.34) is just a practical parametrization, but the factorization in fluxes and cross section, as well as the subindices ν_μ, ν_e and $\bar{\nu}_\mu$, do not have physical meaning except in the SM case and some simple BSM scenarios.

In general, it is not possible to carry out a naive factorization of the event rate in Eq. (5.30) in fluxes and cross sections, since there is a matrix multiplication between production and detection quantities in the generalized squared charges $\tilde{Q}_f^2$ in Eq. (5.31). For simplicity let us consider the case of pion decay production and CEνNS detection, where one can easily see that $R_\mu^\pi \neq \sum_{\alpha\beta} d\Phi(\pi \to \mu\nu_\alpha)/(dE_\nu dt) \times d\sigma(\nu_\alpha\,\mathcal{N} \to \nu_\beta\,\mathcal{N})/dT$ simply because $\left[\mathcal{P}\mathcal{Q}^2\mathcal{P}^\dagger\right]_{\mu\mu} \neq \sum_{\alpha\beta} |\mathcal{P}_{\mu\alpha}|^2\,|\mathcal{Q}_{\alpha\beta}|^2$.

Before discussing some interesting specific cases, let us mention briefly how the analysis is modified if we consider different q^2-dependent form factors for neutron and proton, i.e., $\mathcal{F}_n(q^2) \neq \mathcal{F}_p(q^2) \neq$ const. In that case, the $\tilde{Q}_f^2$ parameters are not convenient objects to summarize experimental results, because they become q^2 dependent. In the COHERENT rate expression, the product of the weak charge matrix squared and the form factor squared, $\mathcal{Q}^2\,(\mathcal{F}(q^2))^2$, would be replaced by the matrices $(g^{\nu p})^2$, $(g^{\nu n})^2$, $g^{\nu p}g^{\nu n}$, and $g^{\nu n}g^{\nu p}$, accompanied by the appropriate powers of the $Z\mathcal{F}_p(q^2)$ and $(A-Z)\mathcal{F}_n(q^2)$ functions. Thus, we would go from 3 parameters per target ($\tilde{Q}^2_{f=e,\mu,\bar{\mu}}$) to 12 target-independent parameters. They are reduced to 9 parameters if the (production and detection) NP parameters are real, because the generalized squared charges obtained "replacing" $\mathcal{Q}^2$ with $g^{\nu p}g^{\nu n}$ and $g^{\nu n}g^{\nu p}$ are equal.

5.2.4. Interesting limits

SM limit. If all NP effects are switched off we recover the SM prediction, with a single nuclear weak charge

$$Q^2_{\rm SM} \equiv \tilde{Q}^2_\mu = \tilde{Q}^2_{\bar{\mu}} \simeq \tilde{Q}^2_e, \tag{5.38}$$

where

$$Q_{\rm SM} = Z[\mathcal{Q}^p_w]^{\rm SM}_{\mu\mu} + (A-Z)[\mathcal{Q}^n_w]^{\rm SM}_{\alpha\alpha} \tag{5.39}$$

and the nucleon weak charges are given in Eq. (5.11). Note that in principle the muon and electron weak charges have slightly different values, however the difference is irrelevant given the COHERENT accuracy, *cf.* Eq. (5.11). In our analysis we will take the muon weak charge as the reference value. The SM scenario has of course been thoroughly studied before [230, 256]. For each target nucleus there is a single quantity, Q_{SM}, to be extracted from experiment, which is predicted in the SM in function of the weak mixing angle. Thus, in the SM limit coherent

elastic neutrino-nucleus scattering can be regarded as a probe of the weak mixing angle, see e.g. [234, 247, 248, 260–262]. One should remark however that other probes, such as Z-pole physics, atomic parity violation, or parity-violating electron scattering have currently a much better sensitivity to the weak mixing angle.

New physics in production. We move to the case where new physics affects the COHERENT observables via neutrino production in pion and muon decay. The matrices $\mathcal{P}$ and $\mathcal{P}_{L,R}$, which encode these effects, are allowed to be completely generic. On the other hand, we assume here that we can ignore new physics in detection. This implies that the weak charge $\mathcal{Q}$ defined in Eq. (5.20) is proportional to the unit matrix and thus it commutes with $\mathcal{P}$ and $\mathcal{P}_{L,R}$. It then follows from Eq. (5.31) that the new physics production effects completely cancel out in the generalized weak charges, and we recover the SM limit in Eq. (5.38) with a single nuclear weak charge. All in all, COHERENT data are completely insensitive to new physics affecting only the CC semileptonic and leptonic WEFT operators due to cancellations between direct and indirect new physics effects. This observation invalidates the bounds found in Ref. [263], where the indirect NP effect was not taken into account.

A more intuitive way of understanding this null sensitivity is the following. The CC operators in Eq. (5.3) certainly affect the pion decay rate to muon and neutrino, but they do not distort the kinematics. Their effect has been fully absorbed into the experimental value of $\mathrm{BR}(\pi \to \mu\nu)$, which is used to calculate the neutrino flux. Moreover, in the particular case at hand $\mathrm{BR} \approx 1$, that is, $\sim$100% of the pions will decay to muon and neutrino for any reasonable values of $[\epsilon_{L,R,P}]_{\alpha\beta}$. Similarly, new leptonic operators in Eq. (5.4) affect the muon decay rate, but their effect has been fully absorbed into the experimental value of the Fermi constant.

Our work is the first one that takes into account the direct and indirect effects in production, as well as the possible cancellations. Let us stress however that new physics in production cannot be ignored completely: its effects do not cancel out if there are accompanying new physics effects in detection.

New physics in detection. If we neglect NP in production our expressions reduce to those found previously in the NSI literature [231, 232, 260], where two free parameters are present (instead of three). Namely

$$\begin{aligned}
\tilde{Q}_\mu^2 =& \tilde{Q}_{\tilde{\mu}}^2 = \left[\mathcal{Q}^2\right]_{\mu\mu} = \sum_\alpha |[\mathcal{Q}]_{\alpha\mu}|^2 = \sum_\alpha \left| Z g_{\alpha\mu}^{\nu p} + (A-Z) g_{\alpha\mu}^{\nu n} \right|^2 \\
=& 4 \sum_\alpha \left[(A+Z)(g_V^{uu}\,\mathbb{1} + \epsilon^{uu}) + (2A-Z)(g_V^{dd}\,\mathbb{1} + \epsilon^{dd}) \right]_{\alpha\mu}^2 , \\
\tilde{Q}_e^2 = & \left[\mathcal{Q}^2\right]_{ee} = \sum_\alpha |[\mathcal{Q}]_{\alpha e}|^2 = \sum_\alpha \left| \left(Z g_{\alpha e}^{\nu p} + (A-Z) g_{\alpha e}^{\nu n} \right) \right|^2 \\
=& 4 \sum_\alpha \left[(A+Z)(g_V^{uu}\,\mathbb{1} + \epsilon^{uu}) + (2A-Z)(g_V^{dd}\,\mathbb{1} + \epsilon^{dd}) \right]_{\alpha e}^2 .
\end{aligned} \tag{5.40}$$

Linear new physics terms. Finally, let us consider the case where only corrections linear in non-standard Wilson coefficients are kept. At this order, direct and indirect BSM effects in production cancel (even if there are NP in detection) and we arrive at a linearized version

of Eq. (5.40):

$$\begin{aligned} \tilde{Q}_\mu^2 &= \tilde{Q}_{\bar{\mu}}^2 = \left[\mathcal{Q}^2\right]_{\mu\mu} = Q_{SM}^2 + 2\,Q_{SM}\,[\delta\mathcal{Q}]_{\mu\mu}\ , \\ \tilde{Q}_e^2 &= \left[\mathcal{Q}^2\right]_{ee} = Q_{SM}^2 + 2\,Q_{SM}\,[\delta\mathcal{Q}]_{ee} \end{aligned} \tag{5.41}$$

where Q_{SM} is given in Eq. (5.39), and

$$\delta\mathcal{Q} = Z\,\delta g^{\nu p} + (A-Z)\,\delta g^{\nu n} = 2\Big((A+Z)\epsilon^{uu} + (2A-Z)\epsilon^{dd}\Big)\ , \tag{5.42}$$

where we defined $\delta g^{\nu N} \equiv g^{\nu N} - [g^{\nu N}]_{SM}$. That is, for a given target, COHERENT is linearly sensitive only to two linear combinations of the four WEFT Wilson coefficients: $\epsilon_{\mu\mu}^{uu}$, $\epsilon_{\mu\mu}^{dd}$, ϵ_{ee}^{uu}, and ϵ_{ee}^{dd}, which describe flavor-diagonal NC interactions between neutrinos and quarks.[12]

5.3. Experimental input

The COHERENT collaboration uses a series of detectors to detect neutrinos produced by the Spallation Neutron Source (Oak Ridge National Laboratory) through CEνNS. At this facility, high-energy protons with $E \sim 1$ GeV hit a mercury target to produce π^+ and π^-. The latter are absorbed, whereas the positive pions decay at rest into the *prompt* neutrinos and positive muons. The latter correspond to the source particles of the *delayed* (anti)neutrinos.

We will analyze the two available measurements of the CEνNS interaction performed by this experiment: one performed on a liquid argon target (LAr) [249] and another one using a target consisting of a mixture of cesium and iodine (CsI) [250]. These two measurements are complementary, allowing us to access slightly different combinations of WEFT WCs [264]. The input needed to calculate the number of prompt and delayed events for these two measurements through Eq. (5.30) is summarized in Table 5.1. The number of target particles N_T is obtained as the ratio of the active mass of the detector $m_{\rm det}$ and the mass of the interacting nuclei. For the CsI measurement, we treat cesium and iodine as a single nucleus with $(Z, A) = (54, 130)$. This will allow us to analyze CsI data in terms of only 3 charges (instead of 6) and we do not expect it to have any impact in the final bounds on the WEFT Wilson coefficients, since the atomic numbers for Cs and I are very similar (namely $Z_{Cs} = 55, Z_I = 53$).

Naively, one only has to integrate the expression in Eq. (5.30) over the recoil energy T in each bin to obtain the expected number of prompt/delayed events (for a given value of the generalized weak charges $\tilde{Q}_f$), that is

$$N_i^a = \int_{\rm i-th\,bin} \frac{dN^a}{dT}\,dT\ , \qquad (a = \text{prompt}, \text{delayed})\ . \tag{5.43}$$

However, this simple step needs to be modified to take into account various experimental effects. The first thing to consider is that COHERENT does not measure its events in nuclear recoil

[12] This statement depends on the definition of the WEFT coefficients and on the input scheme. In particular, if one uses v_0 (instead of v) in Eq. (5.1), then we would find that COHERENT is also linearly sensitive to the CC interaction $[\rho_L]_{e\mu\mu e}$ because of its effect on the muon decay, and hence on G_F (or v), which is used to calculate the CEνNS cross section. In our approach such effects have been absorbed inside the NC coefficients ϵ_{ll}^{qq}. Both approaches are of course equivalent, as can be seen explicitly when they are matched to the Warsaw-basis SMEFT, *cf.* Sections 3.1 and 5.6. Last, we note that this caveat also applies to the previous discussion about NP in production.

Table 5.1: Input used to calculate the differential number of prompt and delayed events dN/dT for each setup, taken directly from the corresponding experimental article. Following those references we approximate the number of pions and muons per proton to be equal $f_{\nu/p} \equiv f^{\pi}_{\nu/p} = f^{\mu}_{\nu/p}$.

Parameter	CsI [250]	LAr [249]
(Z, N)	$(54, 130)$	$(18, 40)$
$n_{\rm POT}$	31.98×10^{22}	13.77×10^{22}
$f_{\nu/p}$	0.0848	0.09
$m_{\rm det}$ (kg)	14.6	24.4
L (m)	19.3	27.5

energy (T), but in electron-equivalent recoil energy (T_{ee}). These two magnitudes are related as follows

$$T_{ee} = \mathrm{QF}(T) \times T \,, \tag{5.44}$$

where $\mathrm{QF}(T)$ is the so-called quenching factor, which depends on the detector and the recoil energy T, as we indicated explicitly. Moreover, one has to introduce an energy resolution function $\mathcal{R}(T^{\rm rec}_{ee}, T_{ee})$, which relates the true value of the electron-equivalent recoil energy, T_{ee}, with the reconstructed one, $T^{\rm rec}_{ee}$, that is registered at the detector. Finally, the efficiency of the detector, $\epsilon(T^{\rm rec}_{ee})$, should also be taken into account. These considerations are collected in the following modified expression for the number of prompt and delayed events in the i-th $T^{\rm rec}_{ee}$ bin [250, 265]

$$N^a_i = \int_{T^{{\rm rec},i}_{ee}}^{T^{{\rm rec},i+1}_{ee}} dT^{\rm rec}_{ee}\, \epsilon(T^{\rm rec}_{ee}) \int_{T_{\rm min}}^{T^a_{\rm max}} dT\, \mathcal{R}(T^{\rm rec}_{ee}, T_{ee}(T)) \frac{dN^a}{dT}\,(T) \,, \tag{5.45}$$

where a = prompt/delayed. The theoretical prediction for the (differential) number of events, dN^a/dT, is given in terms of the nuclear recoil energy T, as provided in Eq. (5.30). Note that we have expressed the energy resolution $\mathcal{R}(T^{\rm rec}_{ee}, T_{ee})$ in terms of T instead of T_{ee} by means of the QF. That way, the integral over T allows us to go from the nuclear recoil energy T to the reconstructed electron-equivalent recoil energy $T^{\rm rec}_{ee}$. The integration limits, the quenching factor and the efficiency and energy resolution functions that we use for each dataset are discussed in Appendix A.

Additionally, the CsI analysis presents the data in terms of the number of photoelectrons (PE) that are recorded for each event instead of using the electron-equivalent recoil energy. These two magnitudes are simply connected by $\mathrm{PE} = \mathrm{LY} \times T^{rec}_{ee}$, where the light yield LY is the number of PE produced by an electron recoil of one keV. Thus, the general expression in Eq. (5.45) holds also for CsI with the replacement $T^{rec}_{ee} \to \mathrm{PE}$.

Above we presented the expression for the prompt and delayed events, which have to be summed to provide the observed number of CEνNS events. Equivalently this result can be obtained integrating t in Eq. (5.29) over the entire bunch cycle and taking into account that the $g_a(t)$ functions are normalized to one. If instead one is interested in the double distribution in nuclear recoil energy T and time t, then we will have

$$N^{\rm signal}_{ij} \;=\; g^{\rm prompt}_j N^{\rm prompt}_i + g^{\rm delayed}_j N^{\rm delayed}_i \,, \tag{5.46}$$

where we introduced a second index j that refers to the j-th time bin. The g^a_j factors are the prompt/delayed probability distributions for the timing of the events (calculated integrating

the $g_a(t)$ functions over the j-th time bin), which can be extracted from the COHERENT publications, *cf.* Appendix A.

Finally, one also has to include background events and nuisance parameters to parametrize the most relevant uncertainty sources. Thus, the predicted number of events has the following generic form

$$N_{ij}^{\rm th}\left(\vec{Q}^2_{\mathcal{N}};\vec{x}\right) = N_{ij}^{\rm signal}\left(\vec{Q}^2_{\mathcal{N}}\right)\left(1+h_{ij}^{\rm signal}(\vec{x})\right) + \sum_a N_{ij}^{{\rm bkg},a}\left(1+h_{ij}^{{\rm bkg},a}(\vec{x})\right)\ , \tag{5.47}$$

where we have indicated explicitly the dependence of the expected number of CEνNS events on the generalized squared weak charges for the nucleus $\mathcal{N}$, denoted by $\vec{Q}^2_{\mathcal{N}} \equiv \{\tilde{Q}^2_\mu, \tilde{Q}^2_{\bar{\mu}}, \tilde{Q}^2_e\}$. These charges can hold all the NP effects that can be parametrized with the WEFT or any NSI model, so they represent the most suitable target for our numerical analysis [246, 264]. The expected number of background events of type a, denoted by $N_{ij}^{{\rm bkg},a}$, is obtained following COHERENT prescriptions, as described in detail in Appendix A. The typical background sources are the steady state (SS) background, the neutrino-induced neutron (NIN) background and the beam-related neutron (BRN) background, although the way each of them is characterized differs slightly in every measurement. Finally, the $h_{ij}^{{\rm signal/bkg},a}(\vec{x})$ functions are linear in the nuisance parameters $\vec{x}$ and vanish at their central values $\vec{x} = \vec{0}$. The specific form of these functions for each experimental analysis is given in Appendix A following once again the COHERENT prescription. The LAr analysis features 14 systematic sources, while the CsI analysis deals with just 6 of them. Out of all these uncertainties, in the two measurements the most important one for the CEνNS signal is that of the neutrino flux, while the most impactful background source is BRN. However, in both cases the dominating error is statistical, far outclassing the contributions from all other sources to the total error.

In our numerical analysis we use the 2D distributions (in time and recoil) measured in the CsI and Ar works [249, 250]. For each of these two datasets we work with a Poissonian chi-squared function with the following generic form

$$\chi^2 = \sum_{i,j} 2 \quad \left(-N_{ij}^{\rm exp} + N_{ij}^{\rm th}\left(\vec{Q}^2_{\mathcal{N}};\vec{x}\right) + N_{ij}^{\rm exp}\ \ln\left(\frac{N_{ij}^{\rm exp}}{N_{ij}^{\rm th}\left(\vec{Q}^2_{\mathcal{N}};\vec{x}\right)}\right)\right) + \sum_n \left(\frac{x_n}{\sigma_n}\right)^2 , \tag{5.48}$$

where σ_n is the uncertainty of the x_n nuisance parameter. All in all we have 52x12 bins in CsI and 4x10 bins in LAr, *cf.* Appendix A for further details.

5.4. Generalized nuclear weak charges analysis

In this section we present the results of the analysis of LAr and CsI data in terms of the generalized nucleus-dependent weak charges $\tilde{Q}_f$. Since the event rate depends quadratically on these charges, it is convenient to work with their squared values $\tilde{Q}^2_f$.

5.4.1. Argon charges

We carry out a 2D fit to the nuclear recoil energy and time distributions, as described in the previous section. This fit has 40 experimental inputs (with their associated uncertainties and backgrounds), 9 nuisance parameters (with their uncertainties) and the three $\tilde{Q}^2_f$ charges that

contain the UV information. We find that the distribution of these three charges is approximately Gaussian, with the following results:[13]

$$\begin{pmatrix}\tilde{Q}^2_\mu\\ \tilde{Q}^2_{\bar{\mu}}\\ \tilde{Q}^2_e\end{pmatrix}_{\rm Ar}\frac{1}{Q^2_{\rm SM,Ar}}=\begin{pmatrix}1.00\pm0.82\\ 0.4\pm6.2\\ 1.9\pm8.2\end{pmatrix}\qquad \rho=\begin{pmatrix}1 & 0.29 & -0.31\\ 0.29 & 1 & -0.99\\ -0.31 & -0.99 & 1\end{pmatrix}\,, \tag{5.49}$$

along with the nine nuisance parameters that we do not display. We have normalized the results using the SM value, $\mathcal{Q}^2_{\rm SM,Ar}=461$, with an associated small error that can be neglected for the purpose of this work. The results in Eq. (5.49) are in perfect agreement with the SM prediction $\tilde{Q}^2_f/Q^2_{SM}=1$. We can disentangle the first charge, $\tilde{Q}^2_\mu$, from the other two thanks to its different time dependence: the former enters the rate via (prompt) pion decay, while the latter do it via (delayed) muon decay. On the other hand the recoil energy distribution only allows for a mild separation of $\tilde{Q}^2_e$ and $\tilde{Q}^2_{\bar{\mu}}$. To get rid of the large correlations, which obscure the strength of the results, let us rewrite them as the following uncorrelated bounds

$$\begin{pmatrix}-0.14 & -3.48 & 4.62\\ -0.69 & 0.98 & 0.71\\ 0.55 & 0.25 & 0.20\end{pmatrix}\begin{pmatrix}\tilde{Q}^2_\mu\\ \tilde{Q}^2_{\bar{\mu}}\\ \tilde{Q}^2_e\end{pmatrix}_{\rm Ar}\frac{1}{Q^2_{\rm SM,Ar}}=\begin{pmatrix}6\pm59\\ \mathbf{1.0\pm1.2}\\ \mathbf{1.03\pm0.48}\end{pmatrix}\,, \tag{5.50}$$

where we have highlighted the most stringent constraints (note that the SM prediction is one by construction). A particularly interesting case is the SM supplemented by the following contributions: $\tilde{Q}^2_\mu=\tilde{Q}^2_{\bar{\mu}}=\left[\mathcal{Q}^2\right]_{\mu\mu}$ and $\tilde{Q}^2_e=\left[\mathcal{Q}^2\right]_{ee}$, which is the most general setup that we can have when considering NP only at detection or in a linear analysis (see Section 5.2.4). In this case we find:

$$\begin{pmatrix}\left[\mathcal{Q}^2\right]_{\mu\mu}\\ \left[\mathcal{Q}^2\right]_{ee}\end{pmatrix}_{\rm Ar}\frac{1}{Q^2_{\rm SM,Ar}}=\begin{pmatrix}1.02\pm0.81\\ 1.1\pm1.9\end{pmatrix}\qquad \rho=\begin{pmatrix}1 & -0.68\\ -0.68 & 1\end{pmatrix}\,, \tag{5.51}$$

which can be rewritten as the following uncorrelated bounds:

$$\begin{aligned}-0.48\left(\left[\mathcal{Q}^2\right]_{\mu\mu}/Q^2_{SM}\right)_{\rm Ar}+1.48\left(\left[\mathcal{Q}^2\right]_{ee}/Q^2_{SM}\right)_{\rm Ar}&=1.1\pm3.0\,,\\ 0.75\left(\left[\mathcal{Q}^2\right]_{\mu\mu}/Q^2_{SM}\right)_{\rm Ar}+0.25\left(\left[\mathcal{Q}^2\right]_{ee}/Q^2_{SM}\right)_{\rm Ar}&=\mathbf{1.03\pm0.45}.\end{aligned} \tag{5.52}$$

The results of this 2D fit are shown in the left panel of Fig. 5.1, where we also present the allowed regions if one only uses the total number of events, the energy distribution or the time distribution.

Finally in the SM scenario there is only one weak charge ($\tilde{Q}^2_\mu=\tilde{Q}^2_{\bar{\mu}}=\tilde{Q}^2_e\equiv Q^2$), and we find $\left(Q^2/Q^2_{SM}\right)_{\rm Ar}=1.03\pm0.45$.

5.4.2. CsI charges

We have carried out a fit to the 2D distributions (nuclear recoil energy and time) provided in the CsI analysis. This fit has 624 experimental inputs (with their associated uncertainties and

[13]The squared charges have to be positive. Our results are approximately Gaussian (before imposing this prior) so we will present them in the usual form, i.e., central values, diagonal errors, and correlation matrix. It is straightforward to impose the $\tilde{Q}^2_f\geq0$ constraint a posteriori. This will induce a large non-Gaussianity if and only if the (Gaussian) errors are large.

backgrounds), 4 nuisance parameters (with their uncertainties) and the three CsI generalized weak charges. Once again we find that the distribution of the $\tilde{Q}_f^2$ charges is approximately Gaussian, with the following results:

$$\begin{pmatrix} \tilde{Q}_\mu^2 \\ \tilde{Q}_{\bar{\mu}}^2 \\ \tilde{Q}_e^2 \end{pmatrix}_{\rm CsI} \frac{1}{Q^2_{\rm SM,CsI}} = \begin{pmatrix} 1.33 \pm 0.35 \\ -1.4 \pm 1.5 \\ 4.4 \pm 2.3 \end{pmatrix} \quad \rho = \begin{pmatrix} 1 & 0.12 & -0.09 \\ 0.12 & 1 & -0.98 \\ -0.09 & -0.98 & 1 \end{pmatrix} , \tag{5.53}$$

along with the nuisance parameters. Here, $Q^2_{\rm SM,CsI} = 5572$. As in the LAr case, we can separate much better $\tilde{Q}_\mu^2$ from the other two charges thanks to the use of the time information. The results can be rewritten as the following uncorrelated bounds:

$$\begin{pmatrix} -0.04 & -1.80 & 2.85 \\ 0.80 & 0.12 & 0.09 \\ -0.15 & 0.71 & 0.45 \end{pmatrix} \begin{pmatrix} \tilde{Q}_\mu^2 \\ \tilde{Q}_{\bar{\mu}}^2 \\ \tilde{Q}_e^2 \end{pmatrix}_{\rm CsI} \frac{1}{Q^2_{\rm SM,CsI}} = \begin{pmatrix} 15.1 \pm 9.1 \\ \mathbf{1.28 \pm 0.28} \\ \mathbf{0.81 \pm 0.19} \end{pmatrix} , \tag{5.54}$$

where we find again good agreement with the SM predictions (one).

Considering only NP at detection we find

$$\begin{pmatrix} [\mathcal{Q}^2]_{\mu\mu} \\ [\mathcal{Q}^2]_{ee} \end{pmatrix}_{\rm CsI} \frac{1}{Q^2_{\rm SM,CsI}} = \begin{pmatrix} 1.32 \pm 0.34 \\ 0.44 \pm 0.61 \end{pmatrix} \quad \rho = \begin{pmatrix} 1 & -0.73 \\ -0.73 & 1 \end{pmatrix} , \tag{5.55}$$

which can be re-written as the following uncorrelated bounds:

$$\begin{aligned} -0.84 \left([\mathcal{Q}^2]_{\mu\mu} / Q^2_{SM} \right)_{\rm CsI} + 1.84 \left([\mathcal{Q}^2]_{ee} / Q^2_{SM} \right)_{\rm CsI} &= (\mathbf{-0.3 \pm 1.4}) , \\ 0.69 \left([\mathcal{Q}^2]_{\mu\mu} / Q^2_{SM} \right)_{\rm CsI} + 0.31 \left([\mathcal{Q}^2]_{ee} / Q^2_{SM} \right)_{\rm CsI} &= (\mathbf{1.04 \pm 0.16}) . \end{aligned} \tag{5.56}$$

The results of this 2D fit are shown in the right panel of Fig. 5.1. We present as well the allowed regions if one uses only the total number of events, the energy distribution or the time distribution. Finally, we also show the result obtained using the full 2D distribution of the first CsI dataset [225], which is in good agreement with Fig. 6 in Ref. [243]. One observes a clear improvement when the entire CsI dataset is used.

Finally in the SM scenario there is only one weak charge ($\tilde{Q}_\mu^2 = \tilde{Q}_{\bar{\mu}}^2 = \tilde{Q}_e^2 \equiv Q^2$), and we find $\left(Q^2/Q^2_{SM}\right)_{\rm CsI} = 1.04 \pm 0.16$.

5.5. WEFT coefficients analysis

In this section we move on to consider the constraints on the nucleon- and quark-level EFT Wilson coefficients, stemming from our analysis of LAr and CsI CEνNS data.

5.5.1. Linear BSM expansion

As shown in Eq. (5.41), at linear order in New Physics there are only 2 free parameters per target: the flavor-diagonal muon and electron weak charges, $[\mathcal{Q}^2]^{\mathcal{N}}_{\mu\mu,ee}$. Using Eq. (5.42) we can express our bounds on the four weak charges (with $\mathcal{N}$ = Ar, CsI, see Eqs. (5.51) and (5.55)) as

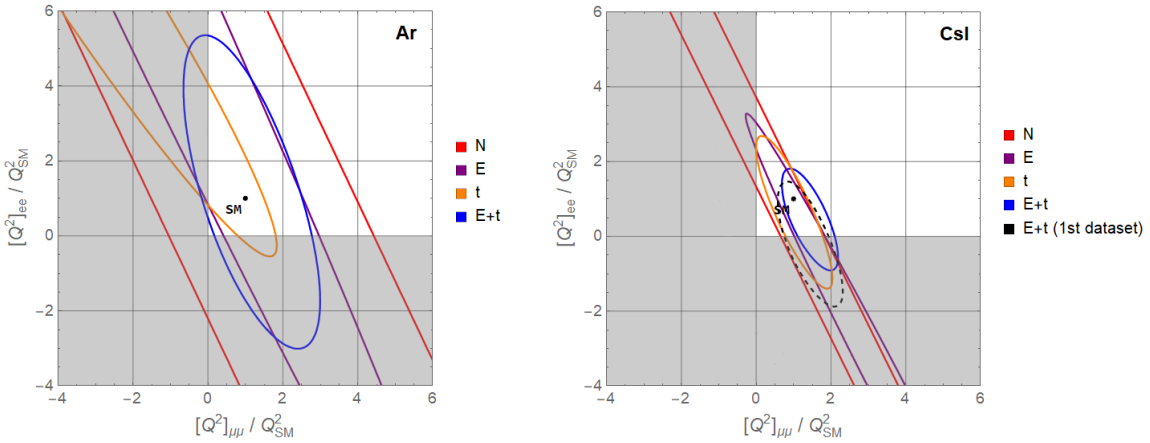

Fig. 5.1: 90% CL allowed regions ($\Delta\chi^2 = 4.61$) for the squared weak charges (normalized to their SM values) using Ar (left) and CsI (right) data and assuming only NP at detection. For each dataset we include information from the total number of events (N), from the recoil energy distribution (E), from the timing distribution (t) and from the 2D distribution (E+t). In the right panel we also show the contour obtained using only the first CsI dataset [225]. The shaded area indicates the unphysical region (negative squared charges).

bounds on the four nucleon-level EFT Wilson coefficients $\delta g^{\nu p}_{ee,\mu\mu}$ and $\delta g^{\nu n}_{ee,\mu\mu}$. We find that we can constrain the following orthogonal and uncorrelated linear combinations of couplings:

$$\begin{pmatrix} 0.55 & -0.19 & -0.77 & 0.26 \\ -0.18 & -0.56 & 0.26 & 0.76 \\ 0.74 & -0.32 & 0.53 & -0.24 \\ 0.32 & 0.74 & 0.23 & 0.54 \end{pmatrix} \begin{pmatrix} \delta g^{\nu p}_{ee} \\ \delta g^{\nu p}_{\mu\mu} \\ \delta g^{\nu n}_{ee} \\ \delta g^{\nu n}_{\mu\mu} \end{pmatrix} = \begin{pmatrix} 4 \pm 12 \\ 0.5 \pm 3.4 \\ 0.22 \pm 0.25 \\ -0.021 \pm 0.079 \end{pmatrix} . \tag{5.57}$$

At the quark level, using the map in Eq. (5.9), we can translate these results into constraints on the following orthogonal and uncorrelated linear combinations of WEFT Wilson coefficients:

$$\begin{pmatrix} 0.63 & -0.70 & -0.22 & 0.24 \\ 0.21 & -0.24 & 0.63 & -0.70 \\ -0.68 & -0.61 & 0.30 & 0.27 \\ 0.30 & 0.27 & 0.68 & 0.61 \end{pmatrix} \begin{pmatrix} \epsilon^{dd}_{ee} \\ \epsilon^{uu}_{ee} \\ \epsilon^{dd}_{\mu\mu} \\ \epsilon^{uu}_{\mu\mu} \end{pmatrix} = \begin{pmatrix} 2.0 \pm 5.7 \\ -0.2 \pm 1.7 \\ -0.037 \pm 0.042 \\ -0.004 \pm 0.013 \end{pmatrix} . \tag{5.58}$$

The last two constraints in Eq. (5.58) are not expected to change with the inclusion of quadratic corrections[14] and they represent another central result of this chapter. Once again, their errors are Gaussian to a good approximation and the application of these EFT constraints to more specific setups is straightforward.

We stress that we did not neglect NP affecting production, as usually done in the past literature. Instead, we showed that, with our Lagrangian input choice, they are absent at this order in the EFT expansion.

To get a grasp of the sensitivity of the COHERENT data sets to these NP couplings, we show in Fig. 5.2 how the predicted event distributions change in the presence of the WEFT Wilson coefficients.

[14]This is true in the vicinity of the SM value. For large ϵ^{qq}_{ll} values one can find new allowed regions, the so-called dark solutions.

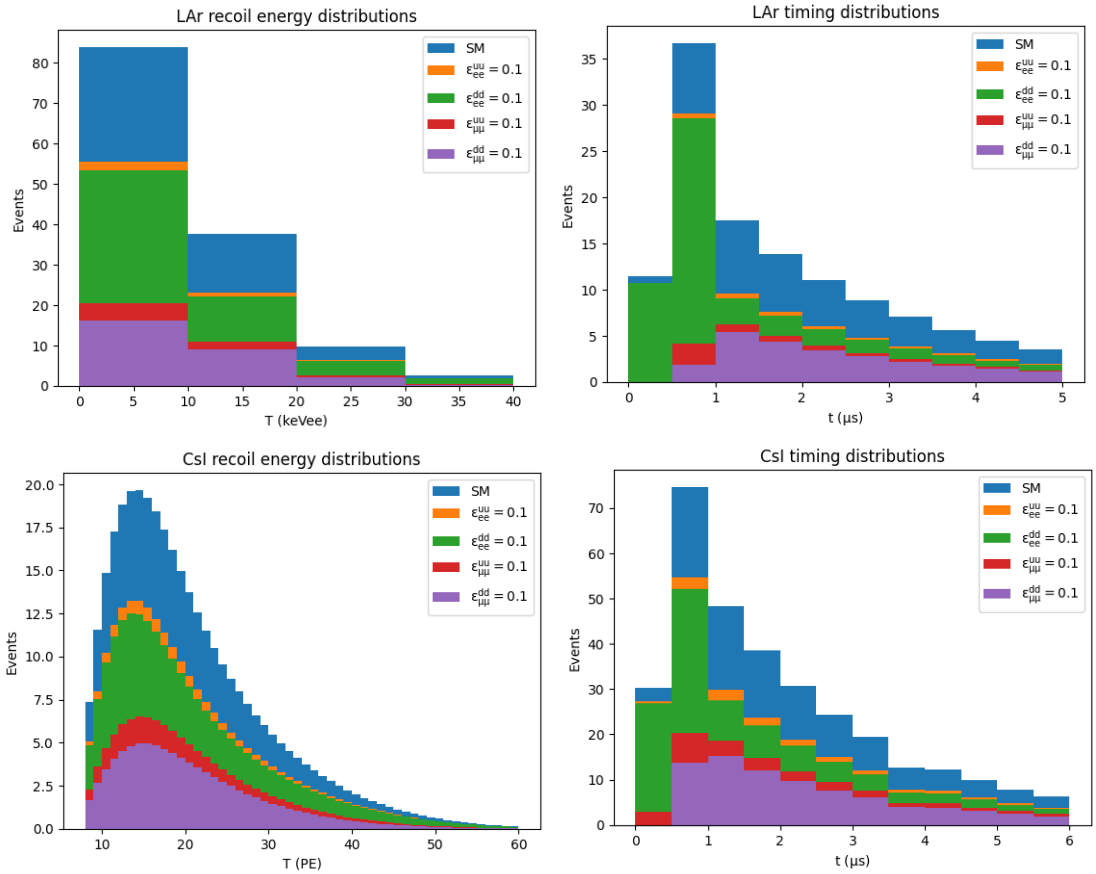

Fig. 5.2: Comparison of the predicted event distributions in recoil energy and time for the LAr (top) and CsI (bottom) nuclear target measurements in the presence of different WEFT operators at linear level in the BSM expansion.

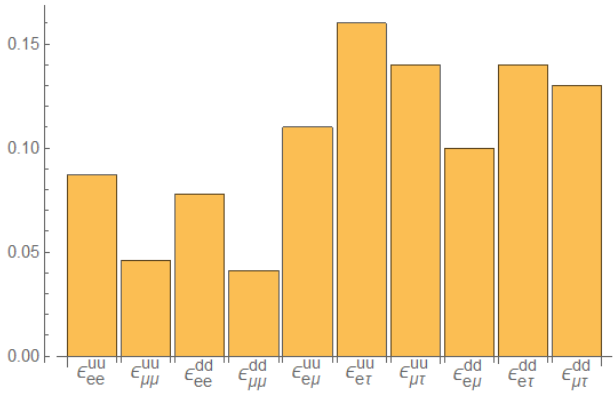

Fig. 5.3: 90% CL one-at-a-time limits for the absolute value of the NSIs probed by COHERENT.

It is interesting to discuss the results in a more constrained WEFT scenario when lepton-flavor universality of the relevant Wilson coefficients is assumed: $\epsilon_{\mu\mu}^{uu} = \epsilon_{ee}^{uu} \equiv \epsilon_u$ and $\epsilon_{\mu\mu}^{dd} = \epsilon_{ee}^{dd} \equiv \epsilon_d$. Then the 4-parameter fit in Eq. (5.58) reduces to the two-parameter one:

$$\epsilon_u = -0.01 \pm 0.98, \qquad \epsilon_d = 0.01 \pm 0.88, \tag{5.59}$$

with the highly degenerate correlation coefficient $\rho = -0.99988$. Disentangling the correlation one finds one strong constraint:

$$0.67\epsilon_u + 0.74\epsilon_d = -\,0.002 \pm 0.010, \tag{5.60}$$

while the orthogonal combination is very loosely constrained: $0.74\epsilon_u - 0.67\epsilon_d = 0.0 \pm 1.3$.

The results above lead to weak and effectively meaningless marginalized constraints on $\delta g_{\ell\ell}^{\nu N}$ and $\epsilon_{\ell\ell}^{qq}$ because only two of the constraints have uncertainties $\lesssim \mathcal{O}(1)$, where the linear expansion makes sense. The situation changes when only one operator is present, which leads to stringent and reliable individual limits:

$$\begin{pmatrix} \epsilon_{ee}^{dd} \\ \epsilon_{ee}^{uu} \\ \epsilon_{\mu\mu}^{dd} \\ \epsilon_{\mu\mu}^{uu} \end{pmatrix} = \begin{pmatrix} 0.011 \pm 0.036 \\ 0.012 \pm 0.040 \\ -0.008 \pm 0.019 \\ -0.008 \pm 0.022 \end{pmatrix} . \tag{5.61}$$

5.5.2. Nonlinear effects

In this section we take into account the full expression for the COHERENT event rate, including nonlinear terms in the new physics Wilson coefficients, and discuss how this changes the results compared to the linear analysis. For simplicity, we start by discussing the impact of nonlinear effects in analyses where only one operator at a time is present.

As expected, the linear bounds presented in Eq. (5.61) for the neutral-current Wilson coefficients, $\epsilon_{\alpha\alpha}^{qq}$, are barely affected by nonlinear terms, *cf.* Table 5.2. The only qualitative difference is the presence of dark solutions placed far away from the SM values (which are not shown in Table 5.2). They appear because COHERENT is only sensitive to the squared charges $\tilde{Q}_\alpha^2$, and so there are allowed regions near the $\pm Q_{SM}$ values.

Table 5.2: One-at-a-time bounds on neutrino NSIs. The second column shows the central value (CV) and their associated 1-sigma errors. The last column shows the 90% C.L. bound for the absolute value of the associated Wilson coefficient (WC), $|\epsilon^{qq}_{\alpha\beta}|$.

Flavor diagonal NSI		
WC	CV $\pm$ 1σ	90% C.L.
ϵ^{dd}_{ee}	$0.012^{+0.045}_{-0.035}$	0.097
ϵ^{uu}_{ee}	$0.013^{+0.050}_{-0.039}$	0.11
$\epsilon^{dd}_{\mu\mu}$	$-0.007^{+0.020}_{-0.018}$	0.036
$\epsilon^{uu}_{\mu\mu}$	$-0.008^{+0.022}_{-0.020}$	0.040

Flavor off-diagonal NSI		
WC	CV $\pm$ 1σ	90% C.L.
$\epsilon^{uu}_{e\mu}$	$\pm\left(0.031^{+0.053}_{-0.114}\right)$	0.10
$\epsilon^{uu}_{e\tau}$	0 ± 0.11	0.15
$\epsilon^{uu}_{\mu\tau}$	$\pm\left(0.057^{+0.052}_{-0.167}\right)$	0.13
$\epsilon^{dd}_{e\mu}$	$\pm\left(0.027^{+0.048}_{-0.103}\right)$	0.094
$\epsilon^{dd}_{e\tau}$	0 ± 0.098	0.13
$\epsilon^{dd}_{\mu\tau}$	$\pm\left(0.052^{+0.047}_{-0.150}\right)$	0.12

On the other hand, nonlinear terms give us access to NC flavor-changing operators, $\epsilon^{qq}_{\alpha\beta}$ ($\alpha \neq \beta$), which only enter the event rate at quadratic order in NP. The corresponding results, obtained putting one operator at a time, can be found in Table 5.2.[15] They are also compared with the flavor-diagonal ones in Fig. 5.3. Let us stress that, with our definition of the WEFT coefficients and input parameters, the effect of charged-current operators cancels in the rate (at all orders) if only one operator at a time is considered, as discussed in Chapter 5.2.4.

Let us now discuss some cases where more than one operator is present at the same time. In Figs. 5.4 and 5.5 we consider scenarios with two free NP parameters, with the remaining ones set to zero. A quick glance reveals that the CsI data drives the constraining power of the fit in all cases.

Comparing the upper two panels, we can see that the fit with only electron couplings yields noticeably weaker constraints than the one with muon parameters. This is to be expected since the contribution to the event rate coming from the muonic neutrinos is larger than the one coming from the electronic ones. We see that the CsI data is precise enough to separate the allowed region in two bands: one compatible with the SM and a second one corresponding to the above-mentioned dark solution. The well-known blind directions that these panels display is due to the cancellations among the linear combinations of up- and down-quark couplings in the weak charges, namely $(A+Z)\epsilon^{uu}_V + (2A-Z)\epsilon^{dd}_V = \text{constant}$, *cf.* Eq. (5.40). Since the blind directions are almost parallel for CsI and Ar, the combined dataset also shows this feature.

The second row in Fig. 5.4 studies the cases where neutrinos are coupled only to down quarks and only to up quarks. In these fits we have NP in both the electron and muon charges and thus there are four solutions, corresponding to $([\mathcal{Q}]_{ee} = \pm Q_{SM}, [\mathcal{Q}]_{\mu\mu} = \pm Q_{SM})$. Current COHERENT data is only able to separate the upper two dark solutions, whereas a third dark solution remains connected with the SM one. Adding CEνNS measurements at reactors isolates the SM solution [246].

[15] In this work we have assumed that all Wilson coefficients are real. However, our one-at-a-time bounds on lepton-flavor off-diagonal coefficients are trivially generalized to bounds on their modulus squared if they are complex, since they do not interfere with the SM contributions.

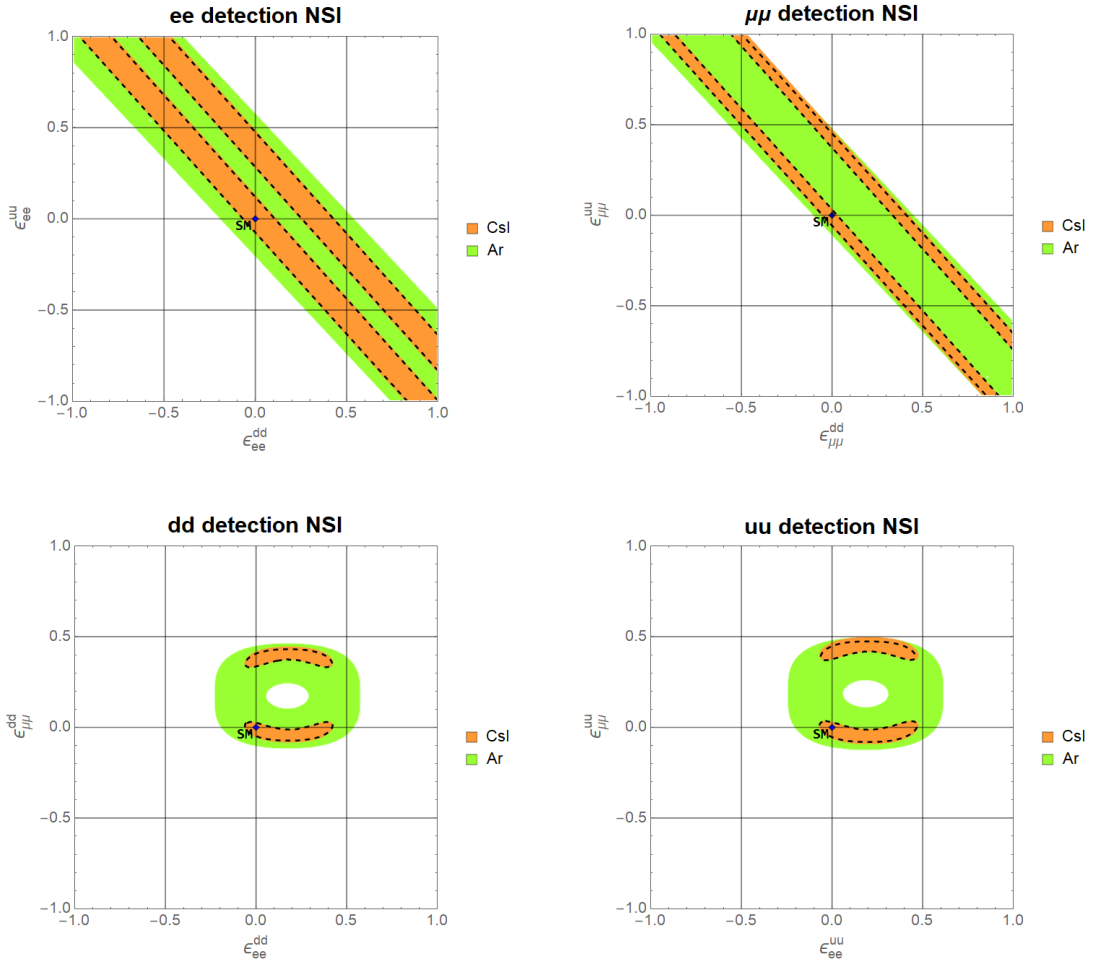

Fig. 5.4: $\Delta\chi^2 = 4.61$ regions for flavor-preserving Wilson coefficients as probed by COHERENT data. In each of the upper four panels the two Wilson coefficients displayed are the only non-zero NSI parameters. We display the bounds that the CsI and Ar datasets yield separately and the combination of the two through dashed lines.

Finally, Fig. 5.5 shows the lepton-universal case, where all four couplings are present, but electron and muon couplings are equal. The result is similar to the upper plots in Fig. 5.4, but with a larger sensitivity.

The scenarios that we have discussed above have been thoroughly discussed in previous works using different COHERENT datasets and projections [233, 234, 237, 240, 241, 243–247]. This analysis together with the recent work of Ref. [248] are the first ones to use the entire COHERENT dataset presently available (2D distribution in LAr and CsI) [249, 250] to constrain NSI coefficients, and thus represent the current state of the art. Since the CsI detector has been decommissioned, they represent the final results with that target. Previous works have studied these NP scenarios using the SM fluxes and modified cross sections. Our more general approach reduces to this "factorized" NSI description if one neglects NP effects in production, as discussed in Chapter 5.2.4. Our numerical results for the separated LAr and CsI analyses agree well with previous works, including COHERENT analyses [249, 250]. Our combined bounds (LAr+CsI) are also in good agreement with the recent results in Ref. [248].

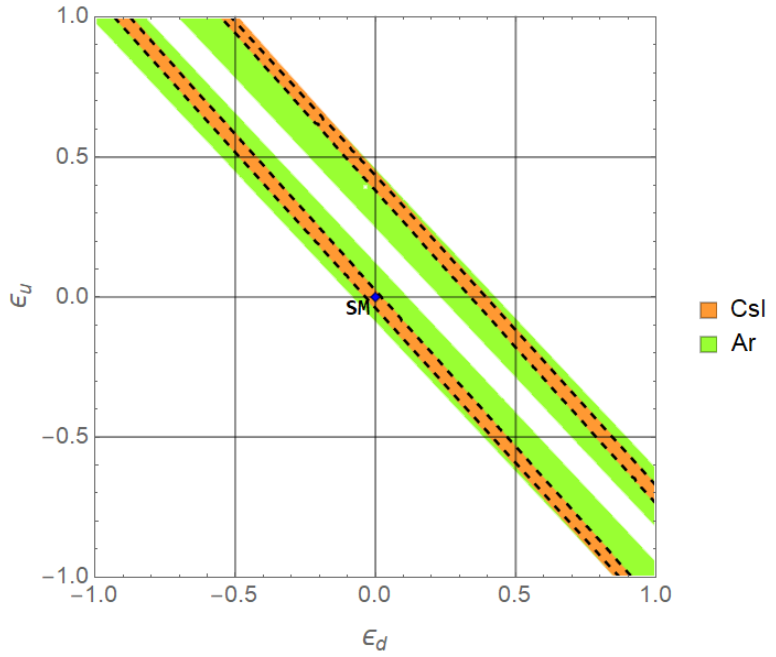

Fig. 5.5: $\Delta\chi^2 = 4.61$ regions for flavor-preserving Wilson coefficients as probed by COHERENT data assuming lepton universality: $\epsilon^{uu}_{\mu\mu} = \epsilon^{uu}_{ee} \equiv \epsilon_u$ and $\epsilon^{dd}_{\mu\mu} = \epsilon^{dd}_{ee} \equiv \epsilon_d$. We display the bounds that the CsI and Ar datasets yield separately and the combination of the two through dashed lines.

Let us now compare our COHERENT results with other NSI probes, which were reviewed and compiled in Ref. [266]. For simplicity we focus on bounds obtained switching on one operator at a time. For the muonic couplings, $\epsilon^{dd}_{\mu\mu}$ and $\epsilon^{uu}_{\mu\mu}$, the bounds obtained from COHERENT data match the best existing constraints, which come from atmospheric and accelerator neutrino data [267]. For the electronic couplings, ϵ^{dd}_{ee} and ϵ^{uu}_{ee}, our COHERENT results are much stronger than the limits extracted from CHARM data [268] and comparable to those obtained from Dresden-II reactor data [246, 269]. For the flavor-violating NSIs, our results for $\epsilon^{qq}_{\mu\tau}$ are roughly $20\times$ weaker than those obtained from IceCube [270]. Finally, our one-at-a-time bounds on $\epsilon^{qq}_{e\mu}$ coefficients from COHERENT data are roughly two times weaker than those obtained in a global fit to oscillation data [243], whereas for the $\epsilon^{qq}_{e\tau}$ coefficients they are similar. The relatively weak sensitivity from our analysis to off-diagonal NSIs is to be expected since oscillation observables are linearly sensitive to them, whereas CEνNS is only quadratically sensitive. On the other hand, CEνNS is best suited to study flavor-conserving NSIs, with interesting synergies observed in combined analyses with oscillation data [243].

5.5.3. Production and detection effects together

Our general approach allows us to go beyond the well-known cases discussed above, and study situations where NP effects are present both in production and detection.

For instance, we can study a setup where the NC coefficient $\epsilon^{dd}_{\mu\tau}$ is accompanied by the CC semileptonic Wilson coefficient $\epsilon^{ud}_{\mu\tau} \equiv [\epsilon^{ud}_L]_{\mu\tau}$. The latter affects neutrino production (it generates $\pi \to \mu\,\nu_\tau$), whereas the former affects the detection of muon and tau (anti)neutrinos (it generates $\nu_\mu\,\mathcal{N} \to \nu_\tau\,\mathcal{N}$, $\nu_\tau\,\mathcal{N} \to \nu_\mu\,\mathcal{N}$ and likewise for antineutrinos). Fig. 5.6 (left panel) shows the allowed regions when both parameters are present at the same time. Let us stress

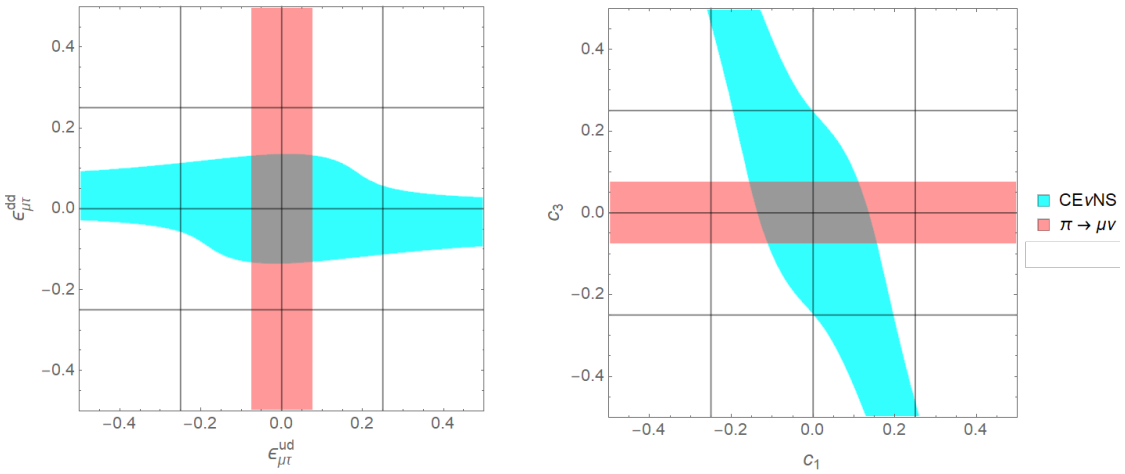

Fig. 5.6: 90% CL allowed regions for NP setups with flavor-violating Wilson coefficients in production and detection from the WEFT (left panel) and from the SMEFT (right panel) as probed by COHERENT data. In these fits only two couplings are allowed to be present at a time. Finally, we also include the constraint from the ratio $\Gamma(\pi \to e\nu)/\Gamma(\pi \to \mu\nu)$ [153, 271, 272].

once again that in our formalism these bounds are obtained without introducing a ν_τ flux. As explained in Section 5.2.3, one would obtain different (and thus incorrect) results if one calculates the event rate in a flux-times-cross-section factorized form. Namely, one would lose all sensitivity to the $\epsilon_{\mu\tau}^{ud}$ parameter.

The study of simultaneous NP effects in neutrino production and detection is particularly relevant in setups with explicit electroweak symmetry, since neutrinos and charged leptons form $SU(2)_L$ gauge doublets. As a result, non-standard contributions to $\nu_\alpha \mathcal{N} \to \nu_\beta \mathcal{N}$ come in general with non-standard effects in leptonic pion decay, $\pi \to \nu_\alpha \ell_\beta$. Let us consider for instance the SMEFT operators $[\mathcal{O}_{lq}^{(3)}]_{\mu\tau 11} \equiv (\bar{l}_L^2 \gamma_\mu \sigma^k l_L^3)(\bar{q}_L^1 \gamma^\mu \sigma^k q_L^1)$ and $[\mathcal{O}_{lq}^{(1)}]_{\mu\tau 11} \equiv (\bar{l}_L^2 \gamma_\mu l_L^3)(\bar{q}_L^1 \gamma^\mu q_L^1)$ (along with their conjugates so that the Lagrangian is Hermitian), and let us abbreviate their associated Wilson coefficients as $c_3 \equiv v^2 [C_{lq}^{(3)}]_{\mu\tau 11}$ and $c_1 \equiv v^2 [C_{lq}^{(1)}]_{\mu\tau 11}$. At tree level they generate the following WEFT coefficients relevant for COHERENT:

$$[\epsilon_L^{ud}]_{\mu\tau} = c_3 \ , \qquad \epsilon_{\mu\tau}^{uu} = c_1 - c_3 \ , \qquad \epsilon_{\mu\tau}^{dd} = c_1 + c_3 \ . \tag{5.62}$$

We show in Fig. 5.6 (right panel) the bounds that we obtained on the coefficients c_1 and c_3 using COHERENT data.

We can also constrain charged-current NSIs using the measurements of leptonic pion decay widths. To make things simpler, we work with the ratio $R_\pi \equiv \Gamma(\pi \to e\nu)/\Gamma(\pi \to \mu\nu)$, which is the strongest probe to the $[\epsilon_L^{ud}]_{\mu\tau}$ coupling coming from hadronic decays [153, 271, 272]. As in the specific cases discussed above, it gets modified as $R_\pi = R_\pi^{\rm SM}/(1+(\epsilon_{\mu\tau}^{ud})^2)$ in a new physics regime. Fig. 5.6 shows the interplay between this constraint and the one obtained from COHERENT data.

5.6. Comparison and combination with other precision observables

In this section we discuss the place of the COHERENT experiment in the larger landscape of electroweak precision observables. To this end we will employ the SMEFT framework to combine

information from COHERENT and other experiments below the Z-pole, with that obtained by the high-energy colliders at or above the Z-pole.[16] More specifically, we will add the results obtained in this chapter to the ones obtained in Chapter 3 and Chapter 4. These previous limits here will feature several updates with respect to the results in Eqs. (3.11), (7.1) and (4.33), which were implemented between the publication of Ref. [133] and Ref. [134]. We will discuss all these changes in detail before incorporating the COHERENT input into the EW global fit.

5.6.1. Update to the electroweak global fit

Here we list the observables that are included in our update of the global SMEFT fit carried out in Ref. [132] and presented in Chapter 3, with special emphasis on the changes with respect to that work:

- e^+e^- collisions at energies above [147, 148], at [153, 156, 275], and below [149, 150, 154] the Z-pole. Concerning the Z-pole results we follow Ref. [133], where we took into account recent theoretical calculations [173, 174] that lead to minor modifications of the Z width, the hadronic cross section, and the forward-backward asymmetry of b quarks.

- For W boson data we follow Ref. [133] as well: we include the mass and total width [153], leptonic branching ratios from LEP [147], Tevatron [276] and LHC [277–279], and the ratio $R_{Wc} \equiv \Gamma(W \to cs)/\Gamma(W \to ud, cs)$ [153], which has a limited precision, but helps to break a flat direction. These data include three significant updates with respect to the fit in Ref. [132]: (i) the recent LHC results concerning the leptonic branching ratios [277–279], which play an important role in removing certain LEP-2 tensions and improving the constraints on the $W\ell\nu$ vertices; (ii) the W boson mass, which is updated using the current PDG combination $m_W = 80.377(12)$ GeV [147, 153, 159, 280–282][17]; (iii) we no longer use Ref. [283] to extract the Wt_Lb_L vertex (and hence $[\delta g_L^{Zu}]_{33}$), as this measurement is also sensitive to other operators in the top sector.

- Forward-backward asymmetries in $\ell^+\ell^-$ production at the LHC [191] and D0 [284]. The LHC bounds tighten the LEP constraints on the Z boson couplings to first generation quarks (see Chapter 4).

- Electron-neutrino scattering on nuclei by the CHARM experiment [142].

- Muon-neutrino scattering on nuclei in the CHARM [285], CDHS [286], and CCFR [287] experiments. As in Ref. [132], we use the PDG combination of these data, which includes as well additional experimental input (with very limited precision) from elastic neutrino-proton scattering and neutrino-induced coherent neutral-pion production from nuclei.

- Parity violation in atoms and in scattering: (i) measurements of atomic parity violation in cesium [288] and thallium [289, 290] atoms; (ii) the weak charge of the proton measured in scattering of low-energy polarized electrons by QWEAK [291]; and (iii) deep-inelastic scattering of polarized electrons on deuterium by the PVDIS experiment [292]. As in Ref. [132], we use the PDG combination of these data, supplemented by the SAMPLE

[16] See Refs. [273, 274] for previous SMEFT analyses that included some COHERENT observables.

[17] We note this average does *not* include the recent CDF result [160], which is in tension with the other most precise measurements. Later in this section we will explore how the fit results change upon considering this new measurement.

measurement of the scattering of polarized electrons on deuterons in the quasi-elastic kinematic regime [144]. The only difference with Ref. [132] is that we use the 2022 PDG combination (Table 10.9 of Ref. [153]), which includes the updated measurement of the proton weak charge by the QWEAK experiment [291].

- Deep-inelastic scattering of polarized muons on carbon at the CERN SPS [145].
- Various (semi-)leptonic hadron decays (nuclear beta, pion, kaon) mediated by the quark-level process $d(s) \to u\ell\bar{\nu}_\ell$. The global fit in Ref. [132] used the bounds obtained in Ref. [146], whereas here we use instead the updated version of Ref. [293]. These updates concern new nuclear beta decay input, lattice calculations and a refined analysis of radiative pion decay $\pi^- \to e^-\bar{\nu}_e\gamma$ [255, 293]. The new measurements of the neutron lifetime [294] and beta asymmetry [295, 296] are particularly important, entailing a significant improvement in the tensor 4-fermion interaction $[C^{(3)}_{lequ}]_{ee11}$.[18]
- Muon-neutrino scattering on electrons [151, 297, 298]. As in Ref. [132], we use the PDG combination for the low-energy $\nu_\mu - e$ couplings [153].
- Parity-violating scattering of electrons at low energies in the SLAC E158 experiment [299]. As in Ref. [132], we use the PDG combination for the low-energy parity-violating electron self-coupling [153].
- Trident production $\nu_\mu\gamma^* \to \nu_\mu\mu^+\mu^-$ in the CHARM-II [300] and CCFR [152] experiments.
- Leptonic decays of taus and muons [153]. Unlike [132], we no longer use the ratio of effective Fermi constants $G_{\tau\mu}/G_F$ from the *τ-Lepton Decay Parameters* review in Ref. [143], since its large correlation with the poorly known $[C_{le}]_{\mu\tau\tau\mu}$ coefficient was not provided. Instead, we directly use the measured $\tau \to e\nu\bar{\nu}$ branching fraction and the associated Michel parameter [153]. For completeness we also include the measurement of the Michel parameter in muon decay [153]. These modifications allow us to target additional 4-fermion semileptonic operators, not constrained by the fit in Ref. [132], namely the $[C_{le}]_{\mu\tau\tau\mu}$ and $[C_{le}]_{e\mu\mu e}$ coefficients.
- We include a set of hadronic tau decay observables described in Ref. [293]. These constraints, which were obtained subsequently to the global fit of Ref. [132], give access to contact interactions between first generation quarks and third generation leptons. They also improve our knowledge of the vertex corrections.

We refer to Refs. [132, 133, 293] and to the original experimental papers for the central values and errors used in our fit.

5.6.2. Impact from COHERENT

Translating the COHERENT limits to the SMEFT language will allow us to combine the information from NC and CC processes, which are related by the $SU(2)_L$ gauge symmetry. We consider operators up to dimension six, using the standard SMEFT power counting where the corresponding Wilson coefficients are $\mathcal{O}(\Lambda^{-2})$ in the new physics scale Λ. Consequently, we

[18] There is a nonzero correlation between up-down effective couplings (the focus of this work) and up-strange couplings (which we marginalized over). This must be taken into account when going to specific scenarios, such as the one-a-time results in Table 5.3 or the flavor-blind fit in Eq. (5.67). The full likelihood is available in Ref. [293].

expand observables to order $1/\Lambda^2$, ignoring higher order corrections. This implies that we only need the linearized version of the COHERENT results obtained in the WEFT formalism, cf. Eq. (5.58).

The COHERENT experiment probes contact 4-fermion interactions between the left-handed lepton doublets l_L and quark doublets q_L, and singlets u_R, d_R. The relevant dimension-6 operators are [76]

$$\begin{aligned}\mathcal{L}_{\text{SMEFT}} \supset \Big[&C_{lq}^{(1)}(\bar{l}_L\gamma_\mu l_L)(\bar{q}_L\gamma^\mu q_L) + C_{lq}^{(3)}(\bar{l}_L\gamma_\mu\sigma^k l_L)(\bar{q}_L\gamma^\mu\sigma^k q_L)\\ &+ C_{lu}(\bar{l}_L\gamma_\mu l_L)(\bar{u}_R\gamma^\mu u_R) + C_{ld}(\bar{l}_L\gamma_\mu l_L)(\bar{d}_R\gamma^\mu d_R)\Big]\,\frac{1}{v^2},\end{aligned} \tag{5.63}$$

where all Wilson coefficients are rewritten as $C_k \equiv c_k \frac{v^2}{\Lambda^2}$ with $v \simeq 246.22$ GeV (*cf.* Eq. (2.13)). The SM fields are 3-component vectors in the generation space, however the flavor index is suppressed here to reduce clutter. In this section we assume that the Wilson coefficients are flavor-universal, more precisely, that they respect the $U(3)^5$ flavor symmetry acting on the three generations of q_L, u_R, d_R, l_L, e_R. This is by far the most studied SMEFT setup, especially in the context of global fits, and often described simply as the EWPO fit. As we will show below, even in this restricted framework, COHERENT has a significant impact on the global fit. Later on we will relax this assumption and check that the impact of COHERENT is even more spectacular thanks to lifting degeneracies in the multi-dimensional parameter space of Wilson coefficients.

From the SMEFT point of view, the COHERENT experiment also probes the coupling strength of the Z boson to quarks and neutrinos. For these interactions we use the same parametrization that we used for the Lagrangian in Eq. (3.3). We reinstate the Z interactions expressed there here and we expand the sum over the quark flavors:

$$\begin{aligned}\mathcal{L}_{\text{SMEFT}} \supset -\Bigg\{&\left[\frac{1}{2} - \frac{2}{3}\sin^2\theta_W + \delta g_L^{Zu}\right](\bar{u}_L\gamma^\mu u_L) + \left[-\frac{2}{3}\sin^2\theta_W + \delta g_R^{Zu}\right](\bar{u}_R\gamma^\mu d_R)\\ &+ \left[-\frac{1}{2} + \frac{1}{3}\sin^2\theta_W + \delta g_L^{Zd}\right](\bar{d}_L\gamma^\mu d_L) + \left[\frac{1}{3}\sin^2\theta_W + \delta g_R^{Zd}\right](\bar{d}_R\gamma^\mu d_R)\\ &+ \left[\frac{1}{2} + \delta g_L^{W\ell} + \delta g_L^{Ze}\right](\bar{\nu}_L\gamma^\mu\nu_L)\Bigg\}\sqrt{g_L^2+g_Y^2}Z_\mu\ .\end{aligned} \tag{5.64}$$

The analyzed COHERENT results constrain the 4-fermion Wilson coefficients in Eq. (5.63) and the vertex corrections in Eq. (5.64). These Wilson coefficients are related to the NC WEFT Wilson coefficients in Eq. (5.1) by [132]

$$\begin{aligned}\epsilon_{\alpha\alpha}^{uu} =&\delta g_L^{Zu} + \delta g_R^{Zu} + \left(1 - \frac{8s_\theta^2}{3}\right)\delta g_L^{Z\nu} - \frac{1}{2}\left(C_{lq}^{(1)} + C_{lq}^{(3)} + C_{lu}\right) \equiv \epsilon_u\ ,\\ \epsilon_{\alpha\alpha}^{dd} =&\delta g_L^{Zd} + \delta g_R^{Zd} - \left(1 - \frac{4s_\theta^2}{3}\right)\delta g_L^{Z\nu} - \frac{1}{2}\left(C_{lq}^{(1)} - C_{lq}^{(3)} + C_{ld}\right) \equiv \epsilon_d\ ,\end{aligned} \tag{5.65}$$

where there is no implicit sum over the repeated index α. Because of our assumption of $U(3)^5$ symmetry, the expression is the same for any value of the index α, that is to say, the quarks interact with the same strength with all flavors of the neutrino. Therefore, it is appropriate to use the results of the constrained WEFT fit in Eq. (5.59). Translated to the SMEFT Wilson coefficients, the strong constraint in Eq. (5.60) becomes

$$0.71C_{lq}^{(1)} - 0.04C_{lq}^{(3)} + 0.34C_{lu} + 0.37C_{ld} + [\delta g]_{\text{piece}} = -0.002 \pm 0.010\ , \tag{5.66}$$

Table 5.3: Uncertainty (in units of 10^{-3}) on the Wilson coefficients probed by the COHERENT experiment (central values are not given). The COHERENT row shows the constraints based on the results obtained in this analysis. W/o COHERENT refers to a host of electroweak precision observables analyzed in Ref. [132], with the updates described in Chapter 5.6.1.

Coefficient	$\delta g_L^{W\ell}$	δg_L^{Ze}	δg_L^{Zu}	δg_R^{Zu}	δg_L^{Zd}	δg_R^{Zd}	$C_{lq}^{(1)}$	$C_{lq}^{(3)}$	C_{lu}	C_{ld}
w/o COHERENT	0.14	0.11	0.23	0.63	0.19	0.78	0.81	0.26	1.5	1.8
COHERENT alone	71	71	15	15	14	14	14	260	30	27

where $[\delta g]_{\text{piece}} \equiv -0.67(\delta g_L^{Zu} + \delta g_R^{Zu}) - 0.74(\delta g_L^{Zd} + \delta g_R^{Zd}) + 0.26\delta g_L^{Z\nu}$ collects the contributions from vertex corrections.

In the remainder of this section we will compare the strength of the COHERENT constraints on SMEFT coefficients to that of the other electroweak precision measurements. In the following we compare and combine the constraints compiled in Chapter 3 (plus the updates discussed in Chapter 5.6.1) with the ones obtained from the COHERENT data.

The first comment is that the impact of COHERENT is negligible if only a single Wilson coefficient appearing in Eq. (5.65) is present at a time. In Table 5.3 we show the uncertainty obtained in such a one-at-a-time fit. We can see that the sensitivity of COHERENT is inferior by 1-2 orders of magnitude compared to that achieved by a combination of other electroweak precision measurements. This is not surprising, given that the latter contain a number of observables that have been measured with a (sub)permille precision (namely LEP1, APV, or baryon decays), while COHERENT currently offers a percent level precision.

However, most new physics models generate several operators simultaneously, and thus a global analysis is required to assess the importance of COHERENT data. With this in mind, we turn to analyzing the situation when all flavor-universal dimension-6 SMEFT Wilson coefficients are allowed to be present with arbitrary magnitudes within the regime of validity. Now we are dealing with a multi-dimensional parameter space, where certain directions may not be constrained by the most precise observables, and where the input from COHERENT may be valuable. More precisely, in the flavor-universal case the observables taken into account in our analysis probe 18 independent Wilson coefficients. In addition to the six defined in Eq. (5.64), our analysis probes 11 more four-fermion operators as well as the vertex correction to the Z boson coupling to right-handed leptons. For their definition see Chapter 3.1, in particular (3.9).

We find the fully marginalized constraints

$$\begin{pmatrix} \\ \delta g_L^{W\ell} \\ \delta g_L^{Ze} \\ \delta g_R^{Ze} \\ \delta g_L^{Zu} \\ \delta g_R^{Zu} \\ \delta g_L^{Zd} \\ \delta g_R^{Zd} \\ C_{lq}^{(1)} \\ C_{lq}^{(3)} \\ C_{lu} \\ C_{ld} \\ C_{eq} \\ C_{eu} \\ C_{ed} \\ C_{ll}^{(1)} \\ C_{ll}^{(3)} \\ C_{le} \\ C_{ee} \end{pmatrix} = \begin{pmatrix} \text{w/o COHERENT} \\ -0.27(79) \\ -0.10(0.21) \\ -0.20(22) \\ -1.0(1.6) \\ -0.5(3.2) \\ 1.5(1.3) \\ 12.8(6.7) \\ -16.6(9.0) \\ -2.4(1.9) \\ 10(23) \\ 5(41) \\ -13(22) \\ 7(10) \\ 25(18) \\ 5.4(3.2) \\ -0.9(1.6) \\ 0.2(1.3) \\ -2.7(3.0) \end{pmatrix} \times 10^{-3} \to \begin{pmatrix} \text{w/ COHERENT} \\ -0.26(78) \\ -0.09(21) \\ -0.17(22) \\ -1.3(1.6) \\ -1.1(3.1) \\ 1.1(1.2) \\ 10.4(5.8) \\ -18.3(8.7) \\ -2.2(1.8) \\ 23(16) \\ 29(24) \\ -1(15) \\ 3.5(9.4) \\ 29(17) \\ 5.3(3.2) \\ -0.9(1.6) \\ 0.2(1.3) \\ -2.7(3.0) \end{pmatrix} \times 10^{-3}. \tag{5.67}$$

We highlighted the constraints on C_{lu}, C_{ld}, and C_{eq}, which improve significantly, by about 30-40%, after including the COHERENT input. The improvement is visualized in the left panel of Fig. 5.7. While neutrino scattering experiments have long played an important role in SMEFT fits of electroweak precision observables, this is the first time *coherent* neutrino scattering is included in such a fit. In fact, of all neutrino experiments, COHERENT currently makes the largest impact on the flavor-blind SMEFT fit. The correlation matrix for the fit including COHERENT is given in Table 5.4.

In the $U(3)^5$-invariant SMEFT, one can obtain bounds on 10 new (combinations of) Wilson coefficients from diboson production at LEP2 and Higgs measurements [301]. The rest of $U(3)^5$-invariant SMEFT coefficients, which are not probed by these 2 global fits, are made up of only Higgs doublets, only quarks, or only gluons, or violate CP.

Another way to illustrate the impact of COHERENT is to consider global constraints on the combinations ϵ_u and ϵ_d of the SMEFT Wilson coefficients, defined in Eq. (5.65). Let us recall that COHERENT alone constrains one linear combination at a percent level: $0.67\epsilon_u + 0.74\epsilon_d = 0.003(10)$, while the orthogonal combination is poorly constrained. This is shown in the right panel of Fig. 5.7 as the diagonal beige band (this is simply a zoomed in version of Fig. 5.6). We can use the results of our flavor-diagonal global SMEFT fit of electroweak precision observables in Eq. (5.67) (without COHERENT) to constrain the $\epsilon_{u,d}$ coefficients, finding $\epsilon_u = 0.003(10)$ and $\epsilon_d = 0.019(21)$. This constraint is also percent level, indicating that COHERENT has an important impact on the global fit. Indeed, the combination of the COHERENT results with other precision observables leads to $\epsilon_u = -0.0037(54)$, $\epsilon_d = 0.0054(93)$, which represents a factor of two improvement. These results are represented in the right panel of Fig. 5.7.

One last way to gauge the importance of the COHERENT input is to check how the fit is affected by removing it. If we do the same with other probes coming from neutrino-detection experiments, we will be able to get an idea about the relevance of each input towards the fit. We

Table 5.4: Correlation matrix for the limits obtained in Eq. (5.67) from the $U(3)^5$ symmetric global fit built with information from EWPO including inputs from the COHERENT experiment.

$$\rho = \begin{pmatrix}
1. & -0.58 & 0.21 & 0.08 & 0.1 & 0.02 & -0.01 & -0.06 & 0.48 & 0.12 & 0. & 0.03 & 0.12 & -0.04 & -0.46 & 0.98 & -0.01 & -0.05 \\
-0.58 & 1. & 0.29 & -0.1 & -0.07 & -0.12 & -0.19 & 0.11 & -0.25 & -0.17 & -0.06 & -0.09 & -0.1 & -0.1 & 0.2 & -0.57 & 0. & 0.11 \\
0.21 & 0.29 & 1. & 0. & -0.03 & -0.27 & -0.25 & 0.1 & 0.27 & -0.08 & -0.1 & -0.08 & 0. & -0.21 & -0.19 & 0.21 & -0.01 & 0.08 \\
0.08 & -0.1 & 0. & 1. & 0.69 & 0.39 & 0.14 & -0.3 & 0.64 & 0.29 & 0.32 & 0.3 & 0.39 & 0.27 & -0.03 & 0.07 & 0. & -0.01 \\
0.1 & -0.07 & -0.03 & 0.69 & 1. & 0.15 & 0.31 & -0.4 & 0.53 & 0.35 & 0.42 & 0.37 & 0.42 & 0.39 & -0.04 & 0.1 & 0. & -0.01 \\
0.02 & -0.12 & -0.27 & 0.39 & 0.15 & 1. & 0.82 & -0.38 & -0.3 & 0.42 & 0.36 & 0.35 & 0.14 & 0.65 & 0.02 & 0.01 & 0. & -0.03 \\
-0.01 & -0.19 & -0.25 & 0.14 & 0.31 & 0.82 & 1. & -0.46 & -0.41 & 0.48 & 0.43 & 0.4 & 0.14 & 0.76 & 0.04 & -0.02 & 0. & -0.03 \\
-0.06 & 0.11 & 0.1 & -0.3 & -0.4 & -0.38 & -0.46 & 1. & -0.03 & -0.83 & -0.72 & -0.05 & -0.73 & -0.85 & 0.01 & -0.05 & 0. & 0.02 \\
0.48 & -0.25 & 0.27 & 0.64 & 0.53 & -0.3 & -0.41 & -0.03 & 1. & 0.04 & 0.03 & 0.05 & 0.3 & -0.22 & -0.25 & 0.51 & -0.01 & -0.01 \\
0.12 & -0.17 & -0.08 & 0.29 & 0.35 & 0.42 & 0.48 & -0.83 & 0.04 & 1. & 0.9 & 0.48 & 0.4 & 0.87 & -0.05 & 0.12 & 0. & -0.02 \\
0. & -0.06 & -0.1 & 0.32 & 0.42 & 0.36 & 0.43 & -0.72 & 0.03 & 0.9 & 1. & 0.66 & 0.26 & 0.8 & 0.02 & -0.01 & 0. & -0.01 \\
0.03 & -0.09 & -0.08 & 0.3 & 0.37 & 0.35 & 0.4 & -0.05 & 0.05 & 0.48 & 0.66 & 1. & -0.41 & 0.35 & -0.01 & 0.03 & 0. & -0.01 \\
0.12 & -0.1 & 0. & 0.39 & 0.42 & 0.14 & 0.14 & -0.73 & 0.3 & 0.4 & 0.26 & -0.41 & 1. & 0.5 & -0.05 & 0.12 & 0. & -0.01 \\
-0.04 & -0.1 & -0.21 & 0.27 & 0.39 & 0.65 & 0.76 & -0.85 & -0.22 & 0.87 & 0.8 & 0.35 & 0.5 & 1. & 0.04 & -0.05 & 0. & -0.02 \\
-0.46 & 0.2 & -0.19 & -0.03 & -0.04 & 0.02 & 0.04 & 0.01 & -0.25 & -0.05 & 0.02 & -0.01 & -0.05 & 0.04 & 1. & -0.47 & -0.18 & -0.58 \\
0.98 & -0.57 & 0.21 & 0.07 & 0.1 & 0.01 & -0.02 & -0.05 & 0.51 & 0.12 & -0.01 & 0.03 & 0.12 & -0.05 & -0.47 & 1. & -0.01 & -0.05 \\
-0.01 & 0. & -0.01 & 0. & 0. & 0. & 0. & 0. & -0.01 & 0. & 0. & 0. & 0. & 0. & -0.18 & -0.01 & 1. & -0.23 \\
-0.05 & 0.11 & 0.08 & -0.01 & -0.01 & -0.03 & -0.03 & 0.02 & -0.01 & -0.02 & -0.01 & -0.01 & -0.01 & -0.02 & -0.58 & -0.05 & -0.23 & 1.
\end{pmatrix}$$

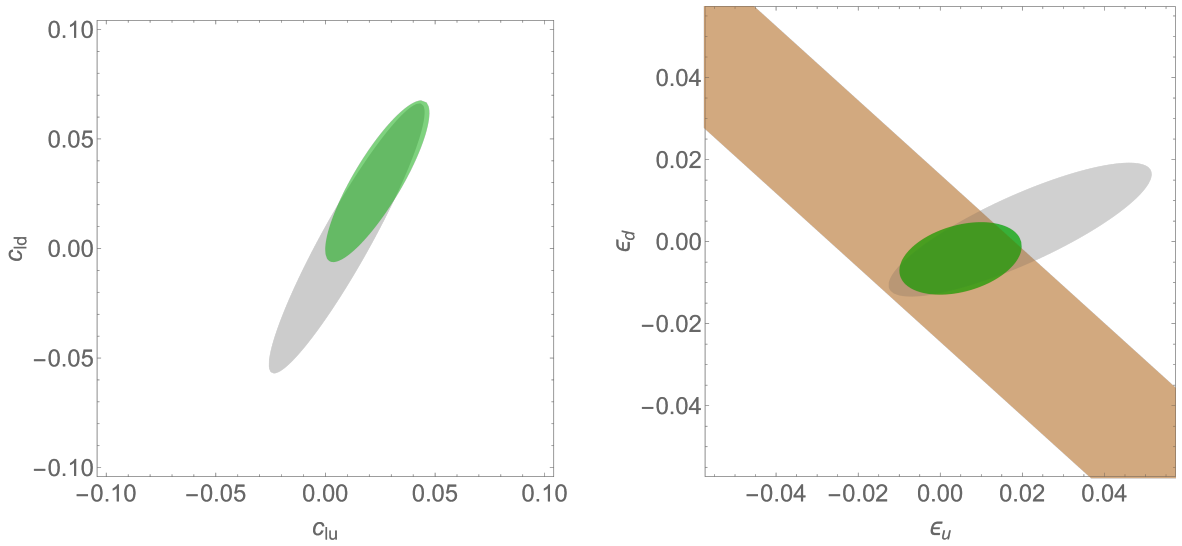

Fig. 5.7: Left panel: Marginalized 1-sigma bounds ($\Delta\chi^2 \simeq 2.3$) on the 4-fermion SMEFT coefficients C_{lu} and C_{ud} from a global fit to EWPO in the flavor-universal SMEFT without (gray) and with (green) COHERENT data. We stress that the other 16 Wilson coefficients are not set to zero, but marginalized over. Right panel: 1-sigma bounds ($\Delta\chi^2 \simeq 2.3$) on the 4-fermion lepton-universal WEFT coefficients ϵ_u and ϵ_d, obtained from COHERENT data (beige), other EWPO (gray) and the combination of both (green). The latter two are obtained in the flavor-universal SMEFT.

Table 5.5: Estimation of the impact of some experimental inputs on the $U(3)^5$ symmetric global fit upon their removal. The estimation is done by two methods, based on a list of the ratios of the Wilson coefficient error bar sizes before and after the removal of a given set of experimental inputs. The first one simply takes the smallest element on said list, and the second consists of computing the product of all list elements. We can see that for both procedures COHERENT has the biggest effect.

Input	$\nu_e N$ [142]	Trident [152, 300]	$\nu_\mu N$ [285–287]	$\nu_\mu e$ [153]	CEνNS [249, 250]
Minimum	1	1	0.98	0.83	0.59
Product	1	1	0.96	0.31	0.15

perform this exercise considering data from observables involving electron-neutrino scattering on nuclei (CHARM [142]), muon-neutrino scattering on nuclei (CHARM [285], CCFR [287], CDHS [286]), parity-violating $\nu_\mu e$ scattering (SLAC E158 [153]), trident production (CHARM-II [300], CCFR [152]) and CEνNS (COHERENT [249, 250]), and find that only the absence of COHERENT has a non-negligible effect on the fit. The exact results can be found in Table 5.5. Thus, from the point of view of the SMEFT fits, COHERENT is the most relevant neutrino-detection experiment, clearly superior in comparison to previous neutrino scattering experiments at higher energies.

Finally, if we relax the $U(3)^5$ symmetry, we end up with 65 independent (combinations of) SMEFT Wilson coefficients, including all correlations. Fitting all of them simultaneously, we

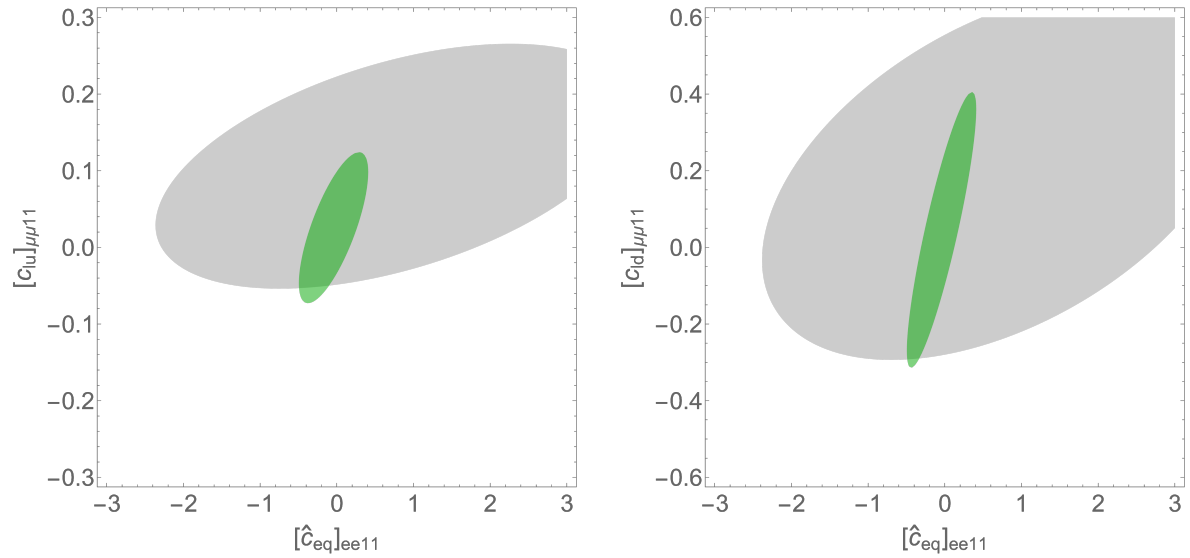

Fig. 5.8: Left panel: Marginalized 1-sigma bounds ($\Delta\chi^2 \simeq 2.3$) on the (combination of) SMEFT Wilson coefficients $[\hat{C}_{eq}]_{ee11}$ and $[C_{lu}]_{\mu\mu 11}$ from a global fit to EWPO in the flavor-generic SMEFT without (gray) and with (green) COHERENT data. Right panel: The same for the $[\hat{C}_{eq}]_{ee11}$-$[C_{ld}]_{\mu\mu 11}$ pair of Wilson coefficients.

find the following 1σ intervals

$$\begin{pmatrix} \delta g_L^{We} \\ \delta g_L^{W\mu} \\ \delta g_L^{W\tau} \\ \delta g_L^{Ze} \\ \delta g_R^{Ze} \\ \delta g_L^{Z\mu} \\ \delta g_R^{Z\mu} \\ \delta g_L^{Z\tau} \\ \delta g_R^{Z\tau} \\ \delta g_R^{Wq_1} \\ \delta g_L^{Zu} \\ \delta g_R^{Zu} \\ \delta g_L^{Zd} \\ \delta g_R^{Zd} \\ \delta g_L^{Zc} \\ \delta g_R^{Zc} \\ \delta g_L^{Zs} \\ \delta g_R^{Zs} \\ \delta g_L^{Zb} \\ \delta g_R^{Zb} \end{pmatrix} = \begin{pmatrix} -1.8(2.6) \\ -0.6(2.2) \\ 0.2(3.5) \\ -0.21(28) \\ -0.42(27) \\ 0.2(1.2) \\ 0.0(1.4) \\ -0.09(59) \\ 0.61(62) \\ -3.8(8.1) \\ -7(22) \\ 4(29) \\ -13(35) \\ 10(120) \\ -1.5(3.6) \\ -3.3(5.3) \\ 14(27) \\ 34(46) \\ 3.2(1.7) \\ 22(8.8) \end{pmatrix} \times 10^{-3}, \qquad \begin{pmatrix} [C_{ll}]_{eeee} \\ [C_{le}]_{eeee} \\ [C_{ee}]_{eeee} \\ [C_{ll}]_{e\mu\mu e} \\ [C_{ll}]_{ee\mu\mu} \\ [C_{le}]_{e\mu\mu e} \\ [C_{le}]_{ee\mu\mu} \\ [C_{le}]_{\mu\mu ee} \\ [C_{ee}]_{ee\mu\mu} \\ [C_{ll}]_{e\tau\tau e} \\ [C_{ll}]_{ee\tau\tau} \\ [C_{le}]_{ee\tau\tau} \\ [C_{le}]_{\tau\tau ee} \\ [C_{ee}]_{ee\tau\tau} \\ [\hat{C}_{ll}]_{\mu\mu\mu\mu} \\ [C_{ll}]_{\mu\tau\tau\mu} \\ [C_{le}]_{\mu\tau\tau\mu} \end{pmatrix} = \begin{pmatrix} 1.03(38) \\ -0.22(22) \\ 0.19(38) \\ -0.56(80) \\ 0.1(2.0) \\ 11.4(6.8) \\ 0.3(2.2) \\ -0.2(2.1) \\ 0.2(2.3) \\ -0.60(68) \\ 2(11) \\ -2.3(7.2) \\ 1.7(7.2) \\ -1(12) \\ 2(21) \\ 1.5(1.9) \\ 19(15) \end{pmatrix} \times 10^{-2}, \tag{5.68}$$

$$\begin{pmatrix} [C_{lq}^{(3)}]_{ee11} \\ [\hat{C}_{eq}]_{ee11} \\ [\hat{C}_{lu}]_{ee11} \\ [\hat{C}_{ld}]_{ee11} \\ [\hat{C}_{eu}]_{ee11} \\ [\hat{C}_{ed}]_{ee11} \\ [C_{lequ}^{(1)}]_{ee11} \\ [C_{ledq}]_{ee11} \\ [C_{lequ}^{(3)}]_{ee11} \\ [\hat{C}_{lq}^{(3)}]_{ee22} \\ [C_{lu}]_{ee22} \\ [\hat{C}_{ld}]_{ee22} \\ [C_{eq}]_{ee22} \\ [C_{eu}]_{ee22} \\ [\hat{C}_{ed}]_{ee22} \\ [\hat{C}_{lq}^{(3)}]_{ee33} \\ [C_{ld}]_{ee33} \\ [C_{eq}]_{ee33} \\ [C_{ed}]_{ee33} \end{pmatrix} = \begin{pmatrix} 0.1(2.8) \\ -4(30) \\ -2.5(8.7) \\ -2(18) \\ -3.1(9.4) \\ -2(17) \\ -0.017(60) \\ -0.018(57) \\ 0.023(66) \\ -61(32) \\ 2.4(8.0) \\ -300(130) \\ -21(28) \\ -87(46) \\ 250(140) \\ -8.5(8.0) \\ -1(10) \\ -3.1(5.1) \\ 18(20) \end{pmatrix} \times 10^{-2} \,, \qquad \begin{pmatrix} [C_{lq}^{(3)}]_{\mu\mu 11} \\ [C_{lq}^{(1)}]_{\mu\mu 11} \\ [C_{lu}]_{\mu\mu 11} \\ [C_{ld}]_{\mu\mu 11} \\ [\hat{C}_{eq}]_{\mu\mu 11} \\ \epsilon_P^{d\mu}(2\text{ GeV}) \\ [C_{lq}^{(3)}]_{\tau\tau 11} \\ [C_{lequ}^{(3)}]_{\tau\tau 11} \\ \epsilon_P^{d\tau}(2\text{ GeV}) \end{pmatrix} = \begin{pmatrix} 3.0(3.5) \\ -0.2(5.8) \\ 2.5(6.5) \\ 5(24) \\ 3(41) \\ -0.080(95) \\ -0.3(2.8) \\ -0.3(1.2) \\ 0.93(85) \end{pmatrix} \times 10^{-2},$$

where the limits are to be compared with (3.11). We have followed the same notation that was used there, including the hatted variables used to cover for blind directions. We again restrain ourselves from copying here the 65×65 correlation matrix. We highlighted in red the Wilson coefficients whose bounds have improved significantly thanks to including the COHERENT results. The improvement is illustrated in Fig. 5.8. The most spectacular effect is observed for the combination $[\hat{C}_{eq}]_{ee11} = [C_{eq}]_{ee11} + [C_{lq}^{(1)}]_{ee11}$. In the fit of Ref. [132] it was constrained only by the CHARM measurement of electron neutrino scattering on nuclei [142], which is however very imprecise. The COHERENT results analyzed in this chapter reduce the error bars on $[\hat{C}_{eq}]_{ee11}$ by a factor of 5.

The results presented in this chapter could be upgraded by including additional measurements of observables in the neutrino sector [302–304]. However, for each of these a careful study would be necessary to determine their exact sensitivity to the Wilson coefficients in the WEFT and the SMEFT. Without leaving the CEνNS interaction, our analysis could also benefit from future measurements on additional nuclear targets [305].

As a final aside, we have checked how the results in this fit change if we consider the new W mass value measured with high precision in Ref. [160], which is in great tension with the SM prediction. Its impact on the limits of the general marginalized fit in Eq. (6.10) and on its $U(3)^5$ limit in Eq. (5.67) is important mainly in the correlation patterns, the central values and the individual errors show barely no change under the W mass shift. This is to be expected in global fits with so many parameters and experimental inputs. Even in the face of a great alteration in one of the inputs, it is unlikely that it will cause a major change on the individual limits. Instead, its presence will mainly show up in the correlations between the coefficient bounds.

All in all, the results of this chapter demonstrate that COHERENT has become an indispensable ingredient in the family of electroweak precision observables constraining the SMEFT Wilson coefficients.

Chapter 6

Precision Z physics at the LHC beyond the peak

Back in Chapter 4, we concluded our discussion on the impact of the Drell-Yan A_4 LHC data in the electroweak SMEFT global fit by listing a series of outlooks that could be pursued to improve the current fit results. Out of all of them, a promising one was rooted in the extension of the dilepton energy spectrum in the Drell-Yan production dataset. The main motivation for this option was the possibility of probing 4-fermion operators at low energies in a hadron collider context. However, it would also be interesting even if only vertex corrections were examined. Having access to more measured bins offers additional directions in SMEFT parameter space for us to probe, so it is expected that current limits on vertex corrections could improve just by their addition.

That is precisely the focus of a project still in progress aimed at extending the work published in Ref. [133] and presented in Chapter 4. In this chapter, we will describe the steps we are currently taking to incorporate off-peak LHC measurements of the Drell-Yan forward backward asymmetry into the electroweak SMEFT global fit, taking as a starting point the results obtained in Chapter 5. Once the approach we are following is established, we will move on to discuss some preliminary results.

Moving beyond the Z mass peak implies that a subset of the 4-fermion operators listed in Table 3.1 and Table 3.2 needs to be considered in the fit for consistency. In particular, Drell-Yan production observables at the LHC will be sensitive to 2-quark and 2-lepton contact interactions that conserve both flavor and chirality. Adding them to the previously studied vertex corrections results in the following NP parameter list:

$$\delta g_L^{Zu}, \delta g_R^{Zu}, \delta g_L^{Zd}, \delta g_R^{Zd}, \left[\hat{C}_{lq}\right]_{11}, [C_{ed}]_{11}, [C_{eu}]_{11}, [C_{eq}]_{11}, [C_{ld}]_{11}, [C_{lu}]_{11}, \tag{6.1}$$

where we have defined $[C_X]_{JJ} \equiv \left([C_X]_{eeJJ} + [C_X]_{\mu\mu JJ}\right)/2$. We sum over the electron and muon indices because the measurements we will consider do not distinguish them. In this sum only the first two flavors are included since we will not deal with any process that produces τ leptons as part of its final state. Additionally, we will always find $J = 1$ because the ATLAS observables we will study will be sensitive only to interactions involving first generation quarks. Finally, flavor conservation implies that we are only sensitive to the combination $\left[\hat{C}_{lq}\right]_{11} \equiv \left[C_{lq}^{(1)}\right]_{11} + \left[C_{lq}^{(3)}\right]_{11}$

instead of the two separate coefficients. All in all, an analysis considering off-peak data will be sensitive to 10 independent combinations of SMEFT Wilson coefficients, 4 vertex corrections and 6 four-fermion couplings.

The data we used in Chapter 4 originating from Ref. [191] cannot help us very much in the current task, as it only features measurements at a very limited dilepton energy range around the Z pole ($\sqrt{\hat{s}} \in \{70, 125\}$ GeV). This is a well motivated choice by ATLAS, since the main objective of that study was to extract $\sin^2\theta_W$ and the information from the Z peak is the most adequate probe for that task. On the other hand, the ATLAS measurement reported in Ref. [185] also focuses on Drell-Yan observables, but it covers a much wider dilepton mass range. The main focus of that study was to access the Drell-Yan triple differential cross section. The measurements were performed for different ranges in the decay angle θ^*, the dilepton rapidity Y and the dilepton mass $\sqrt{\hat{s}}$. However, it also includes a dedicated measurement of the Drell-Yan forward-backward asymmetry, with rapidity and dilepton mass ranges $\sqrt{s} \in \{46, 200\}$ GeV and $Y \in \{0.0, 2.4\}$, amounting to a total of 84 data points. Here we will look at this 2D dataset.

The quoted range of rapidities is labeled as the central region in Ref. [185]. Additionally, there is another rapidity region defined in that study, the so-called forward rapidity region, covering the range $Y \in \{1.2, 3.6\}$, for which ATLAS also reports measurements of the Drell-Yan cross section and the FB asymmetry. However, the results in this last region only consider events with electrons as final-state particles, so for now we will focus just in the measurements at the central rapidity region, which feature both electron and muon channels. We will discuss the potential place of these forward rapidity events within the fit at the end of our discussion.

These experimental results have a lot in common with those in Ref. [191] besides focusing on the same observable sector, as both of them were obtained from the very same sample of events, measured from 20.2 fb^{-1} proton-proton collisions at a centre-of-mass energy of $\sqrt{s} = 8$ TeV. They were also published very close in time, but the theoretical predictions for Ref. [185] were released in HEPData [306] just recently.

Thus, the A_{FB} measurements in Ref. [185] are perfect for expanding the Z-pole analysis described in Chapter 4. The new data features a better resolution in both dilepton mass and rapidity bins, so we can anticipate probing a larger variety of directions in parameter space even when looking just at the Z peak. On the other hand, they cover a smaller range in rapidity and their precision is slightly smaller than that of the A_4 bins, so it is possible that the sensitivity to vertex corrections turns out to be worse despite the increase in energy range and granularity. Regardless, the results that we will obtain will represent an important cross-check for our previous analysis. The experimental results in [185] for the forward-backward asymmetry along with their corresponding SM estimations and uncertainties are presented in Table 6.1. As for the triple differential cross section distributions, they also constitute an interesting input for new physics searches, but we will not consider them here due to their relatively lower degree of precision.

To produce theoretical predictions for this observable, we will opt for a more sophisticated computational method than the semianalytic approach we described in Chapter 4. We choose to use DYTurbo [307, 308], which is a Monte Carlo integrator built for calculating Drell-Yan cross sections up to NNLO in fixed order perturbation theory and featuring transverse momentum resummation up to N^{4}LL QCD accuracy [309]. DYTurbo is widely used by the LHC experimental collaborations and its code is publiicly available [310]. This software is built primarily for SM calculations, but we modified its latest version so that it incorporates contributions from vertex corrections and 4-fermion operators. In this study we will consider new physics effects at leading

Table 6.1: ATLAS A_{FB} measurements obtained in Ref. [185] using $\sqrt{s} = 8$ TeV data. The SM predictions, obtained at NNLO in QCD and NLO in EW, are taken from the associated HEPData page.

$\sqrt{s}$ (GeV)	$\lvert Y\rvert$	A_{FB} ($\times 10^{-3}$)	A_{FB}^{SM} ($\times 10^{-3}$)
46 - 66	0.0 - 0.2	-6.0 ± 7.3	-8.7 ± 3.3
46 - 66	0.2 - 0.4	-8.1 ± 7.4	-14.3 ± 3.3
46 - 66	0.4 - 0.6	-27.1 ± 7.5	-29.0 ± 3.4
46 - 66	0.6 - 0.8	-29.6 ± 7.2	-34.4 ± 3.4
46 - 66	0.8 - 1.0	-42.8 ± 7.3	-50.8 ± 3.3
46 - 66	1.0 - 1.2	-56.0 ± 7.2	-62.6 ± 3.4
46 - 66	1.2 - 1.4	-88.8 ± 7.2	-75.4 ± 3.4
46 - 66	1.4 - 1.6	-103.0 ± 7.5	-90.8 ± 3.4
46 - 66	1.6 - 1.8	-9.35 ± 7.8	-99.5 ± 3.6
46 - 66	1.8 - 2.0	-9.23 ± 8.5	-91.4 ± 4.0
46 - 66	2.0 - 2.2	-10 ± 11	-84.7 ± 4.9
46 - 66	2.2 - 2.4	-4 ± 18	-25.9 ± 8.3
66 - 80	0.0 - 0.2	-0.2 ± 4.8	-6.8 ± 3.1
66 - 80	0.2 - 0.4	-26.1 ± 4.9	-24.3 ± 3.1
66 - 80	0.4 - 0.6	-27.6 ± 4.9	-43.5 ± 3.2
66 - 80	0.6 - 0.8	-52.7 ± 5.1	-57.6 ± 3.3
66 - 80	0.8 - 1.0	-70.3 ± 5.1	-72.8 ± 3.3
66 - 80	1.0 - 1.2	-87.6 ± 5.0	-88.0 ± 3.2
66 - 80	1.2 - 1.4	-114 ± 5.0	-111.0 ± 3.3
66 - 80	1.4 - 1.6	-125 ± 5.3	-133.0 ± 3.4
66 - 80	1.6 - 1.8	-126 ± 5.8	-132.9 ± 3.7
66 - 80	1.8 - 2.0	-120 ± 6.8	-130.0 ± 4.3
66 - 80	2.0 - 2.2	-110 ± 8.6	-111.7 ± 5.5
66 - 80	2.2 - 2.4	-50.3 ± 1.5	-66.1 ± 9.6
80 - 91	0.0 - 0.2	0.8 ± 1.3	-1.0 ± 0.8
80 - 91	0.2 - 0.4	1.9 ± 1.4	0.1 ± 0.8
80 - 91	0.4 - 0.6	2.6 ± 1.4	1.1 ± 0.8
80 - 91	0.6 - 0.8	1.5 ± 1.4	0.0 ± 0.8
80 - 91	0.8 - 1.0	-0.1 ± 1.5	-1.0 ± 0.8
80 - 91	1.0 - 1.2	0.1 ± 1.5	0.5 ± 0.8
80 - 91	1.2 - 1.4	-2.2 ± 1.5	-0.1 ± 0.8
80 - 91	1.4 - 1.6	-2.6 ± 1.6	-1.7 ± 0.9
80 - 91	1.6 - 1.8	-0.8 ± 1.8	-0.9 ± 1.0
80 - 91	1.8 - 2.0	-2.7 ± 2.0	-1.0 ± 1.2
80 - 91	2.0 - 2.2	-3.3 ± 2.7	-3.2 ± 1.5
80 - 91	2.2 - 2.4	-6.4 ± 4.2	0.6 ± 2.6
91 - 102	0.0 - 0.2	3.8 ± 1.2	1.6 ± 0.7
91 - 102	0.2 - 0.4	6.5 ± 1.3	7.2 ± 0.7
91 - 102	0.4 - 0.6	12.3 ± 1.3	12.3 ± 0.8
91 - 102	0.6 - 0.8	17.4 ± 1.4	17.6 ± 0.8
91 - 102	0.8 - 1.0	23.3 ± 1.4	23.8 ± 0.9
91 - 102	1.0 - 1.2	28.8 ± 1.4	29.1 ± 0.9
91 - 102	1.2 - 1.4	33.8 ± 1.5	35.4 ± 0.9
91 - 102	1.4 - 1.6	37.7 ± 1.6	39.3 ± 0.9
91 - 102	1.6 - 1.8	39.6 ± 1.7	42.0 ± 0.9
91 - 102	1.8 - 2.0	39.7 ± 2.0	37.7 ± 1.1
91 - 102	2.0 - 2.2	33.3 ± 2.6	30.2 ± 1.4
91 - 102	2.2 - 2.4	19.9 ± 4.2	16.1 ± 2.5
102 - 116	0.0 - 0.2	12.9 ± 5.9	13 ± 16
102 - 116	0.2 - 0.4	25.9 ± 5.9	33.1 ± 3.5
102 - 116	0.4 - 0.6	43.9 ± 6.0	51.6 ± 3.6
102 - 116	0.6 - 0.8	53.7 ± 6.1	67.0 ± 3.7
102 - 116	0.8 - 1.0	91.5 ± 6.1	94.2 ± 3.7
102 - 116	1.0 - 1.2	110.0 ± 6.0	120.0 ± 3.5
102 - 116	1.0 - 1.4	130.0 ± 6.1	133.4 ± 3.9
102 - 116	1.0 - 1.6	144.0 ± 6.3	152.1 ± 4.1
102 - 116	1.0 - 1.8	163.0 ± 7.0	151 ± 14
102 - 116	1.0 - 2.0	154.0 ± 7.7	143.5 ± 5.3
102 - 116	2.0 - 2.2	120 ± 10	113.6 ± 7.0
102 - 116	2.2 - 2.4	61 ± 18	74 ± 12
116 - 150	0.0 - 0.2	26.0 ± 9.0	20.0 ± 2.9
116 - 150	0.2 - 0.4	56.9 ± 9.2	46.9 ± 3.0
116 - 150	0.4 - 0.6	73.9 ± 9.3	77.1 ± 3.2
116 - 150	0.6 - 0.8	106.0 ± 9.1	111.6 ± 3.2
116 - 150	0.8 - 1.0	128.0 ± 9.2	146.8 ± 3.3
116 - 150	1.0 - 1.2	168.0 ± 9.3	183.0 ± 3.2
116 - 150	1.2 - 1.4	209.0 ± 9.6	206.2 ± 3.3
116 - 150	1.4 - 1.6	219 ± 10	228.0 ± 3.5
116 - 150	1.6 - 1.8	243 ± 12	246.4 ± 3.8
116 - 150	1.8 - 2.0	212 ± 14	219.4 ± 4.6
116 - 150	2.0 - 2.2	164 ± 16	150.1 ± 6.1
116 - 150	2.2 - 2.4	94 ± 34	105 ± 11
150 - 200	0.0 - 0.2	19 ± 17	20.6 ± 3.5
150 - 200	0.2 - 0.4	51 ± 18	67.1 ± 3.6
150 - 200	0.4 - 0.6	101 ± 17	111.4 ± 3.4
150 - 200	0.6 - 0.8	137 ± 17	146.3 ± 3.6
150 - 200	0.8 - 1.0	169 ± 17	196.7 ± 3.7
150 - 200	1.0 - 1.2	236 ± 17	238.7 ± 3.6
150 - 200	1.2 - 1.4	268 ± 18	264.9 ± 3.6
150 - 200	1.4 - 1.6	280 ± 21	294.9 ± 3.6
150 - 200	1.6 - 1.8	302 ± 20	297.7 ± 4.3
150 - 200	1.8 - 2.0	266 ± 23	264.8 ± 5.6
150 - 200	2.0 - 2.2	197 ± 30	192.8 ± 7.5
150 - 200	2.2 - 2.4	127 ± 49	105.7 ± 1.6

order, but DYTurbo is fully prepared to consider the BSM operators at higher orders in QCD. At the current state, it is not ready to perform a full calculation in the SMEFT at NLO, since it does not include any new loop induced terms, but it can still be valuable if we want to compare qualitatively the impact of NP-corrected loop diagrams with other subleading contributions in the SM regime. Apart from that, DYTurbo is capable of imposing the same kinematic cuts that are present in any LHC measurement and it natively outputs cross section distributions in the transverse momentum $\{p_T, Y, \sqrt{\hat{s}}, \theta^*\}$ kinematic variables.

Alternatively, we could have also used a Monte Carlo (MC) event generator such as MadGraph [196] to produce the theoretical predictions in both the SM and NP regimes. We ultimately settled for DYTurbo due to the lack of statistical uncertainties in their estimations, which are the main error source both in Drell-Yan $\mathrm{A_{FB}}$ measurements at the LHC and in the MadGraph calculations. More generally, integrators provide more precise predictions than MC generators, and they do not require intensive parameter tuning to produce acceptable results.

We use DYTurbo to produce predictions for the 2D $\mathrm{A_{FB}}$ distribution in Table 6.1 in the NP regime at linear order. We use the CT10 PDF set [311] and apply the same kinematic cuts present in the analysis of Ref. [185]. As for further experimental effects, we minimize their presence by building the theoretical expression of the asymmetry in an analogue way to Eq. (4.23):

$$\mathrm{A}^{\mathrm{th}}_{\mathrm{FB,ij}} = \mathrm{A}^{\mathrm{SM}}_{\mathrm{FB,ij}} \left(1 + \alpha_{ij,k}\, C_k\right), \tag{6.2}$$

where the i, j indices correspond to the rapidity and dilepton mass bins and C_k cover the entire Wilson coefficient list in Eq. (6.1). The numerical factors $\alpha_{ij,k}$ are calculated with DYTurbo, while the SM predictions are taken from Table 6.1.

As for the statistic test, we apply again a Gaussian likelihood akin to the one in Eq. (3.7):

$$\chi^2\left(c_k\right) = \sum_{i,j} \left(\frac{\mathrm{A}^{\mathrm{SM}}_{\mathrm{FB},ij}\left(1 + \alpha_{ij,k} C_k\right) - \mathrm{A}^{\mathrm{exp}}_{\mathrm{FB,ij}}}{\delta \mathrm{A}_{\mathrm{FB,ij}}} \right)^2, \tag{6.3}$$

where the $\mathrm{A_{FB}}$ theoretical and experimental errors are summed in quadrature in $\delta \mathrm{A}_{\mathrm{FB},ij}$. We neglect small correlation effects between bins. Upon minimizing this expression, we obtain the following uncorrelated limits on orthogonal combinations of the couplings:

$$M \begin{pmatrix} \delta g_L^{Zu} \\ \delta g_R^{Zu} \\ \delta g_L^{Zd} \\ \delta g_R^{Zd} \\ \left[\hat{C}_{lq}\right]_{11} \\ \left[C_{lu}\right]_{11} \\ \left[C_{ld}\right]_{11} \\ \left[C_{eq}\right]_{11} \\ \left[C_{eu}\right]_{11} \\ \left[C_{ed}\right]_{11} \end{pmatrix} = \begin{pmatrix} -5.3 \pm 2.6 \\ 4.1 \pm 1.5 \\ 1.1 \pm 0.8 \\ -0.01 \pm 0.37 \\ -0.08 \pm 0.25 \\ 0.081 \pm 0.046 \\ -0.055 \pm 0.018 \\ -0.022 \pm 0.012 \\ 0.0320 \pm 0.0089 \\ -0.0052 \pm 0.0044 \end{pmatrix}, \tag{6.4}$$

where the matrix M is given by:

$$M = \begin{pmatrix} 0.042 & -0.128 & 0.050 & -0.500 & 0.161 & -0.030 & -0.282 & -0.021 & -0.302 & -0.729 \\ 0.050 & -0.219 & 0.073 & -0.807 & -0.110 & 0.115 & 0.185 & -0.119 & 0.230 & 0.408 \\ -0.014 & 0.063 & -0.169 & 0.098 & 0.311 & 0.492 & 0.197 & -0.756 & -0.052 & -0.075 \\ 0.00 & -0.035 & 0.109 & -0.015 & 0.134 & 0.052 & 0.849 & 0.319 & -0.353 & -0.139 \\ 0.141 & 0.165 & -0.086 & 0.021 & -0.535 & 0.146 & 0.255 & -0.015 & 0.569 & -0.499 \\ -0.081 & -0.233 & 0.689 & 0.158 & -0.389 & 0.467 & -0.140 & -0.031 & -0.223 & 0.017 \\ 0.740 & 0.137 & -0.324 & -0.027 & -0.239 & 0.273 & -0.113 & 0.128 & -0.380 & 0.149 \\ 0.633 & -0.362 & 0.377 & 0.179 & 0.264 & -0.338 & 0.088 & -0.203 & 0.242 & -0.053 \\ -0.102 & -0.816 & -0.448 & 0.172 & -0.011 & 0.218 & -0.026 & 0.186 & 0.090 & -0.055 \\ 0.105 & 0.185 & 0.147 & -0.031 & 0.532 & 0.515 & -0.147 & 0.467 & 0.379 & -0.013 \end{pmatrix}. \tag{6.5}$$

As we can see, we are able to set limits on five independent combinations of the NP couplings at the percent level. This represents a significant upgrade over the two directions that we were able to constrain convincingly in Chapter 4. Thus, we already appreciate an immediate benefit from the inclusion of data from outside the Z peak when considering the role that hadron colliders can play in the electroweak fit.

We can also study the limits that we get when considering only one operator at a time:

$$\begin{pmatrix} \delta g_L^{Zu} \\ \delta g_R^{Zu} \\ \delta g_L^{Zd} \\ \delta g_R^{Zd} \\ \left[\hat{C}_{lq}\right]_{11} \\ [C_{lu}]_{11} \\ [C_{ld}]_{11} \\ [C_{eq}]_{11} \\ [C_{eu}]_{11} \\ [C_{ed}]_{11} \end{pmatrix} = \begin{pmatrix} -0.029 \pm 0.014 \\ -0.0165 \pm 0.0094 \\ -0.040 \pm 0.014 \\ 0.031 \pm 0.039 \\ -0.0166 \pm 0.0080 \\ -0.0069 \pm 0.0080 \\ 0.033 \pm 0.028 \\ -0.0098 \pm 0.0090 \\ -0.022 \pm 0.011 \\ 0.053 \pm 0.085 \end{pmatrix}. \tag{6.6}$$

Looking at these limits, we observe that the ATLAS observables are similarly sensitive to vertex corrections and four-fermion couplings. Instead, the main gradient in sensitivity is found between up quark couplings and down quark couplings. This is not surprising considering that the limits are extracted from proton-proton collisions. Due to the parton composition of the proton, we will generally be more sensitive to up quark interactions than to down quark interactions.

Now, restricting ourselves to the information coming from the peak, we obtain the limits:

$$\begin{pmatrix} -0.10 & 0.23 & -0.09 & 0.96 \\ -0.72 & -0.63 & 0.28 & 0.10 \\ -0.15 & -0.26 & -0.95 & -0.04 \\ -0.68 & 0.69 & -0.08 & -0.24 \end{pmatrix} \begin{pmatrix} \delta g_L^{Zu} \\ \delta g_R^{Zu} \\ \delta g_L^{Zd} \\ \delta g_R^{Zd} \end{pmatrix} = \begin{pmatrix} -2.2 \pm 3.4 \\ 0.11 \pm 0.12 \\ 0.013 \pm 0.043 \\ 0.011 \pm 0.013 \end{pmatrix}, \tag{6.7}$$

to be compared with the limits from Eq. (4.28), which we reinstate here:

$$\begin{pmatrix} 0.21 & 0.19 & 0.46 & 0.84 \\ 0.03 & -0.07 & -0.87 & 0.49 \\ 0.83 & -0.54 & 0.02 & -0.10 \\ 0.51 & 0.82 & -0.17 & -0.22 \end{pmatrix} \begin{pmatrix} \delta g_L^{Zu} \\ \delta g_R^{Zu} \\ \delta g_L^{Zd} \\ \delta g_R^{Zd} \end{pmatrix} = \begin{pmatrix} -10 \pm 4 \\ 0.5 \pm 0.4 \\ 0.04 \pm 0.06 \\ -0.001 \pm 0.005 \end{pmatrix}, \tag{6.8}$$

If we look at both sets of bounds, we can immediately notice that the best limit that we get from the A_{FB} data is around three times worse than the ones we get from A_4. This is mainly

because the high rapidity data bins in the A_4 data set ($1.6 < |Y| < 2.5$ and $2.5 < |Y| < 3.6$) are the ones that constrain the best the vertex corrections. Comparatively, the rapidity in the A_{FB} measurement only goes up to 2.4, so here we do not have access to the full constraining power held within the LHC Drell-Yan events. This should change if we decided to include the forward rapidity region data measured on the electron channel.

Now, we incorporate the results in Eq. (6.4) to the EW global fit, removing the previous input coming from the ATLAS A_4 measurement at the Z peak. We start by computing the marginalized limits in the $U(3)^5$-symmetric limit:

$$\begin{pmatrix} \\ \delta g_L^{W\ell} \\ \delta g_L^{Ze} \\ \delta g_R^{Ze} \\ \delta g_L^{Zu} \\ \delta g_R^{Zu} \\ \delta g_L^{Zd} \\ \delta g_R^{Zd} \\ C_{lq}^{(1)} \\ C_{lq}^{(3)} \\ C_{lu} \\ C_{ld} \\ C_{eq} \\ C_{eu} \\ C_{ed} \\ C_{ll}^{(1)} \\ C_{ll}^{(3)} \\ C_{le} \\ C_{ee} \end{pmatrix} = \begin{pmatrix} \text{w/o ATLAS DY} \\ -0.31(0.79) \\ -0.10(0.21) \\ -0.18(0.22) \\ -2.0(1.8) \\ -2.7(3.8) \\ 1.2(1.2) \\ 11.0(5.9) \\ -17.3(8.8) \\ -3.1(2.2) \\ 21(16) \\ 26(24) \\ -2(15) \\ 1.4(9.8) \\ 29(17) \\ 5.4(3.2) \\ -1.0(1.6) \\ 0.2(1.3) \\ -2.7(3.0) \end{pmatrix} \times 10^{-3} \to \begin{pmatrix} \text{w/ } Z \text{ peak } A_4 \\ -0.26(0.78) \\ -0.09(0.21) \\ -0.17(0.22) \\ -1.3(1.6) \\ -1.1(3.1) \\ 1.1(1.2) \\ 10.4(5.8) \\ -18.3(8.7) \\ -2.2(1.8) \\ 23(16) \\ 29(24) \\ -1(15) \\ 3.5(9.4) \\ 29(17) \\ 5.3(3.2) \\ -0.9(1.6) \\ 0.2(1.3) \\ -2.7(3.0) \end{pmatrix} \times 10^{-3} \to \begin{pmatrix} \text{w/ 2D } A_{FB} \\ -0.25(0.77) \\ -0.11(0.21) \\ -0.18(0.22) \\ -2.9(1.5) \\ -4.8(3.1) \\ 1.3(1.1) \\ 11.8(5.5) \\ -18.9(8.1) \\ -4.0(1.9) \\ 28(11) \\ 33(17) \\ -1.0(9.5) \\ 0.2(9.7) \\ 33(14) \\ 5.3(3.2) \\ -0.9(1.6) \\ 0.2(1.3) \\ -2.7(3.0) \end{pmatrix} \times 10^{-3}, \tag{6.9}$$

where we omit the correlation matrix and the limits in the second column correspond to the ones calculated in Eq. (5.67). Note that, even though they share the same name, the δg couplings in this expression also account for interactions involving second and third generation quarks. As we can observe, we get a mild improvement on the couplings that were constrained the least in the original fit from Ref. [132], which we highlighted in red. If we compute the one-at-a-time limits, we observe that hardly any change is produced by the inclusion of the ATLAS inputs.

The inclusion of the new input from ATLAS is much more spectacular if we go to a flavor general setup. The main improvement is that we gain a new probe into several new combinations of four-fermion WCs. Critically, these additions allow us to drop some of the $\hat{C}$ parameters that were introduced in Eq. (3.10) to deal with the blind directions in the global fit of Chapter 3. Namely, we can stop constraining $[\hat{C}_{eq}]_{ee11}$, $[\hat{C}_{lu}]_{ee11}$, $[\hat{C}_{ld}]_{ee11}$, $[\hat{C}_{eu}]_{ee11}$, $[\hat{C}_{ed}]_{ee11}$ and $[\hat{C}_{eq}]_{\mu\mu 11}$ and instead set limits on the corresponding "non-hatted" parameters plus $[C_{lq}^{(1)}]_{ee11}$, $[C_{ed}]_{\mu\mu 11}$ and $[C_{eu}]_{\mu\mu 11}$.

Taking these changes into account, we obtain the following marginalized limits

$$\begin{pmatrix} \delta g_L^{We} \\ \delta g_L^{W\mu} \\ \delta g_L^{W\tau} \\ \delta g_L^{Ze} \\ \delta g_R^{Ze} \\ \delta g_L^{Z\mu} \\ \delta g_R^{Z\mu} \\ \delta g_L^{Z\tau} \\ \delta g_R^{Z\tau} \\ \delta g_R^{Wq_1} \\ \delta g_L^{Zu} \\ \delta g_R^{Zu} \\ \delta g_L^{Zd} \\ \delta g_R^{Zd} \\ \delta g_L^{Zc} \\ \delta g_R^{Zc} \\ \delta g_L^{Zs} \\ \delta g_R^{Zs} \\ \delta g_L^{Zb} \\ \delta g_R^{Zb} \end{pmatrix} = \begin{pmatrix} -1.9(2.6) \\ -0.7(2.2) \\ 0.4(3.5) \\ -0.21(28) \\ -0.42(27) \\ 0.1(1.2) \\ 0.0(1.4) \\ -0.09(59) \\ 0.62(62) \\ -4.7(8.1) \\ -25(15) \\ 1(24) \\ -14(24) \\ 2(73) \\ -1.1(3.6) \\ -3.4(5.3) \\ -3(22) \\ 31(43) \\ 3.2(1.7) \\ 22(8.8) \end{pmatrix} \times 10^{-3}, \quad \begin{pmatrix} [C_{ll}]_{eeee} \\ [C_{le}]_{eeee} \\ [C_{ee}]_{eeee} \\ [C_{ll}]_{e\mu\mu e} \\ [C_{ll}]_{ee\mu\mu} \\ [C_{le}]_{e\mu\mu e} \\ [C_{le}]_{ee\mu\mu} \\ [C_{le}]_{\mu\mu ee} \\ [C_{ee}]_{ee\mu\mu} \\ [C_{ll}]_{e\tau\tau e} \\ [C_{ll}]_{ee\tau\tau} \\ [C_{le}]_{ee\tau\tau} \\ [C_{le}]_{\tau\tau ee} \\ [C_{ee}]_{ee\tau\tau} \\ [\hat{C}_{ll}]_{\mu\mu\mu\mu} \\ [C_{ll}]_{\mu\tau\tau\mu} \\ [C_{le}]_{\mu\tau\tau\mu} \end{pmatrix} = \begin{pmatrix} 1.03(38) \\ -0.22(22) \\ 0.19(38) \\ -0.56(79) \\ 0.1(2.0) \\ 11.4(6.8) \\ 0.3(2.2) \\ -0.2(2.1) \\ 0.3(2.3) \\ -0.61(68) \\ 2(11) \\ -2.3(7.2) \\ 1.7(7.2) \\ -1(12) \\ 2(21) \\ 1.5(1.9) \\ 19(15) \end{pmatrix} \times 10^{-2}, \tag{6.10}$$

$$\begin{pmatrix} [C_{lq}^{(1)}]_{ee11} \\ [C_{lq}^{(3)}]_{ee11} \\ [C_{eq}]_{ee11} \\ [C_{lu}]_{ee11} \\ [C_{ld}]_{ee11} \\ [C_{eu}]_{ee11} \\ [C_{ed}]_{ee11} \\ [C_{lequ}^{(1)}]_{ee11} \\ [C_{ledq}]_{ee11} \\ [C_{lequ}^{(3)}]_{ee11} \\ [\hat{C}_{lq}^{(3)}]_{ee22} \\ [C_{lu}]_{ee22} \\ [\hat{C}_{ld}]_{ee22} \\ [C_{eq}]_{ee22} \\ [C_{eu}]_{ee22} \\ [\hat{C}_{ed}]_{ee22} \\ [\hat{C}_{lq}^{(3)}]_{ee33} \\ [C_{ld}]_{ee33} \\ [C_{eq}]_{ee33} \\ [C_{ed}]_{ee33} \end{pmatrix} = \begin{pmatrix} -15(15) \\ -1.8(2.2) \\ 2(11) \\ 4.9(9.0) \\ 6(11) \\ -15(18) \\ -16(22) \\ -0.017(60) \\ -0.018(57) \\ 0.023(66) \\ -61(32) \\ 2.4(8.0) \\ -300(130) \\ -21(28) \\ -87(46) \\ 270(140) \\ -8.5(8.0) \\ -1(10) \\ -3.1(5.1) \\ 18(20) \end{pmatrix} \times 10^{-2}, \quad \begin{pmatrix} [C_{lq}^{(3)}]_{\mu\mu 11} \\ [C_{lq}^{(1)}]_{\mu\mu 11} \\ [C_{lu}]_{\mu\mu 11} \\ [C_{ld}]_{\mu\mu 11} \\ [C_{eq}]_{\mu\mu 11} \\ [C_{eu}]_{\mu\mu 11} \\ [C_{ed}]_{\mu\mu 11} \\ \epsilon_P^{d\mu}(2\text{ GeV}) \\ [C_{lq}^{(3)}]_{\tau\tau 11} \\ [C_{lequ}^{(3)}]_{\tau\tau 11} \\ \epsilon_P^{d\tau}(2\text{ GeV}) \end{pmatrix} = \begin{pmatrix} 0.9(3.0) \\ -2.4(4.3) \\ 2.4(5.7) \\ 2(15) \\ -7(19) \\ 40(47) \\ 30(79) \\ -0.069(95) \\ -2.1(2.2) \\ -0.4(1.2) \\ 0.98(85) \end{pmatrix} \times 10^{-2},$$

where we omit the correlation matrix and we have again substituted the ATLAS A_4 input at the Z peak we used in Chapter 4 by the (on- and off-peak) A_{FB} measurements from Ref. [185]. We

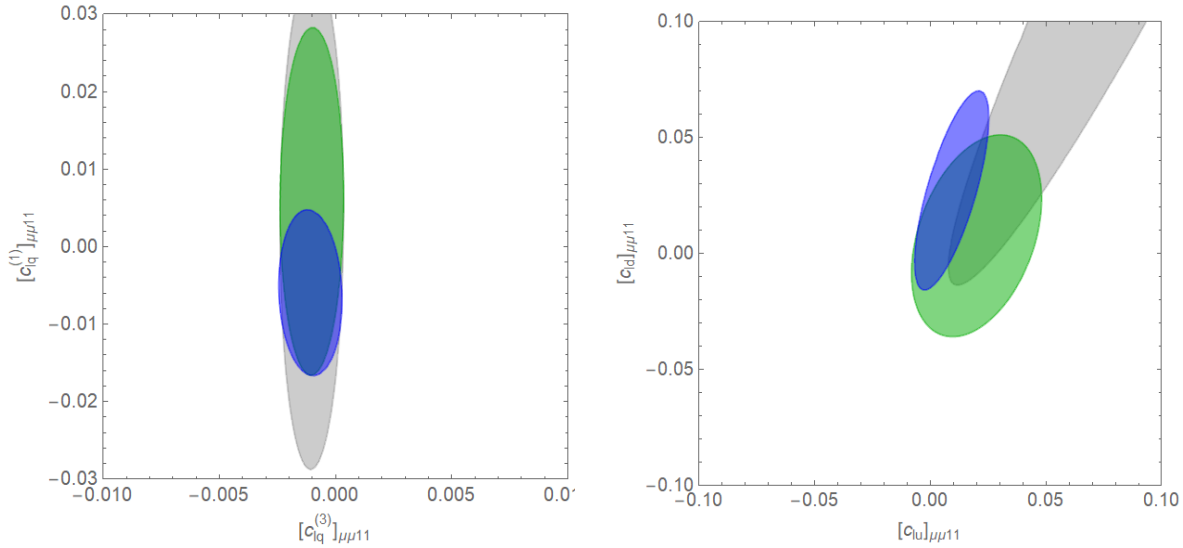

Fig. 6.1: Left panel: 1-sigma bounds $\left(\Delta\chi^2 \simeq 2.3\right)$ on the SMEFT Wilson coefficients $[C_{lq}^{(3)}]_{\mu\mu 11}$ and $[C_{lq}^{(1)}]_{\mu\mu 11}$ from a global fit on the EWPO in the flavor-generic SMEFT including different combinations of the COHERENT and 2D A_{FB} inputs. We omit the Z peak A_4 measurements since it has no sensitivity to 4-fermion couplings. We show regions with just the EWPO (gray), with the EWPO and COHERENT (green), and with both ATLAS A_{FB} and COHERENT inputs added to the EWPO (blue). Right panel: The same for the $[C_{ld}]_{\mu\mu 11}$-$[C_{lu}]_{\mu\mu 11}$ pair of Wilson coefficients. All WCs not shown in the plots are set to zero.

have highlighted in blue the limits on the new variables and in red the notable improvements on the preexisting ones.

Concerning the new variables, in the majority of cases we observe that the limits are worse than what we found for their hatted counterparts. This is not surprising if we consider that the new ATLAS input is strongly sensitive only to very specific combinations of these couplings, so their corresponding limits end up being suboptimal due to large correlations.

As for the improvement on previous limits, we can appreciate that the 2D A_{FB} ATLAS information is able to constrain the light-quark vertex corrections better than the Z-peak A_4 data in a marginalized setting. We can also observe that we have achieved a tighter constraint on δg_L^{Zs}, despite it not being probed directly by the new inputs. We attribute this change to the reorganization of the correlation patterns. Finally, we get better limits on the LLQQ couplings that involve muons. This can be explained by noting that these parameters cannot be constrained using LEP, which being an electron-positron collider has zero sensitivity to muon and quark interactions at tree level. Instead, we can only obtain limits on them using less precise experiments such as CHARM [285], CDHS [286], and CCFR [287], which were primarily designed to investigate muon-neutrino scattering on nuclei. Thus, having any additional input easily allows us to substantially improve on the preexisting bounds. The impact that the new ATLAS data has on the LLQQ muon couplings is much more notable on NP settings with a smaller number of parameters. The role that the 2D A_{FB} measurements can play in some of these scenarios is illustrated in Fig. 6.1.

This is the extent of the results we currently have for this project as of the writing of this thesis. Before moving on, it is interesting to comment how our study compares to other works that also seek to probe four-fermion operators in Drell-Yan observables using the LHC as their primary

input. This kind of studies are relatively popular in the particle physics community mainly due to their potential connection to B meson anomalies and leptoquark models. For example, Refs. [312, 313] were the first ones to set limits on four-fermion coefficients by considering collider inputs, in particular the $pp \to e + \text{MET} + X$ and $pp \to e^+e^- + X$ channels at the LHC. A bit later, Ref. [314] did the same by looking at the Drell-Yan cross section and forward-backward asymmetry measured in the context of older ATLAS [315] and CMS [316, 317] dilepton searches. On their own end, Refs. [190, 318, 319] performed new physics searches on high-p_T tails of Drell-Yan events measured at run-II of LHC, and Refs. [320, 321] did the same but with a special focus on the complementarity of four-fermion operators and flavor-violating processes. Additionally, Ref. [222] examined four-fermion and other NP operators that first appear at 1 loop, and Refs. [322, 323] examined the potential interplay between PDFs and EFT operators.[1]

The main difference between the majority of these studies and our own is that we are working at a low energy range well away from the high-p_T tails. The limits obtained in that kind of phenomenological analyses will always be better than ours when it comes to four-fermion couplings, since they take advantage of the enhancement that these operators exhibit with the center-of-mass energy. However, this kind of constraining power comes with a caveat, which is that it requires the use of data measured at very high energy scales, in environments where the applicability of the SMEFT can be reasonably called into question. This issue is specially relevant in high-p_T analyses, since their limits are often driven by quadratic terms in the NP couplings. For a more detailed discussion on this topic, see Ref. [324] and section 5 in Ref. [132].

In contrast, our approach does not run into this problem at all, since all of our observables are measured at or below the electroweak scale. Furthermore, it gives us the opportunity to study the potential impact of four-fermion operators around scales well away from any UV cutoff and also to understand their complementarity with relevant BSM operators in lower energy environments.

We close this chapter by commenting on the next steps that we plan to take on this project. First of all, the measurements that were performed in the forward rapidity region for the electron channel in Ref. [185] offer a very interesting prospect for us, since they would enable us to probe combinations of NP couplings involving just one lepton species. This would be specially valuable in the context of a global fit, since it would allow us to set independent limits on more four-fermion couplings and thus diminish the correlations in the marginalized bounds. Plus, this data set covers a rapidity range that is very sensitive to vertex corrections, so we can expect to improve the limits on both types of WCs through its inclusion.

There is another piece of data in Ref. [185] that could be used for disentangling the different lepton couplings. When processing its data, ATLAS analyzes Drell-Yan production observables considering final state electron events and final state muon events separately and then combines them to produce the final measurements on the cross section and the FB asymmetry. However, these intermediate results could be very interesting for us, since they represent the exact same data set that we have examined here but distinguishing between different lepton flavors. Unfortunately, ATLAS does not publicly provide its data segmented on the lepton channels as of now.

Additionally, we plan on adding the totality of the measurements presented in Ref. [185] to the fit. In the results we have shown here we only considered the information coming from

[1]This last kind of studies are interesting beyond the specific context of four-fermion searches in Drell-Yan observables, since they explore the general possibility that new physics effects can be fitted away when performing PDF estimations. So far, this type of analyses indicate that the effects are small for SMEFT studies working with the current LHC results, but they could become important in the context of high-luminosity LHC data.

the A_{FB} observable, but ATLAS also reports results on the total cross section and the triple differential cross section measured across many bins in θ^*, Y and $\sqrt{\hat{s}}$. We expect that A_{FB} will be the most precise NP probe, but it is still worthwhile to consider every other available piece of data.

Apart from that, we are also considering the possibility of including similar measurements on Drell-Yan observables performed at other hadron collider experiments such as CMS and LHCb [325–328]. Even if they explore the exact same observables, their differences in the treatment of uncertainties, kinematic cuts and PDFs among other things can provide valuable information to contrast and complement any inputs coming from ATLAS.

Beyond the scope of the electroweak global fit, there is additional motivation for extending DYTurbo to include new physics contributions. Recently, Ref. [181] reported the most precise determination of the strong coupling constant ever obtained from collider data, extracted from the Drell-Yan transverse-momentum distribution measured by ATLAS. The theoretical framework involved in such an accomplishment is based on DYTurbo, and no new physics effects are considered in the estimation. At present there is no actual proof that BSM terms do not have a relevant impact on the p_T distribution at these scales. However, the framework developed for the present global fit could be repurposed to check this assumption quantitatively. Such a confirmation would also be interesting for the sake of our analysis, since it would indicate that p_T distributions of LHC Drell-Yan observables do not have access to any additional BSM effects other than the ones we have identified in the dilepton energy and rapidity distributions. Plus, it would reinforce the assumption that PDF extractions from Drell-Yan data at low and intermediate p_T are free of BSM effects.

All in all, these preliminary results follow up and expand on the prospects that we discussed at the end of Chapter 4. Hadron colliders over the recent years have carved themselves a place among the most important inputs for new physics searches at the electroweak scale. This fact is obvious when it comes to probes in the W boson sector, and over the course of this thesis we have repeatedly argued that the same is true for Z boson physics. In Chapter 4 we showed how ATLAS measurements were able to have a great impact on established bounds on vertex corrections set by very high precision experiments such as LEP, and here we have demonstrated how results extracted from the very same dataset also have the potential of greatly improving state-of-the-art limits on four-fermion contact interactions.

Chapter 7

Final remarks

Particle physics currently finds itself at an impasse for which no obvious solution is at hand. Indications coming from both the theoretical and experimental sides suggest that the SM, despite its enormous achievements, cannot be considered as the definitive theory of fundamental interactions. There is no clear clue pointing at what the physics beyond the Standard Model may be, but over the last years countless approaches have been tested out with the common objective of discovering any signal pointing to new physics. Out of all these ideas, the main one we have explored in this thesis is rooted in the use of EFTs. Having as a main priority covering as many types of NP signatures as possible, EFTs offer the ideal tool for performing phenomenological analyses in a systematic and model independent way. Critically, they are especially well suited for performing indirect NP searches, based on the examination of already established data. This kind of searches have merit even if no positive result is ever found. A multitude of NP scenarios can have an indirect observable impact on physics phenomena we already understand, so we can rule them out if no NP trace shows up in the end results of these studies.

In more concrete terms, this thesis has been devoted to the objective of mapping out all possible new physics contributions that can be characterized through the EFT framework in a low energy environment. Making use of the SMEFT as our main theoretical tool, we have performed a multiparameter global fit to determine which BSM signatures can be accessed and constrained by the information provided by precision measurements in the electroweak sector. Our starting point has been a global fit presented in Chapter 3. Using information from multiple high precision experiments including LEP, Tevatron, the LHC and low-energy data, that fit was able to provide solid constraints to 65 combinations of dimension-6 SMEFT Wilson coefficients at once. However, the observables in the fit were mainly sensitive to first generation quarks and leptons, which meant that a large collection of NP couplings were left unexplored. This, coupled with the presence of several blind directions, opened the door to many ways of expanding and optimizing this electroweak fit.

We started capitalizing on this opportunity in Chapter 4. There we presented the information from the Drell-Yan forward backward asymmetry measured by ATLAS at the Z boson pole as a valuable input to be added to the global fit. Our main motivation for its inclusion was the increasing levels of precision that the LHC was starting to display at the Z boson sector and their sensitivity to light quark vertex corrections. These NP couplings were the components of a linear combination of SMEFT parameters that was not constrained very well in the electroweak fit, so we hypothesized that the input from ATLAS could help in establishing a more convincing bound.

We were successful in this task, finding a direction in parameter space that was constrained at the permille level. This result, apart from strengthening the weak bound, served to illustrate the great constraining power that the LHC held for interactions linked to the Z boson and the important place that it can occupy in the electroweak fit.

We explored another type of improvement for the SMEFT global fit in Chapter 5, based on incorporating measurements from the COHERENT experiment to the collection of experimental inputs. To accomplish this, we implemented a new method developed for the description of generic NP corrections to neutrino experiments. The main result of our analysis was a set of marginalized limits on the three generalized weak charges $\tilde{Q}_f$, defined in association to the production and scattering of ν_e, ν_μ and $\bar{\nu}_\mu$ on the nuclear target. Upon translating these limits to the SMEFT language, we found a large collection of NP parameters that could be accessed by the observables at COHERENT. When added to the global fit, the data from COHERENT allowed us constrain two new combinations of WCs at percent level. All these results led us to the conclusion that, from the point of view of the SMEFT, COHERENT is the most sensitive neutrino-detection experiment, clearly superior in comparison to previous neutrino scattering experiments at higher energies.

Finally, in Chapter 6 we presented a work in development directed at expanding and improving on the results presented in Chapter 4. The main addition with respect to the previous work was a collection of measurements of the Drell-Yan forward-backward asymmetry covering a wide range of dilepton energies beyond the Z peak. The main attractive of the off-pole information was in its sensitivity to several combinations of 4-fermion couplings. The preliminary results we obtained were very promising, since they seem to be able to lift some blind directions that were found in the original electroweak fit. Further work needs to be done in order to exploit the full potential of the new LHC inputs, but we expect that they will prove themselves to be a very important piece in the optimization of the SMEFT global limits.

All in all, the main purpose of this thesis has been to contribute a little bit to the monumental challenge of understanding which physics can exist beyond the SM. Our focus has been on establishing model independent bounds on electroweak observables, a subfield of new physics searches in which much remains to be done. As particle physics continues its incursion into the precision era, we can expect that the limits on new physics coefficients will become more and more stringent. Despite all the work ahead of us, perhaps one day it will all add up and new physics will have no choice but to reveal itself through these precision studies.

Resumen de la tesi

A continuació, presentem una descripció resumida dels continguts de la tesi. Aquesta contindrà una introducció als temes principals del treball, una síntesi dels objectius a assolir, una explicació de la metodologia seguida, un resumen dels resultats principals i, per últim, una relació de les conclusions de la tesi al complet.

Introducció

El Model Estàndard és la teoria més important en el camp de la física de partícules. El seu major Su mayor mèrit és la descripció que ofereix de tres de les quatre interaccions fundamentals que es coneixen a la natura: la força electromagnètica, la força nuclear feble y la força nuclear forta. El Model Estàndard té la capacitat de emitir prediccions teòriques amb un nivell de precisió extraordinari, i ha sido contrastat de manera incessant en experimentos durante los últimos setenta años. Com a resultat d'aquest exhaustiu procés d'avaluació, el Model Estàndard avui s'erigeix com un formalisme teòric sòlid i com una ferramenta essencial per a qualsevol persona involucrada en el camp de la física de partícules. Al llarg del Capítol 1 vam presentar una descripció extensiva dels seus fonaments i característiques més importants.

No obstant això, malgrat els nombrosos èxits que ha aconseguit, és ben sabut que el Model Estàndard no es pot considerar com la descripció definitiva de la naturalesa al seu nivell més fonamental. Hi ha diverses indicacions que apunten a aquesta conclusió, tant del costat de la teoria com de l'experiment, les quals discutim breument al Capítol 1.4. Per exemple, el Model Estàndard no pot donar resposta a qüestions teòriques com el problema de CP fort, el problema de jerarquies o la dinàmica gravitatòria. D'altra banda, tampoc és capaç d'explicar observacions experimentals com les de la massa dels neutrins, la matèria i l'energia fosques o certes anomalies que posen en dubte les seves prediccions.

Malgrat totes aquestes flaqueses, de moment no s'ha trobat solució per a cap d'aquestes qüestions. El motiu principal pel qual succeeix això és que cap d'aquests problemes implica una inconsistència interna en el si de la teoria o una contradicció directa a les seues prediccions. En la majoria dels casos, es tracta d'assumptes sobre els quals el Model Estàndard simplement no es pronuncia. Això ens deixa sense cap senyal concret que apunte a la millor manera de millorar la teoria i ens obliga a tantejar en la foscor buscant el que siga que hi haja més enllà del Model Estàndard.

Davant aquest panorama, molts professionals de la física de partícules s'han llançat a l'aventura de trobar l'extensió correcta del Model Estàndard o d'observar qualsevol tipus de fenomen que es puga catalogar inequívocament com a nova física. Aquesta és la línia d'investigació en la qual s'inscriu aquesta tesi. Existeixen molts enfocaments que es poden prendre a l'hora de realitzar

cerques de nova física. En el nostre cas, vam decidir prioritzar la independència de models i vam tractar d'identificar efectes de nova física a través de cerques indirectes. Amb aquest mètode, l'objectiu era determinar quines restriccions imposen els experiments de precisió sobre la física més enllà del Model Estàndard.

Objectius

L'objectiu principal d'aquesta tesi ha sigut la identificació de nous observables de precisió que puguen aportar informació rellevant sobre efectes més enllà del Model Estàndard. Per a estudiar aquest assumpte, vam emprar teories de camp efectives per a introduir contribucions de nova física en els observables. El motiu principal per a usar aquest formalisme va ser que ens permetia executar de manera simple cerques de nova física indirectes i amb independència de model. Les teories efectives segueixen els mateixos principis que una teoria quàntica de camps ordinària, però estan formulades de tal manera que només són capaces de descriure de manera directa la física que té lloc per davall d'una certa escala d'energia. Tota la física que es dona més enllà d'aqueix llindar és descrita de manera indirecta mitjançant operadors de dimensionalitat alta. Una teoria efectiva es pot formular a partir d'una teoria quàntica de camps "completa" si retenim tota la informació per davall d'una certa escala, l'anomenat entorn de baixa energia, i reexpressem tot el que quede per damunt a l'entorn d'alta energia com a contribucions indirectes. Un formalisme amb aquestes característiques ens pot ajudar a determinar quins elements d'una teoria són més importants entorn d'una escala determinada, i eixa informació en moltes ocasions es pot explotar per a simplificar computacions complicades. El fonament i la utilitat de les teories efectives s'expliquen detalladament al llarg del Capítol 2.

En el context d'anàlisi de física més enllà del Model Estàndard, les teories efectives ens poden resultar útils si assumim que la nova física en la formulació d'una teoria completa pertany naturalment a escales d'energia altes. Si extraiem la teoria efectiva associada a un model com aquest, tots els efectes de nova física seran capturats de manera indirecta pels operadors d'alta dimensionalitat o operadors efectius. Aquesta caracterització és útil fins i tot si no coneixem els detalls exactes de la física que existeix més enllà del Model Estàndard, ja que aquesta sempre prendrà la forma d'operadors efectius. Aquesta propietat era perfecta de cara a les nostres pretensions de fer cerques de nova física amb independència de models, ja que ens permetia abastar amb un mateix formalisme una gran varietat d'entorns de nova física.

Al llarg dels nostres estudis, emprem com a eina teòrica principal una teoria efectiva amb aquestes característiques, la qual vam introduir en el Capítol 2.2.1. Aquesta rep el nom de Teoria de Camp Efectiva del Model Estàndard (o SMEFT, per les seues sigles en anglés) en la literatura científica. La SMEFT pren com a entorn de baixa energia tota la física del Model Estàndard, mentre que l'entorn d'alta energia s'identifica mitjançant una caracterització indefinida de nova física. Aquest marc teòric és idoni per a realitzar cerques indirectes, ja que, de cara a plantejar una anàlisi fenomenològica, és possible reutilitzar els càlculs que ja s'han realitzat per a estudiar observables del Model Estàndard. Las caracterizaciones de dichos observables en el contexto de la SMEFT solamente se ven modificadas por pequeñas correcciones asociadas a los operadores efectivos. Les caracteritzacions d'aquests observables en el context de la SMEFT solament es veuen modificades per xicotetes correccions associades als operadors efectius. D'aquesta manera, les cerques de nova física indirectes amb la SMEFT es basen a ajustar els possibles valors dels nous paràmetres (els anomenats coeficients de Wilson) tenint en compte les observacions experimentals i les seues corresponents prediccions teòriques.

Les cerques de nova física que hem realitzat al llarg d'aquesta tesi s'han desenvolupat sobre la base de tot aquest suport teòric. D'aquesta manera, de cara a aconseguir el nostre objectiu principal, vam tractar d'estimar simultàniament els valors d'un gran nombre de coeficients de Wilson de la SMEFT mitjançant un ajust global. Sent més concrets, ens vam centrar en l'estudi d'efectes més enllà del Model Estàndard en observables electrofebles en escales menors al valor esperat en el buit del bosó de Higgs. Pel camí, vam intentar entendre quines contribucions de nova física afectaven a cada observable que vam investigar. A més, també vam voler estudiar com les aportacions de diferents experiments poden complementar-se de cara a optimitzar la qualitat de les estimacions.

Metodologia

Per a dur a terme els objectius d'aquesta tesi, vam treballar amb una combinació de diverses ferramentes teòriques i fonamentals. La ferramenta teòrica principal que hem utilitzat ha sigut la SMEFT, la qual presentem i descrivim en el Capítol 2 i també en la secció anterior. A l'hora de manejar-la, solament vam considerar operadors de dimensió sis com a màxim, ja que eren les contribucions més rellevants alienes al Model Estàndard. Per consistència, tan sols vam incloure contribucions lineals en aquests operadors en el càlcul d'observables. També vam haver d'encarregar-nos de seleccionar una base per als operadors, per a assegurar-nos que cobríem tots els termes independents a dimensió 6. En el nostre cas, vam triar la base de Higgs, la qual ens oferia el gran avantatge de tindre una correspondència intuïtiva entre els operadors de nova física i els observables als quals afecten. Des d'un punt de vista més tècnic, aquesta base també ens assegurava que els termes cinètics del lagrangià sempre foren diagonals i mantenia sota control contribucions de nova física indirectes associades a paràmetres lliures.

A part de la SMEFT, una altra teoria efectiva que utilitzem al llarg dels nostres estudis va ser la Teoria de Camps Efectiva Feble (o WEFT, per les seues sigles en anglés). Aquesta teoria segueix els mateixos principis que la SMEFT, però el seu rang de validesa té com a límit l'escala electrofeble. La WEFT ens va servir principalment per a examinar efectes de física més enllà del Model Estàndard en observables de baixa energia.

La resta de conceptes teòrics rellevants per al nostre treball els vam prendre del camp de l'estadística. Les nostres estimacions per als coeficients de Wilson les vam deduir a partir d'unes suposicions molt concretes sobre les dades experimentals que examinem. En el cas de comptar amb un gran nombre de dades, preníem que seguien una distribució de probabilitat gaussiana, en cas contrari els caracteritzàvem mitjançant una distribució poissoniana. Això ens va permetre aplicar una estimació de màxima versemblança per a extraure límits correlacionats i regions de confiança per als nostres paràmetres. En emprar aquest mètode, a vegades recorrem a l'ús de paràmetres de pertorbació per a modelitzar certs errors sistemàtics.

Un últim concepte estadístic important per a nosaltres va ser el de la marginalització. Aquest procediment es basa a avaluar la versemblança tenint en compte solament un subconjunt de coeficients de Wilson, al mateix temps que la minimitzem sobre tots els altres. Això ens va resulta útil sempre que volíem projectar l'espai de paràmetres sobre un subespai concret. Vam emprar aquest procediment sempre que volíem representar regions de confiança de manera gràfica, i també ens va servir per a minimitzar la presència dels paràmetres de pertorbació en els límits.

En el nostre treball sempre vam prioritzar la computació dels límits marginalitzats dels coeficients de Wilson, procurant incloure el major nombre possible en la funció de versemblança. D'aquesta manera, vam aconseguir maximitzar la utilitat dels ajustos globals de la SMEFT, per-

metent que els nostres límits siguen aplicables a una major quantitat de models de nova física. No obstant això, perquè això fora factible, vam haver de considerar conjunts de dades experimentals sensibles a una gran varietat combinacions dels coeficients de Wilson. Una descripció més detallada de tots aquests conceptes pot trobar-se en el Capítol 2.2.2.

Això és tot sobre les ferramentes teòriques que vam emprar per a les nostres cerques de nova física. Quant als recursos computacionals, la majoria de les nostres anàlisis estadístiques els vam fer servint-nos del programa Mathematica. Mitjançant aquest programa vam executar la minimització de les versemblances i vam representar les regions de confiança oportunes. A l'hora de produir prediccions teòriques per als observables que vam anar considerant, va haver-hi ocasions en les quals no era possible obtindre-les mitjançant un càlcul analític. Això va ser degut principalment al fet que molts dels observables que ens interessaven es mesuraven en col·lisionadors d'hadrons, els quals en general requereixen molts recursos per a estimar les dades que es mesuren en els seus experiments. En alguns casos, va ser suficient amb usar mètodes semianalítics en Mathematica per a tindre en compte efectes com les funcions de distribució de partons. No obstant això, en alguns moments les computacions es van tornar tan complicades que no vam tindre més remei que utilitzar ferramentes més sofisticades, com ara MadGraph o DYTurbo.

Considerant tots aquests instruments, passem a descriure el procediment que hem seguit per a realitzar l'ajust global electrofeble de la SMEFT en el Capítol 3. En primer lloc, vam prendre com a punt de partida un estudi previ que emprava una col·lecció d'observables de precisió provinents de LEP, Tevatron, LHC i altres experiments de baixa energia per a restringir 65 paràmetres de nova física independents simultàniament en un ajust global. Aquests els podem subdividir en 21 correccions a vèrtexs δg, 27 operadors de contacte amb 2 leptons i 2 quarks (LLQQ) i 17 operadors de contacte amb 4 leptons (LLLL). Els límits que es van obtindre en aquest ajust van ser:

$$\begin{pmatrix} \delta g_L^{We} \\ \delta g_L^{W\mu} \\ \delta g_L^{W\tau} \\ \delta g_L^{Ze} \\ \delta g_R^{Ze} \\ \delta g_L^{Z\mu} \\ \delta g_R^{Z\mu} \\ \delta g_L^{Z\tau} \\ \delta g_R^{Z\tau} \\ \delta g_R^{Wq_1} \\ \delta g_L^{Zu} \\ \delta g_R^{Zu} \\ \delta g_L^{Zd} \\ \delta g_R^{Zd} \\ \delta g_L^{Zc} \\ \delta g_R^{Zc} \\ \delta g_L^{Zs} \\ \delta g_R^{Zs} \\ \delta g_L^{Zt} \\ \delta g_L^{Zb} \\ \delta g_R^{Zb} \end{pmatrix} = \begin{pmatrix} -1.3(3.2) \\ -2.8(2.6) \\ 1.5(4.0) \\ -0.19(28) \\ 0.43(27) \\ 0.1(1.2) \\ 0.0(1.4) \\ -0.09(59) \\ 0.62(62) \\ -13(17) \\ -8(31) \\ 14(51) \\ -9(44) \\ 30(160) \\ -1.5(3.6) \\ -3.3(5.3) \\ 9(28) \\ 34(49) \\ -3(38) \\ 3.3(1.7) \\ 23(8.8) \end{pmatrix} \times 10^{-3}, \qquad \begin{pmatrix} [C_{ll}]_{eeee} \\ [C_{le}]_{eeee} \\ [C_{ee}]_{eeee} \\ [C_{ll}]_{e\mu\mu e} \\ [C_{ll}]_{ee\mu\mu} \\ [C_{le}]_{ee\mu\mu} \\ [C_{le}]_{\mu\mu ee} \\ [C_{ee}]_{ee\mu\mu} \\ [C_{ll}]_{e\tau\tau e} \\ [C_{ll}]_{ee\tau\tau} \\ [C_{le}]_{ee\tau\tau} \\ [C_{le}]_{\tau\tau ee} \\ [C_{ee}]_{ee\tau\tau} \\ [\hat{C}_{ll}]_{\mu\mu\mu\mu} \\ [C_{ll}]_{\mu\tau\tau\mu} \end{pmatrix} = \begin{pmatrix} 1.01(38) \\ -0.22(22) \\ 0.20(38) \\ -4.8(1.6) \\ 1.5(2.1) \\ 1.5(2.2) \\ -1.4(2.2) \\ 3.4(2.6) \\ 1.5(1.3) \\ 0(11) \\ -2.3(7.2) \\ 1.7(7.2) \\ -1(12) \\ -2(21) \\ 3.0(2.3) \end{pmatrix} \times 10^{-2},$$

$$\begin{pmatrix} [C_{lq}^{(3)}]_{ee11} \\ [\hat{C}_{eq}]_{ee11} \\ [\hat{C}_{lu}]_{ee11} \\ [\hat{C}_{ld}]_{ee11} \\ [\hat{C}_{eu}]_{ee11} \\ [\hat{C}_{ed}]_{ee11} \\ [C_{lequ}^{(1)}]_{ee11} \\ [C_{ledq}]_{ee11} \\ [C_{lequ}^{(3)}]_{ee11} \\ [\hat{C}_{lq}^{(3)}]_{ee22} \\ [C_{lu}]_{ee22} \\ [\hat{C}_{ld}]_{ee22} \\ [C_{eq}]_{ee22} \\ [C_{eu}]_{ee22} \\ [\hat{C}_{ed}]_{ee22} \\ [\hat{C}_{lq}^{(3)}]_{ee33} \\ [C_{ld}]_{ee33} \\ [C_{eq}]_{ee33} \\ [C_{ed}]_{ee33} \end{pmatrix} = \begin{pmatrix} -2.2(3.2) \\ 100(180) \\ -5(11) \\ -5(23) \\ -1(12) \\ -4(21) \\ -0.080(75) \\ -0.079(74) \\ -0.02(19) \\ -61(32) \\ 2.4(8.0) \\ -310(130) \\ -21(28) \\ -87(46) \\ 270(140) \\ -8.6(8.0) \\ -1(10) \\ -3.2(5.1) \\ 18(20) \end{pmatrix} \times 10^{-2} \ , \quad \begin{pmatrix} [C_{lq}^{(3)}]_{\mu\mu 11} \\ [C_{lq}^{(1)}]_{\mu\mu 11} \\ [C_{lu}]_{\mu\mu 11} \\ [C_{ld}]_{\mu\mu 11} \\ [\hat{C}_{eq}]_{\mu\mu 11} \\ \epsilon_P^{d\mu}(2 \text{ GeV}) \end{pmatrix} = \begin{pmatrix} -1.2(3.9) \\ 1.3(7.6) \\ 15(12) \\ 25(34) \\ 4(41) \\ -0.02(15) \end{pmatrix} \times 10^{-2},$$

on ometem la matriu de correlació. Aquests límits aprofiten al màxim la sensibilitat a l'efecte de nova física dels observables electrofebles, però també presenten un ampli marge de millora. Per a començar, les dades emprades tenen sensibilitat principalment a partícules de la primera generació, per la qual cosa existeixen molts paràmetres que no es poden explorar mitjançant les dades incloses en aquest ajust. A més, existeixen moltes combinacions de paràmetres que, o bé no es poden restringir en absolut amb la informació dels observables, o solament és possible establir una restricció molt feble per ells.

Tenint en compte aquests punts a millorar, el gruix del treball d'aquesta tesi, descrit en els Capítols 4, 5 i 6, va consistir a incloure noves dades experimentals per a optimitzar aquest ajust global. Ens vam enfocar en experiments que recentment han aconseguit nivells de precisió suficients com per a contribuir significativament a l'ajust. En particular, vam examinar dades mesurades en el pol del bosó Z pel LHC i mesures de dispersió coherent i elàstica entre neutrins i nuclis fetes per l'experiment COHERENT. Per a cadascun d'aquests experiments vam reproduïr en primer lloc els observables que han mesurat, després els vam introduir correccions de nova física i finalment vam tractar de posar límits als coeficients de Wilson als quals tenien sensibilitat. Una vegada vam aconseguir entendre bé sobre quines combinacions de paràmetres podem establir restriccions, vam incorporar aquestes noves mesures a l'ajust global.

Resultats

Nova física de precisió al pol del Z del LHC

Amb vista a millorar els resultats de l'ajust global, en el Capítol 4 vam exposar la nostra primera aportació. Aquesta va consistir a incloure els límits a paràmetres de nova física que es podien extraure d'unes certes mesures del LHC. En particular, aqueixes dades corresponien a l'observable de l'asimetria *forward-backward* ($\mathrm{A_{FB}}$) dels processos Drell-Yan. Els processos

Drell-Yan són aquells que tenen com a estat inicial un parell quark antiquark i produeixen un parell de leptons amb càrregues oposades per mitjà d'un bosó Z o un fotó. Aquest procés incorre en una asimetria en l'angle en el qual s'emeten els leptons finals a causa de la violació de paritat que es dona en les interaccions del Z. Aquest observable en particular ens interessava perquè tenia una sensibilitat notable a correccions de vèrtexs del Z amb quarks up i down. En l'ajust global original, aquesta família de paràmetres no estan molt restringits. Donat l'alt nivell de precisió que el LHC és capaç d'aconseguir en les anàlisis d'aquest observable, esperàvem que les seues mesures foren capaces de proporcionar-nos una col·lecció de límits més sòlids.

A l'hora d'implementar-la, vam recòrrer a una mesura d'ATLAS del coeficient angular A_4. Aquesta quantitat, en ser integrada sobre la totalitat de l'espai fàsic, està relacionada amb A_{FB} mitjançant un factor de proporcionalitat: $\mathrm{A}_{\mathrm{FB}} = 3/8\,\mathrm{A}_4$. Fixant-nos en el pol del bosó Z, teníem accés a 4 mesures independents de l'observable, obtingudes a partir de la seua integració en quatre rangs de *rapidity*.

Quant a la seua predicció teòrica, la vam deduir a partir d'un càlcul semianalític a nivell d'arbre. Tenint en compte els efectes de nova física a ordre lineal, vam extraure com a factor global el valor de l'observable en el Model Estàndard i el vam substituïr pel valor predit per l'experiment. D'aquesta manera, vam ser capaços de tindre en compte moltes correccions necessàries per a modelitzar l'observable correctament en el context d'un col·lisionador d'hadrons.

Incloent tota aquesta informació en una versemblança gaussiana, vam obtindre els següents límits sobre combinacions ortogonals i sense correlació dels coeficients de Wilson:

$$\begin{pmatrix} 0.21\delta g_L^{Zu} + 0.19\delta g_R^{Zu} + 0.46\delta g_L^{Zd} + 0.84\delta g_R^{Zd} \\ 0.03\delta g_L^{Zu} - 0.07\delta g_R^{Zu} - 0.87\delta g_L^{Zd} + 0.49\delta g_R^{Zd} \\ 0.83\delta g_L^{Zu} - 0.54\delta g_R^{Zu} + 0.02\delta g_L^{Zd} - 0.10\delta g_R^{Zd} \\ 0.51\delta g_L^{Zu} + 0.82\delta g_R^{Zu} - 0.17\delta g_L^{Zd} - 0.22\delta g_R^{Zd} \end{pmatrix} = \begin{pmatrix} -10 \pm 4 \\ 0.5 \pm 0.4 \\ 0.04 \pm 0.06 \\ -0.001 \pm 0.005 \end{pmatrix} .$$

Com podem veure, les dades d'ATLAS només ens serveixen per a obtindre dues restriccions per davall del 10% sobre les correccions de vèrtexs. No obstant això, un d'aquests límits aconsegueix un nivell del 0.5%. Això significa que la A_{FB} per si sola no ens serveix per a restringir simultàniament tots els paràmetres que ens interessen. No obstant això, la qualitat de la restricció ens indica que pot arribar a ser molt important si combinem aquests resultats amb la resta de components de l'ajust global.

Això va ser just el que vam fer a continuació. Com a resultat de l'ajust global combinat, vam obtindre els següents límits:

$$\begin{pmatrix} \delta g_L^{We} \\ \delta g_L^{W\mu} \\ \delta g_L^{W\tau} \\ \delta g_L^{Ze} \\ \delta g_L^{Z\mu} \\ \delta g_L^{Z\tau} \\ \delta g_R^{Ze} \\ \delta g_R^{Z\mu} \\ \delta g_R^{Z\tau} \\ \delta g_L^{Zu} \\ \delta g_R^{Zu} \\ \delta g_L^{Zd} \\ \delta g_R^{Zd} \\ \delta g_L^{Zs} \\ \delta g_R^{Zs} \\ \delta g_L^{Zc} \\ \delta g_R^{Zc} \\ \delta g_L^{Zb} \\ \delta g_R^{Zb} \\ \delta m_W \end{pmatrix} = \begin{pmatrix} -1.2 \pm 3.2 \\ -2.7 \pm 2.6 \\ 1.5 \pm 4.0 \\ -0.20 \pm 0.28 \\ 0.1 \pm 1.2 \\ -0.09 \pm 0.59 \\ -0.43 \pm 0.27 \\ 0.0 \pm 1.4 \\ 0.62 \pm 0.62 \\ -12 \pm 24 \\ -5 \pm 32 \\ -20 \pm 37 \\ -30 \pm 130 \\ 11 \pm 28 \\ 32 \pm 48 \\ -1.5 \pm 3.6 \\ -3.3 \pm 5.3 \\ 3.1 \pm 1.7 \\ 21.9 \pm 8.8 \\ 0.29 \pm 0.16 \end{pmatrix} \times 10^{-3}. \tag{7.1}$$

on només mostrem les restriccions sobre les correccions de vèrtexs i ometem de nou la matriu de correlació. Per a computar aquests resultats, també vam tindre en compte algunes actualitzacions menors sobre les dades emprades en l'ajust global original.

Examinant aquests resultats, la conclusió principal que vam extraure d'aquest estudi és que existia una complementarietat clara entre les mesures d'observables Drell-Yan en col·lisionadors d'hadrons i les dades de LEP en el context de l'ajust global. Per tant, vam determinar que la informació del LHC era indispensable de cara a optimitzar els nostres límits sobre els coeficients de Wilson de la SMEFT. A més, una observació addicional que vam poder fer és que la importància de les dades d'ATLAS també era present en escenaris en els quals apareixen solament uns pocs paràmetres de nova física. Aquesta apreciació es veu il·lustrada en la Fig. 7.1.

Aquest treball, malgrat els excel·lents resultats que ha aportat, presentava diversos punts en els quals es pot millorar. En primer lloc, pel costat experimental, la qualitat de les mesures es podia incrementar mitjançant la reducció de l'error estadístic. Açò és fàcil d'aconseguir simplement mitjançant l'extracció d'un major nombre de dades. Així mateix, els nostres límits també podien millorar mitjançant un refinament equivalent de la predicció teòrica, tant en el Model Estàndard com en el context de la SMEFT.

Des d'un punt de vista més fenomenològic, vam observar que l'ajust es podia beneficiar de la inclusió d'informació d'altres experiments, així com de l'examinació d'altres observables Drell-Yan mesurats al LHC. Aquest últim punt en concret el vam estar explorant nosaltres mateixos en un estudi que representava una continuació directa al qual hem discutit ací. Els avanços en aquest projecte els descrivim en el Capítol 6, i també oferim una discussió sobre aquest tema més endavant en aquest resum.

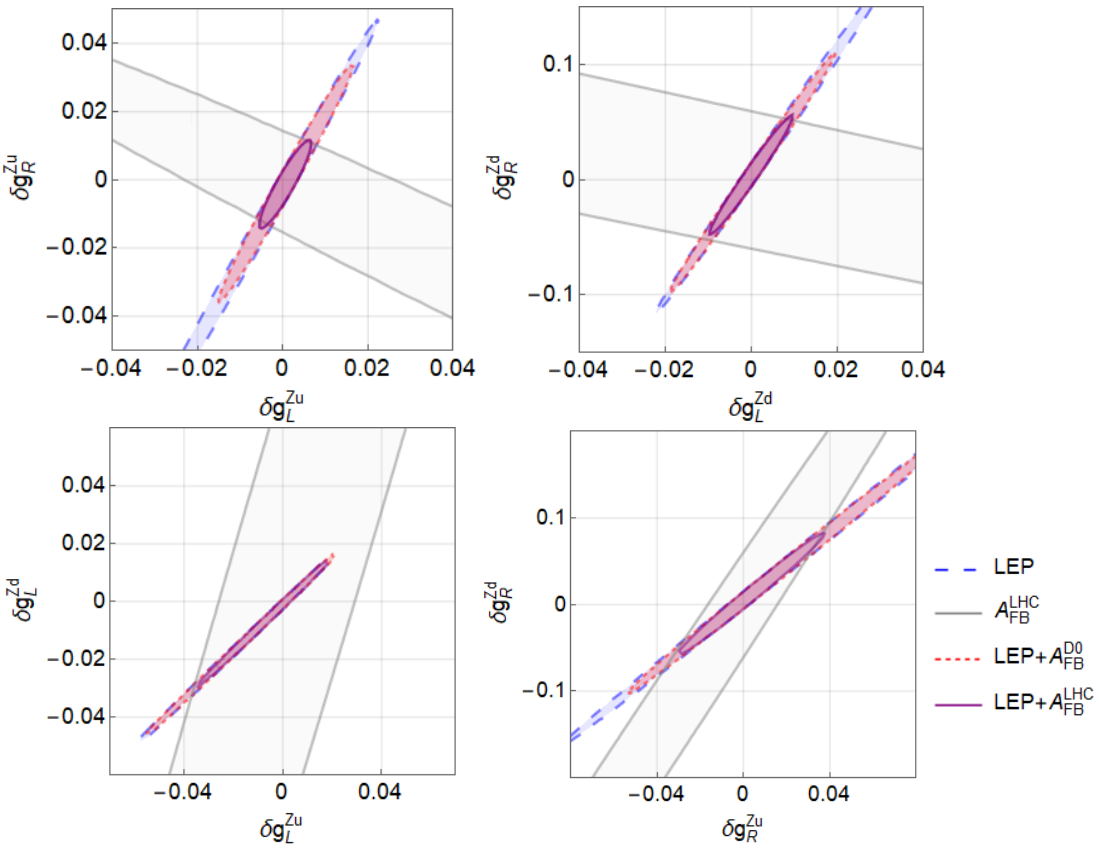

Fig. 7.1: Regions permeses (amb un nivell de confiança del 95%) per a quatre parells de correccions al vèrtex del Z amb quarks lleugers. En cada cas, només les correccions que es mostren en la figura són diferents de zero.

Cerca de nova física amb neutrins a l'experiment COHERENT

Un altre experiment que ens va ajudar en la nostra missió pertanyia al sector dels neutrins. Una circumstància que dificulta l'exploració d'efectes de nova física en observables de neutrins és que aquest tipus de partícules tenen menys probabilitats d'interactuar que la resta d'elements del Model Estàndard. Una excepció a aquesta norma es dona en el cas de la dispersió coherent i elàstica de neutrins i nuclis (o CEνNS per les seues sigles en anglés). El motiu és que les interaccions vectorials entre els neutrins i els nucleons se sumen de manera coherent, per la qual cosa la seua amplitud de probabilitat és inusualment gran. Aquest tipus d'interaccions de neutrins s'havien mesurat experimentalment fa poc temps, per la qual cosa era el moment idoni per a explorar quina nova física podia estar associada al CEνNS en el context de l'ajust global.

El desenvolupament complet d'aquest estudi va ser presentat en el Capítol 5. Per a dur-ho a terme, una circumstància important que calia tindre en compte des del principi era que ens disposàvem a estudiar un observable de baixa energia. A les escales característiques del procés, la SMEFT no era la ferramenta més adequada per a estudiar efectes de nova física. En el seu lloc, vam pensar en gastar la WEFT, que és una teoria efectiva enfocada en la física que té lloc a energies més xicotetes. No obstant això, la interacció de CEνNS involucra de manera directa a elements nuclears, per la qual cosa la WEFT tampoc ens oferia la descripció més natural de l'observable. Com a molt, ens permetia descriure el procés en termes d'interaccions de 4 fermions

entre quarks i neutrins. Per tant, vam haver d'establir una connexió unívoca entre la WEFT i una teoria efectiva de nucleons. En aquesta nova teoria, les interaccions vindrien descrites en termes de càrregues febles associades als protons i neutrons.

Una vegada ja ens havíem decidit pel marc teòric més adequat per al CEνNS, vam haver d'entendre bé com s'havia mesurat la interacció. L'experiment que va realitzar la primera mesura de CEνNS és COHERENT. Per a fer-ho, van emprar un muntatge experimental que consistia en una font d'espal·lació que emetia neutrins com a resultats de les desintegracions successives d'un pion i un muon. Aquest procés feia que es produïren tres neutrins amb un perfil temporal característic: un per part del pion i dos més per part del muon amb un retard temporal. Tots ells eren dirigits cap a uns objectius nuclears, on interactuaven mitjançant CEνNS. En el moment de realitzar l'estudi COHERENT havia sigut capaç de detectar CEνNS en dos objectius nuclears, en una mescla de cesi i iode i en argó líquid.

Tenint en compte tot aquest procés, vam dur a terme una caracterització completa de tot l'observable en el règim de nova física abastant tant producció com detecció, així com els tres tipus de neutrins. Per a això, vam emprar un procediment basat completament en fonaments de teoria quàntica de camps. El marc teòric amb el qual vam treballar tenia un caràcter general, sent aplicable a qualsevol observable que es puga interpretar com una combinació d'interaccions de corrent carregat en producció i corrent neutre en detecció, com és el cas per a COHERENT.

Fent ús d'ell, vam ser capaços de tindre en compte correctament la combinació més general d'efectes de nova física associats a l'observable que es mesurava en COHERENT. Com a resultat, vam ser capaços de produir prediccions d'esdeveniments de CEνNS en distribucions bidimensionals d'energia de reculada i temps per als dos objectius nuclears. De forma resumida, les nostres prediccions es poden expressar com:

$$\frac{dN}{dt\,dT} = g_\pi(t)\,\frac{dN^{\text{prompt}}}{dT} + g_\mu(t)\,\frac{dN^{\text{delayed}}}{dT}\ , \tag{7.2}$$

on $g_{\pi,\mu}(t)$ capturen les dependències temporals dels neutrins provinents del pion i del muon respectivament. La dependència dels neutrins del pion (*prompt*) i els del muon (*delayed*) en l'energia de reculada T venen donats per

$$\begin{aligned}
\frac{dN^{\text{prompt}}}{dT} &= n_{\text{POT}} f^{\pi}_{\nu/p} \frac{N_T\,\mathcal{F}(q^2)^2\ (m_{\mathcal{N}}+T)}{8\,\pi^2 v^4 L^2} f_\mu(T)\tilde{Q}^2_\mu\ , \\
\frac{dN^{\text{delayed}}}{dT} &= n_{\text{POT}} f^{\mu}_{\nu/p} \frac{N_T\,\mathcal{F}(q^2)^2\ (m_{\mathcal{N}}+T)}{8\,\pi^2 v^4 L^2} \left(f_e(T)\,\tilde{Q}^2_e + f_{\bar{\mu}}(T)\,\tilde{Q}^2_{\bar{\mu}}\right)\ ,
\end{aligned} \tag{7.3}$$

on els paràmetres $\tilde{Q}$ són les càrregues febles generalitzades, que contenen totes les contribucions de nova física. El significat de la resta de paràmetres involucrats en aquestes expressions està explicat detalladament en el Capítol 5.2. Aquestes expressions representaven un dels resultats més importants del nostre estudi, ja que són capaços de donar compte de totes les relacions que es poden donar entre efectes de nova física de producció i detecció. A més, també es poden reduir a la caracterització NSI si prenem que només existeix nova física en detecció.

A part de servir-nos d'aquesta caracterització, per a reproduir els resultats de COHERENT també necessitàvem tindre en compte les múltiples conjuntures experimentals que es donaven per a cada mesura. Una vegada fet això, vam produir estimacions marginalitzades per a les càrregues febles tant del cesi-iode com de l'argó. Aquests límits els vam reexpressar a continuació en termes dels coeficients de Wilson de la WEFT. És en aquesta teoria efectiva on és més senzill identificar les combinacions de paràmetres que es veuen restringides directament per COHERENT. En

l'ajust lineal vam obtindre els límits:

$$\begin{pmatrix} 0.63 & -0.70 & -0.22 & 0.24 \\ 0.21 & -0.24 & 0.63 & -0.70 \\ -0.68 & -0.61 & 0.30 & 0.27 \\ 0.30 & 0.27 & 0.68 & 0.61 \end{pmatrix} \begin{pmatrix} \epsilon_{ee}^{dd} \\ \epsilon_{ee}^{uu} \\ \epsilon_{\mu\mu}^{dd} \\ \epsilon_{\mu\mu}^{uu} \end{pmatrix} = \begin{pmatrix} 2.0 \pm 5.7 \\ -0.2 \pm 1.7 \\ -0.037 \pm 0.042 \\ -0.004 \pm 0.013 \end{pmatrix} . \tag{7.4}$$

Per tant, gràcies a COHERENT podem restringir al per cent dues noves direccions en l'espai de paràmetres. Els coeficients que les componen van associats a operadors de 4 fermions amb dos quarks i dos neutrins en la WEFT.

A partir d'aquests resultats, el següent pas era incorporar-los en el llenguatge de la SMEFT a l'ajust global. Juntament amb aquestes noves mesures, també vam afegir nombroses actualitzacions respecte als observables que vam considerar en l'estudi anterior del A_{FB}. En conjunt, ens van servir per a obtindre els següents límits marginalitzats:

$$\begin{pmatrix} \delta g_L^{We} \\ \delta g_L^{W\mu} \\ \delta g_L^{W\tau} \\ \delta g_L^{Ze} \\ \delta g_R^{Ze} \\ \delta g_L^{Z\mu} \\ \delta g_R^{Z\mu} \\ \delta g_L^{Z\tau} \\ \delta g_R^{Z\tau} \\ \delta g_R^{Wq_1} \\ \delta g_L^{Zu} \\ \delta g_R^{Zu} \\ \delta g_L^{Zd} \\ \delta g_R^{Zd} \\ \delta g_L^{Zc} \\ \delta g_R^{Zc} \\ \delta g_L^{Zs} \\ \delta g_R^{Zs} \\ \delta g_L^{Zb} \\ \delta g_R^{Zb} \end{pmatrix} = \begin{pmatrix} -1.8(2.6) \\ -0.6(2.2) \\ 0.2(3.5) \\ -0.21(28) \\ -0.42(27) \\ 0.2(1.2) \\ 0.0(1.4) \\ -0.09(59) \\ 0.61(62) \\ -3.8(8.1) \\ -7(22) \\ 4(29) \\ -13(35) \\ 10(120) \\ -1.5(3.6) \\ -3.3(5.3) \\ 14(27) \\ 34(46) \\ 3.2(1.7) \\ 22(8.8) \end{pmatrix} \times 10^{-3}, \qquad \begin{pmatrix} [C_{ll}]_{eeee} \\ [C_{le}]_{eeee} \\ [C_{ee}]_{eeee} \\ [C_{ll}]_{e\mu\mu e} \\ [C_{ll}]_{ee\mu\mu} \\ [C_{le}]_{e\mu\mu e} \\ [C_{le}]_{ee\mu\mu} \\ [C_{le}]_{\mu\mu ee} \\ [C_{ee}]_{ee\mu\mu} \\ [C_{ll}]_{e\tau\tau e} \\ [C_{ll}]_{ee\tau\tau} \\ [C_{le}]_{ee\tau\tau} \\ [C_{le}]_{\tau\tau ee} \\ [C_{ee}]_{ee\tau\tau} \\ [\hat{C}_{ll}]_{\mu\mu\mu\mu} \\ [C_{ll}]_{\mu\tau\tau\mu} \\ [C_{le}]_{\mu\tau\tau\mu} \end{pmatrix} = \begin{pmatrix} 1.03(38) \\ -0.22(22) \\ 0.19(38) \\ -0.56(80) \\ 0.1(2.0) \\ 11.4(6.8) \\ 0.3(2.2) \\ -0.2(2.1) \\ 0.2(2.3) \\ -0.60(68) \\ 2(11) \\ -2.3(7.2) \\ 1.7(7.2) \\ -1(12) \\ 2(21) \\ 1.5(1.9) \\ 19(15) \end{pmatrix} \times 10^{-2},$$

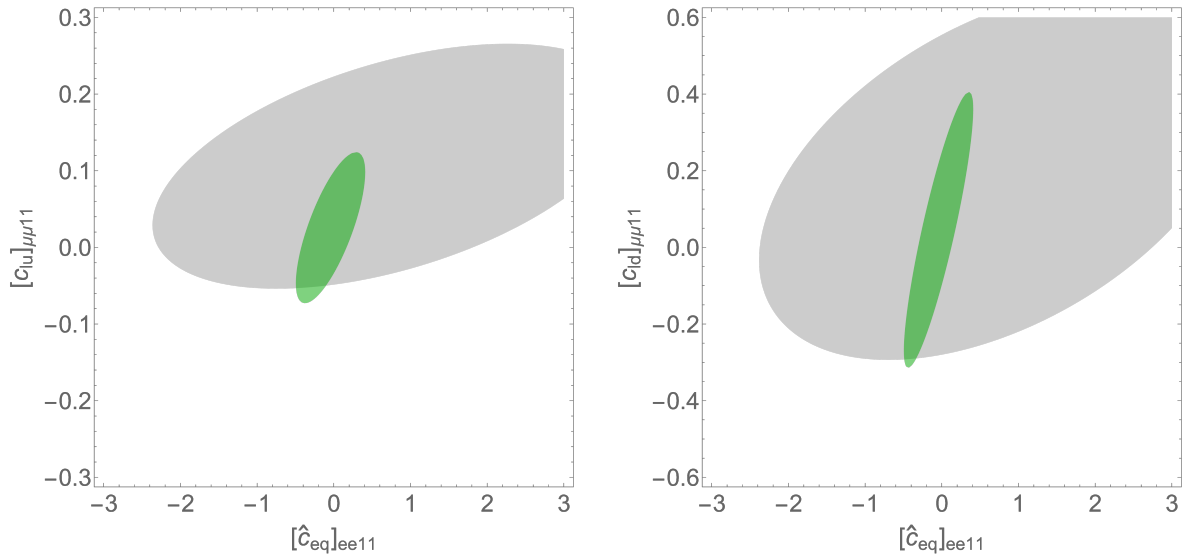

Fig. 7.2: Panell esquerre: Límits marginalitzats a 1 sigma ($\Delta\chi^2 \simeq 2.3$) sobre els coeficients de la SMEFT $[\hat{C}_{eq}]_{ee11}$ i $[C_{lu}]_{\mu\mu 11}$ a partir d'un ajust global als observables de precisió electrofebles sense (grisa) i amb (verda) dades de COHERENT. Panell dret: El mateix per als coeficients de Wilson $[\hat{C}_{eq}]_{ee11}$-$[C_{ld}]_{\mu\mu 11}$.

$$\begin{pmatrix} [C_{lq}^{(3)}]_{ee11} \\ [\hat{C}_{eq}]_{ee11} \\ [\hat{C}_{lu}]_{ee11} \\ [\hat{C}_{ld}]_{ee11} \\ [\hat{C}_{eu}]_{ee11} \\ [\hat{C}_{ed}]_{ee11} \\ [C_{lequ}^{(1)}]_{ee11} \\ [C_{ledq}]_{ee11} \\ [C_{lequ}^{(3)}]_{ee11} \\ [\hat{C}_{lq}^{(3)}]_{ee22} \\ [C_{lu}]_{ee22} \\ [\hat{C}_{ld}]_{ee22} \\ [C_{eq}]_{ee22} \\ [C_{eu}]_{ee22} \\ [\hat{C}_{ed}]_{ee22} \\ [\hat{C}_{lq}^{(3)}]_{ee33} \\ [C_{ld}]_{ee33} \\ [C_{eq}]_{ee33} \\ [C_{ed}]_{ee33} \end{pmatrix} = \begin{pmatrix} 0.1(2.8) \\ -4(30) \\ -2.5(8.7) \\ -2(18) \\ -3.1(9.4) \\ -2(17) \\ -0.017(60) \\ -0.018(57) \\ 0.023(66) \\ -61(32) \\ 2.4(8.0) \\ -300(130) \\ -21(28) \\ -87(46) \\ 250(140) \\ -8.5(8.0) \\ -1(10) \\ -3.1(5.1) \\ 18(20) \end{pmatrix} \times 10^{-2} \,, \quad \begin{pmatrix} [C_{lq}^{(3)}]_{\mu\mu 11} \\ [C_{lq}^{(1)}]_{\mu\mu 11} \\ [C_{lu}]_{\mu\mu 11} \\ [C_{ld}]_{\mu\mu 11} \\ [\hat{C}_{eq}]_{\mu\mu 11} \\ \epsilon_P^{d\mu}(2\text{ GeV}) \\ [C_{lq}^{(3)}]_{\tau\tau 11} \\ [C_{lequ}^{(3)}]_{\tau\tau 11} \\ \epsilon_P^{d\tau}(2\text{ GeV}) \end{pmatrix} = \begin{pmatrix} 3.0(3.5) \\ -0.2(5.8) \\ 2.5(6.5) \\ 5(24) \\ 3(41) \\ -0.080(95) \\ -0.3(2.8) \\ -0.3(1.2) \\ 0.93(85) \end{pmatrix} \times 10^{-2},$$

on hem ressaltat els límits que milloren substancialment gràcies a COHERENT. Il·lustrem també l'impacte d'aquest experiment de manera gràfica en la Fig. 7.2.

A la vista d'aquests resultats, vam poder comprovar què la informació provinent de l'experiment COHERENT és molt important en el context de l'ajust global de la SMEFT. De fet, COHERENT va resultar ser l'experiment més rellevant de cara a establir límits en el sector de nova física de neutrins.

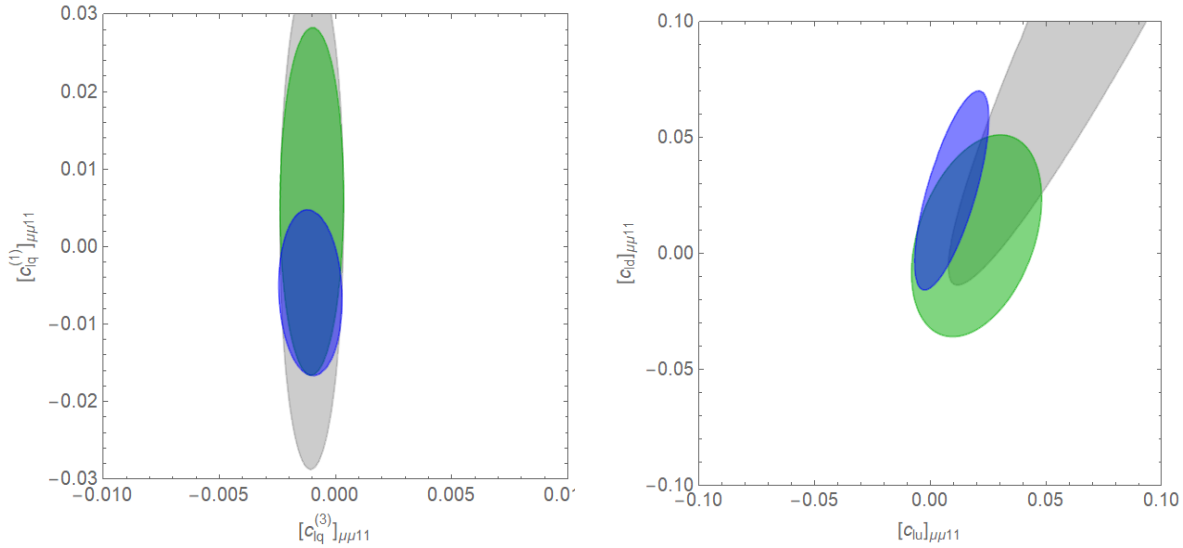

Fig. 7.3: Panell esquerre: Límits a 1 sigma $\left(\Delta\chi^2 \simeq 2.3\right)$ sobre els coeficients de Wilson de la SMEFT $[C_{lq}^{(3)}]_{\mu\mu 11}$ i $[C_{lq}^{(1)}]_{\mu\mu 11}$ a partir d'un ajust global amb observables de precisió electrofebles incloent diferents combinacions de dades de COHERENT i la distribució 2D del $\mathrm{A_{FB}}$. Ometem les mesures de $\mathrm{A_4}$ en el pic del Z ja que no tenen sensibilitat als coeficients de 4 fermions. Mostrem regions amb els observables electrofebles originals (gris), amb els observables electrofebles i amb COHERENT (verd), i amb aquests dos al costat de les mesures del $\mathrm{A_{FB}}$ d'ATLAS (blau). Panell dret: El mateix per al parell de coeficients de Wilson $[C_{ld}]_{\mu\mu 11}$-$[C_{lu}]_{\mu\mu 11}$. Tots els paràmetres de la SMEFT que no ensenyem estan posats a zero.

Més enllà del pol del Z al LHC

Després de concloure el projecte que vam presentar en el Capítol 4, hi havia moltes maneres de millorar l'ajust global usant informació del LHC. D'entre elles, vam optar per l'opció d'ampliar l'espectre d'energies en el conjunt de mesures de l'asimetria *forward-backward* dels processos Drell-Yan. Aquesta via ens permetia accedir de manera immediata a un major nombre de combinacions de les correccions de vèrtexs. A més ens donava l'oportunitat d'explorar la sensibilitat del LHC a operadors de 4 fermions entorn de l'escala electrofeble.

El desenvolupament d'aquest estudi el presentem detalladament en el Capítol 6, sent aquest encara un treball en desenvolupament. En ell, vam tractar d'executar una cerca de nova física en processos Drell-Yan dins i fora del pol del Z. Per a això, vam realitzar una examinació de dades de la $\mathrm{A_{FB}}$ mesurats per ATLAS que cobrien un ampli rang de valors d'energia i *rapidity* en una distribució 2D. En aquest cas, de cara a emetre prediccions teòriques per als observables, ens vam servir d'una ferramenta més sofisticada que un simple càlcul semianalític. En el seu lloc, vam gastar el programa DYTurbo, especialitzat en càlculs d'observables Drell-Yan en el context de col·lisionadors d'hadrons.

Gràcies a la nova informació del LHC vam ser capaços d'establir els següents límits a 10 combinacions dels paràmetres de la SMEFT:

$$M \begin{pmatrix} \delta g_L^{Zu} \\ \delta g_R^{Zu} \\ \delta g_L^{Zd} \\ \delta g_R^{Zd} \\ \left[\hat{C}_{lq}\right]_{11} \\ [C_{ed}]_{11} \\ [C_{eu}]_{11} \\ [C_{eq}]_{11} \\ [C_{ld}]_{11} \\ [C_{lu}]_{11} \end{pmatrix} = \begin{pmatrix} 5.3 \pm 3.2 \\ 3.9 \pm 1.8 \\ 1.3 \pm 1.0 \\ -0.02 \pm 0.48 \\ -0.18 \pm 0.30 \\ -0.084 \pm 0.058 \\ -0.058 \pm 0.022 \\ -0.018 \pm 0.015 \\ 0.030 \pm 0.011 \\ -0.0051 \pm 0.0059 \end{pmatrix}.$$

Els coeficients dels operadors de 4 fermions es defineixen al Capítol 6 y la matriu M és:

$$M = \begin{pmatrix} -0.043 & -0.130 & -0.049 & -0.510 & -0.161 & 0.724 & 0.299 & 0.028 & 0.277 & 0.024 \\ 0.049 & 0.217 & 0.071 & 0.799 & -0.111 & 0.416 & 0.234 & -0.124 & 0.193 & 0.120 \\ -0.013 & -0.068 & -0.170 & -0.109 & 0.304 & -0.084 & -0.048 & -0.750 & 0.215 & 0.493 \\ 0.008 & 0.027 & 0.112 & 0.012 & 0.091 & -0.168 & -0.322 & 0.330 & 0.857 & 0.058 \\ 0.138 & -0.164 & -0.083 & -0.024 & -0.550 & -0.488 & 0.589 & -0.023 & 0.199 & 0.139 \\ 0.088 & -0.240 & -0.685 & 0.159 & 0.383 & -0.023 & 0.222 & 0.031 & 0.152 & -0.469 \\ 0.766 & -0.152 & -0.292 & 0.026 & -0.223 & 0.148 & -0.367 & 0.121 & -0.115 & 0.265 \\ 0.600 & 0.410 & 0.364 & -0.189 & 0.258 & -0.061 & 0.250 & -0.207 & 0.094 & -0.345 \\ -0.106 & 0.788 & -0.480 & -0.160 & -0.022 & -0.048 & 0.072 & 0.205 & -0.035 & 0.245 \\ 0.106 & -0.183 & 0.163 & 0.028 & 0.543 & -0.016 & 0.390 & 0.459 & -0.142 & 0.500 \end{pmatrix}.$$

Aquests resultats preliminars són molt prometedors, ja que en incloure'ls juntament amb la resta d'observables en l'ajust global, ens permeten retirar múltiples direccions cegues a les quals no podíem accedir prèviament. Els límits complets que vam obtindre en el nou ajust global van ser els següents:

$$\begin{pmatrix} \delta g_L^{We} \\ \delta g_L^{W\mu} \\ \delta g_L^{W\tau} \\ \delta g_L^{Ze} \\ \delta g_R^{Ze} \\ \delta g_L^{Z\mu} \\ \delta g_R^{Z\mu} \\ \delta g_L^{Z\tau} \\ \delta g_R^{Z\tau} \\ \delta g_R^{Wq_1} \\ \delta g_L^{Zu} \\ \delta g_R^{Zu} \\ \delta g_L^{Zd} \\ \delta g_R^{Zd} \\ \delta g_L^{Zc} \\ \delta g_R^{Zc} \\ \delta g_L^{Zs} \\ \delta g_R^{Zs} \\ \delta g_L^{Zb} \\ \delta g_R^{Zb} \end{pmatrix} = \begin{pmatrix} -1.9(2.6) \\ -0.6(2.2) \\ 0.3(3.5) \\ -0.21(28) \\ -0.42(27) \\ 0.2(1.2) \\ 0.0(1.4) \\ -0.08(59) \\ 0.61(62) \\ -4.5(8.1) \\ -29(17) \\ 22(28) \\ -9(25) \\ 28(89) \\ -0.9(3.6) \\ -3.7(5.3) \\ -11(22) \\ 37(43) \\ 3.2(1.7) \\ 22(8.8) \end{pmatrix} \times 10^{-3}, \quad \begin{pmatrix} [C_{ll}]_{eeee} \\ [C_{le}]_{eeee} \\ [C_{ee}]_{eeee} \\ [C_{ll}]_{e\mu\mu e} \\ [C_{ll}]_{ee\mu\mu} \\ [C_{le}]_{e\mu\mu e} \\ [C_{le}]_{ee\mu\mu} \\ [C_{le}]_{\mu\mu ee} \\ [C_{ee}]_{ee\mu\mu} \\ [C_{ll}]_{e\tau\tau e} \\ [C_{ll}]_{ee\tau\tau} \\ [C_{le}]_{ee\tau\tau} \\ [C_{le}]_{\tau\tau ee} \\ [C_{ee}]_{ee\tau\tau} \\ [\hat{C}_{ll}]_{\mu\mu\mu\mu} \\ [C_{ll}]_{\mu\tau\tau\mu} \\ [C_{le}]_{\mu\tau\tau\mu} \end{pmatrix} = \begin{pmatrix} 1.03(38) \\ -0.22(22) \\ 0.19(38) \\ -0.56(80) \\ 0.1(2.0) \\ 11.4(6.8) \\ 0.3(2.2) \\ -0.2(2.1) \\ 0.2(2.3) \\ -0.60(68) \\ 2(11) \\ -2.3(7.2) \\ 1.7(7.2) \\ -1(12) \\ 2(21) \\ 1.5(1.9) \\ 19(15) \end{pmatrix} \times 10^{-2},$$

$$\begin{pmatrix} [C_{lq}^{(1)}]_{ee11} \\ [C_{lq}^{(3)}]_{ee11} \\ [C_{eq}]_{ee11} \\ [C_{lu}]_{ee11} \\ [C_{ld}]_{ee11} \\ [C_{eu}]_{ee11} \\ [C_{ed}]_{ee11} \\ [C_{lequ}^{(1)}]_{ee11} \\ [C_{ledq}]_{ee11} \\ [C_{lequ}^{(3)}]_{ee11} \\ [\hat{C}_{lq}^{(3)}]_{ee22} \\ [C_{lu}]_{ee22} \\ [\hat{C}_{ld}]_{ee22} \\ [C_{eq}]_{ee22} \\ [C_{eu}]_{ee22} \\ [\hat{C}_{ed}]_{ee22} \\ [\hat{C}_{lq}^{(3)}]_{ee33} \\ [C_{ld}]_{ee33} \\ [C_{eq}]_{ee33} \\ [C_{ed}]_{ee33} \end{pmatrix} = \begin{pmatrix} -11(16) \\ -2.6(2.3) \\ -6(13) \\ 6.5(9.8) \\ 6(11) \\ -9(19) \\ -10(24) \\ -0.017(60) \\ -0.018(57) \\ 0.023(66) \\ -61(32) \\ 2.4(8.0) \\ -300(130) \\ -21(28) \\ -87(46) \\ 250(140) \\ -8.5(8.0) \\ -1(10) \\ -3.1(5.1) \\ 18(20) \end{pmatrix} \times 10^{-2} \,, \quad \begin{pmatrix} [C_{lq}^{(3)}]_{\mu\mu 11} \\ [C_{lq}^{(1)}]_{\mu\mu 11} \\ [C_{lu}]_{\mu\mu 11} \\ [C_{ld}]_{\mu\mu 11} \\ [C_{eq}]_{\mu\mu 11} \\ [C_{eu}]_{\mu\mu 11} \\ [C_{ed}]_{\mu\mu 11} \\ \epsilon_P^{d\mu}(2\text{ GeV}) \\ [C_{lq}^{(3)}]_{\tau\tau 11} \\ [C_{lequ}^{(3)}]_{\tau\tau 11} \\ \epsilon_P^{d\tau}(2\text{ GeV}) \end{pmatrix} = \begin{pmatrix} 1.7(3.1) \\ -2.3(4.4) \\ 6.7(6.5) \\ 8(19) \\ -19(24) \\ 35(46) \\ 39(73) \\ -0.071(95) \\ -0.3(2.3) \\ -0.4(1.2) \\ 0.97(85) \end{pmatrix} \times 10^{-2},$$

on una vegada més ometem la matriu de correlació i hem ressaltat amb color blau els nous paràmetres que restringim i en color roig aquells que milloren gràcies a la distribució 2D del A_{FB}.

A la vista d'aquests resultats, va ser fàcil observar que els límits sobre les correccions de vèrtexs de quarks lleugers i els coeficients de 4 fermions que involucraven muons es veien millorats notablement. Aquesta millora sobre el sector de muons era d'esperar, ja que LEP no era sensible en absolut a ells i només podíem restringir aquest tipus de paràmetres mitjançant dades menys precises d'experiments de neutrins. L'impacte de la informació d'ATLAS és també visible en escenaris simples amb pocs paràmetres de nova física, tal com es pot observar en la Fig. 7.3.

Aquests han sigut els resultats principals que vam obtindre a partir de l'estudi presentat en el Capítol 6. Com a tasques addicionals de cara a finalitzar el treball, ens hem proposat examinar altres mesures del A_{FB} que siguen capaços de distingir canals leptònics. A més, ens interessa investigar més dades d'altres observables Drell-Yan mesurats per ATLAS i altres experiments del LHC.

Conclusions

El treball d'aquesta tesi representa un pas més cap a l'enteniment de la física que existeix més enllà del Model Estàndard. El nostre enfocament particular s'ha basat en anàlisis indirectes i amb independència de model. Aquesta cerca de nova física s'ha substanciat en la construcció d'un ajust global amb l'objectiu de restringir de manera simultània el major nombre de coeficients de Wilson de la SMEFT. Per a això, hem explotat la informació provinent de mesures de precisió a observables electrofeles.

La contribució més important d'aquesta tesi ha sigut la inclusió de dos nous tipus de mesures a l'ajust global: els processos Drell-Yan investigats al LHC i la dispersió coherent i elàstica de neutrins amb nuclis. En el futur, esperem que més observables es vagen afegint per a continuar delimitant tots els possibles efectes de nova física que es poden explorar en el sector electrofeble i finalment descobrir-la.

Appendix A

Numerical analysis of COHERENT observables

In this section we describe in detail the input used in our numerical analysis from Chapter 5.3, which is chosen in every case following closely the corresponding COHERENT prescription.

Before discussing the details that are specific to each measurement, let us show the expression that we use for the form factor, $\mathcal{F}(q^2)$, since that is a common input to all cases. We use the Helm parametrization [259], which gives the following expression for the neutron and proton form factors:

$$\mathcal{F}_{p/n}(q^2) = 3\frac{j_1(q\,R_{0,p/n})}{q\,R_{0,p/n}}e^{-q^2s^2/2}\ . \tag{A.1}$$

Here $j_1(x)$ is the order-1 spherical Bessel function of the first kind, $s = 0.9$ fm is the nuclear skin thickness [329] and $R_{0,p/n}$ is a function of s and the proton/neutron root-mean-square (rms) radius $R_{p/n}$ given by

$$R^2_{0,p/n} = \frac{5}{3}R^2_{p/n} - 5s^2\ . \tag{A.2}$$

The proton and neutron rms radii for the studied nuclei are taken from Refs. [252, 330, 331]

$$\begin{aligned} &R_p(\mathrm{Cs}) = 4.821(5)\ \mathrm{fm}, \quad &&R_p(\mathrm{I}) = 4.766(8)\ \mathrm{fm}, \quad &&R_p(\mathrm{Ar}) = 3.448(2)\ \mathrm{fm}, \\ &R_n(\mathrm{Cs}) = 5.09\ \mathrm{fm}, \quad &&R_n(\mathrm{I}) = 5.03\ \mathrm{fm}, \quad &&R_n(\mathrm{Ar}) = 3.55\ \mathrm{fm}. \end{aligned} \tag{A.3}$$

Following the COHERENT prescription, the uncertainty associated to this description of the form factor is included in our analysis through a nuisance parameter, as described below.

For the CsI analysis, we will take the average of $R_{p/n}(\mathrm{Cs})$ and $R_{p/n}(\mathrm{I})$ and of the nuclei masses. Moreover, as discussed in the main text, in both the LAr and the CsI cases we approximate neutron and proton form factors to be equal by taking the average of R_p and R_n. This simplifies significantly the presentation of intermediate results and it is not expected to have any impact in the final results for the WEFT Wilson coefficients, taking into account current COHERENT uncertainties. Different values for R_p and R_n, the Klein-Nystrand form factor [332] and the parametrization introduced in Ref. [333] were tested for the calculation of the total number of events, with no noticeable effects in the final results.

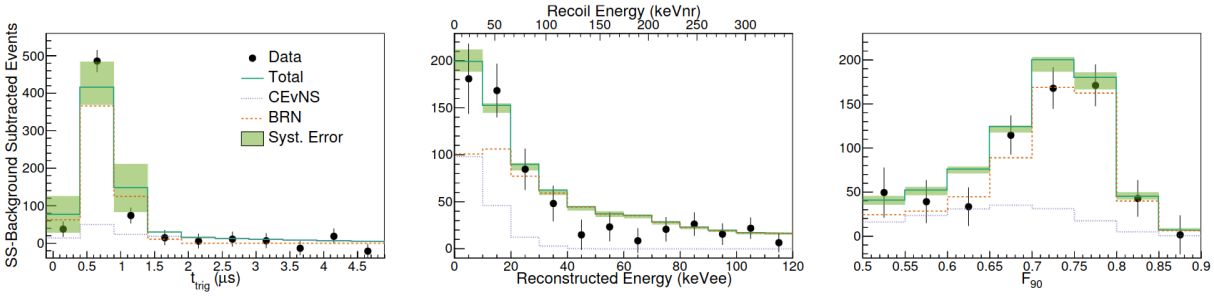

Fig. A.1: Projections of the predicted probability density function (PDF) for the events detected at the COHERENT LAr nuclear target on $t_{trigger}$ (left), recoil energy (center), and F_{90} (right) along with measured data and statistical errors. The SS background estimation has been substracted to better display the CEνNS prediction. The green band shows the envelope of fit results resulting from the $\pm 1\sigma$ systematic errors. Plot taken from Ref. [249].

Finally, we do not consider the contribution from neutrino electron scattering, which acts as an additional background source. This contribution was separated from the signal in the LAr analysis, but not in the CsI analysis. In both cases, its effect on the SM event rate is negligible, while for heavy NP scenarios its impact is also irrelevant [246, 248].

A.1. LAr measurement

The LAr dataset consists of a 3D distribution in recoil energy, time and the fraction of integrated amplitude within the first 90 ns after trigger (F_{90}) [249]. The corresponding 1D distributions in each of these quantities are displayed in Fig. A.1. The latter plays no direct role in our analysis, so we integrate over F_{90} and work with the resulting 2D recoil and time distribution. Our analysis covers the range $0 < T_{ee}^{rec}(\text{keV}) < 40$ and $0 < t(\mu s) < 5$, using 4x10 bins of equal width. These are the bins with a significant amount of CEνNS events.

The expected number of events per bin is given by

$$N_{ij}^{\text{th}}\left(\vec{Q}_{\text{Ar}}^2;\vec{x}\right) = N_{ij}^{\text{signal}}\left(\vec{Q}_{\text{Ar}}^2\right)\left(1+\alpha+\sum_{z=1,2}\alpha_{z,ij}(\epsilon_z)\right) + N_{ij}^{\text{bkg,pBRN}}\left(1+\beta_{\text{pBRN}}+\sum_{z=3,4,5}\alpha_{z,ij}(\epsilon_z)\right)+\sum_{a=\text{dBRN,SS}}N_{ij}^{\text{bkg},a}\left(1+\beta_a\right)\ , \tag{A.4}$$

where pBRN, dBRN, SS correspond to prompt BRN, delayed BRN and SS backgrounds (NIN contribution is neglected in this analysis). Their predicted values, $N_{ij}^{\text{bkg},a}$, are readily provided in the LAr measurement data release [265], with efficiencies already applied to them.

Thus, the nuisance parameters in this analysis are $\vec{x} = \{\alpha, \beta_{\text{pBRN}}, \beta_{\text{dBRN}}, \beta_{\text{SS}}, \epsilon_z\}$, with $1 \leq z \leq 5$, with uncertainties equal to $\{13\%, 32\%, 100\%, 0.8\%\}$ and 100% for all five ϵ_z parameters. We see that the generic h_{ij} functions introduced in Eq. (5.47) are in this case $h_{ij}^{signal\,/\,bkg,a}(\vec{x}) = \{\alpha, \beta_{\text{pBRN}}, \beta_{\text{dBRN}}, \beta_{\text{SS}}, \alpha_{z,ij}(\epsilon_z)\}$. We have nuisance parameters associated to the systematic uncertainties of the overall normalization of backgrounds (β_a) and signal (α). The latter includes errors associated to detector efficiency, energy calibration, F_{90} calibration, quenching factor, nuclear form factor and neutrino flux. In addition, this analysis includes systematic uncertainties affecting the shape of the distributions (ϵ_z). In particular, we have two systematic errors affecting

the signal distribution, coming from the energy dependence of the F_{90} distribution and the trigger time mean, and three systematic errors affecting the prompt BRN distribution, with the energy distribution, the trigger time mean and the trigger time width as their sources. These bin-dependent systematics are included through the following functions:

$$\alpha_{z,ij}(\epsilon_z) = \frac{N_{z,ij}^{1\sigma} - N_{ij}^{\rm CV}}{N_{ij}^{\rm CV}}\,\epsilon_z \ , \tag{A.5}$$

where $N_{z,ij}^{1\sigma}$ is the predicted number of events with a 1-σ shift due exclusively to the z-th systematic error and $N_{ij}^{\rm CV}$ is the predicted central value. Note that these quantities include the total number of events and not only the (signal/pBRN) events affected by the z-th systematic error. We take the five 1-σ distributions ($1 \leq z \leq 5$) and the three background CV's (pBRN, dBRN,SS) from the COHERENT data release [265].

The number of expected CEνNS events is obtained using Eq. (5.46), which we repeat here

$$N_{ij}^{\rm signal} \quad = \quad g_j^{\rm prompt} N_i^{\rm prompt} + g_j^{\rm delayed} N_i^{\rm delayed} \ .$$

The timing information (i.e., the g_j factors) is extracted from the neutrino flux characterization presented in the COHERENT data release [265, 334]. The energy distributions, N_i, are calculated using Eq. (5.45), which involves an efficiency function, energy resolution and quenching factor that we describe below.

The quenching factor is parametrized through a polynomial expression, given by

$$\mathrm{QF}(T) = a_{\rm QF} T + b_{\rm QF} T^2, \tag{A.6}$$

where $a_{\rm QF} = 0.246$ keV^{-1} and $b_{\rm QF} = 0.00078$ keV^{-2}.

The detector resolution function is

$$\mathcal{R}\left(T_{ee}^{\rm rec}, T_{ee}\right) = \frac{1}{\sqrt{2\pi}\sigma_{ee}} e^{-\frac{-\left(T_{ee}^{\rm rec} - T_{ee}\right)^2}{2\sigma_{ee}^2}}, \tag{A.7}$$

where the T_{ee}-dependent width is given by $\sigma_{ee} = 0.58\,\mathrm{keV}\sqrt{T_{ee}/\mathrm{keV}}$. For the lower limit of the T integration in Eq. (5.45) we do not use zero but $T_{min} = 79$ eV (average energy to produce a scintillation photon in Ar [335]), but this has a negligible impact in our results.

The efficiency function, $\epsilon(T_{ee}^{\rm rec})$, used in the calculation of the CEνNS events is given by COHERENT as a $T_{ee}^{\rm rec}$ bin dependent quantity [265].

Finally, we list here the constraints coming from every measured bin for this nuclear target. Out of the 40 bins, it turns out that the majority of them probe the same linear combinations of the weak squared charges. Combining those bins, we end up with the following 9 bins that

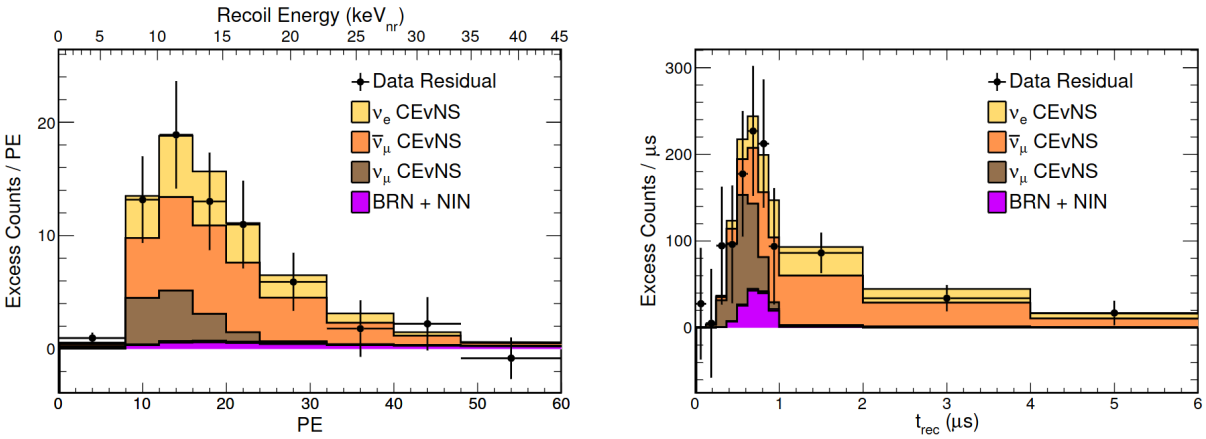

Fig. A.2: Comparison of the measured data at the COHERENT CsI nuclear target with the predicted distributions of CEνNS , BRN, and NIN events projected onto the recoil energy (left) and time (right) axes. The CEνNS distribution has been decomposed into each flavor of neutrino flux at the SNS. Plot taken from Ref. [250].

access different combinations of the squared charges:

$$\begin{aligned}
\text{T} < 10 \text{ keVee}, 0.0 < \text{t} < 0.5\ \mu s: &\quad \{0.91, 0.05, 0.04\}.\vec{Q}_2^{\text{Ar}} &=& \ 0.4 \pm 1.2 \\
\text{T} < 10 \text{ keVee}, 0.5 < \text{t} < 1.0\ \mu s: &\quad \{0.65, 0.19, 0.16\}.\vec{Q}_2^{\text{Ar}} &=& \ 1.72 \pm 0.94 \\
\text{T} < 10 \text{ keVee}, 1.0 < \text{t} < 1.5\ \mu s: &\quad \{0.01, 0.55, 0.45\}.\vec{Q}_2^{\text{Ar}} &=& \ 0.3 \pm 1.3 \\
\text{T} < 10 \text{ keVee}, 1.5 < \text{t} < 5.0\ \mu s: &\quad \{0.00, 0.55, 0.45\}.\vec{Q}_2^{\text{Ar}} &=& \ 0.76 \pm 0.85 \\
10 < \text{T} < 20 \text{ keVee}, 0.0 < \text{t} < 0.5\ \mu s: &\quad \{0.71, 0.17, 0.11\}.\vec{Q}_2^{\text{Ar}} &=& \ 3.6 \pm 5.3 \\
10 < \text{T} < 20 \text{ keVee}, 0.5 < \text{t} < 1.0\ \mu s: &\quad \{0.31, 0.42, 0.27\}.\vec{Q}_2^{\text{Ar}} &=& \ 6.4 \pm 3.3 \\
10 < \text{T} < 20 \text{ keVee}, 1.0 < \text{t} < 5.0\ \mu s: &\quad \{0.00, 0.61, 0.39\}.\vec{Q}_2^{\text{Ar}} &=& \ 0.63 \pm 0.88 \\
20 < \text{T} < 30 \text{ keVee}, 0.0 < \text{t} < 5.0\ \mu s: &\quad \{0.00, 0.68, 0.32\}.\vec{Q}_2^{\text{Ar}} &=& \ 1.0 \pm 3.1 \\
30 < \text{T} < 40 \text{ keVee}, 0.0 < \text{t} < 5.0\ \mu s: &\quad \{0.00, 0.76, 0.25\}.\vec{Q}_2^{\text{Ar}} &=& -3.7 \pm 9.9
\end{aligned} \tag{A.8}$$

where $\vec{Q}_2^{\text{Ar}} \equiv \{(Q_{LL}^{\mu})^2, (Q_{LL}^{\bar{\mu}})^2 + (Q_{RR}^{e})^2, (Q_{LL}^{e})^2 + (Q_{RR}^{\bar{\mu}})^2\}_{\text{Ar}}/Q^2_{\text{SM,Ar}}$.

A.2. CsI measurement

Our CsI analysis uses the 2D distribution in recoil energy and time covering the ranges $8 < \text{PE} < 60$ and $0 < t(\mu s) < 6$ with 1 PE and 0.5 μs of width respectively, which yields a total of 52x12 bins. This is the same bin set as the one used in the original COHERENT analysis [250]. The projections of the measured and predicted event distributions to the energy and time axes are displayed in Fig. A.2, where some bins are clustered for the sake of clarity.

The formula for the expected number of events per bin is given by

$$N_{ij}^{\text{th}}\left(\vec{Q}^2_{\text{CsI}}; \vec{x}\right) = N_{ij}^{\text{signal}}\left(\vec{Q}^2_{\text{CsI}}\right)(1+\alpha) + \sum_a N_{ij}^{\text{bkg},a}\,(1+\beta_a)\ , \tag{A.9}$$

where a = BRN, NIN, SS are the three background sources considered in this analysis. Thus, the nuisance parameters are $\vec{x} = \{\alpha, \beta_{\text{BRN}}, \beta_{\text{NIN}}, \beta_{\text{SS}}\}$, with uncertainties equal to $\vec{\sigma} = \{12\%, 25\%, 35\%, 2.1\%\}$ and the h_{ij} nuisance functions are simply given by $h_{ij}^{\text{signal/bkg},a}(\vec{x}) = x^a$. The α parameter encodes

the systematic uncertainties associated to the signal (due to the QF, neutrino flux, efficiency and form factor), whereas the β ones encode the uncertainty associated to the normalization of the backgrounds.

As in the LAr case, the expected number of CEνNS events, N_{ij}^{signal}, is calculated using Eq. (5.46) (repeated above), and the prompt and delayed energy distributions, N_i^a, are obtained using Eq. (5.45). The latter involves an efficiency function, energy resolution and QF that we describe below. Finally, the time information, i.e., the g_j factors in Eq. (5.46), is described afterwards.

The COHERENT prescription for the QF in this analysis is the following [250]

$$\text{QF}(T) = a_{\text{QF}}T + b_{\text{QF}}T^2 + c_{\text{QF}}T^3 + d_{\text{QF}}T^4, \tag{A.10}$$

where $a_{\text{QF}} = 0.0554628\,\text{MeV}^{-1}$, $b_{\text{QF}} = 4.30681\,\text{MeV}^{-2}$, $c_{\text{QF}} = -111.707\,\text{MeV}^{-3}$ and $d_{\text{QF}} = 840.384\,\text{MeV}^{-4}$. The measured events are organized in PE bins, so we apply the light yield, given in this case by LY=13.35 PE/keV.

The energy resolution function is given by

$$\mathcal{R}(\text{PE}, T_{ee}) = \frac{(a\,(1+b))^{1+b}}{\Gamma(1+b)}(\text{PE})^b e^{-a(1+b)\text{PE}}, \tag{A.11}$$

where a and b encode the T_{ee} dependence: $a = 0.0749\,\text{keV}/T_{ee}$ and $b = 9.56\,\text{keV}^{-1} \times T_{ee}$.

The energy-dependent efficiency applied in this measurement is

$$\epsilon(\text{PE}) \;=\; \frac{a}{1+e^{-b((\text{PE}/\text{LY})-c)}} + d\ , \tag{A.12}$$

where $a = 1.320 \pm 0.023$, $b = (0.28598 \pm 0.00061)\,\text{PE}^{-1}$, $c = (10.9 \pm 1.0)\,\text{PE}$, $d = -0.333 \pm 0.023$. We have checked that these uncertainties have a negligible effect in our fit and thus we have neglected them.

As for the timing information (g_j factors), we extract them from the information about the flux for every neutrino flavor, which is binned in time and recoil energy and provided in the data release [265]. Integrating over the recoil energy we obtain the prompt and delayed distributions. Then we take into account the timing efficiency of the detector, which is available for this measurement. Namely

$$\epsilon_t(t) = \begin{cases} 1 & t < a \\ e^{-b(t-a)} & t \geq a \end{cases}, \tag{A.13}$$

where $a = 0.52\,\mu s$ and $b = 0.0494\,\mu s^{-1}$. Once again, the impact of the uncertainties of these parameters in our fits is negligible. We apply this timing efficiency to the projected time distributions, and then we normalize each of them to recast them as probability distribution functions. The ν_μ flux gives the prompt distribution, and the ν_e (or $\bar{\nu}_\mu$) flux can be used to obtain the delayed distribution.

Concerning the backgrounds, the BRN and NIN distributions are provided in the COHERENT data release [265]. They can be normalized to produce 1D distributions in the recoil energy and timing directions, denoted by $g_a(\text{PE})$ and $f_a(t)$ respectively (a =BRN, NIN). The full 2D distributions are obtained just by taking $N_{tot}^a\, g_a(\text{PE})\, f_a(t)\, \epsilon_t(t)$, where $N_{tot}^{\text{BRN}} = 18.4$ and $N_{tot}^{\text{NIN}} = 5.6$ are the total number of predicted BRN and NIN events.

The SS background can be estimated from the anti-coincidence data (AC), which is also given in a 2D distribution in recoil energy and time. The projection onto the PE axis provides

directly the recoil-energy distribution, while for the description of the time evolution of this background, the collaboration advises the use of an exponential model. That exponential is fitted to the projection of the AC data on the time axis and then normalized, yielding an expression $f_{\rm SS}(t) \propto e^{-a_{\rm SS}t}$, with $a_{\rm SS} = -0.0494\,\mu s^{-1}$. This procedure (instead of working directly with the 2D AC distribution) avoids possible biases in the fit due to limited statistics in the sample [225]. Since this distribution is inferred directly from the data, it is not necessary to apply efficiencies here.

We close this appendix by listing the constraints corresponding to the 624 measured bins for the CsI target. However, many of these bins probe exactly the same combination of squared charges. Here we combine those bins to work with the 109 bins that access different combinations of the squared charges:

$$
\begin{aligned}
8 < \mathrm{T} < 9 \text{ PE}, 0.0 < \mathrm{t} < 0.5\ \mu s: \quad & \{0.90, 0.06, 0.05\}.\vec{Q}_2^{\mathrm{CsI}} = 1.5 \pm 1.0 \\
8 < \mathrm{T} < 9 \text{ PE}, 0.5 < \mathrm{t} < 1.0\ \mu s: \quad & \{0.55, 0.25, 0.20\}.\vec{Q}_2^{\mathrm{CsI}} = 1.4 \pm 1.0 \\
8 < \mathrm{T} < 9 \text{ PE}, 1.0 < \mathrm{t} < 6.0\ \mu s: \quad & \{0.00, 0.56, 0.44\}.\vec{Q}_2^{\mathrm{CsI}} = 0.16 \pm 0.83 \\
9 < \mathrm{T} < 10 \text{ PE}, 0.0 < \mathrm{t} < 0.5\ \mu s: \quad & \{0.89, 0.06, 0.05\}.\vec{Q}_2^{\mathrm{CsI}} = -0.55 \pm 0.53 \\
9 < \mathrm{T} < 10 \text{ PE}, 0.5 < \mathrm{t} < 1.0\ \mu s: \quad & \{0.54, 0.26, 0.20\}.\vec{Q}_2^{\mathrm{CsI}} = 1.87 \pm 0.94 \\
9 < \mathrm{T} < 10 \text{ PE}, 1.0 < \mathrm{t} < 6.0\ \mu s: \quad & \{0.00, 0.56, 0.44\}.\vec{Q}_2^{\mathrm{CsI}} = 0.84 \pm 0.81 \\
10 < \mathrm{T} < 11 \text{ PE}, 0.0 < \mathrm{t} < 0.5\ \mu s: \quad & \{0.88, 0.07, 0.05\}.\vec{Q}_2^{\mathrm{CsI}} = 1.02 \pm 0.96 \\
10 < \mathrm{T} < 11 \text{ PE}, 0.5 < \mathrm{t} < 1.0\ \mu s: \quad & \{0.52, 0.27, 0.21\}.\vec{Q}_2^{\mathrm{CsI}} = 1.83 \pm 0.84 \\
10 < \mathrm{T} < 11 \text{ PE}, 1.0 < \mathrm{t} < 6.0\ \mu s: \quad & \{0.00, 0.57, 0.43\}.\vec{Q}_2^{\mathrm{CsI}} = 1.79 \pm 0.75 \\
11 < \mathrm{T} < 12 \text{ PE}, 0.0 < \mathrm{t} < 0.5\ \mu s: \quad & \{0.88, 0.07, 0.05\}.\vec{Q}_2^{\mathrm{CsI}} = 2.4 \pm 1.2 \\
11 < \mathrm{T} < 12 \text{ PE}, 0.5 < \mathrm{t} < 1.0\ \mu s: \quad & \{0.50, 0.28, 0.21\}.\vec{Q}_2^{\mathrm{CsI}} = 0.89 \pm 0.64 \\
11 < \mathrm{T} < 12 \text{ PE}, 1.0 < \mathrm{t} < 6.0\ \mu s: \quad & \{0.00, 0.57, 0.43\}.\vec{Q}_2^{\mathrm{CsI}} = 0.17 \pm 0.54 \\
12 < \mathrm{T} < 13 \text{ PE}, 0.0 < \mathrm{t} < 0.5\ \mu s: \quad & \{0.87, 0.08, 0.06\}.\vec{Q}_2^{\mathrm{CsI}} = 1.35 \pm 0.93 \\
12 < \mathrm{T} < 13 \text{ PE}, 0.5 < \mathrm{t} < 1.0\ \mu s: \quad & \{0.48, 0.30, 0.22\}.\vec{Q}_2^{\mathrm{CsI}} = 1.94 \pm 0.76 \\
12 < \mathrm{T} < 13 \text{ PE}, 1.0 < \mathrm{t} < 6.0\ \mu s: \quad & \{0.00, 0.57, 0.43\}.\vec{Q}_2^{\mathrm{CsI}} = 2.04 \pm 0.66 \\
13 < \mathrm{T} < 14 \text{ PE}, 0.0 < \mathrm{t} < 0.5\ \mu s: \quad & \{0.85, 0.08, 0.06\}.\vec{Q}_2^{\mathrm{CsI}} = 2.8 \pm 1.3 \\
13 < \mathrm{T} < 14 \text{ PE}, 0.5 < \mathrm{t} < 1.0\ \mu s: \quad & \{0.46, 0.31, 0.23\}.\vec{Q}_2^{\mathrm{CsI}} = 2.07 \pm 0.81 \\
13 < \mathrm{T} < 14 \text{ PE}, 1.0 < \mathrm{t} < 6.0\ \mu s: \quad & \{0.00, 0.58, 0.42\}.\vec{Q}_2^{\mathrm{CsI}} = 1.17 \pm 0.57 \\
14 < \mathrm{T} < 15 \text{ PE}, 0.0 < \mathrm{t} < 0.5\ \mu s: \quad & \{0.84, 0.09, 0.07\}.\vec{Q}_2^{\mathrm{CsI}} = -1.06 \pm 0.43 \\
14 < \mathrm{T} < 15 \text{ PE}, 0.5 < \mathrm{t} < 1.0\ \mu s: \quad & \{0.43, 0.33, 0.24\}.\vec{Q}_2^{\mathrm{CsI}} = 1.69 \pm 0.76 \\
14 < \mathrm{T} < 15 \text{ PE}, 1.0 < \mathrm{t} < 6.0\ \mu s: \quad & \{0.00, 0.58, 0.42\}.\vec{Q}_2^{\mathrm{CsI}} = 0.72 \pm 0.52 \\
15 < \mathrm{T} < 16 \text{ PE}, 0.0 < \mathrm{t} < 0.5\ \mu s: \quad & \{0.82, 0.11, 0.07\}.\vec{Q}_2^{\mathrm{CsI}} = -0.66 \pm 0.79 \\
15 < \mathrm{T} < 16 \text{ PE}, 0.5 < \mathrm{t} < 1.0\ \mu s: \quad & \{0.40, 0.35, 0.25\}.\vec{Q}_2^{\mathrm{CsI}} = 0.27 \pm 0.54 \\
15 < \mathrm{T} < 16 \text{ PE}, 1.0 < \mathrm{t} < 6.0\ \mu s: \quad & \{0.00, 0.59, 0.41\}.\vec{Q}_2^{\mathrm{CsI}} = 0.27 \pm 0.53 \\
16 < \mathrm{T} < 17 \text{ PE}, 0.0 < \mathrm{t} < 0.5\ \mu s: \quad & \{0.80, 0.12, 0.08\}.\vec{Q}_2^{\mathrm{CsI}} = 2.3 \pm 1.4 \\
16 < \mathrm{T} < 17 \text{ PE}, 0.5 < \mathrm{t} < 1.0\ \mu s: \quad & \{0.36, 0.38, 0.26\}.\vec{Q}_2^{\mathrm{CsI}} = 0.96 \pm 0.64 \\
16 < \mathrm{T} < 17 \text{ PE}, 1.0 < \mathrm{t} < 6.0\ \mu s: \quad & \{0.00, 0.59, 0.41\}.\vec{Q}_2^{\mathrm{CsI}} = 1.46 \pm 0.55 \\
17 < \mathrm{T} < 18 \text{ PE}, 0.0 < \mathrm{t} < 0.5\ \mu s: \quad & \{0.77, 0.14, 0.09\}.\vec{Q}_2^{\mathrm{CsI}} = 1.9 \pm 1.5 \\
17 < \mathrm{T} < 18 \text{ PE}, 0.5 < \mathrm{t} < 1.0\ \mu s: \quad & \{0.33, 0.40, 0.27\}.\vec{Q}_2^{\mathrm{CsI}} = 2.02 \pm 0.89 \\
17 < \mathrm{T} < 18 \text{ PE}, 1.0 < \mathrm{t} < 6.0\ \mu s: \quad & \{0.00, 0.60, 0.40\}.\vec{Q}_2^{\mathrm{CsI}} = 0.51 \pm 0.47 \\
18 < \mathrm{T} < 19 \text{ PE}, 0.0 < \mathrm{t} < 0.5\ \mu s: \quad & \{0.74, 0.16, 0.10\}.\vec{Q}_2^{\mathrm{CsI}} = 1.2 \pm 1.6 \\
18 < \mathrm{T} < 19 \text{ PE}, 0.5 < \mathrm{t} < 1.0\ \mu s: \quad & \{0.29, 0.43, 0.28\}.\vec{Q}_2^{\mathrm{CsI}} = 0.75 \pm 0.79
\end{aligned}
$$

$18 < \mathrm{T} < 19$ PE, $1.0 < \mathrm{t} < 6.0$ μs:	$\{0.00, 0.60, 0.40\}.\vec{Q}_2^{\mathrm{CsI}}$	$=$	0.62 ± 0.52
$19 < \mathrm{T} < 20$ PE, $0.0 < \mathrm{t} < 0.5$ μs:	$\{0.70, 0.18, 0.12\}.\vec{Q}_2^{\mathrm{CsI}}$	$=$	1.5 ± 2.0
$19 < \mathrm{T} < 20$ PE, $0.5 < \mathrm{t} < 1.0$ μs:	$\{0.25, 0.45, 0.30\}.\vec{Q}_2^{\mathrm{CsI}}$	$=$	0.62 ± 0.80
$19 < \mathrm{T} < 20$ PE, $1.0 < \mathrm{t} < 6.0$ μs:	$\{0.00, 0.60, 0.40\}.\vec{Q}_2^{\mathrm{CsI}}$	$=$	0.54 ± 0.55
$20 < \mathrm{T} < 21$ PE, $0.0 < \mathrm{t} < 0.5$ μs:	$\{0.66, 0.21, 0.13\}.\vec{Q}_2^{\mathrm{CsI}}$	$=$	0.1 ± 1.9
$20 < \mathrm{T} < 21$ PE, $0.5 < \mathrm{t} < 1.0$ μs:	$\{0.22, 0.48, 0.31\}.\vec{Q}_2^{\mathrm{CsI}}$	$=$	0.62 ± 0.80
$20 < \mathrm{T} < 21$ PE, $1.0 < \mathrm{t} < 6.0$ μs:	$\{0.00, 0.61, 0.39\}.\vec{Q}_2^{\mathrm{CsI}}$	$=$	1.11 ± 0.63
$21 < \mathrm{T} < 22$ PE, $0.0 < \mathrm{t} < 0.5$ μs:	$\{0.61, 0.24, 0.15\}.\vec{Q}_2^{\mathrm{CsI}}$	$=$	0.5 ± 2.3
$21 < \mathrm{T} < 22$ PE, $0.5 < \mathrm{t} < 1.0$ μs:	$\{0.18, 0.50, 0.32\}.\vec{Q}_2^{\mathrm{CsI}}$	$=$	0.01 ± 0.70
$21 < \mathrm{T} < 22$ PE, $1.0 < \mathrm{t} < 6.0$ μs:	$\{0.00, 0.61, 0.39\}.\vec{Q}_2^{\mathrm{CsI}}$	$=$	0.32 ± 0.54
$22 < \mathrm{T} < 23$ PE, $0.0 < \mathrm{t} < 0.5$ μs:	$\{0.55, 0.28, 0.17\}.\vec{Q}_2^{\mathrm{CsI}}$	$=$	-1.6 ± 1.6
$22 < \mathrm{T} < 23$ PE, $0.5 < \mathrm{t} < 1.0$ μs:	$\{0.15, 0.52, 0.32\}.\vec{Q}_2^{\mathrm{CsI}}$	$=$	1.2 ± 1.0
$22 < \mathrm{T} < 23$ PE, $1.0 < \mathrm{t} < 6.0$ μs:	$\{0.00, 0.62, 0.38\}.\vec{Q}_2^{\mathrm{CsI}}$	$=$	1.91 ± 0.75
$23 < \mathrm{T} < 24$ PE, $0.0 < \mathrm{t} < 0.5$ μs:	$\{0.49, 0.32, 0.19\}.\vec{Q}_2^{\mathrm{CsI}}$	$=$	-1.5 ± 2.8
$23 < \mathrm{T} < 24$ PE, $0.5 < \mathrm{t} < 1.0$ μs:	$\{0.12, 0.55, 0.33\}.\vec{Q}_2^{\mathrm{CsI}}$	$=$	0.0 ± 1.0
$23 < \mathrm{T} < 24$ PE, $1.0 < \mathrm{t} < 6.0$ μs:	$\{0.00, 0.62, 0.38\}.\vec{Q}_2^{\mathrm{CsI}}$	$=$	1.51 ± 0.79
$24 < \mathrm{T} < 25$ PE, $0.0 < \mathrm{t} < 0.5$ μs:	$\{0.43, 0.36, 0.21\}.\vec{Q}_2^{\mathrm{CsI}}$	$=$	0.0 ± 2.2
$24 < \mathrm{T} < 25$ PE, $0.5 < \mathrm{t} < 1.0$ μs:	$\{0.10, 0.57, 0.34\}.\vec{Q}_2^{\mathrm{CsI}}$	$=$	1.1 ± 1.3
$24 < \mathrm{T} < 25$ PE, $1.0 < \mathrm{t} < 6.0$ μs:	$\{0.00, 0.63, 0.37\}.\vec{Q}_2^{\mathrm{CsI}}$	$=$	1.37 ± 0.86
$25 < \mathrm{T} < 26$ PE, $0.0 < \mathrm{t} < 0.5$ μs:	$\{0.37, 0.40, 0.23\}.\vec{Q}_2^{\mathrm{CsI}}$	$=$	2.2 ± 5.1
$25 < \mathrm{T} < 26$ PE, $0.5 < \mathrm{t} < 1.0$ μs:	$\{0.08, 0.58, 0.34\}.\vec{Q}_2^{\mathrm{CsI}}$	$=$	0.3 ± 1.1
$25 < \mathrm{T} < 26$ PE, $1.0 < \mathrm{t} < 6.0$ μs:	$\{0.00, 0.63, 0.37\}.\vec{Q}_2^{\mathrm{CsI}}$	$=$	1.48 ± 0.82
$26 < \mathrm{T} < 27$ PE, $0.0 < \mathrm{t} < 0.5$ μs:	$\{0.31, 0.44, 0.25\}.\vec{Q}_2^{\mathrm{CsI}}$	$=$	-7.1 ± 3.6
$26 < \mathrm{T} < 27$ PE, $0.5 < \mathrm{t} < 1.0$ μs:	$\{0.06, 0.60, 0.34\}.\vec{Q}_2^{\mathrm{CsI}}$	$=$	-1.57 ± 0.72
$26 < \mathrm{T} < 27$ PE, $1.0 < \mathrm{t} < 6.0$ μs:	$\{0.00, 0.64, 0.36\}.\vec{Q}_2^{\mathrm{CsI}}$	$=$	-0.14 ± 0.71
$27 < \mathrm{T} < 28$ PE, $0.0 < \mathrm{t} < 0.5$ μs:	$\{0.25, 0.48, 0.27\}.\vec{Q}_2^{\mathrm{CsI}}$	$=$	-4.8 ± 4.2
$27 < \mathrm{T} < 28$ PE, $0.5 < \mathrm{t} < 1.0$ μs:	$\{0.05, 0.61, 0.34\}.\vec{Q}_2^{\mathrm{CsI}}$	$=$	2.0 ± 1.7
$27 < \mathrm{T} < 28$ PE, $1.0 < \mathrm{t} < 6.0$ μs:	$\{0.00, 0.64, 0.36\}.\vec{Q}_2^{\mathrm{CsI}}$	$=$	0.89 ± 0.88
$28 < \mathrm{T} < 29$ PE, $0.0 < \mathrm{t} < 0.5$ μs:	$\{0.20, 0.52, 0.29\}.\vec{Q}_2^{\mathrm{CsI}}$	$=$	10 ± 11
$28 < \mathrm{T} < 29$ PE, $0.5 < \mathrm{t} < 1.0$ μs:	$\{0.03, 0.62, 0.34\}.\vec{Q}_2^{\mathrm{CsI}}$	$=$	2.3 ± 2.1
$28 < \mathrm{T} < 29$ PE, $1.0 < \mathrm{t} < 6.0$ μs:	$\{0.00, 0.64, 0.36\}.\vec{Q}_2^{\mathrm{CsI}}$	$=$	0.9 ± 1.1
$29 < \mathrm{T} < 30$ PE, $0.0 < \mathrm{t} < 0.5$ μs:	$\{0.15, 0.55, 0.30\}.\vec{Q}_2^{\mathrm{CsI}}$	$=$	-0.9 ± 7.9
$29 < \mathrm{T} < 30$ PE, $0.5 < \mathrm{t} < 1.0$ μs:	$\{0.03, 0.63, 0.34\}.\vec{Q}_2^{\mathrm{CsI}}$	$=$	-0.4 ± 1.3
$29 < \mathrm{T} < 30$ PE, $1.0 < \mathrm{t} < 6.0$ μs:	$\{0.00, 0.65, 0.35\}.\vec{Q}_2^{\mathrm{CsI}}$	$=$	0.52 ± 0.94
$30 < \mathrm{T} < 31$ PE, $0.0 < \mathrm{t} < 0.5$ μs:	$\{0.12, 0.58, 0.31\}.\vec{Q}_2^{\mathrm{CsI}}$	$=$	14 ± 13
$30 < \mathrm{T} < 31$ PE, $0.5 < \mathrm{t} < 1.0$ μs:	$\{0.02, 0.64, 0.34\}.\vec{Q}_2^{\mathrm{CsI}}$	$=$	4.0 ± 2.6
$30 < \mathrm{T} < 31$ PE, $1.0 < \mathrm{t} < 6.0$ μs:	$\{0.00, 0.65, 0.35\}.\vec{Q}_2^{\mathrm{CsI}}$	$=$	0.47 ± 0.99
$31 < \mathrm{T} < 32$ PE, $0.0 < \mathrm{t} < 0.5$ μs:	$\{0.09, 0.60, 0.31\}.\vec{Q}_2^{\mathrm{CsI}}$	$=$	-4 ± 10
$31 < \mathrm{T} < 32$ PE, $0.5 < \mathrm{t} < 1.0$ μs:	$\{0.01, 0.65, 0.34\}.\vec{Q}_2^{\mathrm{CsI}}$	$=$	0.3 ± 2.0
$31 < \mathrm{T} < 32$ PE, $1.0 < \mathrm{t} < 6.0$ μs:	$\{0.00, 0.66, 0.34\}.\vec{Q}_2^{\mathrm{CsI}}$	$=$	-0.86 ± 0.98

$$
\begin{aligned}
32 < \mathrm{T} < 33 \text{ PE}, 0.0 < \mathrm{t} < 0.5\ \mu s: &\quad \{0.06, 0.62, 0.32\}.\vec{Q}_2^{\mathrm{CsI}} &=& \ 1 \pm 12 \\
32 < \mathrm{T} < 33 \text{ PE}, 0.5 < \mathrm{t} < 1.0\ \mu s: &\quad \{0.01, 0.66, 0.33\}.\vec{Q}_2^{\mathrm{CsI}} &=& \ 0.0 \pm 1.6 \\
32 < \mathrm{T} < 33 \text{ PE}, 1.0 < \mathrm{t} < 6.0\ \mu s: &\quad \{0.00, 0.66, 0.34\}.\vec{Q}_2^{\mathrm{CsI}} &=& \ 1.0 \pm 1.3 \\
33 < \mathrm{T} < 34 \text{ PE}, 0.0 < \mathrm{t} < 0.5\ \mu s: &\quad \{0.05, 0.64, 0.32\}.\vec{Q}_2^{\mathrm{CsI}} &=& \ 6 \pm 16 \\
33 < \mathrm{T} < 34 \text{ PE}, 0.5 < \mathrm{t} < 1.0\ \mu s: &\quad \{0.01, 0.67, 0.33\}.\vec{Q}_2^{\mathrm{CsI}} &=& \ 3.4 \pm 3.1 \\
33 < \mathrm{T} < 34 \text{ PE}, 1.0 < \mathrm{t} < 6.0\ \mu s: &\quad \{0.00, 0.67, 0.33\}.\vec{Q}_2^{\mathrm{CsI}} &=& \ 2.5 \pm 1.7 \\
34 < \mathrm{T} < 35 \text{ PE}, 0.0 < \mathrm{t} < 0.5\ \mu s: &\quad \{0.03, 0.65, 0.32\}.\vec{Q}_2^{\mathrm{CsI}} &=& -9 \pm 10 \\
34 < \mathrm{T} < 35 \text{ PE}, 0.5 < \mathrm{t} < 6.0\ \mu s: &\quad \{0.00, 0.67, 0.33\}.\vec{Q}_2^{\mathrm{CsI}} &=& \ 2.0 \pm 1.4 \\
35 < \mathrm{T} < 36 \text{ PE}, 0.0 < \mathrm{t} < 0.5\ \mu s: &\quad \{0.02, 0.66, 0.32\}.\vec{Q}_2^{\mathrm{CsI}} &=& -16 \pm 12 \\
35 < \mathrm{T} < 36 \text{ PE}, 0.5 < \mathrm{t} < 6.0\ \mu s: &\quad \{0.00, 0.67, 0.32\}.\vec{Q}_2^{\mathrm{CsI}} &=& \ 2.0 \pm 1.7 \\
36 < \mathrm{T} < 37 \text{ PE}, 0.0 < \mathrm{t} < 0.5\ \mu s: &\quad \{0.02, 0.67, 0.31\}.\vec{Q}_2^{\mathrm{CsI}} &=& -3 \pm 18 \\
36 < \mathrm{T} < 37 \text{ PE}, 0.5 < \mathrm{t} < 6.0\ \mu s: &\quad \{0.00, 0.68, 0.32\}.\vec{Q}_2^{\mathrm{CsI}} &=& -0.6 \pm 1.5 \\
37 < \mathrm{T} < 38 \text{ PE}, 0.0 < \mathrm{t} < 0.5\ \mu s: &\quad \{0.01, 0.68, 0.31\}.\vec{Q}_2^{\mathrm{CsI}} &=& \ 0.0 \pm 5.2 \\
37 < \mathrm{T} < 38 \text{ PE}, 0.5 < \mathrm{t} < 6.0\ \mu s: &\quad \{0.00, 0.69, 0.31\}.\vec{Q}_2^{\mathrm{CsI}} &=& -0.8 \pm 1.7 \\
38 < \mathrm{T} < 39 \text{ PE}, 0.0 < \mathrm{t} < 0.5\ \mu s: &\quad \{0.01, 0.69, 0.31\}.\vec{Q}_2^{\mathrm{CsI}} &=& \ 35 \pm 35 \\
38 < \mathrm{T} < 39 \text{ PE}, 0.5 < \mathrm{t} < 6.0\ \mu s: &\quad \{0.00, 0.69, 0.31\}.\vec{Q}_2^{\mathrm{CsI}} &=& -1.9 \pm 1.7 \\
39 < \mathrm{T} < 40 \text{ PE}, 0.0 < \mathrm{t} < 0.5\ \mu s: &\quad \{0.01, 0.69, 0.30\}.\vec{Q}_2^{\mathrm{CsI}} &=& \ 22 \pm 30 \\
39 < \mathrm{T} < 40 \text{ PE}, 0.5 < \mathrm{t} < 6.0\ \mu s: &\quad \{0.00, 0.70, 0.30\}.\vec{Q}_2^{\mathrm{CsI}} &=& \ 0.4 \pm 1.9 \\
40 < \mathrm{T} < 41 \text{ PE}: &\quad \{0.00, 0.70, 0.30\}.\vec{Q}_2^{\mathrm{CsI}} &=& -2.6 \pm 1.7 \\
41 < \mathrm{T} < 42 \text{ PE}: &\quad \{0.00, 0.70, 0.29\}.\vec{Q}_2^{\mathrm{CsI}} &=& \ 3.6 \pm 2.9 \\
42 < \mathrm{T} < 43 \text{ PE}: &\quad \{0.00, 0.71, 0.29\}.\vec{Q}_2^{\mathrm{CsI}} &=& \ 3.0 \pm 3.4 \\
43 < \mathrm{T} < 44 \text{ PE}: &\quad \{0.00, 0.72, 0.28\}.\vec{Q}_2^{\mathrm{CsI}} &=& -2.9 \pm 2.4 \\
44 < \mathrm{T} < 45 \text{ PE}: &\quad \{0.00, 0.72, 0.28\}.\vec{Q}_2^{\mathrm{CsI}} &=& \ 3.0 \pm 4.1 \\
45 < \mathrm{T} < 46 \text{ PE}: &\quad \{0.00, 0.73, 0.27\}.\vec{Q}_2^{\mathrm{CsI}} &=& \ 4.6 \pm 5.2 \\
46 < \mathrm{T} < 47 \text{ PE}: &\quad \{0.00, 0.73, 0.27\}.\vec{Q}_2^{\mathrm{CsI}} &=& -5.3 \pm 4.4 \\
47 < \mathrm{T} < 48 \text{ PE}: &\quad \{0.00, 0.74, 0.26\}.\vec{Q}_2^{\mathrm{CsI}} &=& -1.9 \pm 4.8 \\
48 < \mathrm{T} < 49 \text{ PE}: &\quad \{0.00, 0.74, 0.26\}.\vec{Q}_2^{\mathrm{CsI}} &=& -3.5 \pm 5.1 \\
49 < \mathrm{T} < 50 \text{ PE}: &\quad \{0.00, 0.74, 0.26\}.\vec{Q}_2^{\mathrm{CsI}} &=& -1.4 \pm 6.4 \\
50 < \mathrm{T} < 51 \text{ PE}: &\quad \{0.00, 0.75, 0.25\}.\vec{Q}_2^{\mathrm{CsI}} &=& -11.8 \pm 6.4 \\
51 < \mathrm{T} < 52 \text{ PE}: &\quad \{0.00, 0.75, 0.25\}.\vec{Q}_2^{\mathrm{CsI}} &=& -14.8 \pm 7.3 \\
52 < \mathrm{T} < 53 \text{ PE}: &\quad \{0.00, 0.76, 0.24\}.\vec{Q}_2^{\mathrm{CsI}} &=& \ 5.9 \pm 9.8 \\
53 < \mathrm{T} < 54 \text{ PE}: &\quad \{0.00, 0.76, 0.24\}.\vec{Q}_2^{\mathrm{CsI}} &=& -13 \pm 10 \\
54 < \mathrm{T} < 55 \text{ PE}: &\quad \{0.00, 0.77, 0.23\}.\vec{Q}_2^{\mathrm{CsI}} &=& -16 \pm 11 \\
55 < \mathrm{T} < 56 \text{ PE}: &\quad \{0.00, 0.77, 0.23\}.\vec{Q}_2^{\mathrm{CsI}} &=& \ 6 \pm 17 \\
56 < \mathrm{T} < 57 \text{ PE}: &\quad \{0.00, 0.78, 0.22\}.\vec{Q}_2^{\mathrm{CsI}} &=& \ 17 \pm 21 \\
57 < \mathrm{T} < 58 \text{ PE}: &\quad \{0.00, 0.78, 0.22\}.\vec{Q}_2^{\mathrm{CsI}} &=& \ 3 \pm 21 \\
58 < \mathrm{T} < 59 \text{ PE}: &\quad \{0.00, 0.78, 0.22\}.\vec{Q}_2^{\mathrm{CsI}} &=& \ 26 \pm 31 \\
59 < \mathrm{T} < 60 \text{ PE}: &\quad \{0.00, 0.79, 0.21\}.\vec{Q}_2^{\mathrm{CsI}} &=& -55 \pm 28
\end{aligned}
\tag{A.14}
$$

where $\vec{Q}_2^{\mathrm{CsI}} \equiv \{(Q_{LL}^{\mu})^2, (Q_{LL}^{\bar{\mu}})^2 + (Q_{RR}^{e})^2, (Q_{LL}^{e})^2 + (Q_{RR}^{\bar{\mu}})^2\}_{\mathrm{CsI}}/Q_{\mathrm{SM,CsI}}^2$.

Bibliography

[1] S. L. Glashow, "Partial Symmetries of Weak Interactions," *Nucl. Phys.* **22** (1961) 579–588.

[2] S. Weinberg, "A Model of Leptons," *Phys. Rev. Lett.* **19** (1967) 1264–1266.

[3] A. Salam, "Weak and Electromagnetic Interactions," *Conf. Proc. C* **680519** (1968) 367–377.

[4] S. L. Glashow, J. Iliopoulos, and L. Maiani, "Weak Interactions with Lepton-Hadron Symmetry," *Phys. Rev. D* **2** (1970) 1285–1292.

[5] A. Pich, "The Standard Model of Electroweak Interactions," in *2010 European School of High Energy Physics*, pp. 1–50. 1, 2012. arXiv:1201.0537 [hep-ph].

[6] L. D. Faddeev and V. N. Popov, "Feynman Diagrams for the Yang-Mills Field," *Phys. Lett. B* **25** (1967) 29–30.

[7] P. W. Higgs, "Broken symmetries and the masses of gauge bosons," *Phys. Rev. Lett.* **13** (Oct, 1964) 508–509. https://link.aps.org/doi/10.1103/PhysRevLett.13.508.

[8] F. Englert and R. Brout, "Broken symmetry and the mass of gauge vector mesons," *Phys. Rev. Lett.* **13** (Aug, 1964) 321–323. https://link.aps.org/doi/10.1103/PhysRevLett.13.321.

[9] J. Goldstone, "Field Theories with Superconductor Solutions," *Nuovo Cim.* **19** (1961) 154–164.

[10] **ATLAS** Collaboration, G. Aad *et al.*, "Observation of a new particle in the search for the Standard Model Higgs boson with the ATLAS detector at the LHC," *Phys. Lett. B* **716** (2012) 1–29, arXiv:1207.7214 [hep-ex].

[11] **CMS** Collaboration, S. Chatrchyan *et al.*, "Observation of a New Boson at a Mass of 125 GeV with the CMS Experiment at the LHC," *Phys. Lett. B* **716** (2012) 30–61, arXiv:1207.7235 [hep-ex].

[12] **ATLAS, CMS** Collaboration, G. Aad *et al.*, "Measurements of the Higgs boson production and decay rates and constraints on its couplings from a combined ATLAS and CMS analysis of the LHC pp collision data at $\sqrt{s} = 7$ and 8 TeV," *JHEP* **08** (2016) 045, arXiv:1606.02266 [hep-ex].

[13] **ATLAS, CMS** Collaboration, G. Aad *et al.*, "Combined Measurement of the Higgs Boson Mass in *pp* Collisions at $\sqrt{s} = 7$ and 8 TeV with the ATLAS and CMS Experiments," *Phys. Rev. Lett.* **114** (2015) 191803, arXiv:1503.07589 [hep-ex].

[14] N. Cabibbo, "Unitary Symmetry and Leptonic Decays," *Phys. Rev. Lett.* **10** (1963) 531–533.

[15] M. Kobayashi and T. Maskawa, "CP Violation in the Renormalizable Theory of Weak Interaction," *Prog. Theor. Phys.* **49** (1973) 652–657.

[16] **SNO** Collaboration, B. Aharmim *et al.*, "Combined Analysis of all Three Phases of Solar Neutrino Data from the Sudbury Neutrino Observatory," *Phys. Rev. C* **88** (2013) 025501, arXiv:1109.0763 [nucl-ex].

[17] **Super-Kamiokande** Collaboration, J. Hosaka *et al.*, "Three flavor neutrino oscillation analysis of atmospheric neutrinos in Super-Kamiokande," *Phys. Rev. D* **74** (2006) 032002, arXiv:hep-ex/0604011.

[18] **KamLAND** Collaboration, S. Abe *et al.*, "Precision Measurement of Neutrino Oscillation Parameters with KamLAND," *Phys. Rev. Lett.* **100** (2008) 221803, arXiv:0801.4589 [hep-ex].

[19] **Borexino** Collaboration, C. Arpesella *et al.*, "Direct Measurement of the Be-7 Solar Neutrino Flux with 192 Days of Borexino Data," *Phys. Rev. Lett.* **101** (2008) 091302, arXiv:0805.3843 [astro-ph].

[20] **K2K** Collaboration, M. H. Ahn *et al.*, "Measurement of Neutrino Oscillation by the K2K Experiment," *Phys. Rev. D* **74** (2006) 072003, arXiv:hep-ex/0606032.

[21] **MINOS** Collaboration, P. Adamson *et al.*, "Improved search for muon-neutrino to electron-neutrino oscillations in MINOS," *Phys. Rev. Lett.* **107** (2011) 181802, arXiv:1108.0015 [hep-ex].

[22] **OPERA** Collaboration, N. Agafonova *et al.*, "Observation of a first ν_τ candidate in the OPERA experiment in the CNGS beam," *Phys. Lett. B* **691** (2010) 138–145, arXiv:1006.1623 [hep-ex].

[23] **T2K** Collaboration, K. Abe *et al.*, "Indication of Electron Neutrino Appearance from an Accelerator-produced Off-axis Muon Neutrino Beam," *Phys. Rev. Lett.* **107** (2011) 041801, arXiv:1106.2822 [hep-ex].

[24] **Double Chooz** Collaboration, Y. Abe *et al.*, "Indication of Reactor $\bar{\nu}_e$ Disappearance in the Double Chooz Experiment," *Phys. Rev. Lett.* **108** (2012) 131801, arXiv:1112.6353 [hep-ex].

[25] Z. Maki, M. Nakagawa, and S. Sakata, "Remarks on the unified model of elementary particles," *Progress of Theoretical Physics* **28** (1962) 870–880.

[26] B. Pontecorvo, "Inverse beta processes and nonconservation of lepton charge," 1957.

[27] "Zur formulierung quantisierter feldtheorien," *Il Nuovo Cimento (1955-1965)* **1** no. 1, (1955) 205–225. https://app.dimensions.ai/details/publication/pub.1014089461.

[28] G. C. Wick, "The evaluation of the collision matrix," *Phys. Rev.* **80** (Oct, 1950) 268–272. https://link.aps.org/doi/10.1103/PhysRev.80.268.

[29] M. Neubert, "Renormalization Theory and Effective Field Theories," arXiv:1901.06573 [hep-ph].

[30] C. G. Bollini and J. J. Giambiagi, "Dimensional Renormalization: The Number of Dimensions as a Regularizing Parameter," *Nuovo Cim. B* **12** (1972) 20–26.

[31] G. 't Hooft and M. J. G. Veltman, "Regularization and Renormalization of Gauge Fields," *Nucl. Phys. B* **44** (1972) 189–213.

[32] N. N. Bogoliubov and O. S. Parasiuk, "On the Multiplication of the causal function in the quantum theory of fields," *Acta Math.* **97** (1957) 227–266.

[33] K. Hepp, "Proof of the Bogolyubov-Parasiuk theorem on renormalization," *Commun. Math. Phys.* **2** (1966) 301–326.

[34] W. Zimmermann, "Convergence of Bogoliubov's method of renormalization in momentum space," *Communications in Mathematical Physics* **15** no. 3, (1969) 208 – 234.

[35] W. A. Bardeen, A. J. Buras, D. W. Duke, and T. Muta, "Deep Inelastic Scattering Beyond the Leading Order in Asymptotically Free Gauge Theories," *Phys. Rev. D* **18** (1978) 3998.

[36] C. G. Callan, Jr., "Broken scale invariance in scalar field theory," *Phys. Rev. D* **2** (1970) 1541–1547.

[37] K. Symanzik, "Small distance behavior in field theory and power counting," *Commun. Math. Phys.* **18** (1970) 227–246.

[38] K. Symanzik, "Small distance behavior analysis and Wilson expansion," *Commun. Math. Phys.* **23** (1971) 49–86.

[39] F. J. Gilman and M. B. Wise, "Effective Hamiltonian for Delta s = 1 Weak Nonleptonic Decays in the Six Quark Model," *Phys. Rev. D* **20** (1979) 2392.

[40] E. Gardi and L. Magnea, "Factorization constraints for soft anomalous dimensions in QCD scattering amplitudes," *JHEP* **03** (2009) 079, arXiv:0901.1091 [hep-ph].

[41] T. Becher and M. Neubert, "On the Structure of Infrared Singularities of Gauge-Theory Amplitudes," *JHEP* **06** (2009) 081, arXiv:0903.1126 [hep-ph]. [Erratum: JHEP 11, 024 (2013)].

[42] **Muon g-2** Collaboration, B. Abi *et al.*, "Measurement of the Positive Muon Anomalous Magnetic Moment to 0.46 ppm," *Phys. Rev. Lett.* **126** no. 14, (2021) 141801, arXiv:2104.03281 [hep-ex].

[43] **BaBar** Collaboration, J. P. Lees *et al.*, "Measurement of an Excess of $\bar{B} \to D^{(*)}\tau^-\bar{\nu}_\tau$ Decays and Implications for Charged Higgs Bosons," *Phys. Rev. D* **88** no. 7, (2013) 072012, arXiv:1303.0571 [hep-ex].

[44] **LHCb** Collaboration, R. Aaij *et al.*, "Measurement of the ratio of branching fractions $\mathcal{B}(\bar{B}^0 \to D^{*+}\tau^-\bar{\nu}_\tau)/\mathcal{B}(\bar{B}^0 \to D^{*+}\mu^-\bar{\nu}_\mu)$," *Phys. Rev. Lett.* **115** no. 11, (2015) 111803, arXiv:1506.08614 [hep-ex]. [Erratum: Phys.Rev.Lett. 115, 159901 (2015)].

[45] **Belle** Collaboration, G. Caria *et al.*, "Measurement of $\mathcal{R}(D)$ and $\mathcal{R}(D^*)$ with a semileptonic tagging method," *Phys. Rev. Lett.* **124** no. 16, (2020) 161803, arXiv:1910.05864 [hep-ex].

[46] H. Georgi, "Effective field theory," *Ann. Rev. Nucl. Part. Sci.* **43** (1993) 209–252.

[47] A. V. Manohar, "Effective field theories," *Lect. Notes Phys.* **479** (1997) 311–362, arXiv:hep-ph/9606222.

[48] J. Wudka, "Electroweak effective Lagrangians," *Int. J. Mod. Phys. A* **9** (1994) 2301–2362, arXiv:hep-ph/9406205.

[49] A. Pich, "Effective field theory: Course," in *Les Houches Summer School in Theoretical Physics, Session 68: Probing the Standard Model of Particle Interactions*, pp. 949–1049. 6, 1998. arXiv:hep-ph/9806303.

[50] S. Weinberg, "Phenomenological Lagrangians," *Physica A* **96** no. 1-2, (1979) 327–340.

[51] K. G. Wilson, "Nonlagrangian models of current algebra," *Phys. Rev.* **179** (1969) 1499–1512.

[52] H. D. Politzer, "Power Corrections at Short Distances," *Nucl. Phys. B* **172** (1980) 349–382.

[53] H. Georgi, "On-shell effective field theory," *Nucl. Phys. B* **361** (1991) 339–350.

[54] A. V. Manohar and M. B. Wise, "Inclusive semileptonic B and polarized Lambda(b) decays from QCD," *Phys. Rev. D* **49** (1994) 1310–1329, arXiv:hep-ph/9308246.

[55] A. V. Manohar, "The HQET / NRQCD Lagrangian to order alpha / m-3," *Phys. Rev. D* **56** (1997) 230–237, arXiv:hep-ph/9701294.

[56] E. E. Jenkins, A. V. Manohar, and P. Stoffer, "Low-Energy Effective Field Theory below the Electroweak Scale: Anomalous Dimensions," *JHEP* **01** (2018) 084, arXiv:1711.05270 [hep-ph].

[57] E. Fermi, "Tentativo di una teoria dell'emissione dei raggi beta," *Ric. Sci.* **4** (1933) 491–495.

[58] L. P. Kadanoff, "Scaling laws for Ising models near T(c)," *Physics Physique Fizika* **2** (1966) 263–272.

[59] K. G. Wilson and M. E. Fisher, "Critical exponents in 3.99 dimensions," *Phys. Rev. Lett.* **28** (1972) 240–243.

[60] K. G. Wilson and J. B. Kogut, "The Renormalization group and the epsilon expansion," *Phys. Rept.* **12** (1974) 75–199.

[61] I. Brivio and M. Trott, "The Standard Model as an Effective Field Theory," *Phys. Rept.* **793** (2019) 1–98, arXiv:1706.08945 [hep-ph].

[62] A. V. Manohar, "Introduction to Effective Field Theories," arXiv:1804.05863 [hep-ph].

[63] M. Beneke and V. A. Smirnov, "Asymptotic expansion of Feynman integrals near threshold," *Nucl. Phys. B* **522** (1998) 321–344, arXiv:hep-ph/9711391.

[64] T. Appelquist and J. Carazzone, "Infrared Singularities and Massive Fields," *Phys. Rev. D* **11** (1975) 2856.

[65] J. de Blas, J. C. Criado, M. Perez-Victoria, and J. Santiago, "Effective description of general extensions of the Standard Model: the complete tree-level dictionary," *JHEP* **03** (2018) 109, arXiv:1711.10391 [hep-ph].

[66] A. Carmona, A. Lazopoulos, P. Olgoso, and J. Santiago, "Matchmakereft: automated tree-level and one-loop matching," *SciPost Phys.* **12** no. 6, (2022) 198, arXiv:2112.10787 [hep-ph].

[67] J. Fuentes-Martín, M. König, J. Pagès, A. E. Thomsen, and F. Wilsch, "A Proof of Concept for Matchete: An Automated Tool for Matching Effective Theories," arXiv:2212.04510 [hep-ph].

[68] S. Dittmaier and C. Grosse-Knetter, "Integrating out the standard Higgs field in the path integral," *Nucl. Phys. B* **459** (1996) 497–536, arXiv:hep-ph/9505266.

[69] B. Henning, X. Lu, and H. Murayama, "How to use the Standard Model effective field theory," *JHEP* **01** (2016) 023, arXiv:1412.1837 [hep-ph].

[70] B. Henning, X. Lu, and H. Murayama, "One-loop Matching and Running with Covariant Derivative Expansion," *JHEP* **01** (2018) 123, arXiv:1604.01019 [hep-ph].

[71] J. Fuentes-Martin, J. Portoles, and P. Ruiz-Femenia, "Integrating out heavy particles with functional methods: a simplified framework," *JHEP* **09** (2016) 156, arXiv:1607.02142 [hep-ph].

[72] F. del Aguila, Z. Kunszt, and J. Santiago, "One-loop effective lagrangians after matching," *Eur. Phys. J. C* **76** no. 5, (2016) 244, arXiv:1602.00126 [hep-ph].

[73] Z. Zhang, "Covariant diagrams for one-loop matching," *JHEP* **05** (2017) 152, arXiv:1610.00710 [hep-ph].

[74] T. Cohen, X. Lu, and Z. Zhang, "Functional Prescription for EFT Matching," *JHEP* **02** (2021) 228, arXiv:2011.02484 [hep-ph].

[75] W. Buchmuller and D. Wyler, "Effective Lagrangian Analysis of New Interactions and Flavor Conservation," *Nucl. Phys. B* **268** (1986) 621–653.

[76] B. Grzadkowski, M. Iskrzynski, M. Misiak, and J. Rosiek, "Dimension-Six Terms in the Standard Model Lagrangian," *JHEP* **10** (2010) 085, arXiv:1008.4884 [hep-ph].

[77] R. Alonso, M. B. Gavela, L. Merlo, S. Rigolin, and J. Yepes, "The Effective Chiral Lagrangian for a Light Dynamical "Higgs Particle"," *Phys. Lett. B* **722** (2013) 330–335, arXiv:1212.3305 [hep-ph]. [Erratum: Phys.Lett.B 726, 926 (2013)].

[78] G. Buchalla, O. Catà, and C. Krause, "Complete Electroweak Chiral Lagrangian with a Light Higgs at NLO," *Nucl. Phys. B* **880** (2014) 552–573, arXiv:1307.5017 [hep-ph]. [Erratum: Nucl.Phys.B 913, 475–478 (2016)].

[79] A. Pich, I. Rosell, J. Santos, and J. J. Sanz-Cillero, "Fingerprints of heavy scales in electroweak effective Lagrangians," *JHEP* **04** (2017) 012, arXiv:1609.06659 [hep-ph].

[80] A. Falkowski and R. Rattazzi, "Which EFT," *JHEP* **10** (2019) 255, arXiv:1902.05936 [hep-ph].

[81] T. Cohen, N. Craig, X. Lu, and D. Sutherland, "Is SMEFT Enough?," *JHEP* **03** (2021) 237, arXiv:2008.08597 [hep-ph].

[82] **CMS** Collaboration, A. M. Sirunyan *et al.*, "Combination of searches for Higgs boson pair production in proton-proton collisions at $\sqrt{s} = 13$ TeV," *Phys. Rev. Lett.* **122** no. 12, (2019) 121803, arXiv:1811.09689 [hep-ex].

[83] **ATLAS** Collaboration, G. Aad *et al.*, "Combination of searches for Higgs boson pairs in pp collisions at $\sqrt{s}$ =13 TeV with the ATLAS detector," *Phys. Lett. B* **800** (2020) 135103, arXiv:1906.02025 [hep-ex].

[84] S. Weinberg, "Baryon and Lepton Nonconserving Processes," *Phys. Rev. Lett.* **43** (1979) 1566–1570.

[85] A. Helset and A. Kobach, "Baryon Number, Lepton Number, and Operator Dimension in the SMEFT with Flavor Symmetries," *Phys. Lett. B* **800** (2020) 135132, arXiv:1909.05853 [hep-ph].

[86] M. Fierz, "Zur Fermischen Theorie des β-Zerfalls," *Zeitschrift fur Physik* **104** no. 7-8, (July, 1937) 553–565.

[87] C. C. Nishi, "Simple derivation of general Fierz-like identities," *Am. J. Phys.* **73** (2005) 1160–1163, arXiv:hep-ph/0412245.

[88] A. J. Buras and P. H. Weisz, "QCD Nonleading Corrections to Weak Decays in Dimensional Regularization and 't Hooft-Veltman Schemes," *Nucl. Phys. B* **333** (1990) 66–99.

[89] S. Herrlich and U. Nierste, "Evanescent operators, scheme dependences and double insertions," *Nucl. Phys. B* **455** (1995) 39–58, arXiv:hep-ph/9412375.

[90] N. Tracas and N. Vlachos, "Two Loop Calculations in QCD and the $\Delta I = 1/2$ Rule in Nonleptonic Weak Decays," *Phys. Lett. B* **115** (1982) 419.

[91] R. Alonso, E. E. Jenkins, A. V. Manohar, and M. Trott, "Renormalization Group Evolution of the Standard Model Dimension Six Operators III: Gauge Coupling Dependence and Phenomenology," *JHEP* **04** (2014) 159, arXiv:1312.2014 [hep-ph].

[92] G. F. Giudice, C. Grojean, A. Pomarol, and R. Rattazzi, "The Strongly-Interacting Light Higgs," *JHEP* **06** (2007) 045, arXiv:hep-ph/0703164.

[93] J. Elias-Miró, J. R. Espinosa, E. Masso, and A. Pomarol, "Renormalization of dimension-six operators relevant for the Higgs decays $h \to \gamma\gamma, \gamma Z$," *JHEP* **08** (2013) 033, arXiv:1302.5661 [hep-ph].

[94] K. Hagiwara, S. Ishihara, R. Szalapski, and D. Zeppenfeld, "Low-energy effects of new interactions in the electroweak boson sector," *Phys. Rev. D* **48** (1993) 2182–2203.

[95] V. Gherardi, D. Marzocca, and E. Venturini, "Matching scalar leptoquarks to the SMEFT at one loop," *JHEP* **07** (2020) 225, arXiv:2003.12525 [hep-ph]. [Erratum: JHEP 01, 006 (2021)].

[96] J. Fuentes-Martín, M. König, J. Pagès, A. E. Thomsen, and F. Wilsch, "Evanescent operators in one-loop matching computations," *JHEP* **02** (2023) 031, arXiv:2211.09144 [hep-ph].

[97] A. Falkowski, "Higgs Basis: Proposal for an EFT basis choice for LHC HXSWG,". https://cds.cern.ch/record/2001958.

[98] R. S. Gupta, A. Pomarol, and F. Riva, "BSM Primary Effects," *Phys. Rev. D* **91** no. 3, (2015) 035001, arXiv:1405.0181 [hep-ph].

[99] A. Falkowski, "Effective field theory approach to LHC Higgs data," *Pramana* **87** no. 3, (2016) 39, arXiv:1505.00046 [hep-ph].

[100] **LHC Higgs Cross Section Working Group** Collaboration, D. de Florian *et al.*, "Handbook of LHC Higgs Cross Sections: 4. Deciphering the Nature of the Higgs Sector," arXiv:1610.07922 [hep-ph].

[101] A. Azatov *et al.*, "Off-shell Higgs Interpretations Task Force: Models and Effective Field Theories Subgroup Report," arXiv:2203.02418 [hep-ph].

[102] J. Aebischer *et al.*, "WCxf: an exchange format for Wilson coefficients beyond the Standard Model," *Comput. Phys. Commun.* **232** (2018) 71–83, arXiv:1712.05298 [hep-ph].

[103] R. Contino, M. Ghezzi, C. Grojean, M. Muhlleitner, and M. Spira, "Effective Lagrangian for a light Higgs-like scalar," *JHEP* **07** (2013) 035, arXiv:1303.3876 [hep-ph].

[104] **LHC Higgs Cross Section Working Group** Collaboration, D. de Florian *et al.*, "Handbook of LHC Higgs Cross Sections: 4. Deciphering the Nature of the Higgs Sector," arXiv:1610.07922 [hep-ph].

[105] A. Buras, *Gauge Theory of Weak Decays*. Cambridge University Press, 6, 2020.

[106] J. Gasser and H. Leutwyler, "Chiral Perturbation Theory: Expansions in the Mass of the Strange Quark," *Nucl. Phys. B* **250** (1985) 465–516.

[107] J. Gasser and H. Leutwyler, "Low-Energy Expansion of Meson Form-Factors," *Nucl. Phys. B* **250** (1985) 517–538.

[108] J. Gasser and H. Leutwyler, "eta —> 3 pi to One Loop," *Nucl. Phys. B* **250** (1985) 539–560.

[109] N. Isgur and M. B. Wise, "Weak Decays of Heavy Mesons in the Static Quark Approximation," *Phys. Lett. B* **232** (1989) 113–117.

[110] N. Isgur and M. B. Wise, "WEAK TRANSITION FORM-FACTORS BETWEEN HEAVY MESONS," *Phys. Lett. B* **237** (1990) 527–530.

[111] C. W. Bauer, S. Fleming, and M. E. Luke, "Summing Sudakov logarithms in $B \to X_s\gamma$in effective field theory.," *Phys. Rev. D* **63** (2000) 014006, arXiv:hep-ph/0005275.

[112] C. W. Bauer, S. Fleming, D. Pirjol, and I. W. Stewart, "An Effective field theory for collinear and soft gluons: Heavy to light decays," *Phys. Rev. D* **63** (2001) 114020, arXiv:hep-ph/0011336.

[113] C. W. Bauer and I. W. Stewart, "Invariant operators in collinear effective theory," *Phys. Lett. B* **516** (2001) 134–142, arXiv:hep-ph/0107001.

[114] C. W. Bauer, D. Pirjol, and I. W. Stewart, "Soft collinear factorization in effective field theory," *Phys. Rev. D* **65** (2002) 054022, arXiv:hep-ph/0109045.

[115] M. Beneke, A. P. Chapovsky, M. Diehl, and T. Feldmann, "Soft collinear effective theory and heavy to light currents beyond leading power," *Nucl. Phys. B* **643** (2002) 431–476, arXiv:hep-ph/0206152.

[116] M. Beneke and T. Feldmann, "Multipole expanded soft collinear effective theory with nonAbelian gauge symmetry," *Phys. Lett. B* **553** (2003) 267–276, arXiv:hep-ph/0211358.

[117] R. J. Hill and M. Neubert, "Spectator interactions in soft collinear effective theory," *Nucl. Phys. B* **657** (2003) 229–256, arXiv:hep-ph/0211018.

[118] G. Isidori, F. Wilsch, and D. Wyler, "The Standard Model effective field theory at work," arXiv:2303.16922 [hep-ph].

[119] T. Corbett, O. J. P. Éboli, and M. C. Gonzalez-Garcia, "Unitarity Constraints on Dimension-Six Operators," *Phys. Rev. D* **91** no. 3, (2015) 035014, arXiv:1411.5026 [hep-ph].

[120] F. Maltoni, L. Mantani, and K. Mimasu, "Top-quark electroweak interactions at high energy," *JHEP* **10** (2019) 004, arXiv:1904.05637 [hep-ph].

[121] G. Dvali, A. Franca, and C. Gomez, "Road Signs for UV-Completion," arXiv:1204.6388 [hep-th].

[122] C. Zhang and S.-Y. Zhou, "Positivity bounds on vector boson scattering at the LHC," *Phys. Rev. D* **100** no. 9, (2019) 095003, arXiv:1808.00010 [hep-ph].

[123] K. Yamashita, C. Zhang, and S.-Y. Zhou, "Elastic positivity vs extremal positivity bounds in SMEFT: a case study in transversal electroweak gauge-boson scatterings," *JHEP* **01** (2021) 095, arXiv:2009.04490 [hep-ph].

[124] G. N. Remmen and N. L. Rodd, "Signs, spin, SMEFT: Sum rules at dimension six," *Phys. Rev. D* **105** no. 3, (2022) 036006, arXiv:2010.04723 [hep-ph].

[125] B. Bellazzini, J. Elias Miró, R. Rattazzi, M. Riembau, and F. Riva, "Positive moments for scattering amplitudes," *Phys. Rev. D* **104** no. 3, (2021) 036006, arXiv:2011.00037 [hep-th].

[126] M. Chala and J. Santiago, "Positivity bounds in the standard model effective field theory beyond tree level," *Phys. Rev. D* **105** no. 11, (2022) L111901, arXiv:2110.01624 [hep-ph].

[127] A. Manohar and H. Georgi, "Chiral Quarks and the Nonrelativistic Quark Model," *Nucl. Phys. B* **234** (1984) 189–212.

[128] C. Arzt, "Reduced effective Lagrangians," *Phys. Lett. B* **342** (1995) 189–195, arXiv:hep-ph/9304230.

[129] E. E. Jenkins, A. V. Manohar, and M. Trott, "On Gauge Invariance and Minimal Coupling," *JHEP* **09** (2013) 063, arXiv:1305.0017 [hep-ph].

[130] M. B. Einhorn and J. Wudka, "The Bases of Effective Field Theories," *Nucl. Phys. B* **876** (2013) 556–574, arXiv:1307.0478 [hep-ph].

[131] **Particle Data Group** Collaboration, P. A. Zyla *et al.*, "Review of Particle Physics," *PTEP* **2020** no. 8, (2020) 083C01.

[132] A. Falkowski, M. González-Alonso, and K. Mimouni, "Compilation of low-energy constraints on 4-fermion operators in the SMEFT," *JHEP* **08** (2017) 123, arXiv:1706.03783 [hep-ph].

[133] V. Bresó-Pla, A. Falkowski, and M. González-Alonso, "A_{FB} in the SMEFT: prfecision Z physics at the LHC," *JHEP* **08** (2021) 021, arXiv:2103.12074 [hep-ph].

[134] V. Bresó-Pla, A. Falkowski, M. González-Alonso, and K. Monsálvez-Pozo, "EFT analysis of New Physics at COHERENT," arXiv:2301.07036 [hep-ph].

[135] S. Descotes-Genon, A. Falkowski, M. Fedele, M. González-Alonso, and J. Virto, "The CKM parameters in the SMEFT," *JHEP* **05** (2019) 172, arXiv:1812.08163 [hep-ph].

[136] S. Dawson and P. P. Giardino, "Electroweak and QCD corrections to Z and W pole observables in the standard model EFT," *Phys. Rev. D* **101** no. 1, (2020) 013001, arXiv:1909.02000 [hep-ph].

[137] S. Dawson, S. Homiller, and S. D. Lane, "Putting standard model EFT fits to work," *Phys. Rev. D* **102** no. 5, (2020) 055012, arXiv:2007.01296 [hep-ph].

[138] M. González-Alonso, J. Martin Camalich, and K. Mimouni, "Renormalization-group evolution of new physics contributions to (semi)leptonic meson decays," *Phys. Lett. B* **772** (2017) 777–785, arXiv:1706.00410 [hep-ph].

[139] S. Dawson and P. P. Giardino, "New physics through Drell-Yan standard model EFT measurements at NLO," *Phys. Rev. D* **104** no. 7, (2021) 073004, arXiv:2105.05852 [hep-ph].

[140] Z. Han and W. Skiba, "Effective theory analysis of precision electroweak data," *Phys. Rev. D* **71** (2005) 075009, arXiv:hep-ph/0412166.

[141] A. Efrati, A. Falkowski, and Y. Soreq, "Electroweak constraints on flavorful effective theories," *JHEP* **07** (2015) 018, arXiv:1503.07872 [hep-ph].

[142] **CHARM** Collaboration, J. Dorenbosch *et al.*, "Experimental Verification of the Universality of ν_e and ν_μ Coupling to the Neutral Weak Current," *Phys. Lett. B* **180** (1986) 303–307.

[143] **Particle Data Group** Collaboration, C. Patrignani *et al.*, "Review of Particle Physics," *Chin. Phys. C* **40** no. 10, (2016) 100001.

[144] E. J. Beise, M. L. Pitt, and D. T. Spayde, "The SAMPLE experiment and weak nucleon structure," *Prog. Part. Nucl. Phys.* **54** (2005) 289–350, arXiv:nucl-ex/0412054.

[145] A. Argento *et al.*, "Electroweak Asymmetry in Deep Inelastic Muon - Nucleon Scattering," *Phys. Lett. B* **120** (1983) 245.

[146] M. González-Alonso and J. Martin Camalich, "Global Effective-Field-Theory analysis of New-Physics effects in (semi)leptonic kaon decays," *JHEP* **12** (2016) 052, arXiv:1605.07114 [hep-ph].

[147] **ALEPH, DELPHI, L3, OPAL, LEP Electroweak** Collaboration, S. Schael *et al.*, "Electroweak Measurements in Electron-Positron Collisions at W-Boson-Pair Energies at LEP," *Phys. Rept.* **532** (2013) 119–244, arXiv:1302.3415 [hep-ex].

[148] **LEP, ALEPH, DELPHI, L3, OPAL, LEP Electroweak Working Group, SLD Electroweak Group, SLD Heavy Flavor Group** Collaboration, D. Abbaneo *et al.*, "A Combination of preliminary electroweak measurements and constraints on the standard model," arXiv:hep-ex/0312023.

[149] **VENUS** Collaboration, K. Abe *et al.*, "A Study of the charm and bottom quark production in e+ e- annihilation at s**(1/2) = 58-GeV using prompt electrons," *Phys. Lett. B* **313** (1993) 288–298.

[150] **TOPAZ** Collaboration, Y. Inoue *et al.*, "Measurement of the cross-section and forward - backward charge asymmetry for the b and c quark in e+ e- annihilation with inclusive muons at s**(1/2) = 58-GeV," *Eur. Phys. J. C* **18** (2000) 273–282, arXiv:hep-ex/0012033.

[151] **CHARM-II** Collaboration, P. Vilain *et al.*, "Precision measurement of electroweak parameters from the scattering of muon-neutrinos on electrons," *Phys. Lett. B* **335** (1994) 246–252.

[152] **CCFR** Collaboration, S. R. Mishra *et al.*, "Neutrino tridents and W Z interference," *Phys. Rev. Lett.* **66** (1991) 3117–3120.

[153] **Particle Data Group** Collaboration, R. L. Workman *et al.*, "Review of Particle Physics," *PTEP* **2022** (2022) 083C01.

[154] **VENUS** Collaboration, H. Hanai *et al.*, "Measurement of tau polarization in e+ e- annihilation at s**(1/2) = 58-GeV," *Phys. Lett. B* **403** (1997) 155–162, arXiv:hep-ex/9703003.

[155] **D0** Collaboration, V. M. Abazov *et al.*, "Measurement of $\sin^2\theta^{\ell}_{\text{eff}}$ and Z-light quark couplings using the forward-backward charge asymmetry in $p\bar{p} \to Z/\gamma^* \to e^+e^-$ events with $\mathcal{L} = 5.0$ fb^{-1} at $\sqrt{s} = 1.96$ TeV," *Phys. Rev. D* **84** (2011) 012007, arXiv:1104.4590 [hep-ex].

[156] **ALEPH, DELPHI, L3, OPAL, SLD, LEP Electroweak Working Group, SLD Electroweak Group, SLD Heavy Flavour Group** Collaboration, S. Schael *et al.*, "Precision electroweak measurements on the Z resonance," *Phys. Rept.* **427** (2006) 257–454, arXiv:hep-ex/0509008.

[157] **ALEPH, DELPHI, L3, OPAL, LEP Electroweak** Collaboration, S. Schael *et al.*, "Electroweak Measurements in Electron-Positron Collisions at W-Boson-Pair Energies at LEP," *Phys. Rept.* **532** (2013) 119–244, arXiv:1302.3415 [hep-ex].

[158] M. E. Peskin and T. Takeuchi, "Estimation of oblique electroweak corrections," *Phys. Rev. D* **46** (1992) 381–409.

[159] **ATLAS** Collaboration, M. Aaboud *et al.*, "Measurement of the W-boson mass in pp collisions at $\sqrt{s} = 7$ TeV with the ATLAS detector," *Eur. Phys. J. C* **78** no. 2, (2018) 110, arXiv:1701.07240 [hep-ex]. [Erratum: Eur.Phys.J.C 78, 898 (2018)].

[160] **CDF** Collaboration, T. Aaltonen *et al.*, "High-precision measurement of the W boson mass with the CDF II detector," *Science* **376** no. 6589, (2022) 170–176.

[161] **ATLAS** Collaboration, "Improved W boson Mass Measurement using 7 TeV Proton-Proton Collisions with the ATLAS Detector,".

[162] **CDF** Collaboration, T. Aaltonen *et al.*, "A Direct measurement of the W boson width in $p\bar{p}$ collisions at $\sqrt{s} = 1.96$-TeV," *Phys. Rev. Lett.* **100** (2008) 071801, arXiv:0710.4112 [hep-ex].

[163] **D0** Collaboration, V. M. Abazov *et al.*, "Direct measurement of the W boson width," *Phys. Rev. Lett.* **103** (2009) 231802, arXiv:0909.4814 [hep-ex].

[164] **LHCb** Collaboration, R. Aaij *et al.*, "Measurement of forward $W \to e\nu$ production in pp collisions at $\sqrt{s} = 8$ TeV," *JHEP* **10** (2016) 030, arXiv:1608.01484 [hep-ex].

[165] **ATLAS** Collaboration, M. Aaboud *et al.*, "Precision measurement and interpretation of inclusive W^+ , W^- and Z/γ^* production cross sections with the ATLAS detector," *Eur. Phys. J. C* **77** no. 6, (2017) 367, arXiv:1612.03016 [hep-ex].

[166] **ATLAS** Collaboration, G. Aad *et al.*, "Test of the universality of τ and μ lepton couplings in W-boson decays from $t\bar{t}$ events with the ATLAS detector," arXiv:2007.14040 [hep-ex].

[167] **LHCb** Collaboration, R. Aaij *et al.*, "Measurement of the forward-backward asymmetry in $Z/\gamma^* \to \mu^+\mu^-$ decays and determination of the effective weak mixing angle," *JHEP* **11** (2015) 190, arXiv:1509.07645 [hep-ex].

[168] **ATLAS** Collaboration, G. Aad *et al.*, "Measurement of the forward-backward asymmetry of electron and muon pair-production in pp collisions at $\sqrt{s} = 7$ TeV with the ATLAS detector," *JHEP* **09** (2015) 049, arXiv:1503.03709 [hep-ex].

[169] **CMS** Collaboration, A. M. Sirunyan *et al.*, "Measurement of the weak mixing angle using the forward-backward asymmetry of Drell-Yan events in pp collisions at 8 TeV," *Eur. Phys. J. C* **78** no. 9, (2018) 701, arXiv:1806.00863 [hep-ex].

[170] R. R. Wilson, "The Tevatron," *Phys. Today* **30N10** (1977) 23–30.

[171] J. Peoples, "The Fermilab Antiproton Source," *IEEE Trans. Nucl. Sci.* **30** (1983) 1970–1975.

[172] **ATLAS** Collaboration, G. Aad *et al.*, "Search for the lepton flavor violating decay Z→eμ in pp collisions at $\sqrt{s}$ TeV with the ATLAS detector," *Phys. Rev. D* **90** no. 7, (2014) 072010, arXiv:1408.5774 [hep-ex].

[173] P. Janot and S. Jadach, "Improved Bhabha cross section at LEP and the number of light neutrino species," *Phys. Lett. B* **803** (2020) 135319, arXiv:1912.02067 [hep-ph].

[174] D. d'Enterria and C. Yan, "Revised QCD effects on the Z $\to b\bar{b}$ forward-backward asymmetry," arXiv:2011.00530 [hep-ph].

[175] **SLD** Collaboration, K. Abe *et al.*, "First direct measurement of the parity violating coupling of the Z0 to the s quark," *Phys. Rev. Lett.* **85** (2000) 5059–5063, arXiv:hep-ex/0006019.

[176] A. Falkowski and D. Straub, "Flavourful SMEFT likelihood for Higgs and electroweak data," *JHEP* **04** (2020) 066, arXiv:1911.07866 [hep-ph].

[177] **D0** Collaboration, B. Abbott *et al.*, "A measurement of the $W \to \tau\nu$ production cross section in $p\bar{p}$ collisions at $\sqrt{s} = 1.8$ TeV," *Phys. Rev. Lett.* **84** (2000) 5710–5715, arXiv:hep-ex/9912065.

[178] D. d'Enterria and V. Jacobsen, "Improved strong coupling determinations from hadronic decays of electroweak bosons at N^{3}LO accuracy," arXiv:2005.04545 [hep-ph].

[179] M. Awramik, M. Czakon, A. Freitas, and G. Weiglein, "Precise prediction for the W boson mass in the standard model," *Phys. Rev. D* **69** (2004) 053006, arXiv:hep-ph/0311148.

[180] **CDF** Collaboration, A. Abulencia *et al.*, "Measurements of inclusive W and Z cross sections in p anti-p collisions at s**(1/2) = 1.96-TeV," *J. Phys. G* **34** (2007) 2457–2544, arXiv:hep-ex/0508029.

[181] **ATLAS** Collaboration, "A precise determination of the strong-coupling constant from the recoil of Z bosons with the ATLAS experiment at $\sqrt{s} = 8$ TeV,".

[182] P. Fisher, U. Becker, and J. Kirkby, "Very high precision tests of the electroweak theory," *Phys. Lett. B* **356** (1995) 404–408.

[183] M. Dittmar, "Neutral current interference in the TeV region: The Experimental sensitivity at the LHC," *Phys. Rev. D* **55** (1997) 161–166, arXiv:hep-ex/9606002.

[184] **CMS** Collaboration, V. Khachatryan *et al.*, "Forward–backward asymmetry of Drell–Yan lepton pairs in pp collisions at $\sqrt{s} = 8$ TeV," *Eur. Phys. J. C* **76** no. 6, (2016) 325, arXiv:1601.04768 [hep-ex].

[185] **ATLAS** Collaboration, M. Aaboud *et al.*, "Measurement of the Drell-Yan triple-differential cross section in pp collisions at $\sqrt{s} = 8$ TeV," *JHEP* **12** (2017) 059, arXiv:1710.05167 [hep-ex].

[186] E. Accomando, J. Fiaschi, F. Hautmann, and S. Moretti, "Neutral current forward–backward asymmetry: from θ_W to PDF determinations," *Eur. Phys. J. C* **78** no. 8, (2018) 663, arXiv:1805.09239 [hep-ph]. [Erratum: Eur.Phys.J.C 79, 453 (2019)].

[187] A. Bodek, J. Han, A. Khukhunaishvili, and W. Sakumoto, "Using Drell–Yan forward–backward asymmetry to reduce PDF uncertainties in the measurement of electroweak parameters," *Eur. Phys. J. C* **76** no. 3, (2016) 115, arXiv:1507.02470 [hep-ex].

[188] **CMS** Collaboration, S. Chatrchyan *et al.*, "Measurement of the weak mixing angle with the Drell-Yan process in proton-proton collisions at the LHC," *Phys. Rev. D* **84** (2011) 112002, arXiv:1110.2682 [hep-ex].

[189] J. C. Collins and D. E. Soper, "Angular Distribution of Dileptons in High-Energy Hadron Collisions," *Phys. Rev. D* **16** (1977) 2219.

[190] A. Greljo and D. Marzocca, "High-p_T dilepton tails and flavor physics," *Eur. Phys. J. C* **77** no. 8, (2017) 548, arXiv:1704.09015 [hep-ph].

[191] **ATLAS** Collaboration, "Measurement of the effective leptonic weak mixing angle using electron and muon pairs from Z-boson decay in the ATLAS experiment at $\sqrt{s} = 8$ TeV," tech. rep., CERN, Geneva, 2018. https://cds.cern.ch/record/2630340.

[192] G. Bozzi, S. Catani, G. Ferrera, D. de Florian, and M. Grazzini, "Production of Drell-Yan lepton pairs in hadron collisions: Transverse-momentum resummation at next-to-next-to-leading logarithmic accuracy," *Phys. Lett. B* **696** (2011) 207–213, arXiv:1007.2351 [hep-ph].

[193] S. Catani, D. de Florian, G. Ferrera, and M. Grazzini, "Vector boson production at hadron colliders: transverse-momentum resummation and leptonic decay," *JHEP* **12** (2015) 047, arXiv:1507.06937 [hep-ph].

[194] S. Catani, L. Cieri, G. Ferrera, D. de Florian, and M. Grazzini, "Vector boson production at hadron colliders: a fully exclusive QCD calculation at NNLO," *Phys. Rev. Lett.* **103** (2009) 082001, arXiv:0903.2120 [hep-ph].

[195] L. A. Harland-Lang, A. D. Martin, P. Motylinski, and R. S. Thorne, "Parton distributions in the LHC era: MMHT 2014 PDFs," *Eur. Phys. J. C* **75** no. 5, (2015) 204, arXiv:1412.3989 [hep-ph].

[196] J. Alwall, R. Frederix, S. Frixione, V. Hirschi, F. Maltoni, O. Mattelaer, H.-S. Shao, T. Stelzer, P. Torrielli, and M. Zaro, "The automated computation of tree-level and next-to-leading order differential cross sections, and their matching to parton shower simulations," *JHEP* **07** (2014) 79, arXiv:1405.0301 [hep-ph].

[197] E. Conte, B. Fuks, and G. Serret, "MadAnalysis 5, a user-friendly framework for collider phenomenology," *Comput. Phys. Commun.* **184** (2013) 222–256, arXiv:1206.1599 [hep-ph].

[198] A. Celis, J. Fuentes-Martin, A. Vicente, and J. Virto, "DsixTools: The Standard Model Effective Field Theory Toolkit," *Eur. Phys. J. C* **77** no. 6, (2017) 405, arXiv:1704.04504 [hep-ph].

[199] J. Aebischer, J. Kumar, and D. M. Straub, "Wilson: a Python package for the running and matching of Wilson coefficients above and below the electroweak scale," *Eur. Phys. J. C* **78** no. 12, (2018) 1026, arXiv:1804.05033 [hep-ph].

[200] R. Aoude, T. Hurth, S. Renner, and W. Shepherd, "The impact of flavour data on global fits of the MFV SMEFT," *JHEP* **12** (2020) 113, arXiv:2003.05432 [hep-ph].

[201] D. A. Faroughy, G. Isidori, F. Wilsch, and K. Yamamoto, "Flavour symmetries in the SMEFT," *JHEP* **08** (2020) 166, arXiv:2005.05366 [hep-ph].

[202] J. D. Wells and Z. Zhang, "Effective theories of universal theories," *JHEP* **01** (2016) 123, arXiv:1510.08462 [hep-ph].

[203] R. Dermisek, "Light Charged Higgs and Lepton Universality in W boson Decays," arXiv:0807.2135 [hep-ph].

[204] A. Filipuzzi, J. Portoles, and M. Gonzalez-Alonso, "$U(2)^5$ flavor symmetry and lepton universality violation in $W \to \tau\nu_\tau$," *Phys. Rev. D* **85** (2012) 116010, arXiv:1203.2092 [hep-ph].

[205] W. Mader, J.-h. Park, G. M. Pruna, D. Stockinger, and A. Straessner, "LHC Explores What LEP Hinted at: CP-Violating Type-I 2HDM," *JHEP* **09** (2012) 125, arXiv:1205.2692 [hep-ph]. [Erratum: JHEP 01, 006 (2014)].

[206] J. M. Lizana, J. Matias, and B. A. Stefanek, "Explaining the $B_{d,s} \to K^{(*)}\bar{K}^{(*)}$ non-leptonic puzzle and charged-current B-anomalies via scalar leptoquarks," arXiv:2306.09178 [hep-ph].

[207] J. Davighi and B. A. Stefanek, "Deconstructed Hypercharge: A Natural Model of Flavour," arXiv:2305.16280 [hep-ph].

[208] L. Allwicher, G. Isidori, J. M. Lizana, N. Selimovic, and B. A. Stefanek, "Third-family quark-lepton Unification and electroweak precision tests," *JHEP* **05** (2023) 179, arXiv:2302.11584 [hep-ph].

[209] A. de Giorgi, L. Merlo, and S. Pokorski, "The Low-Scale Seesaw Solution to the MWM_W and (g−2)$\mu(g-2)$ Anomalies," *Fortsch. Phys.* **71** no. 4-5, (2023) 2300020, arXiv:2211.03797 [hep-ph].

[210] N. Arkani-Hamed and K. Harigaya, "Naturalness and the muon magnetic moment," *JHEP* **09** (2021) 025, arXiv:2106.01373 [hep-ph].

[211] V. Ilisie, "Non-metricity signatures on the Higgs boson signal strengths at the LHC," *JHEP* **09** (2022) 122, arXiv:2207.07090 [hep-ph].

[212] M. Beccaria, N. Orlando, G. Panizzo, F. M. Renard, and C. Verzegnassi, "The Relevance of polarized bZ production at LHC," *Phys. Lett. B* **713** (2012) 457–461, arXiv:1204.5315 [hep-ph].

[213] **CMS** Collaboration, A. M. Sirunyan *et al.*, "Observation of $t\bar{t}H$ production," *Phys. Rev. Lett.* **120** no. 23, (2018) 231801, arXiv:1804.02610 [hep-ex].

[214] **ATLAS** Collaboration, G. Aad *et al.*, "Measurement of the associated production of a Higgs boson decaying into b-quarks with a vector boson at high transverse momentum in pp collisions at $\sqrt{s} = 13$ TeV with the ATLAS detector," *Phys. Lett. B* **816** (2021) 136204, arXiv:2008.02508 [hep-ex].

[215] B. Yan and C. P. Yuan, "Anomalous Zbb^- Couplings: From LEP to LHC," *Phys. Rev. Lett.* **127** no. 5, (2021) 051801, arXiv:2101.06261 [hep-ph].

[216] ATLAS, "Prospect for a measurement of the Weak Mixing Angle in $pp \to Z/\gamma^* \to e^+e^-$ events with the ATLAS detector at the High Luminosity Large Hadron Collider," *Report number: ATL-PHYS-PUB-2018-037* (2018) .

[217] A. Horne, J. Pittman, M. Snedeker, W. Shepherd, and J. W. Walker, "Shift-Type SMEFT Effects in Dileptons at the LHC," arXiv:2007.12698 [hep-ph].

[218] A. Buckley, C. Englert, J. Ferrando, D. J. Miller, L. Moore, M. Russell, and C. D. White, "Global fit of top quark effective theory to data," *Phys. Rev. D* **92** no. 9, (2015) 091501, arXiv:1506.08845 [hep-ph].

[219] D. Barducci *et al.*, "Interpreting top-quark LHC measurements in the standard-model effective field theory," arXiv:1802.07237 [hep-ph].

[220] J. Ellis, M. Madigan, K. Mimasu, V. Sanz, and T. You, "Top, Higgs, Diboson and Electroweak Fit to the Standard Model Effective Field Theory," arXiv:2012.02779 [hep-ph].

[221] S. Bruggisser, R. Schäfer, D. van Dyk, and S. Westhoff, "The Flavor of UV Physics," arXiv:2101.07273 [hep-ph].

[222] S. Dawson, P. P. Giardino, and A. Ismail, "Standard model EFT and the Drell-Yan process at high energy," *Phys. Rev. D* **99** no. 3, (2019) 035044, arXiv:1811.12260 [hep-ph].

[223] D. Z. Freedman, "Coherent Neutrino Nucleus Scattering as a Probe of the Weak Neutral Current," *Phys. Rev. D* **9** (1974) 1389–1392.

[224] A. Drukier and L. Stodolsky, "Principles and Applications of a Neutral Current Detector for Neutrino Physics and Astronomy," *Phys. Rev. D* **30** (1984) 2295.

[225] **COHERENT** Collaboration, D. Akimov *et al.*, "Observation of Coherent Elastic Neutrino-Nucleus Scattering," *Science* **357** no. 6356, (2017) 1123–1126, arXiv:1708.01294 [nucl-ex].

[226] Y. Grossman, "Nonstandard neutrino interactions and neutrino oscillation experiments," *Phys. Lett. B* **359** (1995) 141–147, arXiv:hep-ph/9507344.

[227] A. M. Gago, M. M. Guzzo, H. Nunokawa, W. J. C. Teves, and R. Zukanovich Funchal, "Probing flavor changing neutrino interactions using neutrino beams from a muon storage ring," *Phys. Rev. D* **64** (2001) 073003, arXiv:hep-ph/0105196.

[228] M. Campanelli and A. Romanino, "Effects of new physics in neutrino oscillations in matter," *Phys. Rev. D* **66** (2002) 113001, arXiv:hep-ph/0207350.

[229] A. Falkowski, M. González-Alonso, and Z. Tabrizi, "Consistent QFT description of non-standard neutrino interactions," *JHEP* **11** (2020) 048, arXiv:1910.02971 [hep-ph].

[230] J. Erler and S. Su, "The Weak Neutral Current," *Prog. Part. Nucl. Phys.* **71** (2013) 119–149, arXiv:1303.5522 [hep-ph].

[231] K. Scholberg, "Prospects for measuring coherent neutrino-nucleus elastic scattering at a stopped-pion neutrino source," *Phys. Rev. D* **73** (2006) 033005, arXiv:hep-ex/0511042.

[232] J. Barranco, O. Miranda, and T. I. Rashba, "Probing new physics with coherent neutrino scattering off nuclei," *JHEP* **12** (2005) 021, arXiv:hep-ph/0508299.

[233] P. Coloma, M. C. Gonzalez-Garcia, M. Maltoni, and T. Schwetz, "COHERENT Enlightenment of the Neutrino Dark Side," *Phys. Rev. D* **96** no. 11, (2017) 115007, arXiv:1708.02899 [hep-ph].

[234] D. K. Papoulias and T. S. Kosmas, "COHERENT constraints to conventional and exotic neutrino physics," *Phys. Rev. D* **97** no. 3, (2018) 033003, arXiv:1711.09773 [hep-ph].

[235] I. M. Shoemaker, "COHERENT search strategy for beyond standard model neutrino interactions," *Phys. Rev. D* **95** no. 11, (2017) 115028, arXiv:1703.05774 [hep-ph].

[236] J. Liao and D. Marfatia, "COHERENT constraints on nonstandard neutrino interactions," *Phys. Lett. B* **775** (2017) 54–57, arXiv:1708.04255 [hep-ph].

[237] D. Aristizabal Sierra, V. De Romeri, and N. Rojas, "COHERENT analysis of neutrino generalized interactions," *Phys. Rev. D* **98** (2018) 075018, arXiv:1806.07424 [hep-ph].

[238] P. B. Denton, Y. Farzan, and I. M. Shoemaker, "Testing large non-standard neutrino interactions with arbitrary mediator mass after COHERENT data," *JHEP* **07** (2018) 037, arXiv:1804.03660 [hep-ph].

[239] I. Esteban, M. C. Gonzalez-Garcia, M. Maltoni, I. Martinez-Soler, and J. Salvado, "Updated constraints on non-standard interactions from global analysis of oscillation data," *JHEP* **08** (2018) 180, arXiv:1805.04530 [hep-ph]. [Addendum: JHEP 12, 152 (2020)].

[240] A. N. Khan and W. Rodejohann, "New physics from COHERENT data with an improved quenching factor," *Phys. Rev. D* **100** no. 11, (2019) 113003, arXiv:1907.12444 [hep-ph].

[241] C. Giunti, "General COHERENT constraints on neutrino nonstandard interactions," *Phys. Rev. D* **101** no. 3, (2020) 035039, arXiv:1909.00466 [hep-ph].

[242] G. Arcadi, M. Lindner, J. Martins, and F. S. Queiroz, "New physics probes: Atomic parity violation, polarized electron scattering and neutrino-nucleus coherent scattering," *Nucl. Phys. B* **959** (2020) 115158, arXiv:1906.04755 [hep-ph].

[243] P. Coloma, I. Esteban, M. C. Gonzalez-Garcia, and M. Maltoni, "Improved global fit to Non-Standard neutrino Interactions using COHERENT energy and timing data," *JHEP* **02** (2020) 023, arXiv:1911.09109 [hep-ph]. [Addendum: JHEP 12, 071 (2020)].

[244] P. B. Denton and J. Gehrlein, "A Statistical Analysis of the COHERENT Data and Applications to New Physics," *JHEP* **04** (2021) 266, arXiv:2008.06062 [hep-ph].

[245] O. G. Miranda, D. K. Papoulias, G. Sanchez Garcia, O. Sanders, M. Tórtola, and J. W. F. Valle, "Implications of the first detection of coherent elastic neutrino-nucleus scattering (CEvNS) with Liquid Argon," *JHEP* **05** (2020) 130, arXiv:2003.12050 [hep-ph]. [Erratum: JHEP 01, 067 (2021)].

[246] P. Coloma, I. Esteban, M. C. Gonzalez-Garcia, L. Larizgoitia, F. Monrabal, and S. Palomares-Ruiz, "Bounds on new physics with data of the Dresden-II reactor experiment and COHERENT," *JHEP* **05** (2022) 037, arXiv:2202.10829 [hep-ph].

[247] M. Atzori Corona, M. Cadeddu, N. Cargioli, F. Dordei, C. Giunti, Y. F. Li, C. A. Ternes, and Y. Y. Zhang, "Impact of the Dresden-II and COHERENT neutrino scattering data on neutrino electromagnetic properties and electroweak physics," *JHEP* **09** (2022) 164, arXiv:2205.09484 [hep-ph].

[248] V. De Romeri, O. G. Miranda, D. K. Papoulias, G. Sanchez Garcia, M. Tórtola, and J. W. F. Valle, "Physics implications of a combined analysis of COHERENT CsI and LAr data," arXiv:2211.11905 [hep-ph].

[249] **COHERENT** Collaboration, D. Akimov *et al.*, "First Measurement of Coherent Elastic Neutrino-Nucleus Scattering on Argon," *Phys. Rev. Lett.* **126** no. 1, (2021) 012002, arXiv:2003.10630 [nucl-ex].

[250] **COHERENT** Collaboration, D. Akimov *et al.*, "Measurement of the Coherent Elastic Neutrino-Nucleus Scattering Cross Section on CsI by COHERENT," *Phys. Rev. Lett.* **129** no. 8, (2022) 081801, arXiv:2110.07730 [hep-ex].

[251] E. E. Jenkins, A. V. Manohar, and P. Stoffer, "Low-Energy Effective Field Theory below the Electroweak Scale: Operators and Matching," *JHEP* **03** (2018) 016, arXiv:1709.04486 [hep-ph].

[252] M. Hoferichter, J. Menéndez, and A. Schwenk, "Coherent elastic neutrino-nucleus scattering: EFT analysis and nuclear responses," *Phys. Rev. D* **102** no. 7, (2020) 074018, arXiv:2007.08529 [hep-ph].

[253] V. Cirigliano, J. Jenkins, and M. Gonzalez-Alonso, "Semileptonic decays of light quarks beyond the Standard Model," *Nucl. Phys. B* **830** (2010) 95–115, arXiv:0908.1754 [hep-ph].

[254] M. González-Alonso, O. Naviliat-Cuncic, and N. Severijns, "New physics searches in nuclear and neutron β decay," *Prog. Part. Nucl. Phys.* **104** (2019) 165–223, arXiv:1803.08732 [hep-ph].

[255] A. Falkowski, M. González-Alonso, and O. Naviliat-Cuncic, "Comprehensive analysis of beta decays within and beyond the Standard Model," *JHEP* **04** (2021) 126, arXiv:2010.13797 [hep-ph].

[256] O. Tomalak, P. Machado, V. Pandey, and R. Plestid, "Flavor-dependent radiative corrections in coherent elastic neutrino-nucleus scattering," *JHEP* **02** (2021) 097, arXiv:2011.05960 [hep-ph].

[257] A. Falkowski, M. González-Alonso, A. Palavrić, and A. Rodríguez-Sánchez, "Constraints on subleading interactions in beta decay Lagrangian," arXiv:2112.07688 [hep-ph].

[258] C. Giunti, C. W. Kim, J. A. Lee, and U. W. Lee, "On the treatment of neutrino oscillations without resort to weak eigenstates," *Phys. Rev. D* **48** (1993) 4310–4317, arXiv:hep-ph/9305276.

[259] R. H. Helm, "Inelastic and Elastic Scattering of 187-Mev Electrons from Selected Even-Even Nuclei," *Phys. Rev.* **104** (1956) 1466–1475.

[260] M. Lindner, W. Rodejohann, and X.-J. Xu, "Coherent Neutrino-Nucleus Scattering and new Neutrino Interactions," *JHEP* **03** (2017) 097, arXiv:1612.04150 [hep-ph].

[261] B. C. Cañas, E. A. Garcés, O. G. Miranda, and A. Parada, "Future perspectives for a weak mixing angle measurement in coherent elastic neutrino nucleus scattering experiments," *Phys. Lett. B* **784** (2018) 159–162, arXiv:1806.01310 [hep-ph].

[262] X.-R. Huang and L.-W. Chen, "Neutron Skin in CsI and Low-Energy Effective Weak Mixing Angle from COHERENT Data," *Phys. Rev. D* **100** no. 7, (2019) 071301, arXiv:1902.07625 [hep-ph].

[263] A. N. Khan, D. W. McKay, and W. Rodejohann, "CP-violating and charged current neutrino nonstandard interactions in CEνNS," *Phys. Rev. D* **104** no. 1, (2021) 015019, arXiv:2104.00425 [hep-ph].

[264] M. Chaves and T. Schwetz, "Resolving the LMA-dark NSI degeneracy with coherent neutrino-nucleus scattering," *JHEP* **05** (2021) 042, arXiv:2102.11981 [hep-ph].

[265] **COHERENT** Collaboration, D. Akimov *et al.*, "COHERENT Collaboration data release from the first detection of coherent elastic neutrino-nucleus scattering on argon," arXiv:2006.12659 [nucl-ex].

[266] Y. Farzan and M. Tortola, "Neutrino oscillations and Non-Standard Interactions," *Front. in Phys.* **6** (2018) 10, arXiv:1710.09360 [hep-ph].

[267] F. J. Escrihuela, M. Tortola, J. W. F. Valle, and O. G. Miranda, "Global constraints on muon-neutrino non-standard interactions," *Phys. Rev. D* **83** (2011) 093002, arXiv:1103.1366 [hep-ph].

[268] S. Davidson, C. Pena-Garay, N. Rius, and A. Santamaria, "Present and future bounds on nonstandard neutrino interactions," *JHEP* **03** (2003) 011, arXiv:hep-ph/0302093.

[269] J. Colaresi, J. I. Collar, T. W. Hossbach, A. R. L. Kavner, C. M. Lewis, A. E. Robinson, and K. M. Yocum, "First results from a search for coherent elastic neutrino-nucleus scattering at a reactor site," *Phys. Rev. D* **104** no. 7, (2021) 072003, arXiv:2108.02880 [hep-ex].

[270] J. Salvado, O. Mena, S. Palomares-Ruiz, and N. Rius, "Non-standard interactions with high-energy atmospheric neutrinos at IceCube," *JHEP* **01** (2017) 141, arXiv:1609.03450 [hep-ph].

[271] **PiENu** Collaboration, A. Aguilar-Arevalo *et al.*, "Improved Measurement of the $\pi \to e\nu$ Branching Ratio," *Phys. Rev. Lett.* **115** no. 7, (2015) 071801, arXiv:1506.05845 [hep-ex].

[272] V. Cirigliano and I. Rosell, "pi/K —> e anti-nu(e) branching ratios to O(e**2 p**4) in Chiral Perturbation Theory," *JHEP* **10** (2007) 005, arXiv:0707.4464 [hep-ph].

[273] J. Terol-Calvo, M. Tórtola, and A. Vicente, "High-energy constraints from low-energy neutrino nonstandard interactions," *Phys. Rev. D* **101** no. 9, (2020) 095010, arXiv:1912.09131 [hep-ph].

[274] A. Crivellin, M. Hoferichter, M. Kirk, C. A. Manzari, and L. Schnell, "First-generation new physics in simplified models: from low-energy parity violation to the LHC," *JHEP* **10** (2021) 221, arXiv:2107.13569 [hep-ph].

[275] **SLD** Collaboration, K. Abe *et al.*, "First direct measurement of the parity violating coupling of the Z0 to the s quark," *Phys. Rev. Lett.* **85** (2000) 5059–5063, arXiv:hep-ex/0006019.

[276] **D0** Collaboration, B. Abbott *et al.*, "A measurement of the $W \to \tau\nu$ production cross section in $p\bar{p}$ collisions at $\sqrt{s} = 1.8$ TeV," *Phys. Rev. Lett.* **84** (2000) 5710–5715, arXiv:hep-ex/9912065.

[277] **LHCb** Collaboration, R. Aaij *et al.*, "Measurement of forward $W \to e\nu$ production in pp collisions at $\sqrt{s} = 8$ TeV," *JHEP* **10** (2016) 030, arXiv:1608.01484 [hep-ex].

[278] **ATLAS** Collaboration, M. Aaboud *et al.*, "Precision measurement and interpretation of inclusive W^+ , W^- and Z/γ^* production cross sections with the ATLAS detector," *Eur. Phys. J. C* **77** no. 6, (2017) 367, arXiv:1612.03016 [hep-ex].

[279] **ATLAS** Collaboration, G. Aad *et al.*, "Test of the universality of τ and μ lepton couplings in W-boson decays with the ATLAS detector," *Nature Phys.* **17** no. 7, (2021) 813–818, arXiv:2007.14040 [hep-ex].

[280] **LHCb** Collaboration, R. Aaij *et al.*, "Measurement of the W boson mass," *JHEP* **01** (2022) 036, arXiv:2109.01113 [hep-ex].

[281] **CDF** Collaboration, T. Aaltonen *et al.*, "Precise measurement of the W-boson mass with the CDF II detector," *Phys. Rev. Lett.* **108** (2012) 151803, arXiv:1203.0275 [hep-ex].

[282] **D0** Collaboration, V. M. Abazov *et al.*, "Measurement of the W Boson Mass with the D0 Detector," *Phys. Rev. Lett.* **108** (2012) 151804, arXiv:1203.0293 [hep-ex].

[283] **CMS** Collaboration, V. Khachatryan *et al.*, "Measurement of the t-channel single-top-quark production cross section and of the $| V_{tb} |$ CKM matrix element in pp collisions at $\sqrt{s}$= 8 TeV," *JHEP* **06** (2014) 090, arXiv:1403.7366 [hep-ex].

[284] **D0** Collaboration, V. M. Abazov *et al.*, "Measurement of $\sin^2\theta^{\ell}_{\text{eff}}$ and Z-light quark couplings using the forward-backward charge asymmetry in $p\bar{p} \to Z/\gamma^* \to e^+e^-$ events with $\mathcal{L} = 5.0$ fb^{-1} at $\sqrt{s} = 1.96$ TeV," *Phys. Rev. D* **84** (2011) 012007, arXiv:1104.4590 [hep-ex].

[285] **CHARM** Collaboration, J. V. Allaby *et al.*, "A Precise Determination of the Electroweak Mixing Angle from Semileptonic Neutrino Scattering," *Z. Phys. C* **36** (1987) 611.

[286] A. Blondel *et al.*, "Electroweak Parameters From a High Statistics Neutrino Nucleon Scattering Experiment," *Z. Phys. C* **45** (1990) 361–379.

[287] **CCFR, E744, E770** Collaboration, K. S. McFarland *et al.*, "A Precision measurement of electroweak parameters in neutrino - nucleon scattering," *Eur. Phys. J. C* **1** (1998) 509–513, arXiv:hep-ex/9701010.

[288] C. S. Wood, S. C. Bennett, D. Cho, B. P. Masterson, J. L. Roberts, C. E. Tanner, and C. E. Wieman, "Measurement of parity nonconservation and an anapole moment in cesium," *Science* **275** (1997) 1759–1763.

[289] N. H. Edwards, S. J. Phipp, P. E. G. Baird, and S. Nakayama, "Precise Measurement of Parity Nonconserving Optical Rotation in Atomic Thallium," *Phys. Rev. Lett.* **74** (1995) 2654–2657.

[290] P. A. Vetter, D. M. Meekhof, P. K. Majumder, S. K. Lamoreaux, and E. N. Fortson, "Precise test of electroweak theory from a new measurement of parity nonconservation in atomic thallium," *Phys. Rev. Lett.* **74** (1995) 2658–2661.

[291] **Qweak** Collaboration, D. Androić *et al.*, "Precision measurement of the weak charge of the proton," *Nature* **557** no. 7704, (2018) 207–211, arXiv:1905.08283 [nucl-ex].

[292] **PVDIS** Collaboration, D. Wang *et al.*, "Measurement of parity violation in electron–quark scattering," *Nature* **506** no. 7486, (2014) 67–70.

[293] V. Cirigliano, D. Díaz-Calderón, A. Falkowski, M. González-Alonso, and A. Rodríguez-Sánchez, "Semileptonic tau decays beyond the Standard Model," *JHEP* **04** (2022) 152, arXiv:2112.02087 [hep-ph].

[294] **UCNτ** Collaboration, F. M. Gonzalez *et al.*, "Improved neutron lifetime measurement with UCNτ," *Phys. Rev. Lett.* **127** no. 16, (2021) 162501, arXiv:2106.10375 [nucl-ex].

[295] **UCNA** Collaboration, M. A. P. Brown *et al.*, "New result for the neutron β-asymmetry parameter A_0 from UCNA," *Phys. Rev. C* **97** no. 3, (2018) 035505, arXiv:1712.00884 [nucl-ex].

[296] B. Märkisch *et al.*, "Measurement of the Weak Axial-Vector Coupling Constant in the Decay of Free Neutrons Using a Pulsed Cold Neutron Beam," *Phys. Rev. Lett.* **122** no. 24, (2019) 242501, arXiv:1812.04666 [nucl-ex].

[297] **CHARM** Collaboration, J. Dorenbosch *et al.*, "EXPERIMENTAL RESULTS ON NEUTRINO - ELECTRON SCATTERING," *Z. Phys. C* **41** (1989) 567. [Erratum: Z.Phys.C 51, 142 (1991)].

[298] L. A. Ahrens *et al.*, "Determination of electroweak parameters from the elastic scattering of muon-neutrinos and anti-neutrinos on electrons," *Phys. Rev. D* **41** (1990) 3297–3316.

[299] **SLAC E158** Collaboration, P. L. Anthony *et al.*, "Precision measurement of the weak mixing angle in Moller scattering," *Phys. Rev. Lett.* **95** (2005) 081601, arXiv:hep-ex/0504049.

[300] **CHARM-II** Collaboration, D. Geiregat *et al.*, "First observation of neutrino trident production," *Phys. Lett. B* **245** (1990) 271–275.

[301] A. Falkowski, M. Gonzalez-Alonso, A. Greljo, and D. Marzocca, "Global constraints on anomalous triple gauge couplings in effective field theory approach," *Phys. Rev. Lett.* **116** no. 1, (2016) 011801, arXiv:1508.00581 [hep-ph].

[302] P. Coloma, M. C. Gonzalez-Garcia, M. Maltoni, J. a. P. Pinheiro, and S. Urrea, "Global constraints on non-standard neutrino interactions with quarks and electrons," *JHEP* **08** (2023) 032, arXiv:2305.07698 [hep-ph].

[303] D. W. P. Amaral, D. Cerdeno, A. Cheek, and P. Foldenauer, "A direct detection view of the neutrino NSI landscape," *JHEP* **07** (2023) 071, arXiv:2302.12846 [hep-ph].

[304] P. Coloma, P. Coloma, M. C. Gonzalez-Garcia, M. C. Gonzalez-Garcia, M. Maltoni, M. Maltoni, J. a. P. Pinheiro, J. a. P. Pinheiro, S. Urrea, and S. Urrea, "Constraining new physics with Borexino Phase-II spectral data," *JHEP* **07** (2022) 138, arXiv:2204.03011 [hep-ph]. [Erratum: JHEP 11, 138 (2022)].

[305] D. Baxter *et al.*, "Coherent Elastic Neutrino-Nucleus Scattering at the European Spallation Source," *JHEP* **02** (2020) 123, arXiv:1911.00762 [physics.ins-det].

[306] https://www.hepdata.net/record/ins1630886.

[307] S. Camarda *et al.*, "DYTurbo: Fast predictions for Drell-Yan processes," *Eur. Phys. J. C* **80** no. 3, (2020) 251, arXiv:1910.07049 [hep-ph]. [Erratum: Eur.Phys.J.C 80, 440 (2020)].

[308] S. Camarda, L. Cieri, and G. Ferrera, "Drell–Yan lepton-pair production: qT resummation at N3LL accuracy and fiducial cross sections at N3LO," *Phys. Rev. D* **104** no. 11, (2021) L111503, arXiv:2103.04974 [hep-ph].

[309] S. Camarda, L. Cieri, and G. Ferrera, "Drell-Yan lepton-pair production: q_T resummation at approximate N^4LL+N^4LO accuracy," arXiv:2303.12781 [hep-ph].

[310] https://dyturbo.hepforge.org/.

[311] H.-L. Lai, M. Guzzi, J. Huston, Z. Li, P. M. Nadolsky, J. Pumplin, and C. P. Yuan, "New parton distributions for collider physics," *Phys. Rev. D* **82** (2010) 074024, arXiv:1007.2241 [hep-ph].

[312] T. Bhattacharya, V. Cirigliano, S. D. Cohen, A. Filipuzzi, M. Gonzalez-Alonso, M. L. Graesser, R. Gupta, and H.-W. Lin, "Probing Novel Scalar and Tensor Interactions from (Ultra)Cold Neutrons to the LHC," *Phys. Rev. D* **85** (2012) 054512, arXiv:1110.6448 [hep-ph].

[313] V. Cirigliano, M. Gonzalez-Alonso, and M. L. Graesser, "Non-standard Charged Current Interactions: beta decays versus the LHC," *JHEP* **02** (2013) 046, arXiv:1210.4553 [hep-ph].

[314] J. de Blas, M. Chala, and J. Santiago, "Global Constraints on Lepton-Quark Contact Interactions," *Phys. Rev. D* **88** (2013) 095011, arXiv:1307.5068 [hep-ph].

[315] **ATLAS** Collaboration, "Search for high-mass dilepton resonances in $20^{\sim} fb^{-1}$ of pp collisions at $\sqrt{s} = 8^{\sim}$TeV with the ATLAS experiment,".

[316] **CMS** Collaboration, "Search for Extra Dimensions in Dimuon Events in pp Collisions at sqrt(s) = 8 TeV,".

[317] **CMS** Collaboration, "Search for Large Extra Spatial Dimensions in Dielectron Production with the CMS Detector,".

[318] M. Farina, G. Panico, D. Pappadopulo, J. T. Ruderman, R. Torre, and A. Wulzer, "Energy helps accuracy: electroweak precision tests at hadron colliders," *Phys. Lett. B* **772** (2017) 210–215, arXiv:1609.08157 [hep-ph].

[319] L. Allwicher, D. A. Faroughy, F. Jaffredo, O. Sumensari, and F. Wilsch, "Drell-Yan tails beyond the Standard Model," *JHEP* **03** (2023) 064, arXiv:2207.10714 [hep-ph].

[320] A. Greljo, J. Salko, A. Smolkovič, and P. Stangl, "Rare b decays meet high-mass Drell-Yan," *JHEP* **05** (2023) 087, arXiv:2212.10497 [hep-ph].

[321] A. Angelescu, D. A. Faroughy, and O. Sumensari, "Lepton Flavor Violation and Dilepton Tails at the LHC," *Eur. Phys. J. C* **80** no. 7, (2020) 641, arXiv:2002.05684 [hep-ph].

[322] S. Carrazza, C. Degrande, S. Iranipour, J. Rojo, and M. Ubiali, "Can New Physics hide inside the proton?," *Phys. Rev. Lett.* **123** no. 13, (2019) 132001, arXiv:1905.05215 [hep-ph].

[323] A. Greljo, S. Iranipour, Z. Kassabov, M. Madigan, J. Moore, J. Rojo, M. Ubiali, and C. Voisey, "Parton distributions in the SMEFT from high-energy Drell-Yan tails," *JHEP* **07** (2021) 122, arXiv:2104.02723 [hep-ph].

[324] R. Contino, A. Falkowski, F. Goertz, C. Grojean, and F. Riva, "On the Validity of the Effective Field Theory Approach to SM Precision Tests," *JHEP* **07** (2016) 144, arXiv:1604.06444 [hep-ph].

[325] **CMS** Collaboration, V. Khachatryan *et al.*, "Forward–backward asymmetry of Drell–Yan lepton pairs in pp collisions at $\sqrt{s} = 8$ TeV," *Eur. Phys. J. C* **76** no. 6, (2016) 325, arXiv:1601.04768 [hep-ex].

[326] **CMS** Collaboration, A. M. Sirunyan *et al.*, "Measurement of the weak mixing angle using the forward-backward asymmetry of Drell-Yan events in pp collisions at 8 TeV," *Eur. Phys. J. C* **78** no. 9, (2018) 701, arXiv:1806.00863 [hep-ex].

[327] **CMS** Collaboration, A. Tumasyan *et al.*, "Measurement of the Drell-Yan forward-backward asymmetry at high dilepton masses in proton-proton collisions at $\sqrt{s} = 13$ TeV," *JHEP* **2022** no. 08, (2022) 063, arXiv:2202.12327 [hep-ex].

[328] **LHCb** Collaboration, R. Aaij *et al.*, "First Measurement of the Z→μ+μ- Angular Coefficients in the Forward Region of pp Collisions at s=13 TeV," *Phys. Rev. Lett.* **129** no. 9, (2022) 091801, arXiv:2203.01602 [hep-ex].

[329] J. D. Lewin and P. F. Smith, "Review of mathematics, numerical factors, and corrections for dark matter experiments based on elastic nuclear recoil," *Astropart. Phys.* **6** (1996) 87–112.

[330] I. Angeli and K. Marinova, "Table of experimental nuclear ground state charge radii: An update," *Atomic Data and Nuclear Data Tables* **99** no. 1, (2013) 69–95. https://www.sciencedirect.com/science/article/pii/S0092640X12000265.

[331] G. Fricke, C. Bernhardt, K. Heilig, L. Schaller, L. Schellenberg, E. Shera, and C. Dejager, "Nuclear ground state charge radii from electromagnetic interactions," *Atomic Data and Nuclear Data Tables* **60** no. 2, (1995) 177–285. https://www.sciencedirect.com/science/article/pii/S0092640X85710078.

[332] S. Klein and J. Nystrand, "Exclusive vector meson production in relativistic heavy ion collisions," *Phys. Rev. C* **60** (1999) 014903, arXiv:hep-ph/9902259.

[333] P. Klos, J. Menéndez, D. Gazit, and A. Schwenk, "Large-scale nuclear structure calculations for spin-dependent WIMP scattering with chiral effective field theory currents," *Phys. Rev. D* **88** no. 8, (2013) 083516, arXiv:1304.7684 [nucl-th]. [Erratum: Phys.Rev.D 89, 029901 (2014)].

[334] E. Picciau, *Low-energy signatures in DarkSide-50 experiment and neutrino scattering processes.* PhD thesis, Cagliari U., 2022.

[335] W. Creus, *Light yield in liquid argon for dark matter detection.* PhD thesis, University of Zurich, 2013.